Application of spherical cap harmonic analysis to plasma convection mapping at high latitudes

A Thesis Submitted to the
College of Graduate Studies and Research
in Partial Fulfillment of the Requirements
for the degree of Doctor of Philosophy
in the Department of Physics and Engineering Physics
University of Saskatchewan
Saskatoon

By
Robyn A. D. Fiori

Permission to Use

In presenting this thesis in partial fulfilment of the requirements for a Postgraduate degree from the University of Saskatchewan, I agree that the Libraries of this University may make it freely available for inspection. I further agree that permission for copying of this thesis in any manner, in whole or in part, for scholarly purposes may be granted by the professor or professors who supervised my thesis work or, in their absence, by the Head of the Department or the Dean of the College in which my thesis work was done. It is understood that any copying or publication or use of this thesis or parts thereof for financial gain shall not be allowed without my written permission. It is also understood that due recognition shall be given to me and to the University of Saskatchewan in any scholarly use which may be made of any material in my thesis.

Requests for permission to copy or to make other use of material in this thesis in whole or part should be addressed to:

Head of the Department of Physics and Engineering Physics
Physics Building
116 Science Place
University of Saskatchewan
Saskatoon, Saskatchewan
Canada
S7N 5E2

Abstract

The primary goal of this work is to develop, validate, and apply a new technique for mapping the high-latitude ionospheric plasma flow (convection pattern) from velocity measurements routinely performed by the Super Dual Auroral Radar (SuperDARN) network of high frequency (HF) radars. The currently employed FIT technique relies heavily on assumptions that are not always justifiable. A spherical cap harmonic analysis (SCHA) technique, traditionally used in handling geomagnetic field data, is introduced for mapping the high-latitude ionospheric convection pattern based on SuperDARN velocity measurements. The SCHA technique does not require contributions from a statistical model which is dependent on the magnitude and orientation of the interplanetary magnetic field (IMF), and does not confine the high-latitude flows to a specific region based on magnetic latitude.

Several steps are taken to validate the SCHA convection mapping technique. First, it is demonstrated that the SCHA technique can reproduce an arbitrary pattern based on simulated data modified by a random noise component. SCHA maps of the global scale plasma flow pattern for various IMF conditions are next shown to be consistent with expectations for patterns reported in the literature. SCHA maps are compared to ion drifts measured by the Defense Meteorological Satellite Program (DMSP) satellites and with convection vectors inferred by merging SuperDARN measurements at beam crossings. The SCHA technique is shown to perform comparably to the FIT technique over regions of good data coverage. The SCHA technique provides a better representation of the ionospheric convection pattern for regions with limited data coverage and over regions of highly variable flow, particularly near the equatorward edge of the mapping region.

SCHA analysis of SuperDARN data to create convection maps is expanded to include magnetometer measurements of the perturbation magnetic field. Plasma flow is determined from magnetometer data by combining the equivalent current determined from the external component of the perturbation magnetic field with a model of the ionospheric conductivity.

The SCHA technique is used to investigate the reconfiguration of the convection pattern and changes to the cross polar-cap potential (CPCP) associated with a sudden transition in

the vertical component of the IMF from stable positive to stable negative values. For such events, the FIT technique might misrepresent the convection pattern if the fitting is dominated by the a-priori statistical convection model. Both magnetometer and SuperDARN data sets are examined. The IMF transition wavefront impinges upon the magnetosphere near the 10 MLT sector; perturbations are clearly seen on the dayside with a $\sim$10 minute delay on the nightside. This translates into a dayside-to-nightside progression of the ionospheric response observed in the magnetic perturbations and SuperDARN velocities, contrary to what was reported for a number of other events in the literature. The foci of the new dawn and duskside convection cells are shown to steadily shift toward the dayside (over a period of 10-12 minutes, beginning 4-6 minutes after the onset of the ionospheric response) and do not 'snap' to their final position. Once the convection foci reach a final location, the overall convection pattern enhances for a period of $\sim$25 minutes. These results support the idea that the ionospheric convection response to a southward turning of the IMF is a two-stage process; (1) an initial dayside-to-nightside progression of the observed ionospheric response and a reconfiguration of the convection pattern, and (2) the subsequent intensification of the convection pattern.

An additional investigation is performed to determine whether the polar cap north (PCN) magnetic index is satisfactory for estimating the CPCP and average cross polar cap flow velocity (CPCV). A roughly linear increase of both the CPCP and CPCV with PCN is found for $0 \leq \text{PCN} \leq 4$, with a tendency for saturation for PCN > 4. The CPCP calculated using the SCHA-technique is found to be larger than that calculated using the FIT-technique. PCN is concluded to be a good proxy for the CPCV and CPCP for $0 \leq \text{PCN} \leq 4$.

Acknowledgements

Thank you to my supervisor Dr. Sasha Koustov for teaching me how to be a researcher. Your guidance, careful attention, and criticisms have pushed me to expand my limits and abilities. Thank you to my supervisor Dr. David Boteler for providing me with both an enthusiastic and supportive learning environment. Working with you has been, and continues to be, both a rewarding and enjoyable experience. Thank you to Gerry Haines for mentoring me.

I would also like to thank my fellow students at the University of Saskatchewan and co-workers at the Geomagnetic Laboratory for the abundance of help, instruction, and advice you've provided.

Thank you to my family, especially Patrick, for your love, support, and understanding. Finally, thank you to Jacob for napping.

Contents

List of Tables

List of Figures

List of Abbreviations

ACE	Advanced Composition Explorer
ACF	Autocorrelation Function
AMIE	Assimilative Mapping of Ionospheric Electrodynamics
BATS-R-US	Block Adaptive-Tree Solar-wind Roe-Type Upwind Scheme
CADI	Canadian Advanced Digital Ionosonde
CANMOS	Canadian Auroral Network for the OPEN Program Unified Study
CARISMA	Canadian Array for Real-time Investigations of Magnetic Activity
CGM	Corrected Geomagnetic
CPCP	Cross Polar Cap Potential
CPCV	Cross Polar Cap Velocity
cf	curl-free
df	divergence-free
DMSP	Defense Meteorological Satellite Program
EFI	Electric Field Instrument
EISCAT	European Incoherent Scatter
emf	electromotive force
FAC	Field Aligned Current
FFT	Fast Fourier Transform
GSM	Geocentric Solar Magnetospheric
HF	High Frequency
HMB	Heppner Maynard Boundary
IAGA	International Association of Geomagnetism and Aeronomy
IGRF	International Geomagnetic Reference Field
IMF	Interplanetary Magnetic Field
INTERMAGNET	International Real-time Magnetic Observatory Network
ISR	Incoherent Scatter Radar
JHU APL	John Hopkins University Applied Physics Laboratory
KRM	Kamide-Richmond-Matsushita
l-o-s	line-of-sight
MACCS	Magnetometer Array for Cusp and Cleft Studies
MHD	magnetohydrodynamic
MLAT	Magnetic Latitude
MLT	Magnetic Local Time
NRCan	Natural Resources Canada
NS	Non-Standard
PC	Polar Cap
PCN	Polar Cap North
PolarDARN	Polar Dual Auroral Radar Network
RTI	Range-Time-Intensity

RKN	Rankin Inlet
SCHA	Spherical Cap Harmonic Analysis
SECS	Spherical Elementary Current System
SHA	Spherical Harmonic Analysis
StormDARN	Storm Dual Auroral Radar Network
SuperDARN	Super Dual Auroral Radar Network
UT	Universal Time

Chapter 1

Introduction

The interaction between plasma continuously streaming out from the Sun (solar wind) and its embedded interplanetary magnetic field (IMF) with the Earth's magnetic field and atmosphere is a key process in space weather which has become an important issue as it affects a wide range of technologies and infrastructure on the ground and in space. Energetic particles from the Sun interact with the Earth's magnetic field, so they are energized and precipitate into the upper atmosphere increasing ionization in the atmosphere from 100 to 1000 km above the Earth's surface. These high energy particles also affect satellites causing incorrect operation or equipment damage that can put the satellite out of operation. Radio waves used for communication systems or GPS navigation are affected by the increased ionization which can cause a disruption of the communication or navigation systems. Precipitating particles, in combination with electric fields, create strong currents at a height of $\sim$ 100 km; these currents produce perturbations of the Earth's magnetic field. Magnetic disturbances associated with the Sun-Earth interaction may directly affect operations that rely on the geomagnetic field, such as magnetic surveys, directional drilling, or compass use. Geomagnetically induced currents in long conductors such as power lines and pipelines can cause power system outages or pipeline corrosion. These examples, which illustrate the widespread effects of space weather, demonstrate the importance of studying the interaction between the Sun and the Earth.

Activity originating from the Sun is transmitted to the Earth by the solar wind and results in a redistribution of particles and the establishment of electric currents in the magnetosphere and ionosphere. Changes in ionospheric processes are reflected in the high-latitude plasma flow, currents, and conductivity that may be measured by various ground-based and satellite instruments. Plasma circulation, or convection, in the ionosphere follows regular

patterns dependent on the polarity and strength of the individual components of the IMF. Sudden changes in the polarity of the y and z components of the IMF (B_y and B_z, respectively) result in a reconfiguration of the ionospheric convection pattern. The transition between quasi-steady state convection patterns is not well understood and will be examined in this thesis following a description of the relative regions and processes which occur in the near Earth space.

In the following sections a short description of the solar wind, magnetosphere, and ionosphere is provided following the works of *Hargreaves* (1992), *Kivelson and Russell* (1995), and *Baumjohann and Treumann* (1997).

1.1 Solar wind and the magnetosphere

The Sun continuously ejects a stream of highly conducting plasma known as the solar wind. As the solar wind flows radially outward from the Sun, the solar magnetic field lines associated with the plasma are dragged along, creating the IMF. The pointing direction of the IMF is defined using the geocentric solar magnetospheric (GSM) coordinate system where the x-axis points sunward, the z-axis is parallel to the Earth's magnetic dipole, and the y-axis completes a right-handed coordinate system, see Figure 1.1. In the time it takes the solar wind to travel from the Sun to the Earth ($\sim 10^{11}$ m), the magnetic field is only able to diffuse a fraction of that distance ($\sim 10^3$ m). The IMF is therefore thought of as being 'frozen-in' to the solar wind. Typical IMF values are 1-10 nT and solar wind particle density and speeds are $\sim$5 cm^{-3} and $\sim$400 km/s, respectively.

As the solar wind travels outward from the Sun, it encounters the Earth's geomagnetic field, which can be approximated by a dipole field with an axis tilted $\sim 11^\circ$ from the Earth's spin axis. The dipole geomagnetic field ($\mathbf{B}$) is (*Baumjohann and Treumann*, 1997)

$$\mathbf{B}(r,\lambda) = \frac{\mu_0 M_E}{4\pi r^3}\left(-2\sin\lambda\hat{\boldsymbol{r}} + \cos\lambda\hat{\boldsymbol{\lambda}}\right), \tag{1.1}$$

where $M_E = 8.05 \times 10^{22}\ Am^2$ is the Earth's dipole moment, and μ_0 is the magnetic permeability of free space. Since the magnetic dipole axis is tilted with respect to the Earth's spin axis, equation (1.1) is expressed in the geomagnetic coordinate system, as opposed to

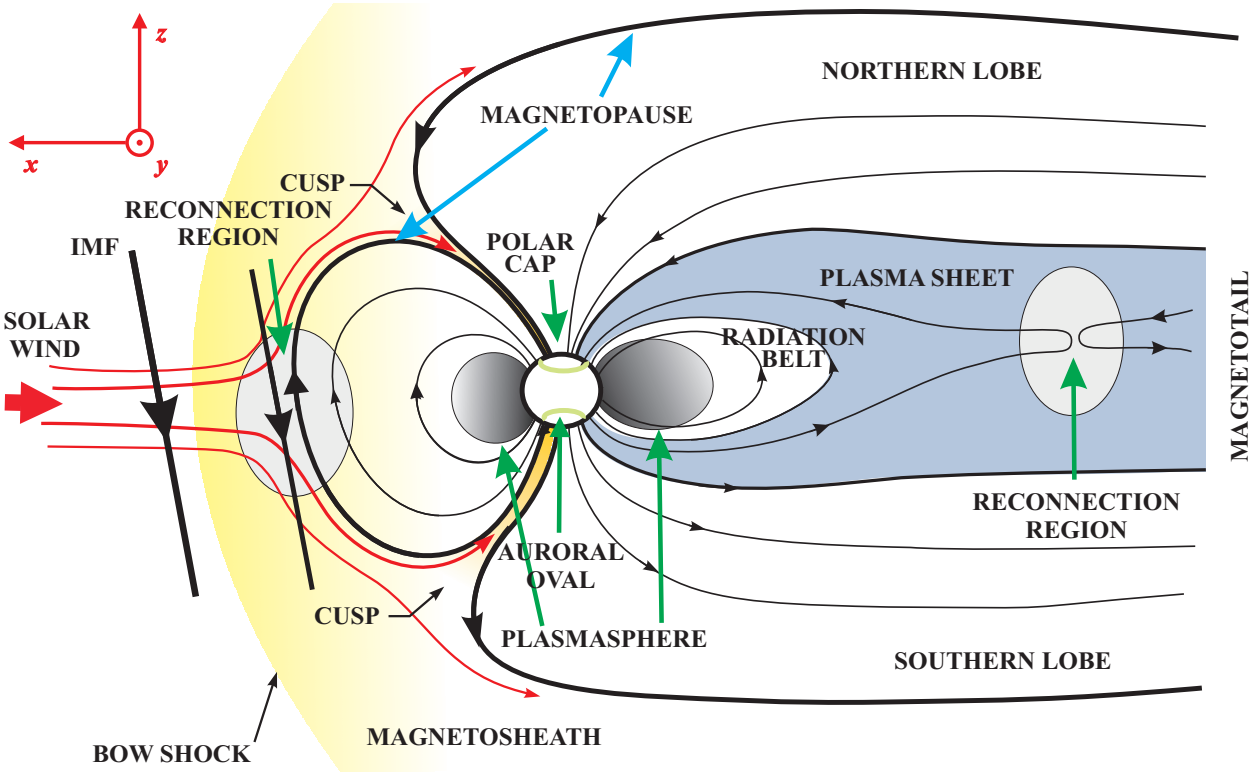

Figure 1.1: Magnetospheric cross-section in the north-south plane with the solar-magnetospheric coordinate system overplotted (adapted from original schematic by K. McWilliams).

the geocentric or geodetic coordinate systems (see Appendix A.1 and A.2) where r is the radius from the center of the Earth, λ is magnetic latitude, and $\mathbf{B}$ is independent of magnetic longitude ϕ. The solar wind is unable to penetrate the geomagnetic field and instead distorts it creating a cavity called the magnetosphere. Figure 1.1 schematically depicts the magnetosphere and surrounding environment. The front-side magnetosphere has a rounded shape and extends to ~10 Earth radii (R_E) on the dayside, whereas the magnetotail is elongated and extends to 50-100 R_E on the nightside.

As the solar wind flows toward the Earth, the magnetosphere blocks its path and a shock wave, or bow shock, is established 2-3 R_E sunward of the outer region of the magnetosphere, called the magnetopause. The solar wind is slowed down to subsonic speeds by dissipating the kinetic energy of its particles at the bow shock. The solar wind then enters the magnetosheath, which is the region between the bow shock and the magnetopause. Plasma in the magnetosheath may directly enter the magnetosphere at the cusp.

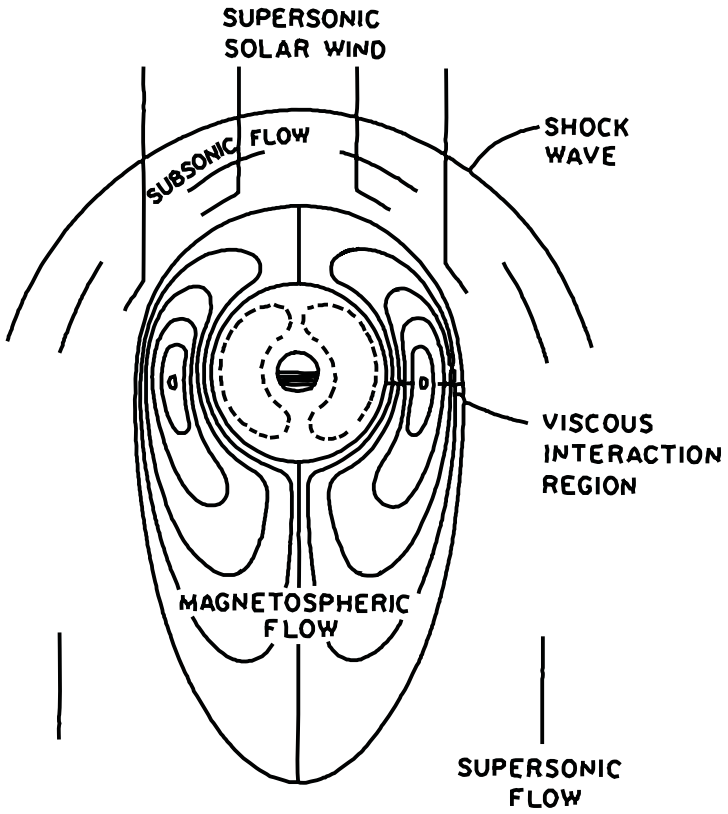

Figure 1.2: Major regions and processes occurring in the course of quasi-viscous interaction of the solar wind and magnetosphere (*Kelley*, 1989).

The solar wind interacts with the magnetosphere through the processes of quasi-viscous interaction and reconnection. In quasi-viscous interaction (*Axford and Hines*, 1961), the solar wind flows around the egg-shaped magnetosphere dragging along the IMF, see Figure 1.2. Energy and momentum are transferred from the solar wind to the outer magnetosphere causing anti-sunward flow in the boundary layer of the enclosed plasma. Because the system is closed, the flow reverses in the magnetotail causing plasma to move toward and around the inner magnetosphere (circular region). Energy and momentum of the sunward motion of the inner edge of the outer magnetosphere is transferred to the outer edges of the inner magnetosphere. This flow reverses on the dayside, causing anti-sunward flow in the central region of the inner magnetosphere.

Reconnection involves the interconnection of IMF and geomagnetic field lines. Reconnection regions differ depending on the orientation of the IMF with respect to the geomagnetic field lines and will be discussed according to the descriptions of *Watanabe and*

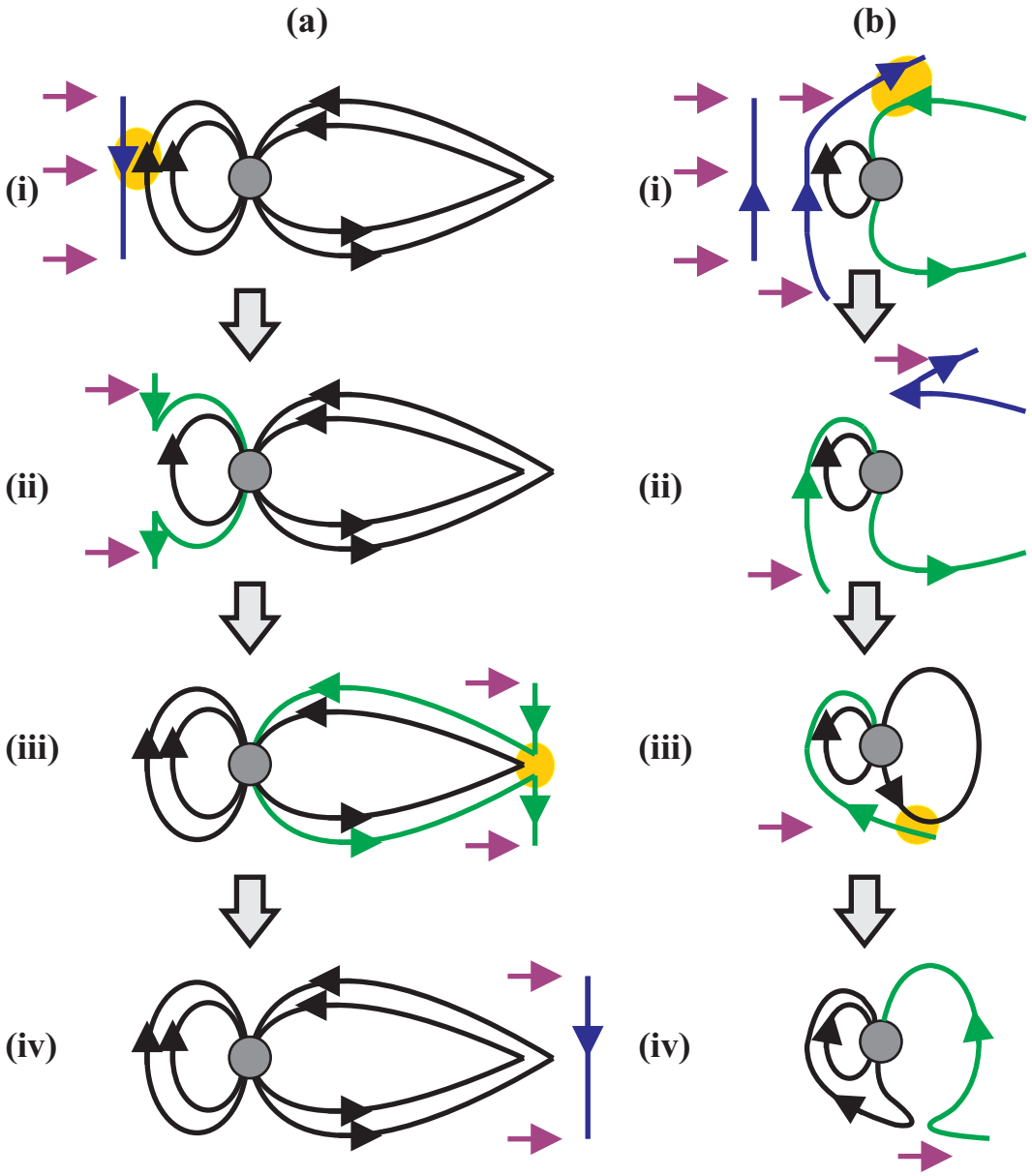

Figure 1.3: Illustration of (a) Dungey and (b) interchange reconnection processes. IMF, open, and closed magnetic field lines are shown in blue, green, and black, respectively. Additional purple arrows indicate the solar wind flow. Regions where reconnection occurs are indicated by yellow shading. See text for explanations.

Sofko (2008). For southward IMF ($B_z < 0$), the Dungey (*Dungey*, 1961) reconnection process occurs; see Figure 1.3a. In Figure 1.3a (i), the southward oriented IMF line (blue) approaches the northward ($B_z > 0$) oriented geomagnetic field line (black) at the front-side magnetosphere. The geomagnetic field lines are closed as both ends are connected to the Earth. When the anti-parallel lines meet, the net field goes to zero and the IMF and geo-

magnetic field lines interconnect in the reconnection region (yellow shading) to form an open magnetic field line (green) in either hemisphere. Each open magnetic field line has one end in the solar wind and the other attached to the Earth's magnetic field lines in either the northern or the southern hemisphere, as shown in Figure 1.3a (ii). The newly formed open field lines are carried by the solar wind into the magnetotail, where they reconnect to form a closed geomagnetic field line, which has essentially been transported from the front-side magnetosphere to the magnetotail, and a separate IMF line traveling away from the Earth (shown in Figure 1.3a (iii) and (iv)). After reconnection, the stretched geomagnetic field lines in the magnetotail move back toward the Earth, causing particles in the magnetotail to be accelerated Earthward.

When the IMF is directed northward, the interchange reconnection process illustrated in Figure 1.3b occurs (*Watanabe and Sofko*, 2009). Figure 1.3b (i) and (ii) show the first step of the interchange cycle. Northward oriented IMF field lines (blue) approach and drape around the front-side magnetosphere. Both the IMF and geomagnetic field lines are oriented northward in the reconnection region previously discussed in the Dungey reconnection process, so reconnection does not take place here. Instead, the IMF field line reconnects with an open magnetic field line (green) from the magnetotail in the high-latitude region, forming an overdraped open magnetic field line wrapping around the front-side magnetosphere and a new IMF magnetic field line (Figure 1.3b (ii)). In the second step of the interchange cycle, Figure 1.3b (iii) and (iv), the overdraped open magnetic field line encounters and reconnects with a closed magnetic field line from the magnetotail to create a closed magnetic field line in the front-side magnetosphere and an open magnetic field line in the magnetotail.

The outer magnetosphere is separated into regions based on the average plasma density and energy of the particles populating that region (see Figure 1.1). The outermost region of the magnetotail, called the plasma mantle (not shown), is populated by particles with energies of 30-150 eV and has a density of 0.1-10 cm^{-3}. The mantle surrounds the sparsely populated (< 0.1 cm^{-3}) north and south magnetotail lobes. Both the plasma mantle and tail lobes lie on regions of open magnetic field lines. The northern and southern tail lobes are characterized by geomagnetic field lines pointing toward and away from the Earth, respectively.

The magnetotail is separated into northern and southern regions by the plasma sheet, which is surrounded by the plasma sheet boundary layer. The plasma sheet is centered near the equatorial plane with its inner edge at $\sim$7 R_E at midnight. Particle density in the plasma sheet is about 0.1-1 cm^{-3}, and it is comprised mostly of H^+ ions and electrons. Typical particle energies lie between 0.1 keV and 10 keV with an average energy of 0.6 eV for electrons and 5 keV for protons (*Hargreaves*, 1992). The plasma sheet has a thickness of 1-5 R_E and extends between the dawn and dusk region. Periods of increased convection cause an inward (Earthward) motion of the plasma sheet. Some of the energetic particles moving Earthward from the plasma sheet become trapped in magnetic field-aligned regions called radiations belts which extend from $\sim$1000 km above the Earth's surface to a distance of $\sim 6R_E$. Radiation belt particles have energies in the 10-100 keV range. These particles gyrate about the magnetic field, bounce between hemispheres, and drift azimuthally about the Earth with ions and electrons moving in opposite directions. The relative drift between charged particles forms a westward flowing ring current at a radial distance of 4-6 R_E. Magnetic field lines within the radiation belts are closed.

Closer to the Earth is another closed-field line region called the plasmasphere which contains a cold (1 eV), dense (10^3 cm^{-3}) particle population. The magnetic field in the plasmasphere can be approximated as a dipole with plasma roughly co-rotating with the Earth. The outer boundary of the plasmasphere, the plasmapause, is typically located between 3 and 4 R_E, depending on the relative strength of plasma co-rotating with the Earth and convecting Earthward from the magnetotail.

1.2 Ionosphere

Above an altitude of $\sim$70 km, photoionization, recombination, and transport processes populate the upper atmosphere with ions and electrons forming a neutral plasma called the ionosphere. The weakly ionized plasma is organized into distinct layers shown by the vertical electron density profile, Figure 1.4. The D region is the lowest and peaks at an altitude of $\sim$90 km, with an electron density of $n_e \sim 10^4$ cm^{-3}. The E region peaks at $\sim$110 km with $n_e \sim 10^5$ cm^{-3}. At approximately 250 km, the F region peaks with an electron density of

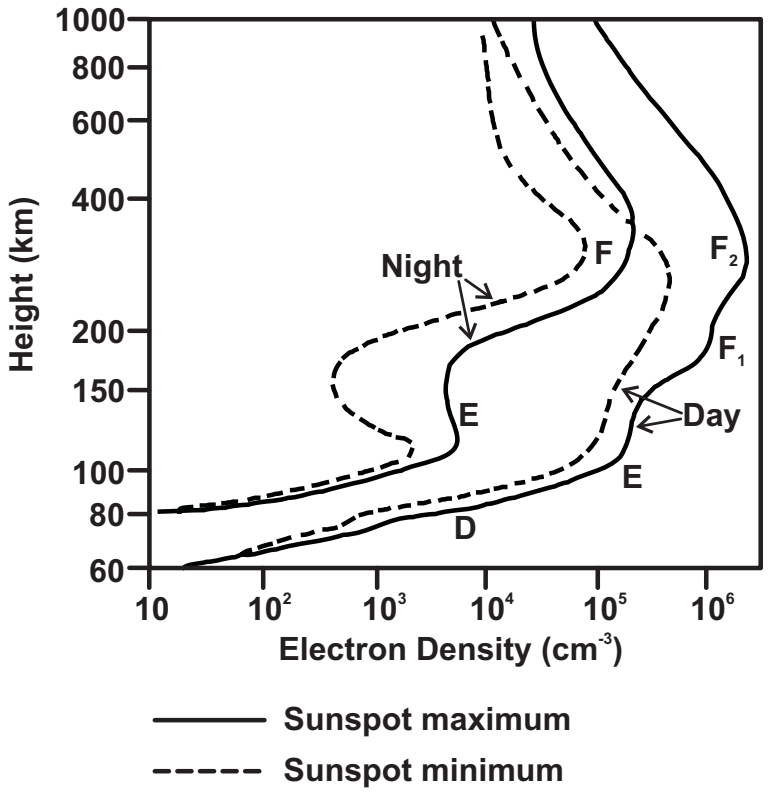

Figure 1.4: Ionospheric electron density profiles at mid-latitudes for day and night at sunspot maximum and minimum (adapted from *Hargreaves* (1992)).

$n_e \sim 10^6\ cm^{-3}$. During the day the F region peaks at ∼170 km (F1 region) and ∼300 km (F2 region).

1.2.1 Formation of the ionosphere

In the E region the photoionization of N_2, which is abundant at these altitudes, by ultraviolet radiation leads to an accumulation of NO^+ and electrons through an interchange reaction involving O. At night, a lack of photons significantly reduces ion production, and the E region disappears as ions and electrons are removed through recombination reactions. At F-region altitudes, there is little N_2 due to rapid diffusion, and O particles dominate. Photoionization reactions therefore cause an accumulation of O^+ and electrons, forming another distinct layer. Although ionization also decreases at night, the F region does not disappear like the E region.

Another source of ionization is the precipitation of energetic (> 1 keV) particles. Energetic particles colliding with neutral particles may cause the separation of the neutral

particle into a positive ion and a secondary electron, provided the energy of the colliding particle exceeds the binding-energy of the neutral. For an oxygen atom, the binding-energy is ∼35 eV (*Rees and Luckey*, 1974). A single energetic particle may cause the ionization of multiple neutral particles before losing its energy. In addition, the secondary electrons produced in the collisions may have enough energy to ionize additional neutrals. Sources of energetic particles include auroral electrons (see Section 1.3) and protons ejected from the Sun during solar flares. Ionization by energetic particles tends to dominate on the nightside where photoionization rates are reduced, and at high-latitudes where the magnetic field lines guide precipitating particles into the ionosphere.

1.2.2 Ohm's law for ionospheric plasma

Ionospheric plasma is affected by the background electric (**E**) and magnetic (**B**) fields. The general equation of motion for ionospheric ions and electrons is (*Kelley*, 1989)

$$m_{i,e}\frac{d\mathbf{v}_{i,e}}{dt} = q_{i,e}\left[\mathbf{E} + \mathbf{v}_{i,e} \times \mathbf{B}\right] - m_{i,e}\nu_{(i,e)n}\left(\mathbf{v}_{i,e} - \mathbf{U}_n\right) \pm m_e\nu_{ei}\left(\mathbf{v}_e - \mathbf{v}_i\right) - \frac{\nabla\left(n_{i,e}T_{i,e}\right)}{n_{i,e}}, \tag{1.2}$$

where the subscripts i and e denote ions and electrons, m is the particle mass, $\mathbf{v}$ is the fluid velocity, q is the charge, $\nu_{(i,e)n}$ is the ion or electron collision frequency with neutrals, ν_{ei} is the electron-ion collision frequency, $\mathbf{U}_n$ is the neutral wind velocity, T is the temperature (in units of energy), and n is the particle density. In the third term of the right hand side, the positive and negative sign applies to ions and electrons, respectively. In the cold approximation ($T_{i,e}$=0 eV) for the bottom of the F region ($\nu_{(i,e)n} \gg \nu_{ei}$) and neglecting the effects of the neutral wind ($\mathbf{U}_n$=0 m/s), equation (1.2) becomes:

$$m_{i,e}\frac{d\mathbf{v}_{i,e}}{dt} = q_{i,e}\left[\mathbf{E} + \mathbf{v}_{i,e} \times \mathbf{B}\right] - m_{i,e}\nu_{(i,e)n}\mathbf{v}_{i,e}. \tag{1.3}$$

For stationary conditions ($\frac{d\mathbf{v}_{i,e}}{dt} = 0$), the $\mathbf{v}_{i,e}$ is given by

$$\mathbf{v}_{i,e} = \frac{\Omega_{i,e}^2}{\Omega_{i,e}^2 + \nu_{(i,e)n}^2}\mathrm{v}_E\frac{\mathbf{E}\times\mathbf{B}}{|\,\mathbf{E}\times\mathbf{B}\,|} + \frac{\Omega_{i,e}\nu_{(i,e)n}}{\Omega_{i,e}^2 + \nu_{(i,e)n}^2}\mathrm{v}_E\frac{\mathbf{E}_\perp}{|\,\mathbf{E}_\perp\,|} + \frac{\Omega_{i,e}}{\nu_{(i,e)n}}\frac{E_{||}}{B}\frac{\mathbf{E}_{||}}{|\,\mathbf{E}_{||}\,|}, \tag{1.4}$$

where $\Omega_{i,e}$ is the ion or electron gyrofrequency defined by $\Omega_{i,e} = \frac{q_{i,e}B}{m_{i,e}}$. In the F region,

the electron and ion collision frequencies with neutrals are to the order of 10 s^{-1} and 1 s^{-1}, respectively. The electron and ion gyrofrequencies are of the order of 10^7 s^{-1} and 10^2 s^{-1}, respectively. In equation (1.4), the electric field can have components perpendicular ($\mathbf{E}_\perp$) and parallel ($\mathbf{E}_{||}$) to the magnetic field. Speed v_E is the magnitude of the drift experienced by the particles in a collisionless plasma in the presence of constant electric and magnetic fields and is defined as

$$\mathbf{v}_E = \frac{\mathbf{E} \times \mathbf{B}}{B^2}, \quad \text{where} \quad \mathrm{v}_E = \frac{E_\perp}{B}, \tag{1.5}$$

and v_E is independent of charge. In the F region $\nu_{\alpha n} \ll \Omega_\alpha$, and equation (1.4) is reduced to

$$\mathbf{v}_\alpha = \mathrm{v}_E \frac{\mathbf{E}_\perp \times \mathbf{B}}{|\, \mathbf{E}_\perp \times \mathbf{B} \,|} + \frac{\nu_{\alpha n}}{\Omega_\alpha} \mathrm{v}_E \frac{\mathbf{E}_\perp}{|\, \mathbf{E}_\perp \,|} + \frac{\Omega_\alpha}{\nu_{\alpha n}} \frac{E_{||}}{B} \frac{\mathbf{E}_{||}}{|\, \mathbf{E}_{||} \,|}. \tag{1.6}$$

According to the first term in equation (1.6), F-region ions and electrons move in the same direction, or convect, in the $\mathbf{E}\times\mathbf{B}$ direction. In contrast, the second and third terms in equation (1.6) show there is a relative drift between ions and electrons along the electric field and along the magnetic field; ions move faster than electrons along the electric field, and electrons move faster than ions along the magnetic field.

The relative drift between ions and electrons in the ionosphere results in the flow of current having a current density of

$$\mathbf{j} = en\mathbf{v}_d, \tag{1.7}$$

where $e = 1.602 \times 10^{-19}$ C is the charge of an electron, $\mathbf{v}_d = \mathbf{v}_i - \mathbf{v}_e$ is the relative drift between ions and electrons, $n = n_e = n_i$ is the electron and ion particle density, and $\mathbf{j}$ has units of A/m^2. The current density can be represented by components and written as Ohm's law

$$\mathbf{j} = \bar{\bar{\sigma}} \cdot \mathbf{E}, \tag{1.8}$$

where $\mathbf{E}$ is the electric field in units of V/m and $\bar{\bar{\sigma}}$ is the conductivity tensor in units of S/m (*Hargreaves*, 1992)

$$\bar{\bar{\sigma}} = \begin{pmatrix} \sigma_P & \sigma_H & 0 \\ -\sigma_H & \sigma_P & 0 \\ 0 & 0 & \sigma_{||} \end{pmatrix}, \quad \text{where} \tag{1.9}$$

$$\sigma_P = \frac{en}{B}\left(\frac{\mid \Omega_i \mid \nu_{in}}{\Omega_i^2 + \nu_{in}^2} + \frac{\mid \Omega_e \mid \nu_{en}}{\Omega_e^2 + \nu_{en}^2}\right), \tag{1.10}$$

$$\sigma_H = \frac{en}{B}\left(\frac{-\Omega_i^2}{\Omega_i^2 + \nu_{in}^2} + \frac{\Omega_e^2}{\Omega_e^2 + \nu_{en}^2}\right), \quad \text{and} \tag{1.11}$$

$$\sigma_{||} = e^2 n\left(\frac{1}{m_i \nu_{in}} + \frac{1}{m_e \nu_{en}}\right). \tag{1.12}$$

The various components of the conductivity tensor describe currents in the ionosphere. The Pedersen (σ_P) and Hall (σ_H) conductivities describe the currents in the $\mathbf{E}_\perp$ and $\mathbf{E}_\perp \times \mathbf{B}$ directions, respectively, whereas the parallel conductivity ($\sigma_{||}$) describes the current along the magnetic field. Figure 1.5 shows the σ_P, σ_H, and $\sigma_{||}$ conductivity profiles.

In the high latitude ionosphere the magnetic field lines are almost vertical and, to a first approximation, $\mathbf{E}_\perp$ is height independent. The height-integrated Pedersen (Σ_P) and Hall (Σ_H) conductances are introduced as

$$\Sigma_P = \int \sigma_P dz, \quad \text{and} \tag{1.13}$$

$$\Sigma_H = \int \sigma_H dz \tag{1.14}$$

to represent the two dimensional horizontal sheet of current perpendicular to the magnetic field in the form

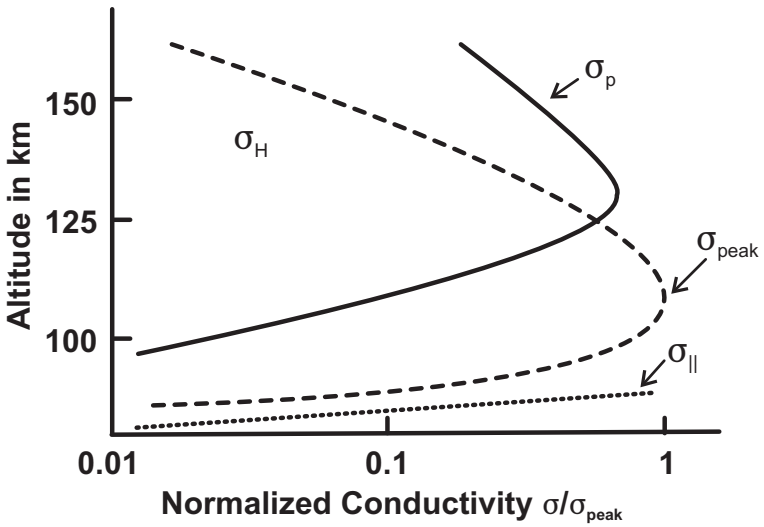

Figure 1.5: Normalized ionospheric Hall, Pedersen, and parallel conductivity profiles (adapted from *Baumjohann and Treumann* (1997)).

$$\mathbf{J}_\perp = \int \mathbf{j}_\perp dz = \bar{\bar{\Sigma}} \cdot \mathbf{E}_\perp, \tag{1.15}$$

where $\bar{\bar{\Sigma}}$ is the 2×2 conductance tensor given by

$$\bar{\bar{\Sigma}} = \begin{pmatrix} \Sigma_P & \Sigma_H \\ -\Sigma_H & \Sigma_P \end{pmatrix}, \tag{1.16}$$

where Σ_P and Σ_H are in units of S. Equation (1.15) may also be written as

$$\mathbf{J}_\perp = \Sigma_P \mathbf{E}_\perp - \Sigma_H \frac{(\mathbf{E}_\perp \times \mathbf{B})}{B}. \tag{1.17}$$

In the absence of measurements, or to obtain a general picture, the ionospheric conductance may be approximated using conductance models such as the Hardy (*Hardy et al.*, 1985; *Hardy et al.*, 1987) or the Fuller-Rowell Evans (*Fuller-Rowell and Evans*, 1987) conductance models.

1.3 Ionospheric currents and the aurora

The strength of ionospheric currents depends on conductance, which is in turn proportional to the electron density (equations (1.7)-(1.12)). Ionospheric currents are therefore stronger in regions of high electron density.

Energetic electrons precipitating into the ionosphere collide with neutral particles in the atmosphere. The result is an ionization reaction in which the energetic electron loses ∼35 eV (*Rees and Luckey*, 1974), and a neutral particle may be excited to higher energies and emit a photon as it decays to the ground state causing optical emissions which lead to spectacular auroral light displays. The auroral green (557.7 nm) and red (630.0 nm) lines of atomic oxygen are commonly observed auroral colors. The region within which the auroral arcs are most frequently observed is called the auroral oval. The auroral oval forms a band-like structure about the poles of the northern (aurora borealis) and southern (aurora australis) hemispheres (see green shading in Figure 1.7 to follow).

During disturbed magnetic periods, the aurora becomes active and the auroral oval expands equatorward. The region poleward of the auroral oval is called the polar cap. It is widely believed that the equatorward edge of the polar cap coincides with the open/closed boundary of the magnetic field lines so that magnetic field lines within the polar cap are connected to the magnetotail lobes or the solar wind.

Particle precipitation enhances conductivity in the auroral oval. Therefore, flow of the high-latitude ionospheric current is concentrated in the auroral oval, forming the auroral electrojet current. Eastward and westward electrojets flow in the dusk and dawn sectors, respectively, carrying a total current on the order of 10^6 A. The electrojets flow at E-region altitudes and create significant magnetic disturbances on the ground. During a substorm, there is increased particle precipitation in the auroral region and an enhancement of the auroral electrojet current.

Coupling between the magnetosphere and the ionosphere is achieved by the flow of field-aligned currents (FACs) along magnetic field lines. FACs exist in two bands located in the auroral region, see Figure 1.6. Typical FAC current densities are a few $\mu A/m^2$. The inner region of current is called the region 1 (R1) FAC; R1 currents flow into the ionosphere

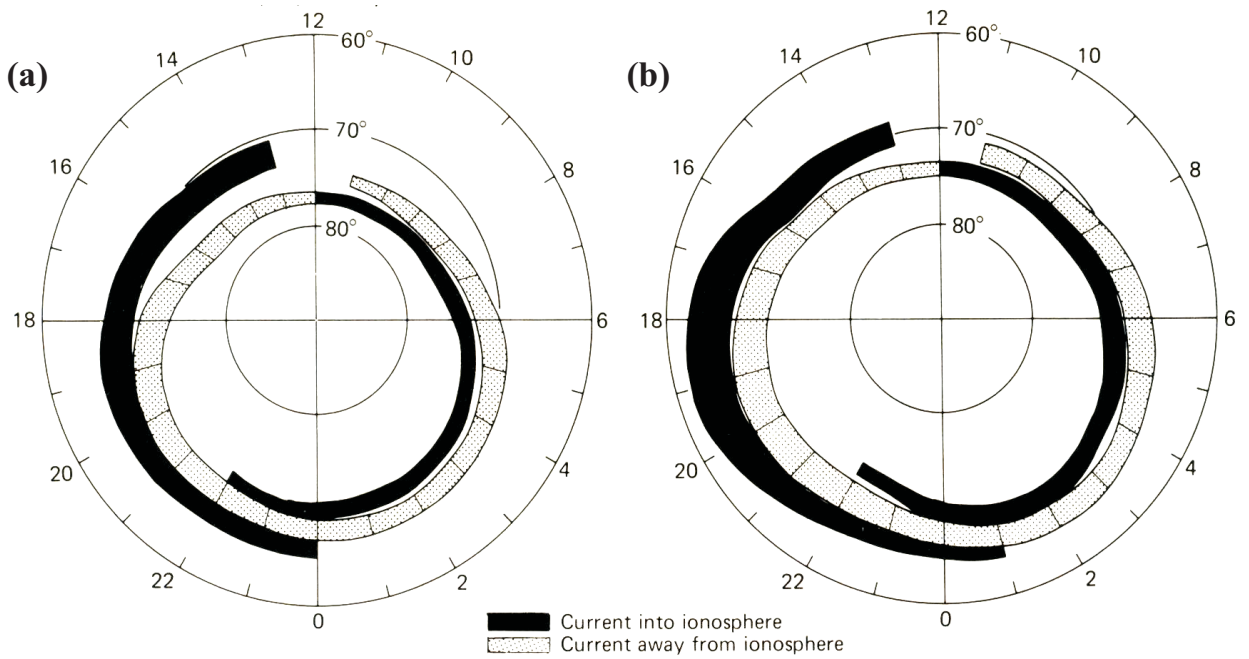

Figure 1.6: Distribution of field aligned currents for (a) quiet and (b) active magnetic periods (*Iijima and Potemra*, 1978).

on the dawnside and out of the ionosphere on the duskside. In contrast, the currents in the outer region, region 2 (R2) FACs, flow into the ionosphere on the duskside and out of the ionosphere on the dawnside.

1.4 Ionospheric convection pattern

At high latitudes, plasma convection is predominantly driven by electric fields established due to the interaction between the IMF and the Earth's magnetosphere. Plasma motion in the magnetosphere is mapped down to the ionosphere and may be interpreted through observations of the ionospheric convection pattern. Studying plasma convection patterns at the ionospheric level will therefore lead to a better understanding of how the solar wind interacts with the magnetosphere.

Statistical convection models have been developed from satellite, magnetometer, and radar data to generalize the ionospheric convection pattern based on the magnitude and polarity of the IMF (*Hairston and Heelis*, 1990; *Rich and Hairston*, 1994; *Papitashvili et al.*, 1994; *Weimer*, 1995; *Ruohoniemi and Greenwald*, 1996; *Ruohoniemi and Greenwald*, 2005;

Cousins and Shepherd, 2010). The configuration of the ionospheric plasma flow is well established for periods where the orientation of the IMF is in a quasi-steady state pointing southward. The situation is more complicated for a northward-oriented IMF, and the transformation of the ionospheric convection pattern during a sudden change in the orientation of the IMF is not well documented.

1.4.1 Case of southward IMF

When IMF $B_z < 0$, the Dungey reconnection process (see Section 1.1) occurs and newly reconnected magnetic field lines travel anti-sunward across the polar cap, and the associated electric field $\mathbf{E}_{pc}$ points from dawn-to-dusk. Because magnetic field lines are equipotential to a first approximation, $\mathbf{E}_{pc}$ is mapped down to the polar ionosphere, causing anti-sunward plasma flow in the central polar cap region. In the magnetotail, as plasma flows sunward toward and around the Earth (after magnetotail reconnection), the corresponding electric fields, $\mathbf{E}_a$, in the magnetosphere are mapped to the dawnside and duskside ionosphere at lower latitudes and drive plasma back toward the Sun. Electric fields $\mathbf{E}_a$ and $\mathbf{E}_{pc}$ create a two-cell convection pattern in magnetic latitude (MLAT) / magnetic local time (MLT) coordinates, Figure 1.7a. Convection cells resulting from Dungey-type reconnection processes produce convection cells which cross the open-closed field line boundary. When the IMF B_y component is small (close to 0), the convection cells are roughly symmetric. Variations in the IMF B_y alter the symmetry of this pattern; in the northern hemisphere if B_y is positive, the dusk cell dominates, and if B_y is negative, the dawn cell dominates.

1.4.2 Case of northward IMF

When the IMF is oriented northward, the interchange reconnection process occurs. The corresponding pattern of convection consists of several cells (*Reiff and Burch*, 1985; *Watanabe and Sofko*, 2009). Figure 1.7b shows a four-cell convection pattern hypothesized for a strongly northward IMF B_z with $B_y \simeq 0$ nT. The two-cell convection pattern characteristic for periods of southward IMF (shown in the outer regions) are joined by a pair of interchange or reverse convection cells on the dayside.

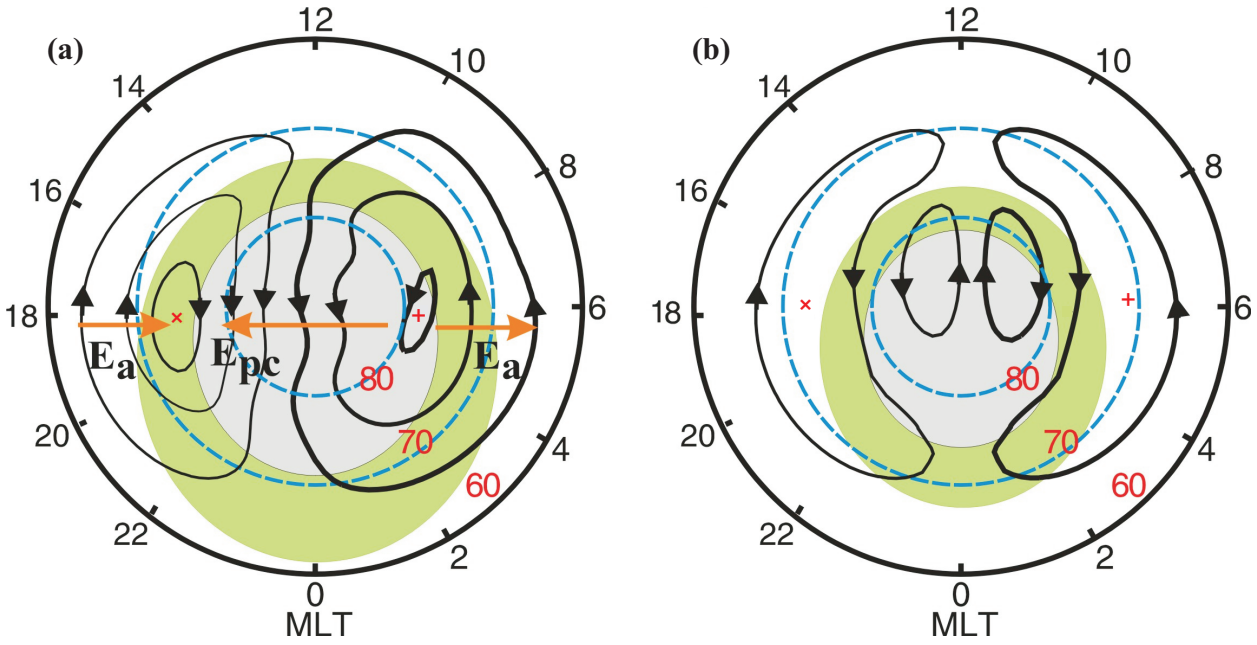

Figure 1.7: (a) Ionospheric electric fields (E_a, auroral zone; E_{pc}, polar cap) and typical two-cell convection pattern for the high latitude ionosphere for a southward IMF and $B_y \simeq 0$. (b) Four-cell convection pattern for a strongly northward IMF and $B_y \simeq 0$. The green and grey shading in both diagrams indicate the auroral oval and polar cap, respectively. MLAT/MLT coordinates are used.

The formation of the reverse convection cells may be explained by examining the location of the footprints of the open and closed field lines illustrated in Figure 1.3b. The open field line in Figure 1.3b (i) maps to the polar cap. Through reconnection, this open field line becomes the overdraped field line in Figure 1.3b (ii), corresponding to a sunward motion of plasma in the polar cap region. Further reconnection in Figure 1.3b (iii) causes the formation of a closed field line. This process corresponds to a sunward motion across the open/closed field line boundary. At the same time, the open magnetotail line shown in Figure 1.3b (iv) becomes the open field line shown in Figure 1.3b (i), corresponding to a sunward drift of plasma in the polar cap region.

It is also possible for the outer two-cell portion of the convection pattern to be compressed toward the nightside, rather than span the entire dawn and dusk sectors as shown. For example, Figure 1.8 shows the 4-cell convection pattern derived by the Super Dual Auroral Radar Network (SuperDARN) radars for a period of strong northward IMF for a two minute interval beginning at 17:04 UT on February 02, 2002.

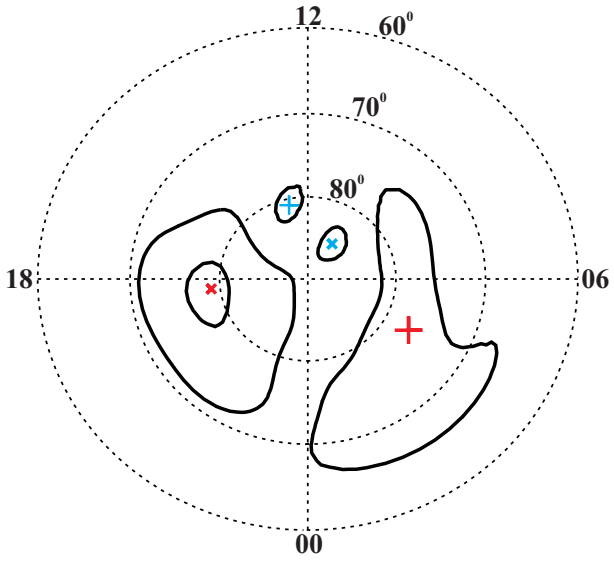

Figure 1.8: Four-cell convection pattern inferred from SuperDARN data for a period of strong northward IMF on February 02, 2002 at 17:04 UT. Contour lines indicate the electrostatic potential (Φ_E) using a 6 kV contour spacing. The plus and cross signs indicate maxima and minima in Φ_E and mark the foci of the normal (red) and reverse (blue) dawn and duskside convection cells.

As for the case of southward IMF, the shape of the convection pattern is dependent on the polarity of the IMF B_y and the magnitude of the IMF B_z (see *Reiff and Burch* (1985)). When B_y is positive, the inner morning cell dominates and when B_y is negative the inner dusk cell dominates. When B_z is only weakly dominant, the inner cells merge into one large cell with westward flowing plasma for $B_y > 0$ and eastward flowing plasma for $B_y < 0$. In the interchange reconnection cycle, interaction between the IMF and lobe magnetic field lines create convection cells that cross the open-closed field line boundary twice in one cycle. In the opposite hemisphere a small convection cell located entirely within the closed field line region is formed due to interaction between the lobe and closed field line.

1.5 Objectives of this undertaken research

The primary objective of this thesis is to develop a versatile technique for monitoring the high-latitude ionospheric convection based on SuperDARN velocity measurements. In the past, various techniques have been developed for mapping convection based on radar, magnetometer, and satellite observations. Even after many years of study, there are still unresolved

questions and disagreements between the results of the different mapping techniques. This is due to limited data, plus distortions introduced by the constraints applied by current mapping techniques. Although the lack of data issue has not been completely surpassed, the situation has improved with an increase to the number of ground-based magnetometers, SuperDARN radars, and satellites in critical locations. Goals for meeting this objective are:

1. To critically review existing convection mapping techniques to expose their deficiencies and shortcomings, focussing on the SuperDARN radar network and the FIT convection mapping technique, which is currently the most popular method.

2. To develop spherical cap harmonic analysis (SCHA) techniques for mapping the ionospheric convection pattern without applying constraints typical of the FIT convection mapping technique.

3. To validate SCHA convection estimates through comparison with Defence Meteorological Satellite Program (DMSP) ion drifts, convection estimated by merging co-located SuperDARN line-of-sight velocities from multiple radars, and FIT convection estimates.

The second objective of this thesis is to examine the possibility of adding magnetometer data in mapping the high-latitude ionospheric convection pattern. Regardless of the fitting technique used, as the number of measurements within the mapping region decreases, the reliability of the convection map that can be produced is reduced. It is therefore highly desirable to involve supplementary data sets. Goals for meeting this second objective are:

1. To critically review existing techniques and propose a new technique that would infer plasma convection patterns from magnetometer data.

2. To map convection with magnetometer measurements and with a combined data set of radar l-o-s velocity and magnetic field measurements.

The third objective of this thesis is to use the convection mapping techniques developed to investigate the reconfiguration of the ionospheric convection pattern from one steady state to another following a sudden southward transition in the IMF. In the past, convection

transitions were studied separately by radars and ground-based magnetometers. The result is two separate scenarios of the convection reconfiguration process. Goals for meeting this objective are:

1. To examine radar and magnetometer data sets independently to investigate the ionospheric signatures of a southward IMF transition.

2. To examine characteristics of the ionospheric convection pattern determined from a joint velocity and magnetometer data set to provide further insights on the associated convection reconfiguration.

1.6 Outline

In Chapter 2, SuperDARN is introduced as the primary instrument for monitoring the ionospheric convection pattern, and a detailed review of current convection mapping techniques is provided. In Chapter 3, spherical cap harmonic analysis is introduced for fitting observations over a limited region to avoid problems caused by adding constraints to force smooth fitting over the entire high-latitude region. This new technique is compared with observations and to previous mapping techniques for periods of both large-scale and spatially confined data coverage. In Chapter 4, magnetometers are discussed for monitoring and mapping the ionospheric convection pattern and techniques for mapping electrodynamic properties based on the observed perturbation magnetic field are presented. Techniques for combining magnetometer and SuperDARN data for convection mapping are introduced. In Chapter 5, magnetometer and SuperDARN measurements are studied to examine the evolution of the ionospheric convection pattern in association with a southward turning of the IMF to describe the mechanism of the convection reconfiguration. In Chapter 6, a brief summary and conclusions are presented and suggestions for future research are made.

Chapter 2

Monitoring ionospheric convection with the SuperDARN radar network

Measurements of the ionospheric plasma flow are made with a variety of instruments including drift meters on satellites, ionosondes, and ground-based radars. To map the evolution of the ionospheric convection pattern, global coverage and a high temporal resolution, of the order of < 5 minutes, are required. Satellite orbits enclose the entire Earth, making measurements every few seconds (or faster) (for example, the DMSP satellites). However, over the period of several minutes an individual satellite only covers a small range of latitudes along a single path, and it is not possible to obtain an instantaneous snapshot of the ionospheric convection pattern over the entire high latitude region. Ionosondes are capable of producing $\mathbf{E} \times \mathbf{B}$ vectors with resolutions of ~ 1 minute, but stations are limited in number, especially at high latitudes. Due to its large field of view and 1-2 minute resolution, SuperDARN is effective for observing the evolution of the ionospheric convection pattern. In this Chapter, the ability of SuperDARN to map ionospheric convection is reviewed.

2.1 SuperDARN HF radars

SuperDARN is a network of high frequency (HF) coherent scatter radars designed to continuously monitor the high-latitude ionosphere (*Greenwald et al.*, 1995; *Chisham et al.*, 2007), see Figures 2.1 and 2.2. Coherent scatter radars transmit radio waves into the ionosphere and examine the return signal or echo scattered off physical structures, such as wave-like perturbations in the electron density called irregularities. The SuperDARN HF radars are sensitive to irregularities elongated in the magnetic field direction, and for effective backscatter, the radio wave fronts should propagate perpendicular to the Earth's magnetic field.

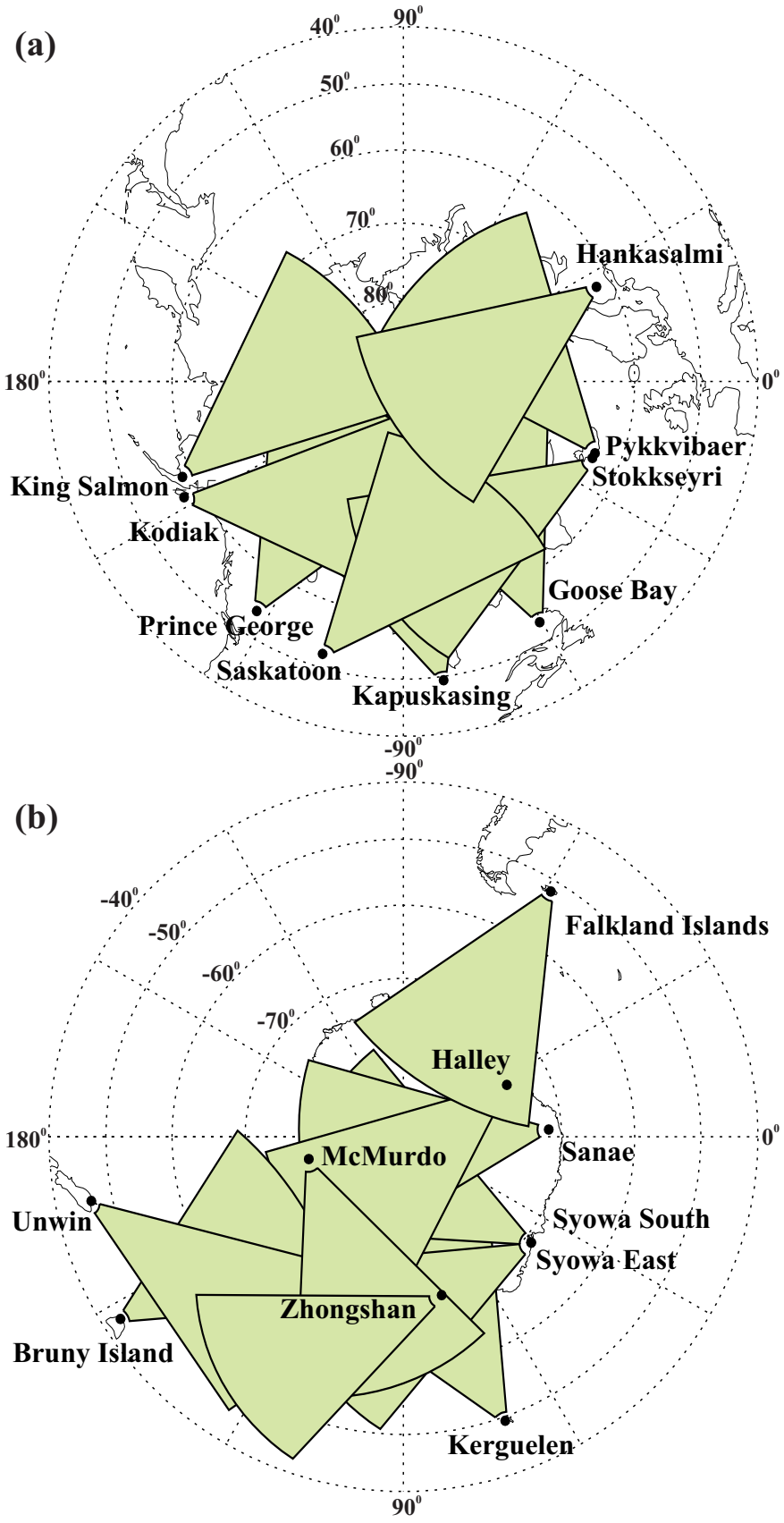

Figure 2.1: Fields of view of the (a) northern and (b) southern hemisphere SuperDARN auroral radars in geographic coordinates.

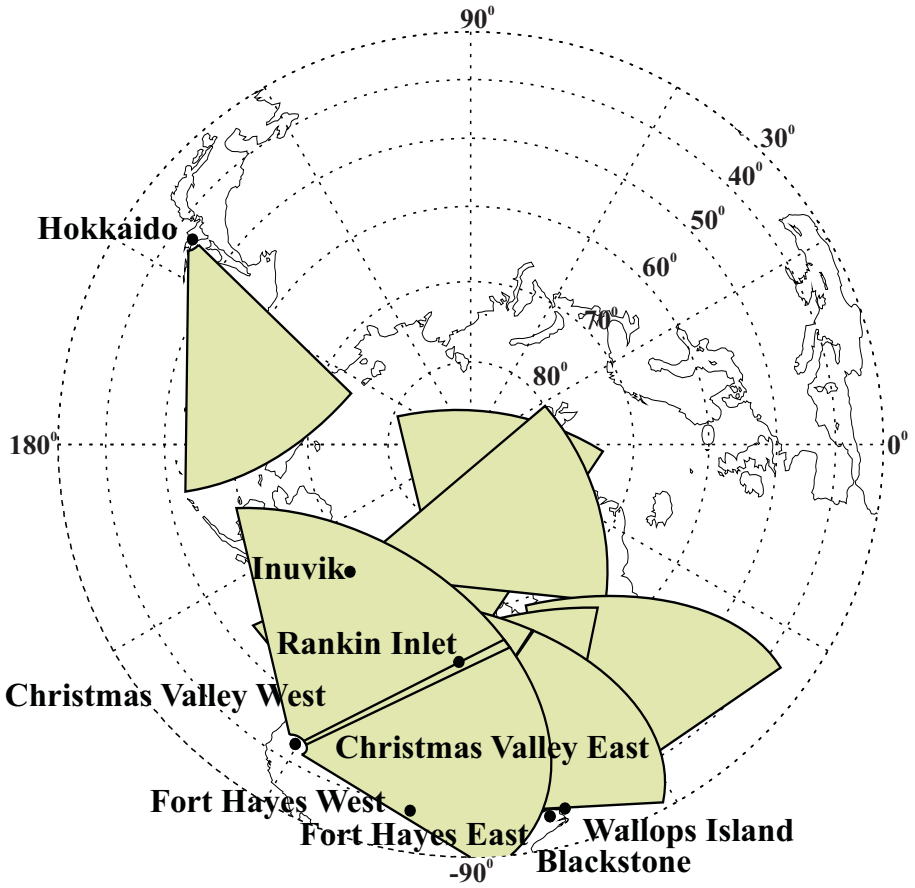

Figure 2.2: Fields of view of the PolarDARN and StormDARN radars in geographic coordinates.

In the F region, ionospheric irregularities are due to the gradient drift instability. The gradient drift instability is excited where there is a plasma gradient set perpendicular to both the electric and magnetic field directions. A sinusoidal perturbation in the electron density in the direction of the electric field can grow due to the charge separation that develops in the electric field direction caused by the difference in the electron and ion Pedersen drift. Excited perturbation of the electric field drives plasma in a region of low-density plasma into a high-density region, and plasma in a region of enhanced plasma density into a low-density region. Such a redistribution enhances the contrast between the background plasma density and the density in the perturbation, implying growth of the irregularity.

The SuperDARN radars operate in the HF (8-20 MHz) band. At these frequencies, radio waves experience significant refraction in the ionosphere and meet the orthogonality condition at a broad range of heights, from 90 to 500 km. For HF backscatter to occur, the

Table 2.1: SuperDARN radar locations, boresite direction, and data availability.

Radar Station	Geographic Latitude (°N)	Geographic Longitude (°E)	Boresite Direction (°)	Availability Start Date
Goose Bay	53.32	-60.46	5.0	June 1983
Kapuskasing	49.39	-82.32	-12.0	September 1993
Saskatoon	52.16	-106.53	23.1	September 1993
Stokkseyri	63.86	-22.02	-59.0	October 1994
Hankasalmi	62.32	26.61	-12.0	April 1995
Pykkvibaer	63.77	-19.20	30.0	December 1995
Kodiak	57.60	-152.19	30.0	January 2000
Prince George	53.98	-122.59	-5.0	March 2000
King Salmon	58.68	-156.65	-20.0	October 2001
Wallops Island	37.93	-75.47	26.14	June 2005
Rankin Inlet	62.82	-93.11	5.71	May 2006
Hokkaido	43.53	143.61	30.0	November 2007
Blackstone	37.10	-77.95	-32.0	February 2008
Inuvik	68.42	-133.50	29.47	August 2008
Fort Hays East	38.86	-99.39	45.00	January 2010
Fort Hays West	38.86	-99.39	-25.00	February 2010
Christmas Valley East	43.27	-120.36	54.00	November 2010
Christmas Valley West	43.27	-120.36	-20.00	November 2010
Halley Bay	-75.52	-26.63	165.0	January 1996
Syowa East	-69.01	39.61	106.5	February 1997
Syowa South	-69.01	39.61	165.0	February 1997
Sanae	-71.68	-2.85	173.2	January 2000
Kerguelen	-49.35	70.26	168.0	June 2000
TIGER Bruny	-43.38	147.23	180.0	January 2001
TIGER Unwin	-46.51	168.38	227.9	November 2004
McMurdo	-77.88	166.73	263.4	January 2010
Falkland Islands	-51.83	-58.98	178.2	February 2010
Zhongshan	-69.40	76.40	72.5	2011

ionospheric irregularity should be of a specific size: $\lambda_{irregularity} = \frac{\lambda_{radar}}{2}$ (*Fejer and Kelley*, 1980). Since the radars operate at 8-20 MHz, they can see scatter from irregularities with 8-19 m wavelengths.

Each SuperDARN radar sequentially scans through 18 beam positions over a period of 1 or 2 minutes with a dwelling time of 3 or 7 seconds in each beam. The Wallops Island, Blackstone, and two Christmas Valley radars use 24 beam positions and the two Fort Hays radars use 22 beam positions. Radar beam directions are separated by 3.24° (3.86° for the two Fort Hayes radars) and the azimuthal range of the combined beams is $\sim 52°$. Measurements are performed in 75 range gates spaced by 45 km beginning at an initial range of 180 km.

The SuperDARN network currently includes 18 (10) radars located in the northern (southern) hemisphere. The majority of these radars monitor auroral zone latitudes. The radar locations and fields of view of the auroral zone radars are illustrated in Figure 2.1 a and b. In recent years, additional radars have been installed at polar (PolarDARN) and sub-auroral (StormDARN) latitudes to increase radar coverage. These radar locations and fields of view are illustrated in Figure 2.2. A list of radar locations and boresite directions is given in Table 2.1. Typically, the altitude-adjusted geomagnetic (AACGM) coordinate system is used when discussing SuperDARN measurements and SuperDARN data products (see Appendix A.3).

2.1.1 SuperDARN radar propagation modes

Radio wave propagation is dependent on the distribution of electron density in the ionosphere. The distribution of the electron density affects the propagation path of the radio wave. A minimum of $n_e \sim 1 \times 10^{11}\ m^{-3}$ is required to ensure radio waves refract in such a way that they are orthogonal to the magnetic field (*Danskin et al.*, 2002). The distribution of the electron density must also be favorable for the establishment of gradients to stimulate the gradient drift instability; echo occurrence rates tend to be reduced in the summer months as solar irradiance tends to smooth density gradients so that fewer irregularities are produced (*Danskin et al.*, 2002). D-region absorption occurs when particle precipitation penetrates to the D-region ionosphere enhancing ionization and reducing the power of the radio signal from the E and F-region ionosphere. Sometimes, very strong densities in the E region cause over refraction, preventing signals from penetrating to the F region.

There are several paths by which a transmitted radio wave may propagate toward the scattering region. Figure 2.3a shows a simple propagation path where the signal travels directly to the scattering region and back (*Chisham et al.*, 2008). This mode is called $\frac{1}{2}$-hop E-region or F-region scatter, depending on the region from which the waves scatter. The black dashed line represents a vector in the radial direction passing from the Earth's center through the scattering region. The distance along the ground between the base of this vector and the radar indicates the ground range. The black ray path shows the straight line propagation path between the radar and scattering region and is called the virtual path.

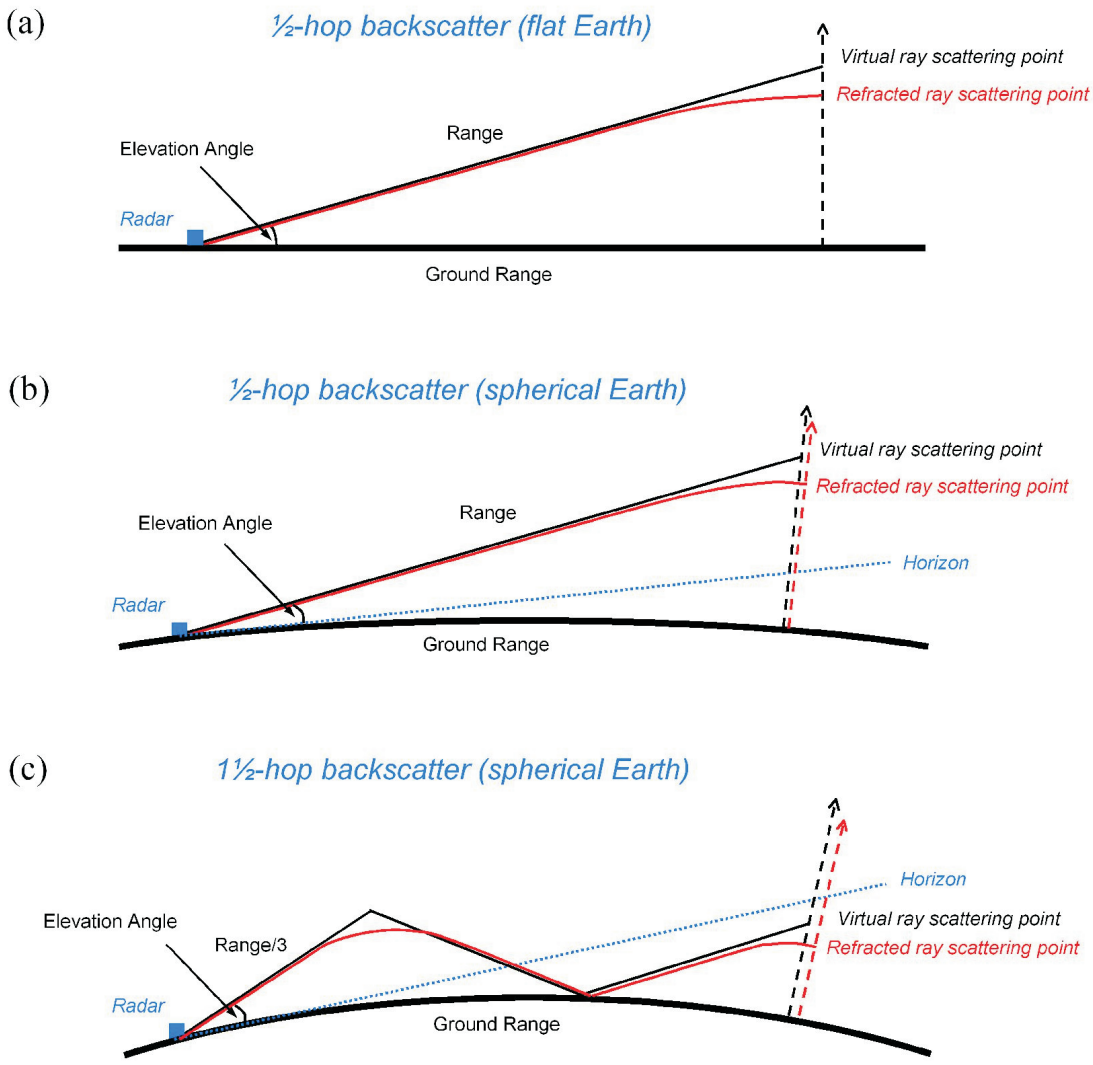

Figure 2.3: Propagation paths for (a) $\frac{1}{2}$-hop propagation for a flat Earth, (b) $\frac{1}{2}$ and (c) 1 $\frac{1}{2}$-hop propagation for a spherical Earth. Black (red) solid lines indicate virtual (real) propagation paths. Black (red) dashed line is perpendicular to the surface of the Earth passing through the virtual (real) scattering point (*Chisham et al.*, 2008).

The length of this line is called the range, and the angle between the propagation path and the ground is called the elevation angle. The red line represents a more realistic propagation path where refraction of the signal in the ionosphere has been taken into account. In Figure 2.3b, the same is shown, but for a spherical Earth. Figure 2.3c shows a 1 $\frac{1}{2}$-hop propagation path for a spherical Earth where the radio wave bounces from the ionosphere to the ground to the scattering region, and back. Multiple-hop propagation may occur between the ground and the ionosphere as well as between different layers of the ionosphere.

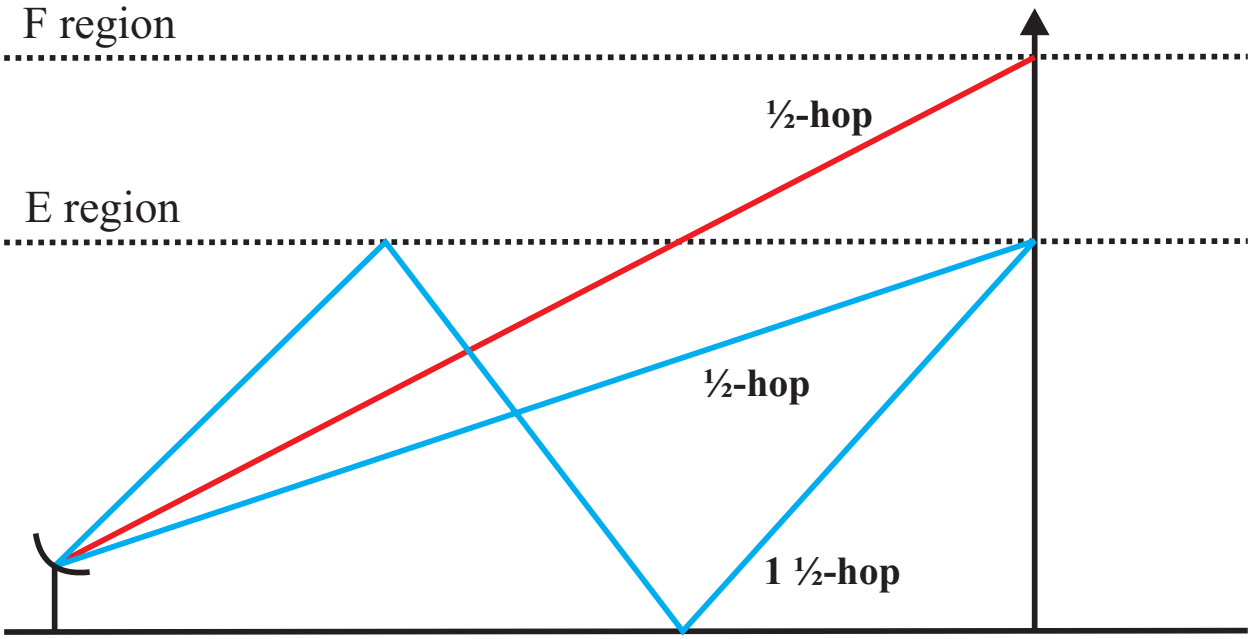

Figure 2.4: Possible propagation paths for E-region (blue) and F-region (red) scatter for a flat-Earth model.

The location of a scatter point, as indicated by the ground range, is calculated based on the flat-Earth model. *Chisham et al.* (2008) show that for a spherical Earth, the virtual scattering point is not located directly above the real scattering point (see Figure 2.3b), and discus how this changes the calculation of ground range. They suggest that the assumption of a flat-Earth model may cause errors of up to 400 km in the range calculation at far ranges.

For observations in a given beam/gate, it is desirable to know whether the scatter originates from the E or F region. This can be estimated from the elevation angle, see Figure 2.4. For scattering at a given range and height, the elevation angle for $\frac{1}{2}$-hop F-region scatter is larger than for $\frac{1}{2}$-hop E-region scatter, and the elevation angle for 1 $\frac{1}{2}$-hop scatter is larger than for $\frac{1}{2}$-hop scatter from the same scattering region.

Figure 2.5 shows an example of the statistical distribution of elevation angle in terms of range for all Rankin Inlet radar observations in 2007. The total number of occurrences of elevation angle was counted in 0.5 increments for each beam/gate of typical ionospheric scatter. Criteria characterizing typical ionospheric scatter include echo power > 3 dB, velocity magnitude > 50 m/s, and a positive spectral width of < 500 m/s. The data set is considerable, containing 62.6 million observations. At ranges of 180 km to ~ 700 km there is

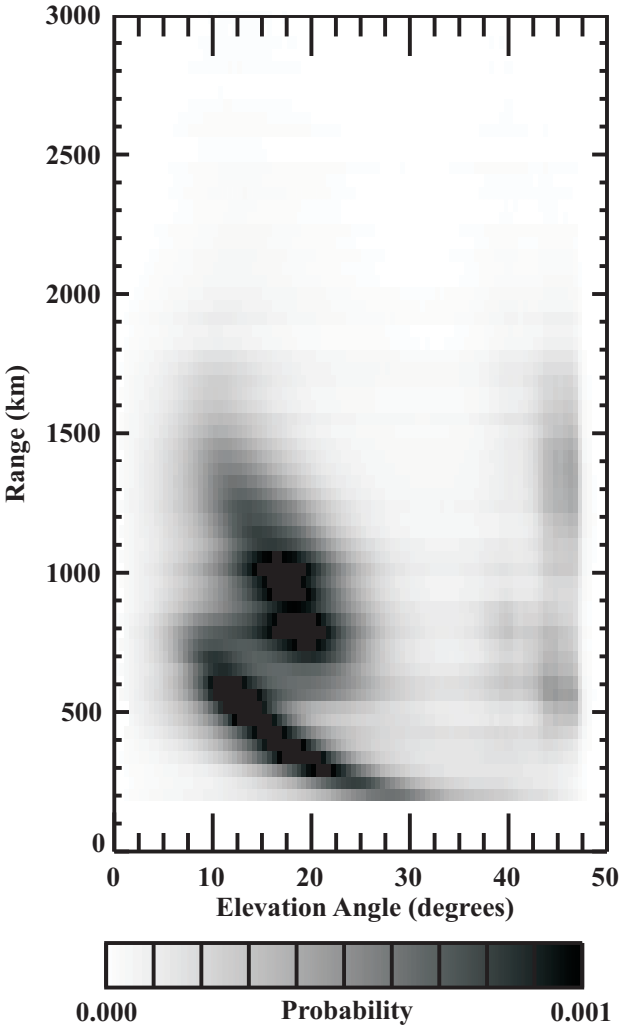

Figure 2.5: Probability distribution of elevation angle in terms of range for the Rankin Inlet radar for observations in 2007.

a narrow band of scattering for elevation angles of 10° (for higher ranges) which sweeps up to $\sim 30°$ as range decreases. There is a second band of scatter spanning from $\sim 10°$ for ranges > 1500 km to $\sim 25°$ at ranges of ~ 600 km. The low range scattering region is likely due to $\frac{1}{2}$-hop E-region scatter while the high-range scattering region is most likely due to $\frac{1}{2}$-hop F-region scatter. There is no clear cut off in terms of solely range or elevation angle that can be used to separate E and F-region scatter, instead both variables must be considered. As a generalization for the Rankin Inlet radar, scatter for ranges <700 km may be considered to originate from the E region and scatter for ranges >700 km may be considered to originate from the F region.

Note that not all echoes scatter from the ionosphere. Echoes may instead reflect from the Earth causing ground scattered echoes. Ground scattered echoes are characterized by low velocities (< 50 m/s) accompanied by low spectral widths (< 20 m/s). Velocity and spectral width are determined from the autocorrelation function generated at each range gate and radar beam, as discussed in the next section.

2.1.2 FITACF approach to determining echo parameters

The SuperDARN radars emit series of radio wave pulses to determine the power, Doppler velocity, and spectral widths of echoes. This is accomplished by digitizing and processing the return signal of a pulse sequence into an autocorrelation function (ACF). Figure 2.6 illustrates the pulse sequence currently used (personal communication with Kathryn McWilliams). Eight pulses of length $\delta l = 300\mu$s (corresponding to a range gate size of 45 km) are emitted at 0, 14, 22, 24, 27, 31, 42, and 43 units of lag time $t = 2400\mu$s. Because the radar cannot transmit and receive signals at the same time, there are missing lags for lag number 6, 23, 25, 26, 30, and 32-41. For a 7 s dwell time in each beam position, the pulse sequence is repeated 70 times and averaged into the ACF to increase the signal to noise ratio.

The Doppler velocity of an ionospheric echo may be determined by considering the Doppler frequency of the return signal. Consider the equation for Doppler frequency

$$f_{Doppler} = f_s \left(\frac{v \pm v_o}{v \mp v_s} \right), \tag{2.1}$$

where f_s represents the frequency emitted by the source, v is the speed of the signal in the medium, v_o is the velocity of the sensor, and v_s is the velocity of the source. An ionospheric irregularity (observer) moving with velocity v_o toward a stationary ground-based radar (source), emitting a signal with frequency f_{radar}, observes a signal frequency of

$$f_{irregularity} = f_{radar} \left(\frac{v + v_o}{v} \right). \tag{2.2}$$

The signal scatters off the irregularity and returns to the radar. Now consider the irregularity (source), still moving at speed v_o, to be emitting a signal ($f_{irregularity}$) toward the stationary

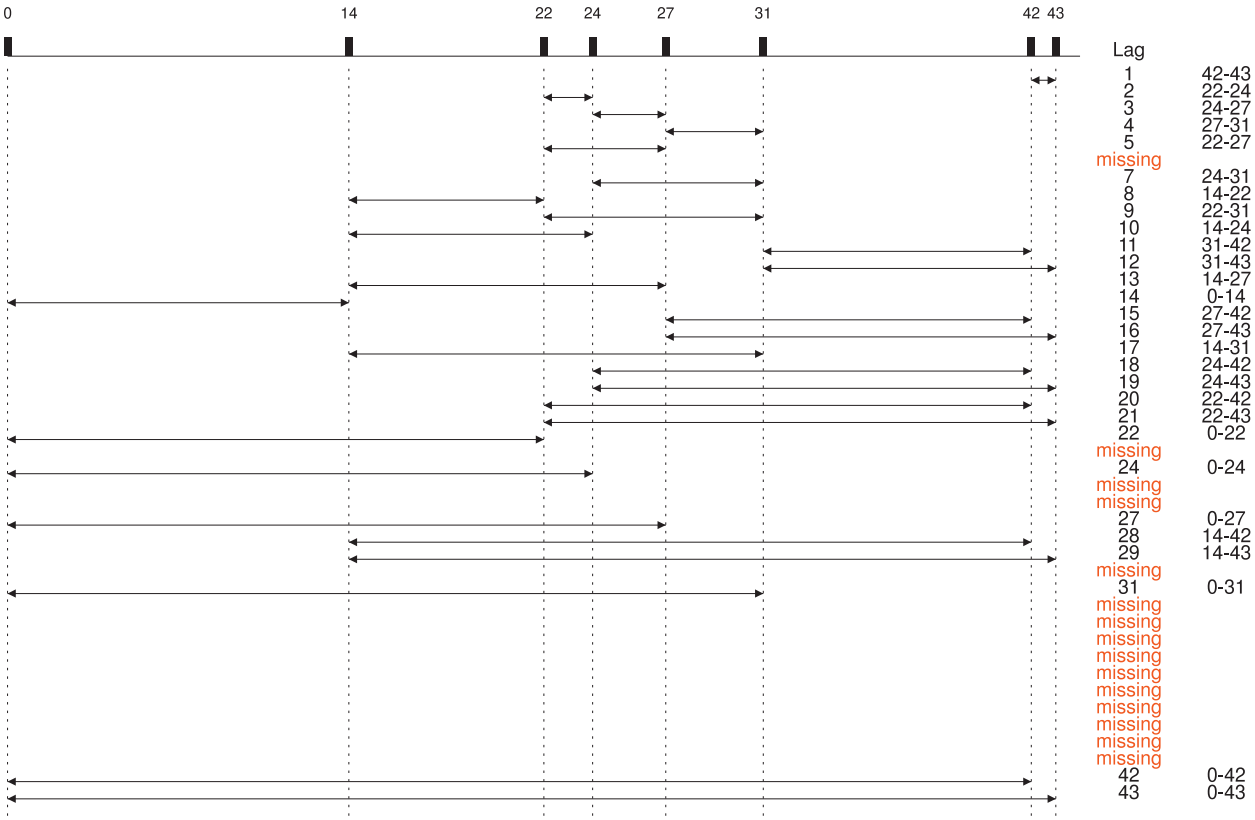

Figure 2.6: The 8-pulse sequence currently used by SuperDARN.

radar (observer). The frequency observed by the radar is

$$\begin{aligned} f'_{radar} &= f_{irregularity}\left(\frac{v}{v - v_o}\right) \\ &= f_{radar}\left(\frac{v + v_o}{v - v_o}\right), \end{aligned} \tag{2.3}$$

where equation (2.2) has been substituted. The Doppler shifted frequency f_D is then given by

$$\begin{aligned} f_D &= f'_{radar} - f_{radar} \\ &= f_{radar}\left[\frac{v + v_o}{v - v_o} - 1\right] \\ &\simeq 2\frac{v_o}{c} f_{radar}. \end{aligned} \tag{2.4}$$

In equation 2.4 the speed of the signal in the ionospheric medium v has been substituted with c, where c is the speed of light in a vacuum, and $c >> v_o$. By rearranging equation (2.4), the velocity of the irregularity is given by

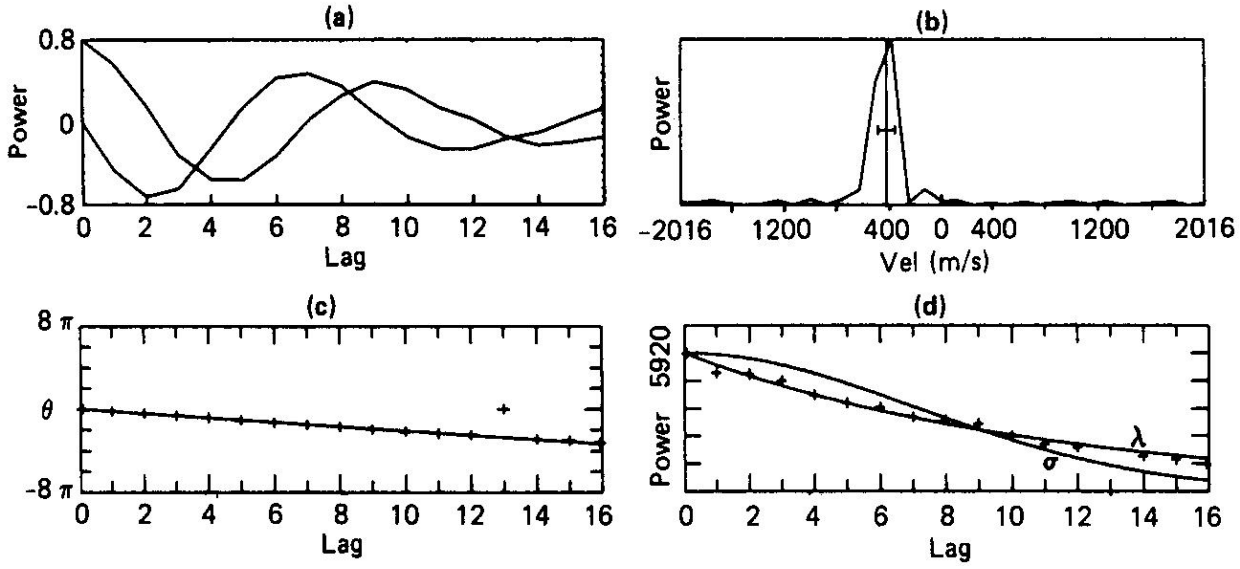

Figure 2.7: (a) Real and imaginary part of the ACF. (b)Magnitude of the FFT of the ACF with velocity (vertical line) and spectral width (horizontal line) obtained using FITACF overplotted. (c) Rate of change of the phase angle. (d) ACF power decay for exponential (λ) and Gaussian (σ) least-square fits (*Villain et al.*, 1987).

$$v_o = \frac{w_D c}{4\pi f_{radar}}, \tag{2.5}$$

where $w_D = 2\pi f_D$ has been introduced, and w_D can be determined from the ACF.

Figure 2.7 shows an example of how the ACF is analyzed in the FITACF approach (*Villain et al.*, 1987). Figure 2.7a plots the real and imaginary components of the ACF against lag number. The real component (R) of the ACF is a maximum at lag zero. The smallest lag numbers are therefore the most important as they define the basic shape and decay of the ACF. The imaginary component (I) of the signal is offset from the real part by the phase. The phase angle, $\phi_k = \arctan(\frac{I}{R})$ is plotted in Figure 2.7c (jumps of 2π have been accounted for). The phase angle decays linearly with slope w_D, which, when found, may be used to calculate the Doppler velocity v_o from equation (2.5).

The power and spectral width of the return signal are determined by modeling the decay of the ACF, which is assumed to follow either a Gaussian (σ) or exponential (λ) distribution. Figure 2.7d plots the signal power decay fitted with both exponential and Gaussian approximations. Using an exponential approximation, the distribution is of the

form

$$P(\tau) = P_\lambda e^{-\lambda\tau}, \tag{2.6}$$

where P_λ represents the maximum backscattered power, and τ is the lag number. The constant λ is determined using a least-squares fit, and used to calculate the spectral width δv of the spectrum from

$$\delta v = \frac{c\lambda}{2\pi f_{radar}}. \tag{2.7}$$

Using the Gaussian approximation, the distribution is of the form

$$P(\tau) = P_\sigma e^{-\sigma^2\tau^2}, \tag{2.8}$$

where P_σ is the maximum backscattered power, and the spectral width is given by

$$\delta v = \frac{c\sigma}{\pi f_{radar}\sqrt{\ln 2}}. \tag{2.9}$$

Figure 2.7b graphs the magnitude of the fast Fourier transform (FFT) of the ACF shown in Figure 2.7a. The vertical line indicates the mean Doppler velocity determined from Figure 2.7c using equation (2.5). The horizontal line indicate the spectral width determined from λ (Figure 2.7d).

2.2 SuperDARN HF velocity and $\mathbf{E} \times \mathbf{B}$ plasma drift

Irregularities in the F-region ionosphere are expected to propagate with a velocity close to the $\mathbf{E} \times \mathbf{B}$ drift of the bulk plasma (*Greenwald et al.*, 1995). SuperDARN was originally intended to measure F-region scatter, and it is therefore expected that the radar measures the l-o-s component of the $\mathbf{E} \times \mathbf{B}$ drift. Past validation work has been performed to confirm this statement through comparison of the SuperDARN l-o-s velocity to observations made by concurrently operating instruments. Such work has been presented in *Drayton et al.* (2005) and *Drayton* (2006).

Baker et al. (1990) investigated the validity of the SuperDARN observations by comparing velocities measured at Halley with flows observed by the DMSP ion drift meter. For one satellite pass, they showed that radar velocities and ion drifts were comparable, with a tendency for radar velocities to be smaller than satellite ion drifts for magnitudes of >600 m/s (their Figure 3). In past papers, joint SuperDARN and incoherent scatter radar (ISR) observations were considered (*Milan et al.*, 1999; *Davies et al.*, 1999, 2000; *Xu et al.*, 2001; *Danskin*, 2003). These comparisons also showed an overall agreement between data sets, but with a noticeable data spread. For some events, almost perfect agreement was reported (*Davies et al.*, 1999; *Danskin*, 2003) while for others significant systematic differences were obvious (*Xu et al.*, 2001; *Danskin*, 2003). For example, *Xu et al.* (2001) reported a general underestimation of the velocity magnitude by SuperDARN compared to ISR measurements.

Drayton et al. (2005) and *Drayton* (2006) performed a more systematic comparison between the l-o-s velocity measurements and DMSP ion drifts. Events were chosen for periods of joint SuperDARN and DMSP observation and measurements were compared at the raw data level. SuperDARN l-o-s velocities were considered provided the echo power was > 3 dB, the spectral width was < 500 m/s, the velocity error was < 150 m/s, and the velocity magnitude was > 50 m/s to eliminate untypical echoes. Events were also discarded if the DMSP ion drifts indicated a transition in the polarity of the velocity to avoid discrepancies caused by the different spatial resolution of the instruments.

The comparison was performed by considering events where the DMSP satellite crossed several beams of an individual SuperDARN radar field of view at right angles so that the SuperDARN and the cross-track component of the DMSP measurements were aligned. The DMSP ion drifts were mapped down from a measurement height of 840 km to an ionospheric altitude of 300 km, which is the assumed height of SuperDARN F- region scatter, by reducing the magnitude of the ion drift by $\sim 11\%$, as estimated by *Sofko and Walker* (2006). The original comparison by *Drayton et al.* (2005) did not consider this effect, and therefore reports findings which are slightly different from those in *Drayton* (2006), which are presented below. All DMSP velocities within a 45 km radius of a given l-o-s velocity were averaged together for comparison with the l-o-s velocity provided the standard deviation of the averaged value was < 150 m/s, and the azimuths of the l-o-s measurement and the aver-

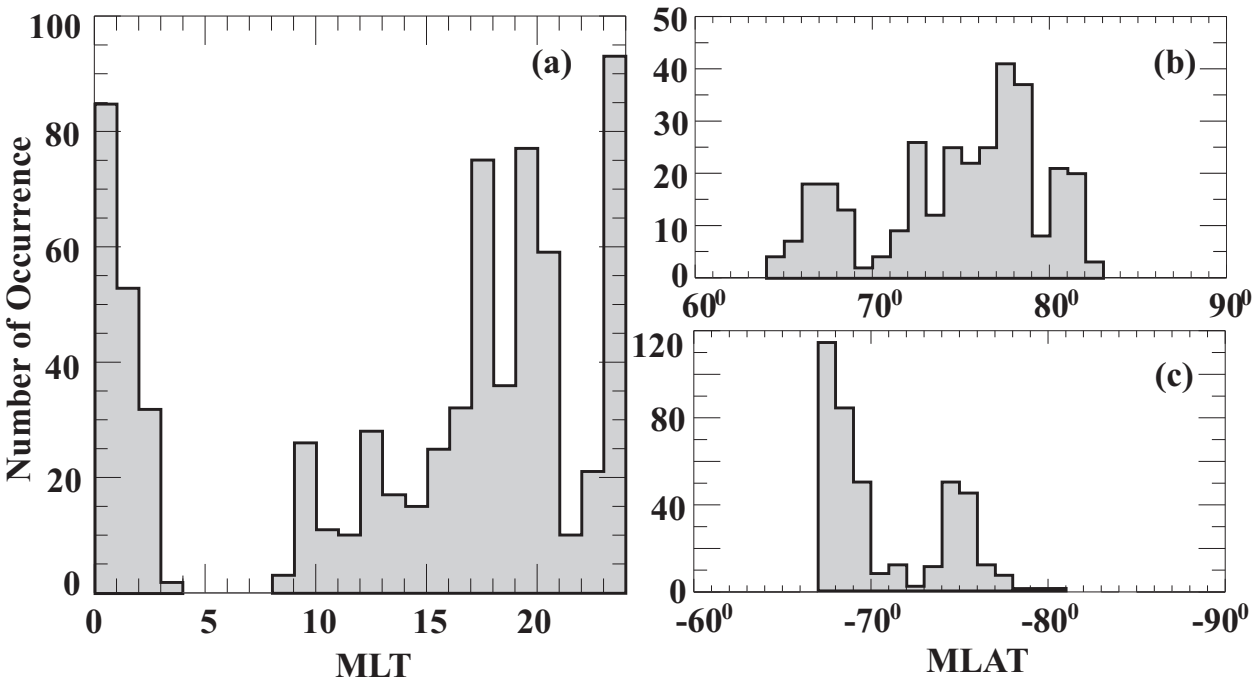

Figure 2.8: Distribution of the (a) magnetic local time and AACGM magnetic latitude for (b) the northern and (c) the southern hemisphere for SuperDARN echoes selected for comparison with DMSP measurements (*Drayton*, 2006).

aged vector were within 5°. Measurements were considered for the Hankasalmi, Pykkvibaer, Stokkseyri, Saskatoon, and Kodiak radars in the northern hemisphere and the Halley, Sanae, Syowa South, and Syowa East radars in the southern hemisphere, and for the DMSP F12, F13, and F15 satellites.

Figures 2.8 and 2.9 provide statistical characteristics of radar echoes considered in this comparison. There were echoes in most MLT sectors (exception in the 04-08 MLT sector) and at magnetic latitudes (MLATs) of 64°-83° in the northern hemisphere and 67°-81° in the southern hemisphere, Figure 2.8. The average echo power was ∼19 dB signal-to-noise ratio, Figure 2.9a. A velocity span of 0-1000 m/s was achieved with a mean velocity magnitude of ∼330 m/s, Figure 2.9b. The average spectral width was ∼140 m/s, Figure 2.9c, and echoes were observed between ranges of ∼400 km and 2600 km with an average range of 1330 km, Figure 2.9d. These values are typical for F-region SuperDARN echoes (e.g., *Hamza et al.*, 2000; *Lacroix and Moorcroft*, 2001; *Villain et al.*, 2002; *Danskin*, 2003).

Figure 2.10 shows a scatter plot of the SuperDARN l-o-s velocity versus the DMSP cross-track ion drift for 209 events and 746 points of comparison (*Drayton*, 2006). Points

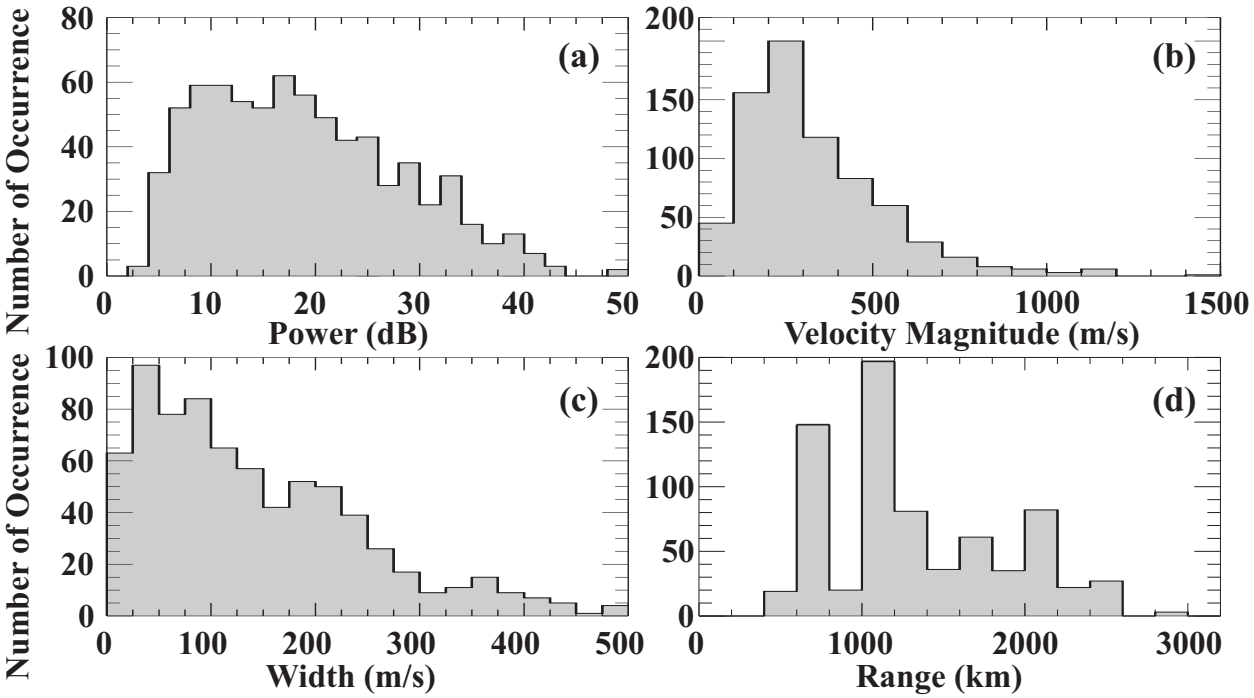

Figure 2.9: Distribution of the SuperDARN radar (a) echo power, (b) velocity magnitude, (c) spectral width and (d) range for all events selected for comparison with DMSP (*Drayton*, 2006).

are clustered about the diagonal bisector indicating good agreement between measurements. The correlation coefficient and the slope of the best-fit line relating the SuperDARN and DMSP velocities are $R = 0.91$ and $m = 0.84$, respectively. Note that velocity errors were considered in the determination of the best-fit line following the methods of *Press et al.* (1992), but error bars have not been indicated in the diagram for ease of viewing. These results indicate a reasonable linear relationship between SuperDARN and DMSP velocities.

Drayton et al. (2005) and *Drayton* (2006) conclude that since the comparison was performed for multiple radars over a wide range of MLATs and MLT sectors, SuperDARN and DMSP observations may be merged into a common data set for periods of smooth spatial and temporal variability of the flow. They further hypothesize that the data spread shown in Figure 2.10 may be explained by the different spatial and temporal resolutions of the instruments, as will be discussed below.

The spatial resolution of the SuperDARN and DMSP instruments differ. The DMSP instrument produces average measurements every 4 seconds. At an average speed of ~ 7.5 km/s, this corresponds to an average spacing of 30 km between measurements. In contrast,

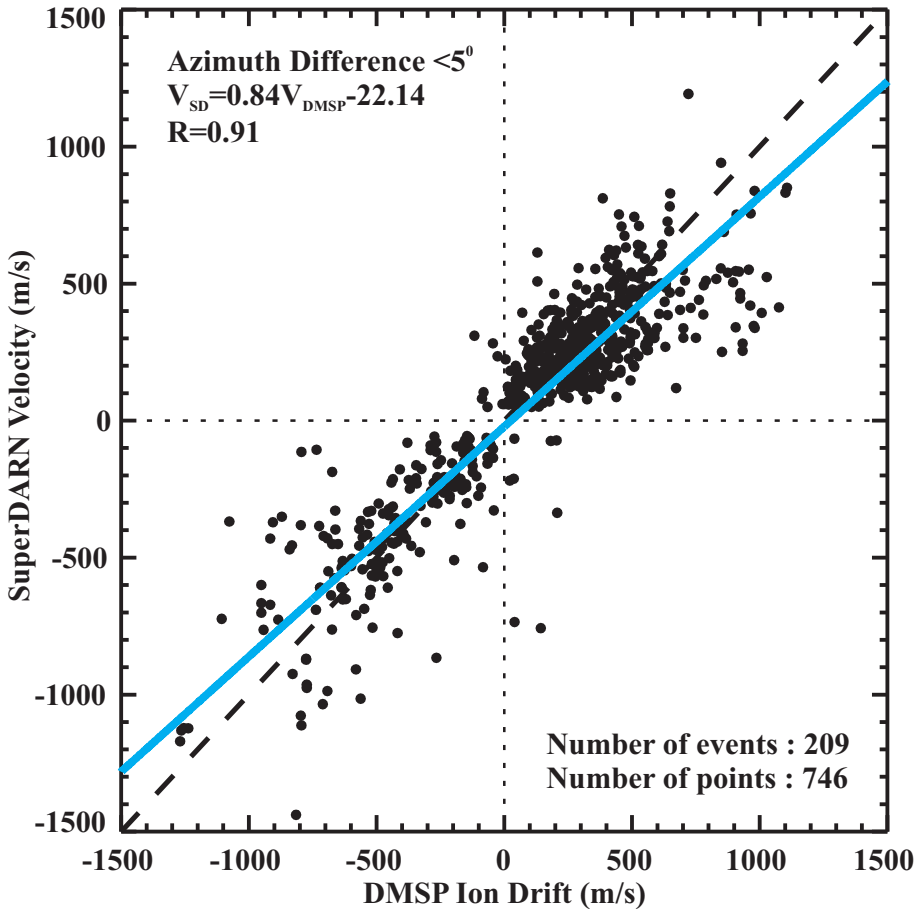

Figure 2.10: A scatter plot of the Hankasalmi, Pykkvibaer, Stokkseyri, Saskatoon, Kodiak, Halley, Sanae, Syowa South, and Syowa East l-o-s velocity versus DMSP F12, F13, and F15 cross-track ion drift for 209 events at radar ranges of 517-2857 km where the azimuthal difference between measurements was $< 5°$. The equation of the best-fit line (blue line) and correlation coefficient of the data are indicated (*Drayton*, 2006).

the SuperDARN radar cells are 45 km apart in range with widths varying from 30 km to 160 km at ranges of 500 km to 2800 km, which is the range of radar measurements considered in the comparison shown in Figure 2.10. For typical ranges of comparison, the DMSP instruments are capable of observing more variability in terms of the spatial structure of the flow than the SuperDARN radars, which may account for some of the discrepancies in Figure 2.10.

Further discrepancies may be explained by temporal variability in the plasma flow. For each event, the DMSP track took 1-6 minutes to cross a given radar field of view. The comparison was performed using a 1-2 minute radar scan having a start time which began closest to the time the DMSP track crossed the central radar field of view. Throughout this

1-6 minute interval, the DMSP measurements are static, as each measurement is taken at a specific instance in time. However, if the plasma flow changes at a faster rate, the radar scan at the start of the DMSP crossing may be considerably different from the radar scan at the end of the DMSP crossing which could introduce regions of poor agreement for comparisons performed away from the central crossing point.

Although *Drayton et al.* (2005) and *Drayton* (2006) concluded there was reasonable agreement between concurrently measured SuperDARN and DMSP measurements of the plasma flow, they also acknowledged a tendency for the SuperDARN l-o-s velocities to be smaller than the DMSP ion drifts. Similar conclusions were drawn from a comparison of SuperDARN data with ISR (*Xu et al.*, 2001) and Canadian Advanced Digital Ionosonde (CADI) ionosonde (*Xu*, 2003) measurements. A more recent validation comparison was performed in *Koustov et al.* (2009) for the Rankin Inlet (RKN) PolarDARN radar. RKN velocities were compared to measurements from the Saskatoon SuperDARN radar, CADI, and DMSP. In agreement with previous comparisons, they concluded that the RKN l-o-s velocities agree with observations from both CADI ionosondes and DMSP satellites, but there is an underestimation of the SuperDARN measurements with respect to the other instruments.

The underestimation effect is a widely documented phenomenon, as is evident by the comparisons cited above. Some factors contributing to a reduction in the SuperDARN velocity include the assumption that the ionospheric index of refraction is $n = 1$ when calculating the l-o-s velocity, and contamination of F-region scatter with E-region and ground scattered echoes. *Gillies et al.* (2009) and *Ponomarenko et al.* (2009) hypothesize that velocity underestimation is due to neglecting the index of refraction of the F-region ionosphere when measuring the SuperDARN l-o-s velocity. In Section 2.1.2 the echo Doppler velocity was found to be $v_o = \frac{w_D c}{4\pi f_{radar}}$, an equation that was derived by assuming the speed of the radio wave signal in the ionospheric medium v was equal to the speed of light c. *Gillies et al.* (2009) state that HF radio wave propagation is dependent on the index of refraction in the ionosphere, and that a substitution of $v = \frac{c}{n}$, where n is the refractive index in the medium, should be used. They develop a technique for estimating the index of refraction from the elevation angle measurement of the returned radar echo and find typical values of

$n = 0.8 - 1.0$, and argue that using $n = 1$ causes an overall underestimation of the Doppler velocity measured by SuperDARN. For a subset of events from the comparison by *Drayton* (2006) in which the elevation angle could be determined, *Gillies et al.* (2009) recalculated the l-o-s velocity and repeated the comparison. The correlation coefficient for the reduced data set before and after the elevation angle correction remained constant at $R = 0.92$. However, the slope of the best-fit line to the data set improved from $m = 0.74$ to $m = 0.83$ after the correction. Although the elevation angle correction did not solve the problem of SuperDARN velocity underestimation, it did improve the agreement between data sets.

Gillies et al. (2010) compared SuperDARN and European Incoherent Scatter (EISCAT) velocity measurements for 1995-1999. Similar to the DMSP comparison results, SuperDARN measurements were shown to be correlated with, but underestimate, the EISCAT measurements (R=0.91, m=0.78). *Gillies et al.* (2010) show that if the index of refraction is corrected by incorporating n_e (determined using either an elevation angle approximation, model, or direct measurement) the underestimation is improved by as much as 14%. *Gillies et al.* (2011) concludes that the remaining disagreement is due to small-scale dense structures in the scattering region which cause local enhancements in n_e, and devise a method for calculating the index of refraction based on SuperDARN measurements which accounts for the SuperDARN underestimation.

Unlike F-region irregularities which are expected to propagate at the rate of the $\mathbf{E} \times \mathbf{B}$ plasma drift, E-region irregularity velocities can saturate at the ion acoustic speed (e.g., *Nielsen and Schlegel*, 1985). The difference between E and F- region scatter is apparent in the results of *Koustov et al.* (2005) and *Drayton* (2006). *Koustov et al.* (2005) compared the l-o-s velocity determined from E-region scatter as observed by the Stokkseyri SuperDARN radar with the DMSP cross-track ion drift. The slope of the best-fit line to the data set was $m = 0.24$ indicating poor agreement between SuperDARN and DMSP observations, which strongly contrasts the slope of $m = 0.98$ determined for a similar comparison in *Drayton* (2006) for F-region scatter observed by the same radar.

Unfortunately, SuperDARN measurements occasionally suffer from E-region contamination when E-region echoes with saturated velocities are received through multiple hop propagation at ranges where F-region echoes are expected (*Milan et al.*, 1997; *Lacroix and*

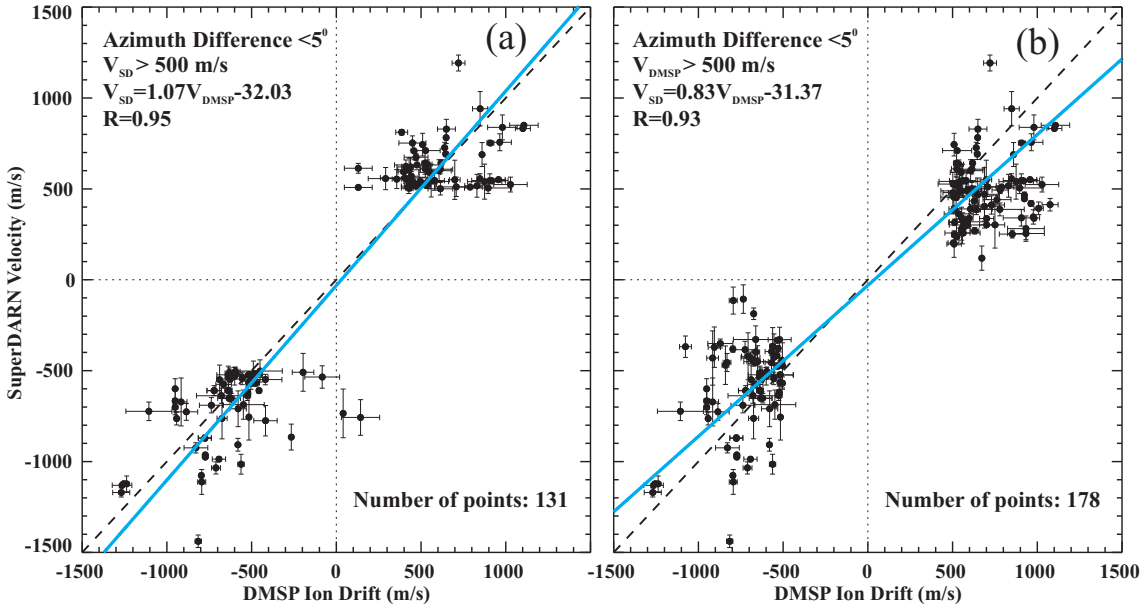

Figure 2.11: The same as in Figure 2.10 but for (a) SuperDARN velocities > 500 m/s, and (b) DMSP velocities > 500 m/s (*Drayton*, 2006). Vertical and horizontal bars indicate the error in the SuperDARN and DMSP measurements.

Moorcroft, 2001). *Milan et al.* (1997) found signatures of E-region contamination at far ranges (> 2000 km) for the Pykkvibaer radar in the form of a clustering of points at low spectral widths (< 200 m/s) and ion-acoustic speeds (see their Figure 10). *Lacroix and Moorcroft* (2001) performed a statistical study of the Pykkvibaer radar for F-region ranges (range > 1755 km) and found a similar contamination of E-region or ion acoustic echoes at shorter ranges.

Drayton (2006) assessed the contributions of E-region contamination to their data set of 746 points by first limiting the comparison to observations having SuperDARN velocities of > 500 m/s to ensure the velocities were not saturated. The resulting comparison is shown in Figure 2.11a. The slope of the best-fit line to the data set is m=1.07, which is closer to m=1 than the original comparison where m=0.84. *Drayton* (2006) repeated the comparison by limiting the results to DMSP ion drifts of > 500 m/s to observe the distribution of the SuperDARN l-o-s velocities. Figure 2.11b shows the results of the comparison. There are a number of points showing SuperDARN l-o-s velocities of ∼400 m/s, corresponding to the approximate ion-acoustic speed. This suggests that a number of the points of comparison shown both in Figure 2.11b, and therefore Figure 2.10, correspond to SuperDARN echoes

reflected from the E region, rather than the F region, as anticipated. The assessment summarized in Figure 2.11 therefore suggests that E-region contamination is a factor in the underestimation reported.

Another possible cause for underestimation of SuperDARN velocities is contamination from ionospheric echoes with ground scattered signals. The presence of ground scattered signals may be determined by examining the FITACF for each individual l-o-s velocity, which is beyond the scope of the present study.

Despite the assumption of $n = 1$ and the possible contamination by both E-region and ground scattered echoes, the relatively good agreement observed between SuperDARN l-o-s velocities and satellite, ISR, and ionosonde observations suggests that in general, the SuperDARN radars reasonably measure the $\mathbf{E} \times \mathbf{B}$ plasma drift, and that the SuperDARN l-o-s velocities are appropriate for determining the high-latitude convection pattern.

2.3 SuperDARN convection mapping techniques

Although each SuperDARN radar typically has data in a number of beams and gates, each measured Doppler velocity is a l-o-s component of the full $\mathbf{E} \times \mathbf{B}$ plasma drift vector. To infer the total vector of plasma flow from SuperDARN data, methods of combining individual measurements to obtain two-dimensional maps have been developed.

2.3.1 Data pre-processing

The l-o-s velocities derived using the FITACF approach are too noisy for direct mapping of the ionospheric convection. A method for smoothing and filtering the data has been developed by *Ruohoniemi and Baker* (1998).

The l-o-s velocities are median filtered based on the surrounding (in time and space) measurements to reflect a smoothed overall convection pattern. Observations in cells classified as ground scatter and in cells having velocity error estimates > 200 m/s are discarded. For each cell of interest, c_i, occurring at scan t_i, a data set is generated including observations from the 3×3 region of cells centered on c_i for the three scans centered at t_i. The median value of the data set is assigned to cell c_i. The uncertainty in each calculated ve-

locity is determined by calculating the standard deviation of the data set used for median filtering, discarding any points > 2 standard deviations from the mean of the data set and re-calculating the standard deviation.

The data are next averaged into a grid of equal area cells, with averaged gridded velocities placed at the centers of the grid cells which are separated by a distance equivalent to 1° of MLAT in order to create a more even distribution of points. A given grid cell is only assigned a velocity provided at least 25% of the measurements possible in that cell returned a velocity value. Figures 2.12 a and b show an example of median filtered and gridded observations, respectively, for a two-minute interval (one scan) on December 19, 2002 starting at 08:00 universal time (UT). Once the data pre-processing is complete, the resultant gridded l-o-s velocities are used to generate maps of the ionospheric convection using either the merge or FIT technique.

2.3.2 SuperDARN merge technique

Careful analysis of Figure 2.12b shows grid cells containing multiple gridded l-o-s velocities due to the overlapping fields of view of the SuperDARN radars. The full convection vector may be determined from the overlapping l-o-s components using the merge-technique (*Cerisier and Senior*, 1994; *Chisham et al.*, 2002). Each gridded l-o-s velocity represents a component of the full convection vector at that point for a given radar. By knowing the magnitude and azimuth of multiple l-o-s velocities in a given grid cell, simple geometry determines the magnitude and azimuth of the full convection vector in that cell. Figure 2.13 shows a grid cell with two overlapping velocities $\mathbf{v}_1$ and $\mathbf{v}_2$, which make up two components of the full convection vector $\mathbf{v}$. If $\hat{\boldsymbol{k}}_1$ and $\hat{\boldsymbol{k}}_2$ represent unit vectors in the l-o-s direction, the magnitude of $\mathbf{v}_1$ and $\mathbf{v}_2$ are found from (*Cerisier and Senior*, 1994)

$$v_1 = \mathbf{v} \cdot \hat{\boldsymbol{k}}_1 \tag{2.10}$$

$$v_2 = \mathbf{v} \cdot \hat{\boldsymbol{k}}_2. \tag{2.11}$$

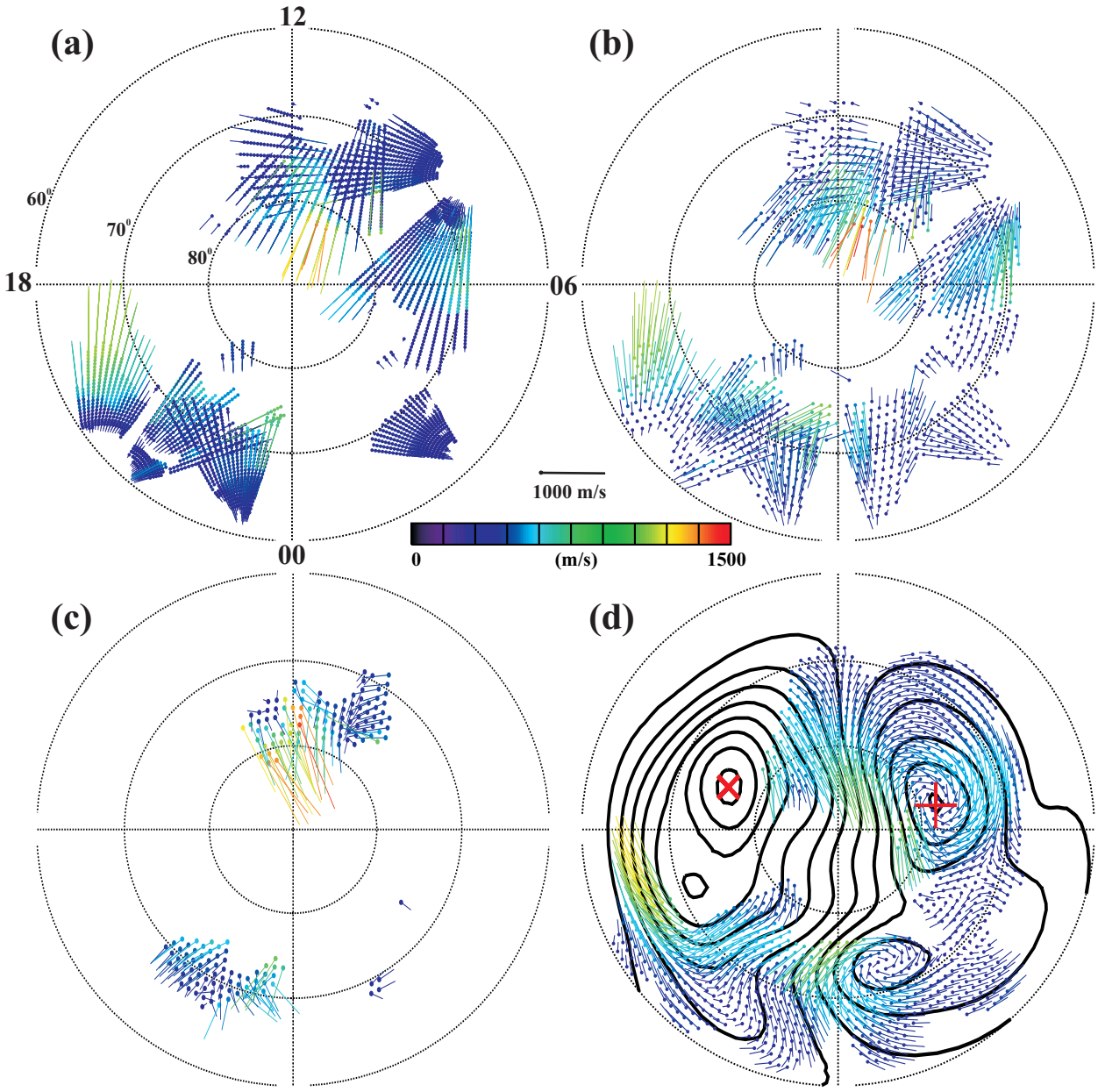

Figure 2.12: (a) Median filtered, (b) gridded l-o-s, (c) merged, and (d) FIT convection (K_{max}=8 and $\theta_{FIT} = 55°$) velocities for observations on December 19, 2002 at 08:00-08:02 UT in the northern hemisphere. In (d), contour lines indicate the electrostatic potential at a 6 kV spacing, and the red plus sign and cross indicate the maximum and minimum potential, respectively. MLT and MLAT labels in (a) may be applied to (b), (c), and (d).

The full two-dimensional velocity vector **v** is solved from equations (2.10) and (2.11) as

$$\mathbf{v} = \frac{[v_1 - v_2(\hat{\boldsymbol{k}}_1 \cdot \hat{\boldsymbol{k}}_2)]\hat{\boldsymbol{k}}_1 + [v_2 - v_1(\hat{\boldsymbol{k}}_1 \cdot \hat{\boldsymbol{k}}_2)]\hat{\boldsymbol{k}}_2}{1 - (\hat{\boldsymbol{k}}_1 \cdot \hat{\boldsymbol{k}}_2)^2.} \tag{2.12}$$

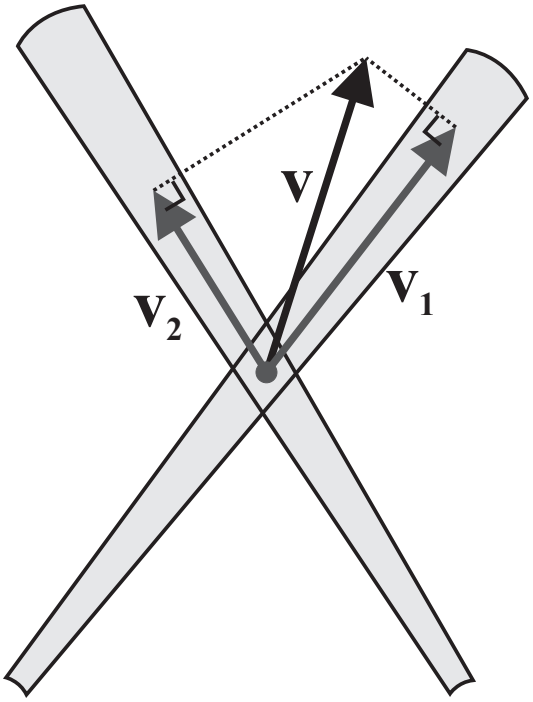

Figure 2.13: Illustration of the derivation (merging) of the full convection vector **v** from l-o-s velocities $\mathbf{v}_1$ and $\mathbf{v}_2$ measured in two different directions.

To get a large-scale picture of the convection flow, observations from all available velocities must be considered. For the example presented in Figure 2.12b, 1094 individual gridded l-o-s velocity measurements are reduced to 175 merged velocity vectors. Figure 2.12c illustrates the convection determined from the merge technique. These velocities represent pairings between the Kodiak/Prince George, Saskatoon/Kapuskasing, and Pykkvibaer/Hankasalmi radars. Although the merged convection velocities are determined directly from the gridded l-o-s velocities, the limited number of overlapping grid cells, and therefore the limited number of convection vectors, does not provide a complete or detailed picture of the global convection pattern. Another technique, called the FIT technique, was developed to alleviate this problem.

2.3.3 SuperDARN FIT technique

The FIT technique is a method by which SuperDARN gridded l-o-s velocities are used to infer a convection pattern over the entire convection zone (*Ruohoniemi and Baker*, 1998; *Shepherd and Ruohoniemi*, 2000). Figure 2.14 illustrates a thin spherical shell of radius r representing

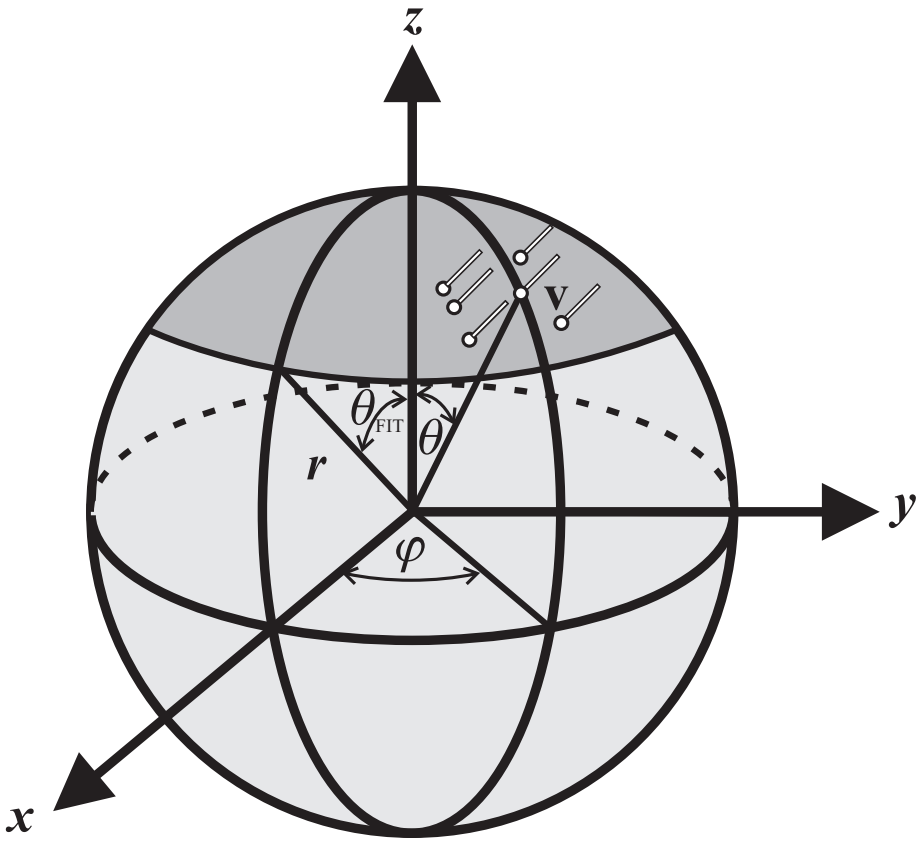

Figure 2.14: Representation of the ionosphere as a thin spherical shell of radius r. The convection zone (dark grey shading) is bounded by θ_{FIT}. Line-of-sight velocity vectors **v** are measured at magnetic co-latitude θ and longitude ϕ.

the ionosphere where gridded l-o-s velocity observations **v** are made at magnetic co-latitude θ and longitude ϕ. The dark shading indicates the high-latitude convection zone bounded by co-latitude θ_{FIT}, which must be pre-determined prior to processing (approximately $\sim 30^\circ - 45^\circ$ magnetic co-latitude). Co-latitude θ_{FIT} is determined based on the distribution and magnitude of the l-o-s velocity observations by selecting the largest boundary containing all gridded l-o-s velocities greater than 100 m/s (*Ruohoniemi and Baker*, 1998). Alternatively, θ_{FIT} might be estimated based on observations from another instrument. For example, *Rich and Hairston* (1994) define the boundary of the flow based on observations of the ion drift measured by the DMSP satellites. For a given satellite pass, measurements centered around 50°, 55°, 60°, and 65° are tested to see if the magnitude of the horizontal component of the flow is < 200 m/s, the magnitude of the vertical component of the flow is < 350 m/s, and that the standard deviation of the velocities in either component is < 77.4 m/s. The most

equatorward latitude meeting these criteria is selected as the equatorward boundary of the flow.

The coordinates of the input gridded l-o-s velocities are confined to the high-latitude convection zone poleward of θ_{FIT}. The velocity coordinates are then redistributed ('stretched') across the entire spherical Earth and a spherical harmonic analysis (SHA) technique is applied to generate a convection map which is then reassigned ('un-stretched') to the high-latitude region.

The redistribution of data points is performed by multiplying the co-latitude of the input vectors with a stretching factor α to obtain a new co-latitude, θ',

$$\theta' = \alpha\theta, \tag{2.13}$$

where $\alpha = 180^\circ/\theta_{FIT}$ is the stretching factor.

To map the ionospheric convection pattern, the input velocities are related to the electrostatic potential as follows. The electrostatic potential, Φ_E, may be represented by a series expansion (*Ruohoniemi and Baker*, 1998)

$$\Phi_E(\theta', \phi) = \sum_{k=0}^{K_{max}} \sum_{m=0}^{k} [A_{km} \cos(m\phi) + B_{km} \sin(m\phi)] P_k^m(\cos\theta'), \tag{2.14}$$

where $P_k^m(cos\theta')$ represents the associated Legendre function of the first kind of integer degree (k) and order (m), K_{max} is the maximum degree, and A_{km} and B_{km} are constant coefficients for each degree/order pair.

Electrostatic potential is related to the electric field ($\mathbf{E}$) by

$$\mathbf{E} = -\nabla\Phi_E, \tag{2.15}$$

which is in turn related to velocity through

$$\mathbf{v} = \frac{\mathbf{E} \times \mathbf{B}}{B^2}, \tag{2.16}$$

where $\mathbf{E}$ and $\mathbf{v}$ represent the electric field and velocity on a spherical shell and $\mathbf{B}$ is the

dipole magnetic field given by $\mathbf{B} = -B\hat{\boldsymbol{r}}$. The magnitude of $\mathbf{B}$ is given by

$$B = \frac{1}{2} B_0 \left(1 - \frac{3h}{R_E}\right) \sqrt{1 + 3\cos^2\theta}, \tag{2.17}$$

where h is the radar scattering height for F-region scatter, R_E is the Earth's radius, and $B_0 = 5.8 \times 10^{-5}$ T is the magnitude of the Earth's magnetic field at the magnetic pole in the northern hemisphere on the surface of the Earth. Note that work is currently being done to replace the dipole magnetic field used in the standard FIT technique with the International Geomagnetic Reference Field (IGRF) (personal communication with Robin Barnes). Such a change has already been implemented in *Cousins and Shepherd* (2010) and in this research. The magnetic field is therefore determined from the IGRF magnetic field components using

$$B = \sqrt{B_N^2 + B_E^2 + B_V^2}, \tag{2.18}$$

where B_N, B_E, and B_V represent the north, east, and vertical components of the IGRF magnetic field (*Haines*, 1988; *Blakely*, 1995)

$$B_N = -\sum_{k=0}^{K_{max}} \sum_{m=0}^{k} \left(\frac{R_E}{R_E + h}\right)^{k+2} \left[g_{km}\cos(m\phi) + h_{km}\sin(m\phi)\right] \frac{dP_k^m(\cos\theta)}{d\theta}, \tag{2.19}$$

$$B_E = -\sum_{k=0}^{K_{max}} \sum_{m=0}^{k} \left(\frac{R_E}{R_E + h}\right)^{k+2} \left[g_{km}\sin(m\phi) - h_{km}\cos(m\phi)\right] m \frac{P_k^m(\cos\theta)}{\sin\theta}, \tag{2.20}$$

$$B_V = -\sum_{k=0}^{K} \sum_{m=0}^{k} \left(\frac{R_E}{R_E + h}\right)^{k+2} \left[g_{km}\cos(m\phi) + h_{km}\sin(m\phi)\right] (k+1) P_k^m(\cos\theta), \tag{2.21}$$

where k and m represent the degree and order of the spherical harmonic expansion, g_{km} and h_{km} are expansion coefficients for each degree/order pair, and the unstretched coordinate system is used. Coefficients g_{km} and h_{km} have been determined at five year increments from 1900 to 2010 to a maximum degree of $K_{max} = 10$ for 1900-1995 and $K_{max} = 13$ for 2000-2010. Up to date IGRF magnetic field coefficients are available online from the International Association of Geomagnetism and Aeronomy (IAGA) at

http://www.ngdc.noaa.gov/IAGA/vmod/igrf.html.

Electric field is calculated by breaking equation (2.15) into components:

$$\begin{aligned} E_\phi &= -\frac{1}{r\sin\theta'}\frac{d\Phi_E}{d\phi} \\ &= \frac{1}{rsin\theta'}\sum_{k=0}^{K_{max}}\sum_{m=0}^{k}\left[A_{km}\sin(m\phi) - B_{km}\cos(m\phi)\right] mP_k^m(\cos\theta') \end{aligned} \tag{2.22}$$

$$\begin{aligned} E_\theta &= -\frac{1}{r}\frac{d\Phi_E}{d\theta} \\ &= \frac{-1}{r}\sum_{k=0}^{K_{max}}\sum_{m=0}^{k}\left[A_{km}\cos(m\phi) + B_{km}sin(m\phi)\right]\frac{dP_k^m(cos\theta')}{d\theta}. \end{aligned} \tag{2.23}$$

The velocity $\mathbf{v}$ is found from equation (2.16) as

$$\mathbf{v} = \frac{E_\phi}{B}\hat{\boldsymbol{\theta}} - \frac{E_\theta}{B}\hat{\boldsymbol{\phi}}, \tag{2.24}$$

where $\hat{\boldsymbol{\theta}}$ and $\hat{\boldsymbol{\phi}}$ are unit vectors in the θ and ϕ directions.

Substitution of equations (2.22) and (2.23) into equation (2.24) results in an equation for velocity using spherical harmonics that depends on the A_{km} and B_{km} coefficients:

$$\begin{aligned} \mathbf{v} &= \sum_{k=0}^{K_{max}}\sum_{m=0}^{k}\frac{\left[A_{km}sin(m\phi) - B_{km}cos(m\phi)\right]}{B}\frac{mP_k^m(cos\theta')}{rsin\theta'}\hat{\boldsymbol{\theta}} \\ &\quad + \sum_{k=0}^{K_{max}}\sum_{m=0}^{k}\frac{\left[A_{km}cos(m\phi) + B_{km}sin(m\phi)\right]}{rB}\frac{dP_k^m(cos\theta')}{d\theta}\hat{\boldsymbol{\phi}}. \end{aligned} \tag{2.25}$$

The component of the velocity in the l-o-s direction is given by

$$\mathbf{v}_i \cdot \hat{\boldsymbol{k}}_i = v_{\theta_i}\cos\gamma_i + v_{\phi_i}\sin\gamma_i, \tag{2.26}$$

where $\hat{\boldsymbol{k}}_i = -\cos\gamma_i\hat{\boldsymbol{\theta}} + \sin\gamma_i\hat{\boldsymbol{\phi}}$ is the unit vector along the l-o-s direction, and γ_i represents the azimuth of the l-o-s velocity v_{los_i}. The fitting coefficients A_{km} and B_{km} are determined

by minimizing the equation (*Ruohoniemi and Baker*, 1998)

$$\chi^2 = \sum_{i=1}^{N} \frac{1}{\sigma_i^2} (\mathbf{v}_i \cdot \hat{\boldsymbol{k}}_i - v_{los_i})^2, \tag{2.27}$$

where σ_i is the error in v_{los_i}. The minimization is performed using singular value decomposition (*Press et al.*, 1992; *Brandt*, 1998). Once A_{km} and B_{km} are known, velocity, electric field, and potential may be described anywhere on the sphere.

Figure 2.12d shows an example of the electrostatic potential and convection velocity (at the location of input data points) for $K_{max} = 8$ and $\theta_{FIT} = 55°$. Contours are spaced every 6 kV and the plus sign and cross indicate the location of maximum and minimum potential, respectively. The convection pattern is two-celled with anti-sunward flow directly along the noon-midnight meridian, consistent with what is expected for the IMF during this time period ($B_y \sim 0$ nT, $B_z < 0$ nT, $6 < B_t < 12$ nT). Although the direction of the flow determined by the FIT technique agrees with that determined by merging vectors, the magnitudes of the flow do not agree on the dayside. The merged vectors report anti-sunward directed flows of as high as 1200-1500 m/s whereas the FIT vectors indicate magnitudes of ∼800 m/s. Such differences might be explained by constraints applied to the FIT technique.

2.4 Constraints to the FIT technique

Although SuperDARN has a large field-of-view, there can still be gaps in the data due to a lack of radars or poor signal propagation conditions. Adding additional velocity vectors to the input gridded l-o-s velocity data set prior to processing helps to constrain the shape of the convection pattern in regions not constrained by data.

Heppner and Maynard (1987) used electric field measurements from the Dynamics Explorer 2 satellite to study the location of the convection boundary. They determined the boundary was circular on the nightside, and contracted poleward on the dayside. *Shepherd and Ruohoniemi* (2000) noticed that the circular convection boundary imposed by θ_{FIT} tends to produce reasonable flow on the nightside, but indicates flows at unrealistically low latitudes on the dayside. To correct this, they introduced the use of a Heppner and Maynard Boundary (HMB) to define the lower latitude boundary of the convection following the observations of *Heppner and Maynard* (1987). An HMB is applied to the data set by filling grid cells in

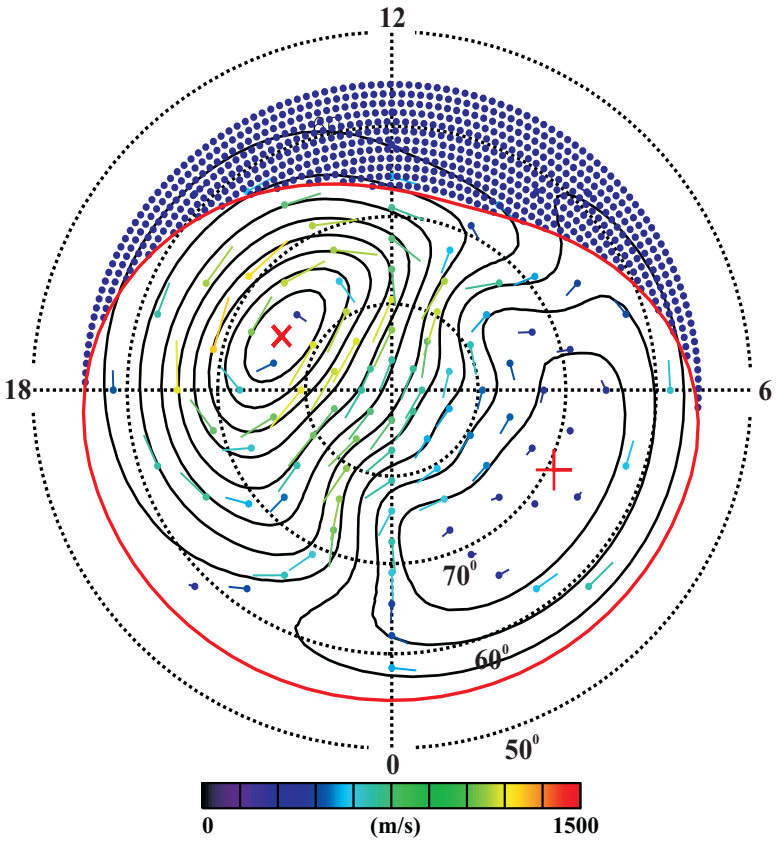

Figure 2.15: Sample statistical model convection pattern. Contours indicate Φ_E at a 6 kV contour spacing. The plus and cross signs represent the maxima and minima Φ_E. Colored vectors show sample model vectors, and the red line indicates the HMB.

the region between the low-latitude circular boundary and the HMB with fill-vectors having magnitudes of 1 m/s and azimuths of 45° to indicate there should not be flow in this region. Each HMB fill vector is assigned an error of 200 m/s. In Figure 2.15 the HMB is indicated by a red curve, and the blue dots equatorward of this curve indicate the grid cells containing fill-vectors to constrain the flow. The latitude of the HMB (λ_{HMB}) in terms of MLT is given by

$$\lambda_{HMB} = \begin{cases} \lambda_{FIT} & : \quad 0 < MLT < 5; 19 < MLT < 24 \\ \lambda_{FIT} + \delta l \left[1 + cos\left(\frac{\pi}{8}(MLT - 11)\right)\right] & : \quad 11 \leq MLT \leq 19 \\ \lambda_{FIT} + \delta l \left[1 + cos\left(\frac{\pi}{6}(11 - MLT)\right)\right] & : \quad 5 \leq MLT < 11 \end{cases} \tag{2.28}$$

where λ_{FIT} is the latitude associated with co-latitude θ_{FIT}, and $\delta l = \frac{\theta_{FIT}}{30^\circ} \times 5.5$. Co-latitude θ_{FIT} therefore refers to the co-latitude at which the HMB crosses the midnight MLT meridian.

In addition to fill-vectors defining an HMB, it is standard practice to add velocity vectors from a statistical convection model to the input data set. Two statistical convection models have been generated based on SuperDARN observations. The first is based on six years of observations from the Goose Bay SuperDARN radar (*Ruohoniemi and Greenwald*, 1996). The second is based on five years of observations from 9 northern hemisphere radars located at King Salmon, Kodiak, Prince George, Saskatoon, Kapuskasing, Goose Bay, Pykkvibaer, and Hankasalmi (*Ruohoniemi and Greenwald*, 2005). Despite the differing data sets used to generate the convection models, *Ruohoniemi and Greenwald* (2005) indicate a general agreement between the more recent 2005 model and the original 1996 model based on both the shape of the overall convection pattern and the magnitude of the cross polar cap potential (CPCP). Unfortunately, the more recent model was lost (personal communication with J. M. Ruohoniemi), and it is necessary to use the original 1996 model (*Pettigrew et al.*, 2010).

Ionospheric convection is highly dependent on the strength and polarity of the B_y and B_z components of the IMF. The model convection patterns are therefore sorted according to the orientation and magnitude of the IMF in the $y-z$ plane (in GSM coordinates). The IMF magnitude in the y-z plane (B_t) is broken into three groupings for 0-4 nT, 4-6 nT, and 6-12 nT for IMF clock angles ($\alpha = \arctan\left[\frac{B_y}{B_z}\right]$) of $[0°, 45°, 90°, 135°, 180°, 225°, 270°, 315°] \pm 22.5°$. During the completion of this thesis, another SuperDARN-based convection model was published by *Pettigrew et al.* (2010) and *Cousins and Shepherd* (2010) which further separates the convection pattern by hemisphere for various solar wind, IMF, and dipole tilt-angle conditions, and creates a dynamic convection model.

Before the raw l-o-s observations from multiple years of observation are used to determine the model convection pattern, they are smoothed and filtered using techniques described in Section 2.3.1. Gridded l-o-s velocities within each grid cell are then grouped according to magnetic azimuth at 10° intervals centered at $0, \pm 10°, \pm 20°, \pm 30°$, etc. Each grouping is averaged to create a series of average gridded l-o-s velocities within each bin. An input data set comprised of these gridded l-o-s velocities along with HMB fill-vectors for the desired value of θ_{FIT} is created and mapped using the FIT technique described in the previous section to create a statistical convection model.

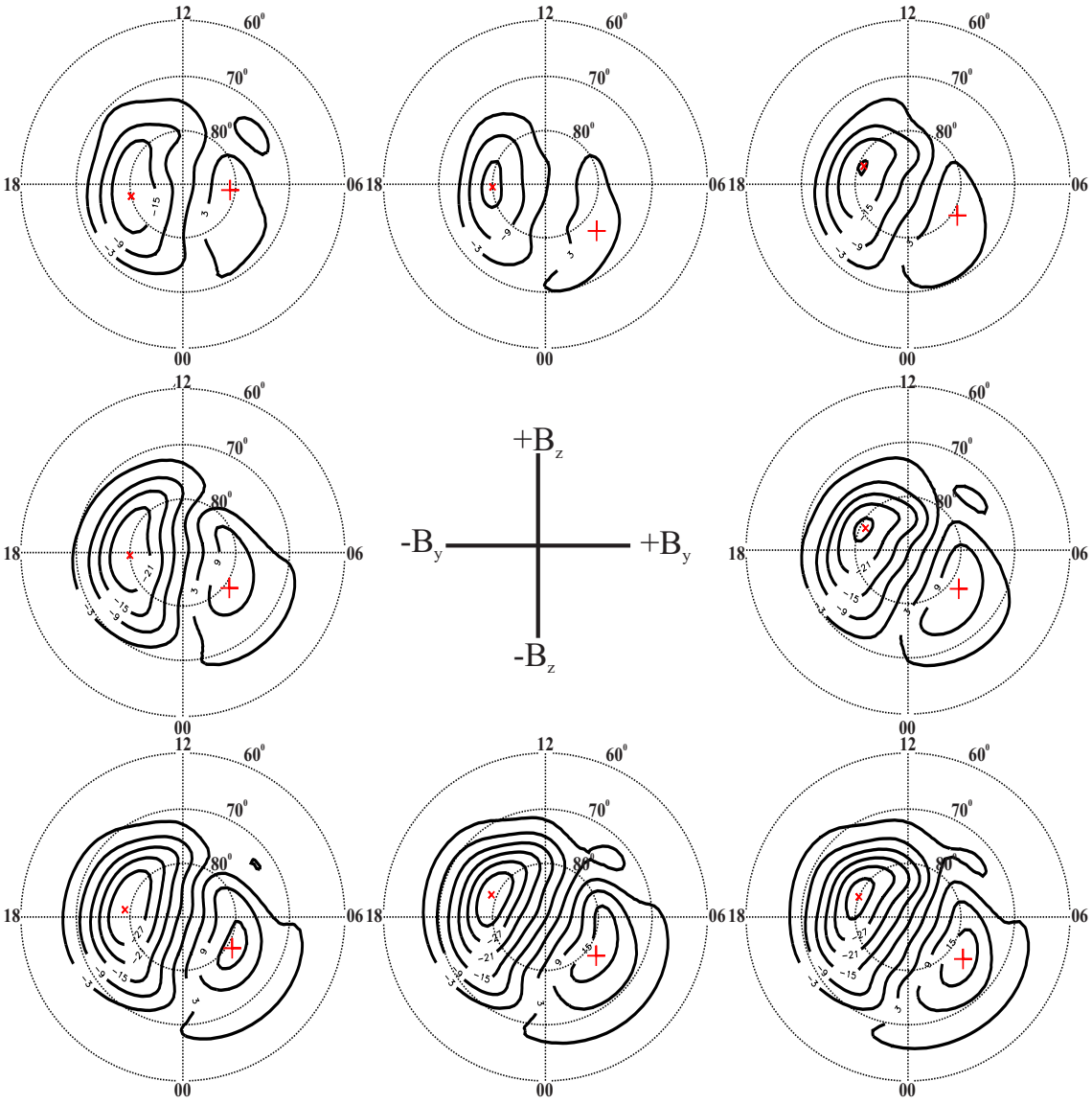

Figure 2.16: SuperDARN statistical convection model for various polarities of IMF B_y and B_z for periods of $0 < B_t \leq 4$ nT, generated for $\theta_{FIT} = 30°$ and $K_{max} = 8$. Convection contours are drawn in 6 kV increments and the red plus and cross signs indicate the location of the maximum and minimum potentials, respectively.

Figures 2.16, 2.17, and 2.18 illustrate the statistical convection patterns for various magnitudes and polarities of the IMF with contributions from an HMB. Table 2.2 lists the magnitude of the CPCP calculated for each map. As an example, the maps have been generated with $\theta_{FIT} = 30°$ and $K_{max} = 8$. The SuperDARN statistical convection model clearly shows a two-celled convection pattern for IMF $B_z < 0$ evolving to a three and four-celled pattern as B_z becomes positive. This pattern is more pronounced as B_t increases.

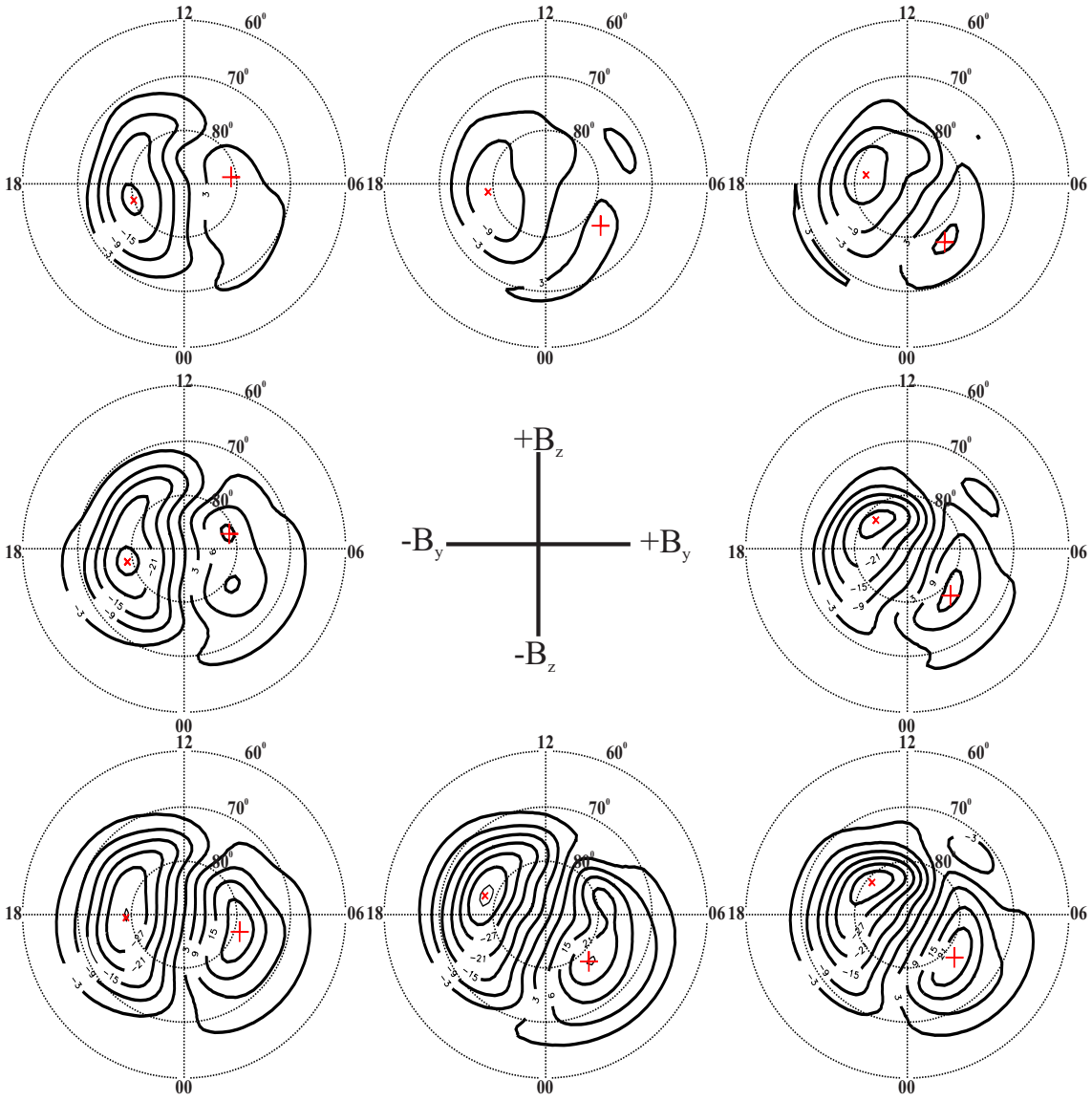

Figure 2.17: Same as Figure 2.16, but for periods of $4 \leq B_t \leq 6$ nT.

Once coefficients have been determined for the statistical model convection pattern, velocity vectors are calculated and added to the velocity data set that needs to be constrained. The fewest number of model vectors required to constrain the fit is determined and coordinate locations are distributed about the entire high-latitude region according to the methods of *Ruohoniemi and Baker* (1998) and *Haines* (2007b). First, the stretched co-latitude spanning from $\theta = 0 - 180°$ is divided into $K_{max} + 2$ intervals. For K_{max} even, the interval at $\theta = 90°$ is divided into $2K_{max}$ intervals of evenly spaced longitude. Moving out from the equator, each subsequent interval is divided into 2 fewer intervals of longitude. Coordinate values are not

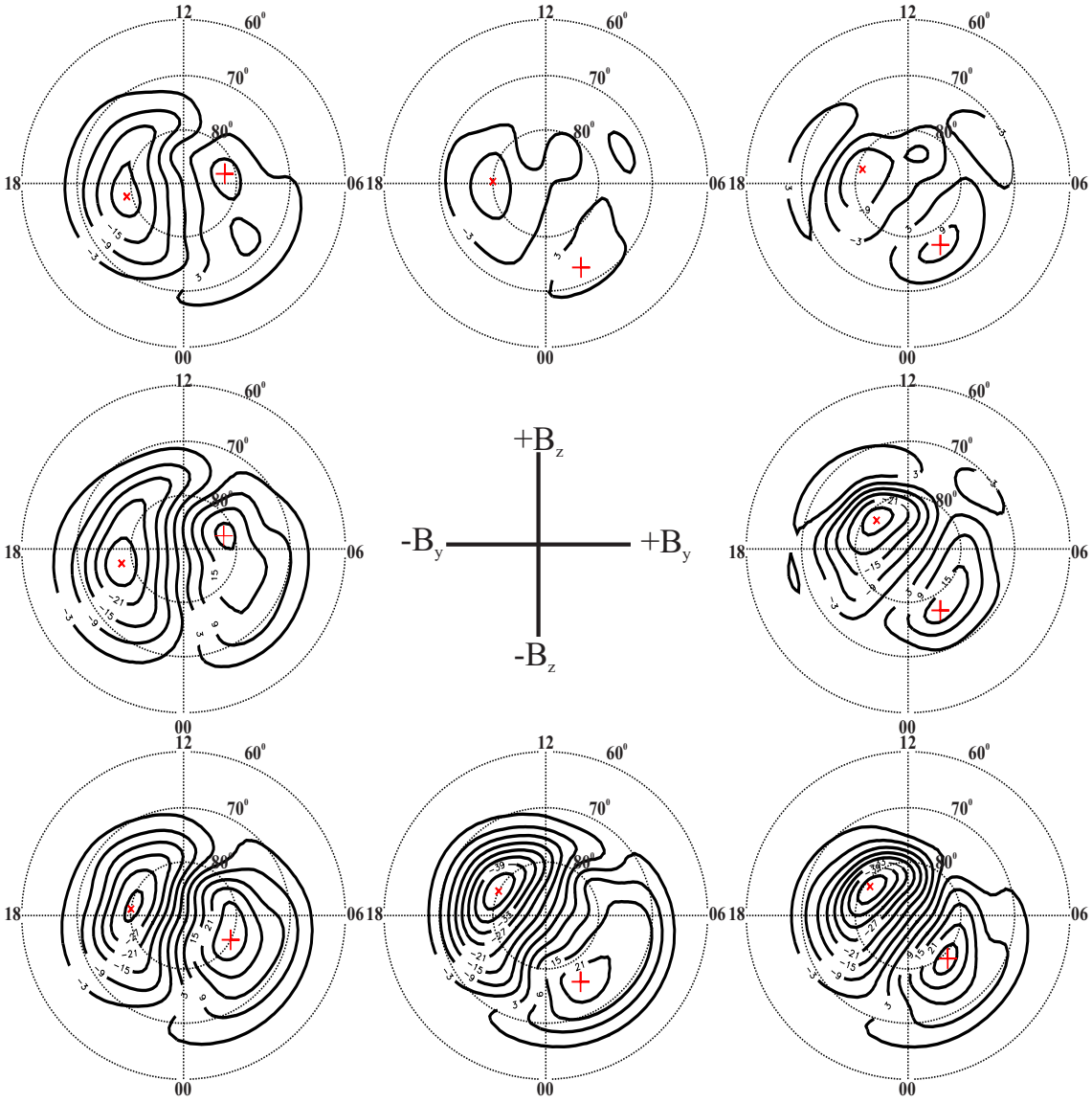

Figure 2.18: Same as Figure 2.16, but for periods of $6 \leq B_t \leq 12$ nT.

assigned at the poles. The coordinates are then stretched back to the high-latitude region. The result is a data-set of $K_{max}\left(3K_{max}+2\right)/2$ coordinates. The procedure is identical for K_{max} odd, except the stretched co-latitude is broken into $K_{max}+3$ intervals resulting in a total of $\left(3K_{max}^2+4K_{max}-3\right)/2$ coordinate locations. The black contours in Figure 2.15 represent one such convection pattern for a period of IMF $B_z < 0$, $B_y \sim 0$, and $6 \leq B_t \leq 12$ nT processed using $K_{max} = 8$. The colored vectors pointing along the contours in Figure 2.15 indicate the coordinate locations and model velocity vectors for $K_{max} = 8$.

Table 2.2: CPCP (in kV) for the SuperDARN statistical convection model for various strengths and polarities of the IMF B_z.

IMF B_y	**IMF B_z**	**B_t (0-4 nT)**	**B_t (4-6 nT)**	**B_t (6-12 nT)**
< 0	< 0	49	57	65
> 0	< 0	54	62	78
< 0	> 0	27	30	34
> 0	> 0	29	27	23
~ 0	< 0	55	67	73
~ 0	> 0	22	18	16
> 0	~ 0	42	45	47
< 0	~ 0	39	44	53

The error assigned to the statistical model vectors (σ_m) is (*Ruohoniemi and Baker*, 1998)

$$\frac{1}{\sigma_m^2} = \frac{1}{N}\sum_{i=1}^{N}\frac{1}{\sigma_i^2}, \tag{2.29}$$

where N is the number of gridded l-o-s velocities. A correction to the error is made through multiplication by $\frac{K_{max}}{4}$ (*Shepherd and Ruohoniemi*, 2000). For higher orders, the number of model vectors used to constrain the fit is larger, and the convection pattern is more dependent on the model vectors than for lower orders. This correction factor decreases dependence on the model vectors at higher orders.

Once the model velocity vectors and the HMB fill-vectors are determined, they are divided into north/south and east/west components for inclusion in the velocity data set.

2.5 SuperDARN convection velocity and measurements by other instruments

The FIT technique is currently the most commonly used approach for mapping ionospheric convection based on SuperDARN measurements. This section will involve an examination of the ability of the FIT technique to accurately map ionospheric convection based on

comparisons with DMSP measurements of the full convection vector as well as a discussion of the constraints applied to the FIT technique.

Xu et al. (2008) compared two-dimensional convection vectors derived using the FIT technique based on SuperDARN measurements to two-dimensional ion drifts determined from the cross-track and along-track component of the ion drift observed by DMSP satellites. They found good agreement between convection vectors in terms of convection azimuth ($R = 0.84$ and $m = 0.96$), but not in terms of magnitude ($R = 0.53$ and $m = 0.29$). They conclude that the SuperDARN FIT technique is able to determine the general direction of the flow, but tends to underestimate the magnitude of the flow. They attribute discrepancies to differing spatial and temporal resolutions of the instruments, and processes associated with the FIT technique, including pre-processing of the l-o-s velocities into gridded l-o-s velocities.

Fiori et al. (2010) examined a subset of 57 northern hemisphere events from the original SuperDARN l-o-s velocity versus DMSP comparison performed in *Drayton et al.* (2005) and *Drayton* (2006) and presented in Section 2.2. For this subset, $R = 0.88$ and $m = 0.74$. Although their analysis was for the specific purpose of validating a new approach for convection mapping, they also present results for the FIT technique with $\theta_{FIT} = 30^\circ$ and maximum plotting degree $K_{max} = 6$ for the corresponding two-minute intervals. Here the data set will be analyzed with $K_{max} = 4$ for direct comparison with the results of *Xu et al.* (2008). Using a similar comparison technique as in *Drayton et al.* (2005) and *Drayton* (2006), all DMSP velocities within either a 45 km (or 55 km if there are too few data points) radius of a given SuperDARN grid point were averaged together for comparison with the corresponding convection vector. Figures 2.19 a and b show the results of a comparison of the magnitude and azimuth of the convection vectors. For convection azimuth, observations are mostly clustered about the central bisecting line and the slope of the best-fit line to the data set is $m = 0.77$. The correlation coefficient is somewhat low at $R = 0.48$ due to a number of points indicating opposite directions of the flow. Even though these points do not dominate the plot, they do lower the value of the correlation coefficient; if they are instead removed (as was done in *Xu et al.* (2008)), the correlation coefficient and slope increase to $R = 0.92$ and $m = 0.87$. The slope of the best-fit line relating the convection magnitude is somewhat reduced ($m = 0.41$), and the correlation coefficient is $R = 0.62$. These results agree with

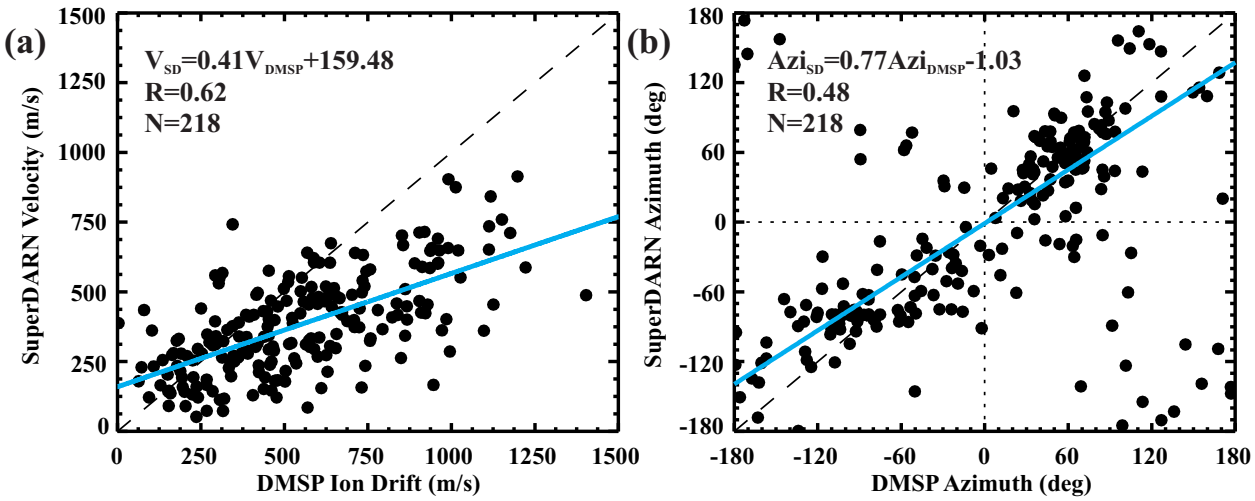

Figure 2.19: Scatter plots of the (a) velocity magnitude and (b) azimuth of the plasma flow inferred from SuperDARN l-o-s velocities using the FIT technique with K_{max}=4 and DMSP ion drifts. The equation of the best-fit line (heavy blue line), correlation coefficient, and number of points of comparison are indicated.

those of *Xu et al.* (2008), and indicate excellent agreement for the FIT-derived convection vectors in terms of azimuth, but a general reduction in terms of convection magnitude.

The slope of the best-fit line to the convection magnitude is somewhat lower than the original l-o-s comparison (m = 0.41 compared to m = 0.74). Such a reduction is likely due to the overall smoothing performed by the FIT procedure. Despite this reduction, the correlation between the data sets, and the excellent results in terms of azimuth suggests the FIT-derived convection is in reasonable agreement with DMSP observations of the ion drift. These results are not surprising, as the DMSP passes in the original comparison were chosen during periods of low spatial and temporal variation of both SuperDARN and DMSP observations. In addition, passes were chosen during periods where the corresponding radar indicated good coverage for F-region echoes, so that a large number of vectors would be available to constrain the convection over the region of comparison at auroral latitudes. Such conditions offer the best opportunity for agreement, and it is therefore likely that discrepancies are due to internal processes of the FIT technique.

Such a comparison between DMSP and raw SuperDARN l-o-s or convection velocities has not been performed during periods of variable convection. Once the frequency of the flow variability increases, different resolutions between the radar and satellite instruments

cause disagreement between concurrent observations, and an inter-instrument comparison would likely show poor results.

In Section 2.2, E-region contamination was discussed as a possible source of error contributing to the general underestimation of the plasma flow measured by SuperDARN compared to that measured by the DMSP satellites. In generating the convection maps used to perform the comparison shown in Figure 2.19, filtering was not performed to remove contributions from E-region echoes. It should therefore be determined if E-region contamination influences the overall convection pattern. As was discussed in Section 2.1.1, E and F-region echoes generally originate at short and far ranges, respectively. One way to determine the effects of E-region contamination would be to compare convection maps generate based on all available echoes versus convection maps generated with F-region echoes for the same time period.

Two sets of convection maps were generated in 4-minute intervals using the FIT technique with constraints from a statistical model and an HMB with K_{max}=6 for the entire day on March 03, 2002, October 21, 2001, October 22, 2001, and January 25, 2000. These dates were chosen due to the large number of echoes available within each 4-minute interval (generally >1000). The first set of convection maps were generated based on all available measurements for all northern hemisphere radars, and the second set of maps were generated based solely on echoes from ranges of $>$ 700 km, representing F-region echoes. Figure 2.20a shows the CPCP determined based on E and F-region echoes versus the CPCP determined from F-region echoes. Convection maps were considered provided there were $>$ 300 echoes from the F region and at least 50 echoes from the E region. The resulting comparison has 697 points which corresponds to approximately 46 hours of observation. The points are clustered about the diagonal bisector of perfect agreement. The correlation coefficient to the data set is R=0.98, and the slope of the best-fit line is m=0.93. The average difference between the CPCP values is $<$ 4 kV with a maximum difference of 19.8 kV. Based on these results, it is clear that for well constrained events dominated by F-region echoes, E-region echoes have little influence on the overall convection pattern.

Events for this comparison were chosen for periods of large echo coverage. During such intervals, the echoes are dominated by F-region echoes. For these events, there were

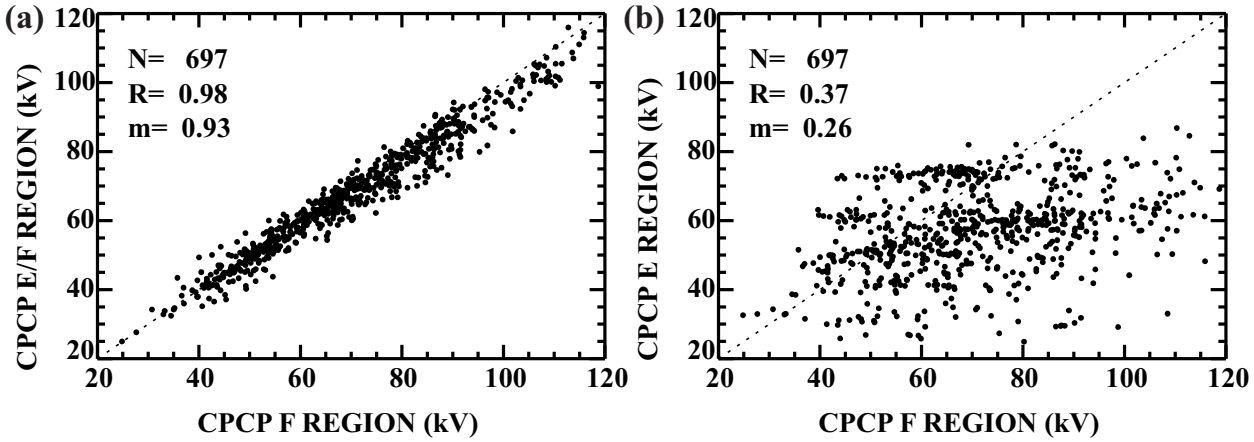

Figure 2.20: Scatter plots of the CPCP based on SuperDARN measurements from (a) E and F-region scatter and (b) E-region scatter only versus the CPCP determined using F-region scatter only. Convection was mapped using the FIT technique with contributions from a statistical model and an HMB. Maps were generated in 4-minute intervals for March 03, 2002, October 21, 2001, October 22, 2001, and January 25, 2000.

generally 400-1600 F-region echoes, compared to 50-170 E-region echoes. Although it is a highly unlikely occurrence, it is possible for a data set to be dominated by E-region echoes. This hypothetical situation may be replicated by generating convection maps based on the E-region echoes only. Figure 2.20b shows the CPCP determined based solely on E-region echoes versus the CPCP determined from the F-region echoes. In general, the CPCP for the E-region maps is <80 kV, and there is poor correlation between the E and F region results (R=0.37).

Although it is unlikely for a data set to be dominated by E-region echoes, such a situation may be avoided by requiring convection maps contain some minimum number of echoes. Throughout this thesis, a minimum of 300 echoes will be required for generating convection maps to ensure F-region domination.

2.6 Summary

The comparisons discussed in this Chapter indicate the SuperDARN l-o-s velocity provides a reasonable estimate of the ionospheric plasma flow. However, convection derived using the FIT technique indicates an overall reduction of the velocity magnitude in comparison to direct observations from the DMSP satellite. This reduction may be attributed to processes

internal to the FIT technique, such as the forcing of the convection and electrostatic potential to zero at θ_{FIT}, the addition of a statistical model and HMB to constrain the fit in regions lacking observations, and truncation of the series expansion used to represent the electrostatic potential.

The FIT-technique obtains a global solution for the convection pattern based on a fitting of both measurements and statistical model data. Such parameters as the total CPCP are estimated and applications that require a solution for the convection everywhere are satisfied. However, the reproduction of convection details over localized regions is compromised by the global constraints, e.g., a local observation of a high speed channel might be suppressed in the global fitting due to a lack of supporting measurements from surrounding regions.

In the next Chapter, spherical cap harmonic analysis (SCHA) is introduced as a new approach for analyzing SuperDARN data. The SCHA technique focuses on regions of dense measurements and generates a solution that is locally more optimal. It does not address the situation in the flows beyond these regions nor attempt a complete mapping over the entire convection region, unless there is a sufficient population of observations across the entire convection zone. The scopes of the FIT and SCHA techniques are different, although there is broad overlap in their purposes. Results from Chapter 3 have been published in *Fiori et al.* (2010).

Chapter 3

SCHA of SuperDARN observations for generating maps of ionospheric convection

Spherical cap harmonic analysis (SCHA) has been used in a wide range of applications involving spherical geometries, including mapping electrostatic potential, geomagnetic fields, and ionospheric current systems (*Haines*, 1985b; *Haines*, 1988; *Haines and Torta*, 1994; *Weimer*, 2005; *Green et al.*, 2006a,b). Here, SCHA will be applied to map ionospheric convection.

Consider a set of observations of the ionospheric plasma drift roughly confined to an arbitrarily located spherical cap of half-angle (or cap-size) θ_c. Recall Figure 2.14 which represents the geometry of a spherical shell on which the l-o-s velocity $\mathbf{v}$ is observed at magnetic co-latitude and longitude (θ, ϕ) within the convection zone bounded by θ_{FIT}. Figure 3.1 shows a spherical cap centered over the region of observations. The coordinates of the velocity vector $\mathbf{v}$ are re-defined as (θ', ϕ') with respect to the central coordinates of the spherical cap. See Appendix A.4 for a description of the spherical cap coordinate system and the coordinate transformation from spherical cap to north-pole centered coordinates.

3.1 Theory of SCHA

To map the ionospheric convection pattern, gridded l-o-s velocities are first related to the electrostatic potential. The electrostatic potential, Φ_E, may be represented by a series expansion (*Haines*, 1985a; *Haines*, 1988; *Haines*, 2007a; *Ruohoniemi and Baker*, 1998)

$$\Phi_E(\theta', \phi') = \sum_{k=0}^{K_{max}} \sum_{m=0}^{k} [A_{km} \cos(m\phi') + B_{km} \sin(m\phi')] P^m_{n_k(m)}(\cos\theta'), \tag{3.1}$$

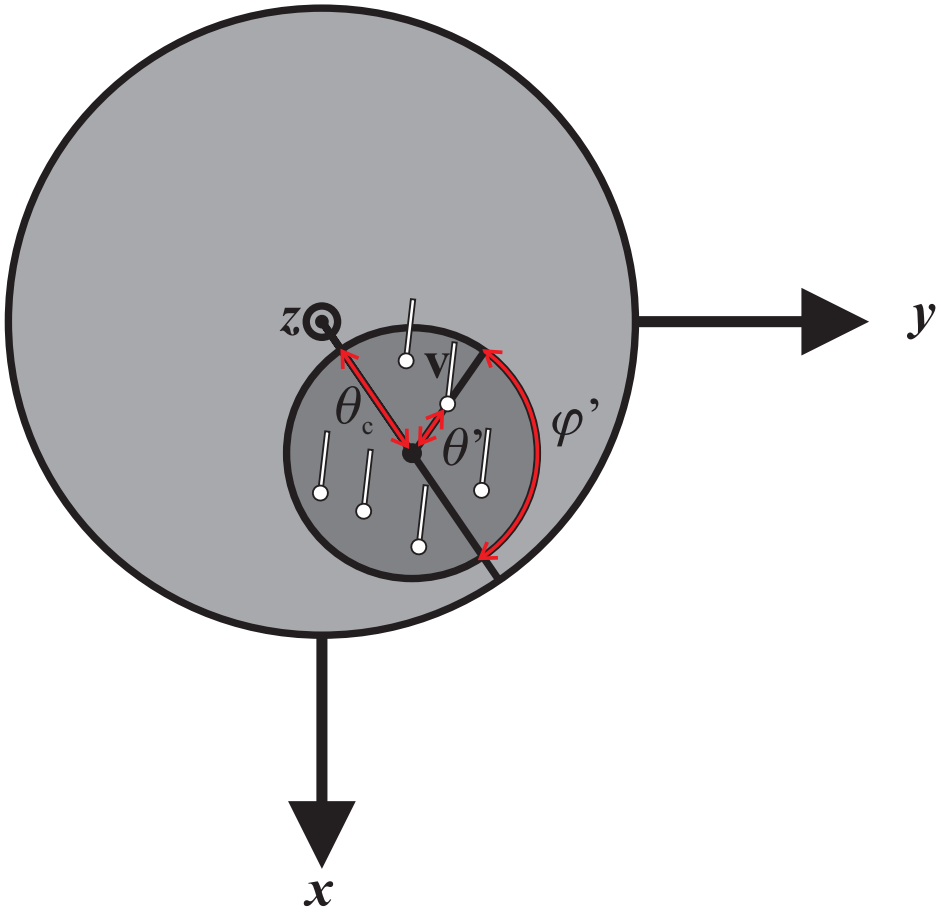

Figure 3.1: Geometry of a spherical cap (dark shading) of cap size θ_c within the convection zone illustrated in Figure 2.14. Observational points (white dots and lines) have coordinates defined in terms of the spherical cap co-latitude and longitude (θ', ϕ').

where $P^m_{n_k(m)}(\cos\theta')$ is the Associated Legendre Function of non-integer degree $n_k(m)$ and integer order m, where k is the integer degree-index, K_{max} is the maximum degree-index, and A_{km} and B_{km} are constant fitting coefficients for each degree-index/order pair.

The associated Legendre functions are defined as a power series (*Haines*, 1988)

$$P^m_{n_k(m)}(\cos\theta) = \sum_{j=0}^{\infty} A_j(m,n)\sin^{2j}\left(\frac{\theta}{2}\right), \tag{3.2}$$

where $A_j(m,n)$ is given by

$$A_j(m,n) = \begin{cases} K^m_n \sin^m\theta & : \quad j=0 \\ A_{j-1}(m,n)\frac{(j+m-1)(j+m)-n(n+1)}{j(j+m)} & : \quad j>0 \end{cases} \tag{3.3}$$

and K_n^m is a normalization constant. For $m = 0$ then $K_n^m = 1$, whereas for $m \neq 0$ then K_n^m is given by either

$$K_n^m = \frac{2^{\frac{1}{2}}}{2^m m!}\left[\frac{(n+m)!}{(n-m)!}\right]^{\frac{1}{2}} \qquad \text{(Schmidt normalization)} \tag{3.4}$$

or

$$K_n^m = (-1)^m \frac{1}{2^m m!}\left[\frac{(n+m)!}{(n-m)!}\right] \qquad \text{(Neumann normalization).} \tag{3.5}$$

In practice, a truncation limit of 60 terms is applied to the power series in equation 3.2 (*Haines*, 1988).

Equation (3.1) is similar to equation (2.14) for mapping electrostatic potential using SHA employed in the FIT technique, except the integer degree k is replaced by the non-integer degree $n_k(m)$. Fitting coefficients A_{km} and B_{km} are determined as before by following equations (2.15)-(2.27) using the unstretched spherical cap coordinate system and the electrostatic potential described in equation (3.1).

The series expansion of $\Phi_E(\theta', \phi')$ in equation (3.1) represents a solution to Laplace's equation found by the method of separation of variables and by solving eigenvalue problems subject to boundary conditions (*Haines*, 1985a; *Haines*, 1988; *Haines*, 2007a). The first boundary condition requires continuity in longitude so that both $\Phi_E(\theta', \phi')$ and its derivative have equal values at ϕ' and $\phi' + 2\pi$ for an arbitrary θ', restricting m to be both real and an integer. The second boundary condition requires regularity of the potential at the spherical cap pole such that

$$\Phi_E(0, \phi') = 0, \qquad m \neq 0 \tag{3.6}$$

$$\frac{\partial \Phi_E(0, \phi')}{\partial \theta'} = 0, \qquad m = 0, \tag{3.7}$$

which ensures $\Phi_E(\theta', \phi')$ is independent of ϕ' at the spherical cap pole. This condition is satisfied by using Associated Legendre Functions of the first kind and excluding those of the second kind. The final boundary condition requires

$$\Phi_E(\theta_c, \phi') = f(\phi') \tag{3.8}$$

$$\frac{\partial \Phi_E(\theta_c, \phi')}{\partial \theta'} = g(\phi'), \tag{3.9}$$

where $f(\phi')$ and $g(\phi')$ are arbitrary functions. Therefore both $\Phi_E(\theta', \phi')$ and its derivative must be arbitrary at $\theta' = \theta_c$. In *Haines* (1985a) it is shown that this boundary condition is met by choosing $n_k(m)$ such that

$$P^m_{n_k(m)}(\cos\theta')|_{\theta'=\theta_c} = 0 \qquad k - m = odd \tag{3.10}$$

$$\frac{dP^m_{n_k(m)}(\cos\theta')}{d\theta'}|_{\theta'=\theta_c} = 0 \qquad k - m = even, \tag{3.11}$$

forming two sets of basis functions having a real degree $n_k(m)$ which is not necessarily an integer.

To solve for $n_k(m)$, consider $P^m_{n_k(m)}(\cos\theta')|_{\theta'=\theta_c}$ and $\frac{dP^m_{n_k(m)}(\cos\theta')}{d\theta'}|_{\theta'=\theta_c}$ in equations (3.10) and (3.11), which are oscillating functions of $n_k(m)$ given m and θ_c. The $n_k(m)$ values represent the roots of equations (3.10) and (3.11). The degree index k starts at m and is incremented every time a root to either equation (3.10) or (3.11) is found. In this way, the difference $k-m$ fluctuates between even and odd values as $P^m_{n_k(m)}(\cos\theta_c)$ fluctuates between a maximum and zero amplitude. Figure 3.2 shows an example of $P^m_{n_k(m)}(\cos\theta_c)$ versus $n_k(m)$ for m=0 and $\theta_c = 10°$, $20°$, and $30°$. Zeroes and peaks in the functions correspond to solutions of $n_k(m)$ for equations (3.10) and (3.11), respectively. By solving equations (3.10) and (3.11) for every combination of k and m, the non-integer values of $n_k(m)$ are determined and may be used to solve for the fitting coefficients. Table 3.1 provides an example of the $n_k(m)$ values for all combinations of k and m for $\theta_c = 30°$. Both *Haines* (1990) and *Amm and Viljanen* (1999) point out that since $n_k(m) > k$ (see Table 3.1), the SCHA technique uses higher order Associated Legendre functions than the SHA technique, and is therefore able to achieve a higher spectral resolution than SHA.

Sometimes it is physically significant to set $\Phi_E(\theta', \phi') = 0$ kV at θ_c, for example, if the spherical cap is centered over the north pole and the boundary of the spherical cap

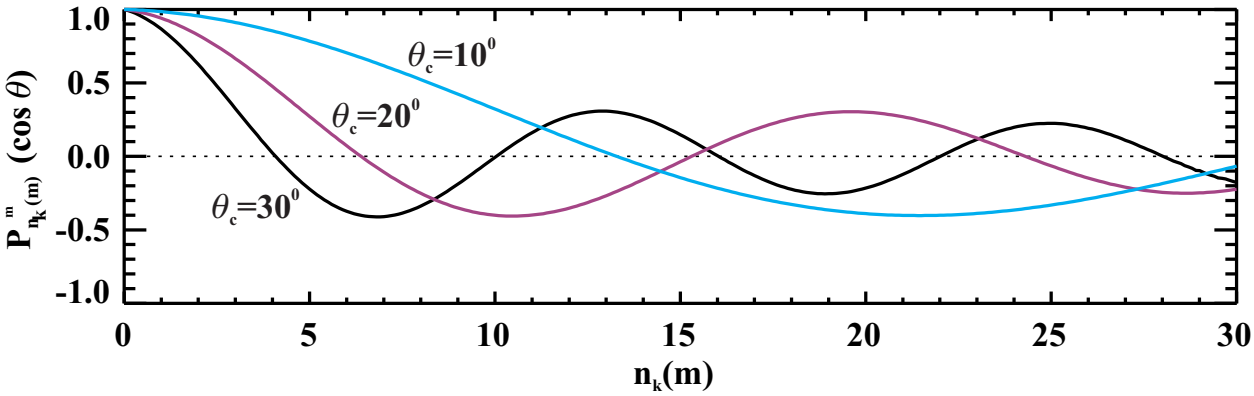

Figure 3.2: Associated Legendre function $P^m_{n_k(m)}(\cos\theta_c)$ versus non-integer degree $n_k(m)$ for m=0 and $\theta_c = 10°$, 20°, and 30°.

Table 3.1: $n_k(m)$ for $\theta_c = 30°$.

		m									
		0	1	2	3	4	5	6	7	8	9
	0	0.00	-	-	-	-	-	-	-	-	-
	1	4.08	3.12	-	-	-	-	-	-	-	-
	2	6.84	6.84	5.49	-	-	-	-	-	-	-
	3	10.04	9.71	9.37	7.75	-	-	-	-	-	-
	4	12.91	12.91	12.37	11.81	9.96	-	-	-	-	-
k	5	16.02	15.82	15.62	14.92	14.18	12.13	-	-	-	-
	6	18.94	18.94	18.58	18.22	17.39	16.50	14.29	-	-	-
	7	22.02	21.87	21.72	21.25	20.76	19.81	18.80	16.42	-	-
	8	24.95	24.95	24.69	24.42	23.84	23.24	22.19	21.07	18.55	-
	9	28.01	27.90	27.78	27.42	27.05	26.38	25.69	24.55	23.31	20.66

overlaps with the boundary of the high-latitude convection zone, or $\theta_c = \theta_{FIT}$. This can be accomplished by calculating $n_k(m)$ with equation (3.10) alone (SCHA-1) (see also *Weimer* (2005) for an example of the SCHA-1 technique applied to map the electrostatic potential). However, if the value of the potential at the boundary of the spherical cap is unknown (for example, θ_{FIT} is unknown), or the region of observation does not reasonably fill the convection zone, then both equations (3.10) and (3.11) should be used to determine $n_k(m)$ (SCHA-2) using an appropriate spherical cap centered over the data. Once the $n_k(m)$ are determined, SCHA may be used to solve for the velocity, electric field, and electrostatic potential at any point on the spherical cap.

To summarize, to generate a convection map with the SCHA mapping technique, one has to: (1) Collect and pre-process velocity observations as described in Section 2.3.1. (2)

Select the central coordinates of the spherical cap. If the observations are reasonably uniform this is accomplished by finding the average coordinates of the observations. (3) If the central coordinates are not located at the North Pole, the observation coordinates and azimuth must be redefined with respect to the center of the spherical cap (see Appendix A.4). (4) Select θ_c such that the angular distance between the edge of the spherical cap and the outlying observation points does not exceed the average angular spacing between observations. Note that if θ_{FIT} is known, it may be desirable to map the entire convection zone using SCHA-1 for a spherical cap centered over the pole with $\theta_c = \theta_{FIT}$. In such a case, it is allowable to have a larger gap between the observations and the boundary of the spherical cap due to the constraints of a zero potential boundary applied in the SCHA-1 technique. (5) Determine the $n_k(m)$ terms using either the SCHA-1 or SCHA-2 technique. (6) Calculate the fitting coefficients as described.

3.2 Spatial resolution of the SCHA technique

For an accurate portrayal of the ionospheric plasma flow, convection should only be mapped where it is adequately constrained by measurements. An algorithm has been developed to determine the mapping 'region of constraint'. The minimum wavelength λ_{min} that can be accurately mapped for a given data set is approximated by (*Bullard*, 1967)

$$\lambda_{min} = \frac{360^\circ}{n_k(m)} \cong \frac{4\theta_c}{K_{max}} = p\Delta\theta, \tag{3.12}$$

where the substitution $n_k(m) \cong (90^\circ K_{max})/\theta_c$ has been used (*Haines*, 1988), θ_c is the angular radius of the spherical cap, K_{max} is the maximum degree-index and order of the fit, p represents the number of observations that must be present on a given wavelength to accurately map that wavelength, and $\Delta\theta$ is the angular spacing between uniformly distributed observations. Observations are generally not evenly distributed and the value of $\Delta\theta$ may instead be used to define a region of reliability surrounding the measurement coordinates within which the convection is considered to be well constrained. For each data point a circle

of radius

$$\Delta\theta = \frac{4\theta_c}{pK_{max}} \tag{3.13}$$

is defined. If there are at least p observations within that circle, then the electrostatic potential and velocity vectors are plotted within the region. The result is a convection map which only displays convection contours and convection vectors in a region adequately constrained by observations.

From equation (3.13), it becomes apparent that the region of constraint defined by $\Delta\theta$ is entirely dependent on a reasonable choice of both p and K_{max}. The SuperDARN statistical model has been calculated for K_{max}=6 (*Ruohoniemi and Baker*, 1998; *Ruohoniemi and Greenwald*, 2005). Values of K_{max}=4-8 will therefore be used. Narrowing down a value for p is more complicated, and not easily automated. For a purely theoretical distribution with measurement coordinates evenly distributed about the entire spherical cap, p=2 is sufficient provided the measurements are separated by a distance no greater than $\Delta\theta$. For a more realistic data set with irregularly spaced observations, a larger value of p is more appropriate to ensure an accurate fit. Choosing a low value of p will artificially inflate the value of $\Delta\theta$ so that the region of constraint contains convection having unphysical structures due to a lack of constraint from measured data, whereas choosing a large value of p will decrease the region of constraint so that convection features are not shown. *Bendat* (1958) suggests that for data with noise, a value of p=10-20 is appropriate. Unfortunately, the changing distribution of SuperDARN measurements makes it difficult to narrow down a choice of p. Based on a visual examination of numerous convection maps, it has been determined that the region of constraint is best-defined using p=6 for typical distributions of SuperDARN data.

To test the SCHA-1 and SCHA-2 procedures, a test convection pattern is adopted to represent a very basic two-celled pattern with and without flow across the boundary of the spherical cap.

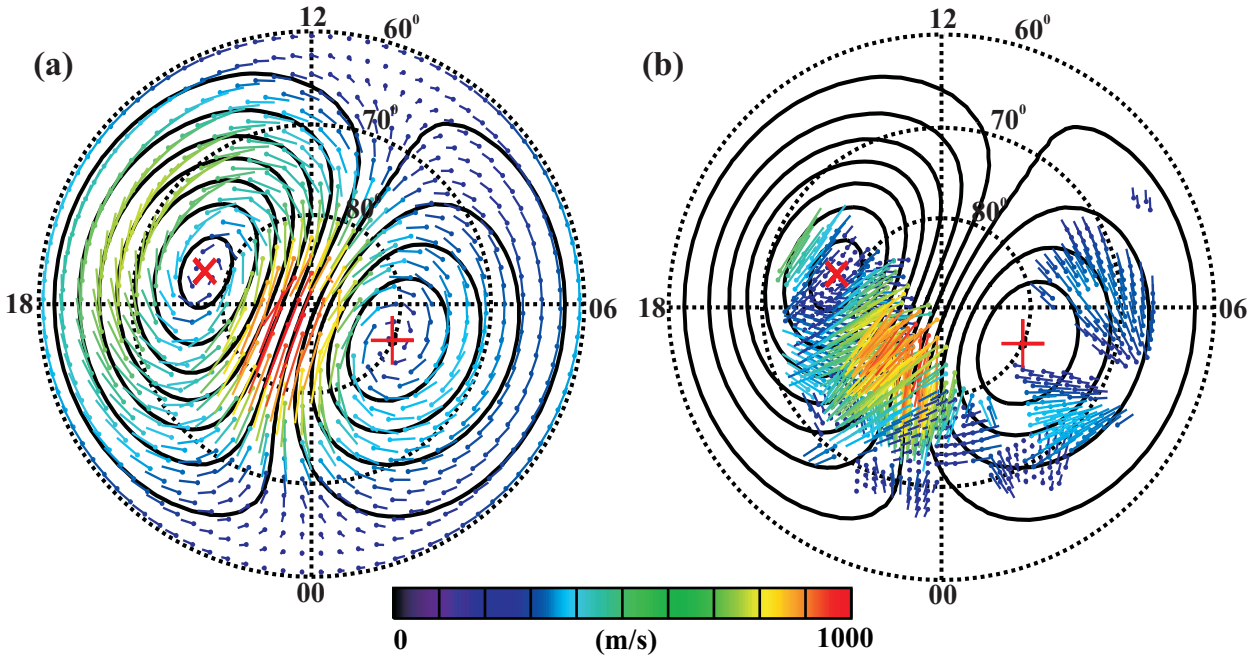

Figure 3.3: Arbitrarily generated convection patterns represented by contours of the electrostatic potential Φ_E with a spacing of 6 kV. The plus and cross signs indicate maxima and minima in Φ_E. In (a) the full convection vectors associated with the convection pattern are plotted on an evenly spaced grid with a separation of $\Delta\theta = 2°$. In (b) the l-o-s component of the full convection vectors associated with the convection pattern is plotted at the location of SuperDARN measurements on January 03, 2001 at 01:14-01:16 UT.

3.3 Mapping model convection patterns using SCHA-1

The contour lines in Figures 3.3 a and b show an arbitrarily generated convection pattern which fills the entire convection zone bounded by $\theta_{FIT} = 30°$ co-latitude and has closed contours at θ_{FIT}. In Figure 3.3a, the full convection vectors associated with this pattern are indicated over an evenly spaced grid with points separated by $\Delta\theta = 2°$. 'Observations' were simulated by adding noise to these vectors by adding a random term sampled from a normal distribution of $mean = 0$ m/s and standard deviation $\sigma = 50$ m/s for the velocity magnitude and $mean = 0°$ and $\sigma = 15°$ for the azimuth. The simulated observations were used as inputs to the SCHA-1 mapping technique for a spherical cap centered on the North Pole with $\theta_c = \theta_{FIT}$ to re-create a map of the ionospheric convection for all values of K_{max} between 2 and 10.

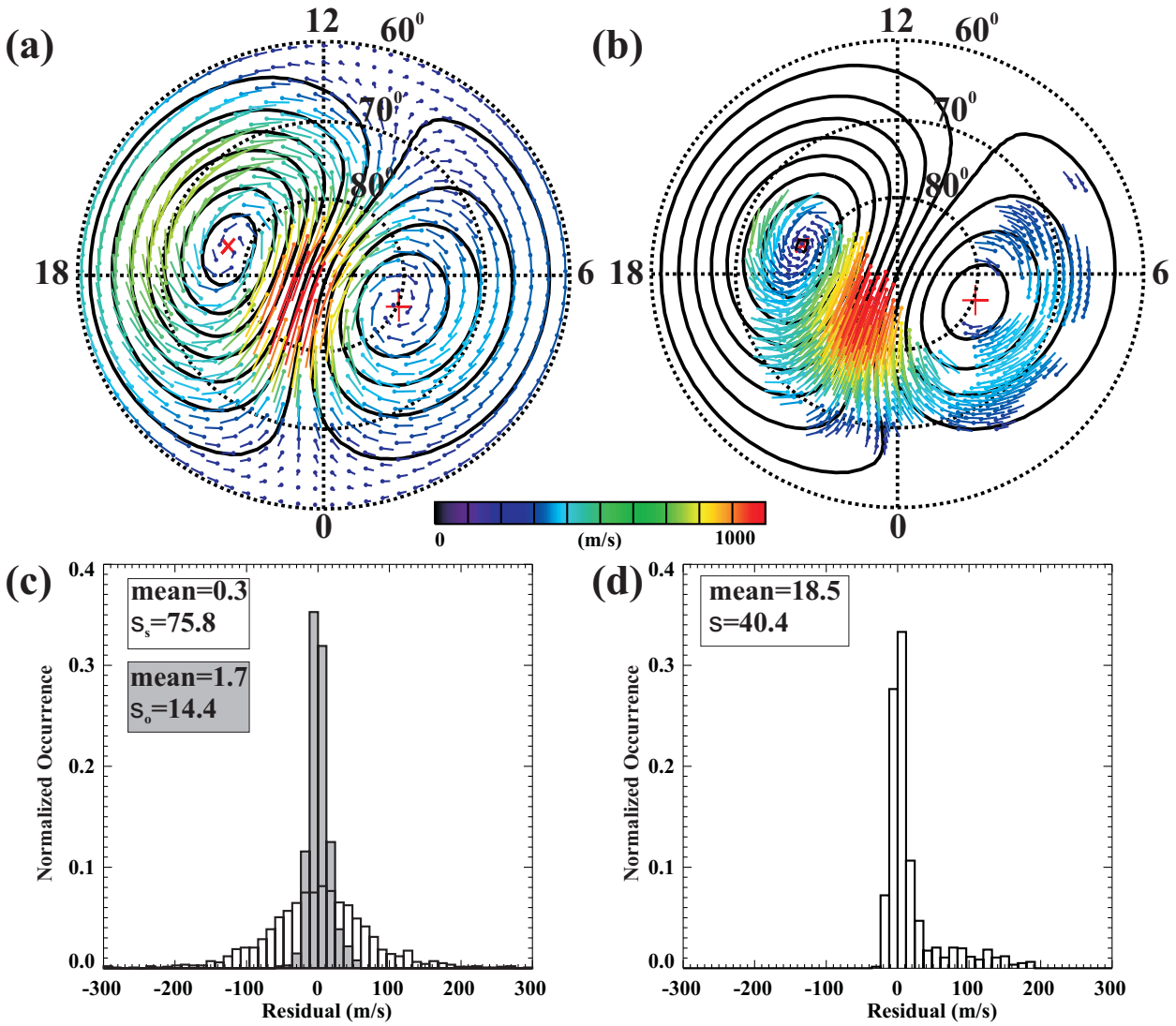

Figure 3.4: SCHA-1 mapping (for $\theta_c = 30°$) of the convection vectors shown in (a) Figure 3.3a for $K_{max} = 5$ and (b) Figure 3.3b for $K_{max} = 3$. Noise was added to the original convection vectors to create simulated vectors prior to using the SCHA-1 technique (see text). (c) Distribution of the difference or residual value between the original (grey) and simulated (white) convection and mapped convection shown in (a). (d) Distribution of the difference or residual value between the theoretical convection and mapped convection sampled in regularly spaced intervals across the entire map shown in (b).

Figure 3.4a shows the resultant convection pattern for $K_{max} = 5$, which appears to be almost identical to the pattern shown in Figure 3.3. The ability of the SCHA-1 technique to re-create the original convection pattern may be evaluated by comparing the output convection vectors to both the original (before noise) and simulated (after noise) vectors. Figure 3.4c shows a distribution of the residual (input-output) values, where the input values

are the north/south and east/west components of the original (grey) and simulated (white) vectors and the output values are the corresponding components of the output convection pattern shown in Figure 3.4a. The width of the distribution of the difference between original and output values is reduced compared to the distribution of the difference between simulated and output values ($\sigma_o = 14.4$ m/s versus $\sigma_s = 75.8$ m/s). This indicates that despite the noise added to generate the simulated observations, the SCHA-1 technique was able to reproduce the original convection pattern.

It should be noted that $K_{max} = 5$ produced the narrowest original and simulated distributions, suggesting it is the most appropriate choice to model the data set. Convection patterns for $K_{max} < 5$ were similar in appearance, but more smoothed, resulting in a wider distributions with slightly lower velocity values (for $K_{max} = 3$, $\sigma_o = 18.3$ m/s, $\sigma_s = 78.1$ m/s). For $K_{max} > 5$, the contours in Figure 3.4a become distorted as the procedure was more affected by the noise added to the distribution rather than the underlying convection pattern, again producing wider distributions (for $K_{max} = 8$, $\sigma_o = 24.2$ m/s, $\sigma_s = 76.1$ m/s). These results show that for an appropriate choice of K_{max}, the SCHA-1 technique can accurately map a known convection pattern based on a uniform distribution of simulated observations.

In reality, observations are not so evenly dispersed about the spherical cap and measured vectors are often only available for one component of the 2-dimensional horizontal convection vector. To represent a more likely distribution, observed convection vectors should be determined at the coordinates of possible observation locations. As an example, Figure 3.3b shows the l-o-s component of the full convection vector associated with the arbitrarily generated convection pattern shown in Figure 3.3 a. The velocities were calculated at the coordinates of 887 gridded l-o-s velocities observed on January 03, 2001 from 01:14-01:16 UT. Noise was added to the calculated l-o-s velocity magnitudes to create simulated inputs for the SCHA-1 mapping technique. The resultant convection map for $K_{max} = 3$ is shown in Figure 3.4b.

Determining the best value of K_{max} for mapping convection based on a non-uniform data set was more complicated as a comparison between input and output vectors could only be made at the data coordinates, completely disregarding the rest of the convection

pattern. As K_{max} increased, the difference between the simulated l-o-s velocities and the output convection projected in the l-o-s direction decreased, but the convection pattern took on an increasingly complicated pattern with multiple unphysical cells forming in the regions not populated by data. Such cells form when the $\Delta\theta$ characterizing a region of patchy observation is greater than the resolution implied by the fitting procedure. Instead, a comparison was made between the original convection pattern along an evenly spaced grid as shown in Figure 3.3a, and the convection pattern shown in Figure 3.4b calculated at the same coordinates using the SCHA-1 fitting coefficients. The width of this distribution was a minimum for $K_{max} = 3$ ($\sigma = 40.4$ m/s) and is shown in Figure 3.4d.

Results shown in Figure 3.4 indicate that the SCHA-1 technique can accurately map convection for a distribution that is closed at the boundary of the spherical cap when the input data are either uniformly distributed or confined to the coordinates of possible radar observations.

3.4 Mapping model convection patterns using SCHA-2

To determine the ability of the SCHA-2 technique to map convection when θ_c does not equal θ_{FIT} and the convection contours are not necessarily closed, simulated observations discussed in Section 3.3 at magnetic latitudes of $< 75°$ were discarded and convection re-calculated using the SCHA-2 approach for a spherical cap again centered over the pole. Figure 3.5 shows the results of using SCHA-2 with $\theta_c = 15°$.

In Figure 3.5a, convection is mapped based on 164 uniformly distributed input values. The best fit was found for $K_{max} = 3$. The resultant convection pattern is almost identical to the input pattern shown poleward of 75° in Figure 3.3a. The residual distributions shown in Figure 3.5c are centered at zero with $\sigma_o = 26.6$ m/s and $\sigma_s = 102.4$ m/s. For the pattern based on a non-uniform distribution of observations (538 points), $\sigma = 13.4$ m/s (Figure 3.5 b, d).

These results indicate the SCHA-2 technique accurately maps convection for a distribution that is open at the boundary of the spherical cap when the input data are either

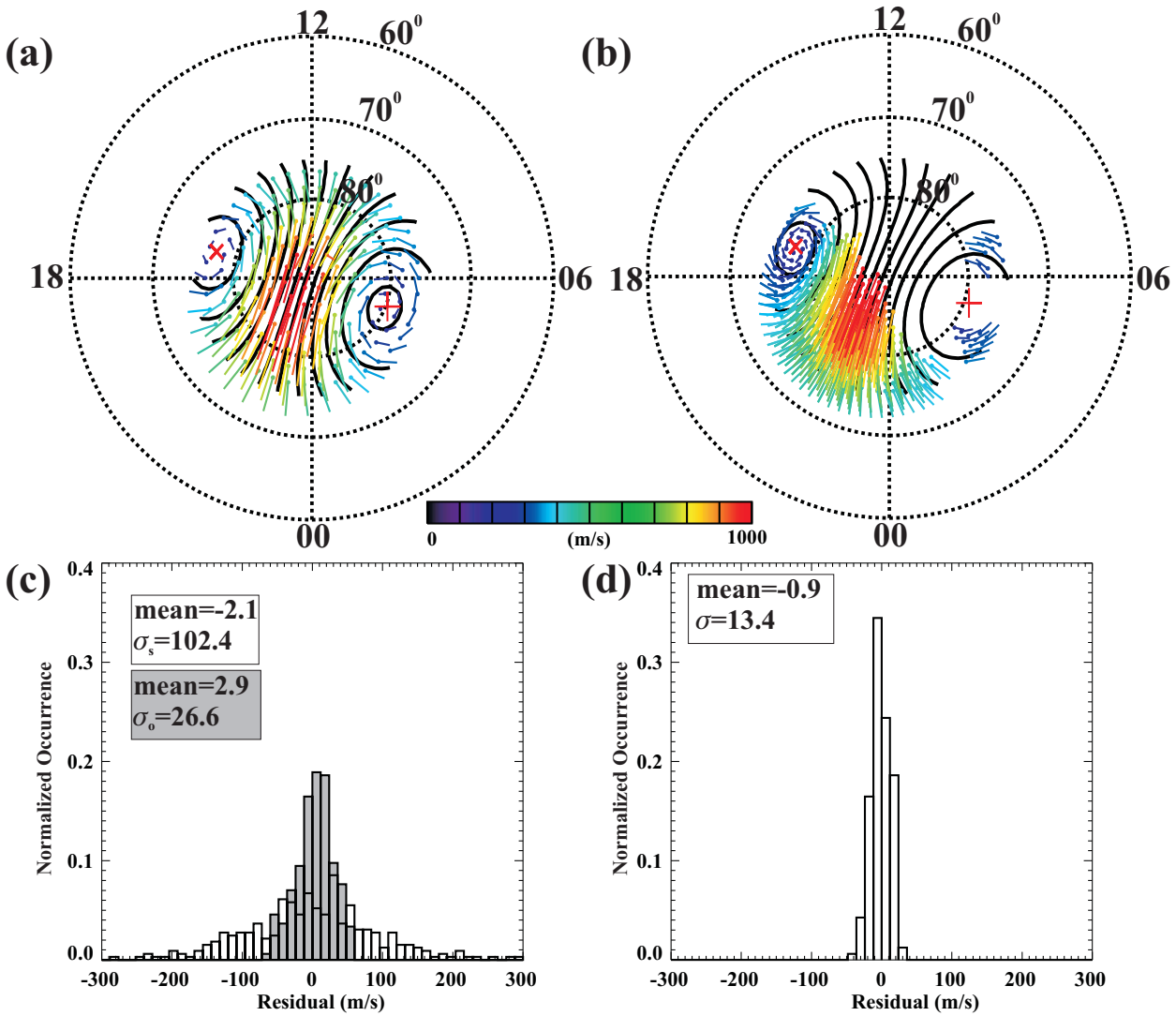

Figure 3.5: Contours of Φ_E with a 6 kV contour spacing determined using SCHA-2 mapping for $\theta_c = 15°$ based on convection vectors shown in (a) Figure 3.3a for K_{max}=3 and (b) Figure 3.3b for $K_{max} = 2$ at co-latitudes poleward of θ_c. Plus and cross signs indicate maxima and minima in Φ_E. Noise was added to the original vectors to create simulated vectors prior to using the SCHA-2 technique (see text). (c) Distribution of the difference or residual value between the original (grey) and simulated (white) convection and mapped convection shown in (a). (d) Distribution of the difference or residual value between the theoretical convection and mapped convection sampled in regularly spaced intervals across the entire map shown in (b).

uniformly distributed or confined to regions of reasonable radar coverage. Now the SCHA technique has been tested in theory, it must be examined for representing real convection patterns based on actual measurements, because in reality, convection patterns are much more complicated having multiple structures which range in size.

3.5 SCHA fitting of SuperDARN data

The goal of this section is to map convection based on SuperDARN observations for known orientations of the IMF. Choosing an appropriate value for K_{max} is difficult, as the true convection pattern is not known, and the number and distribution of data points varies widely. For all maps $K_{max} = 4$ will be used to map convection on a spherical cap centered over the geomagnetic pole in the northern hemisphere with $\theta_c = 30°$, and a masking algorithm will be used to define a region of constraint within which the electrostatic potential and velocity vectors will be plotted (see Section 3.2). Convection vectors are plotted at the location of input measurements to illustrate the spread of data. For the maps produced in this section, data coverage is extensive and the Nyquist wavelength ($p = 2$) was chosen to best represent the data. A higher value of K_{max} may be used to plot more detail in the convection pattern, but $K_{max} = 4$ is sufficient to map the general shape of the convection pattern.

To show how the SCHA-2 technique performs for typical IMF conditions, convection was mapped for 4 different orientations of the IMF B_y and B_z. Magnetic field traces, as observed by the Advanced Composition Explorer (ACE) satellite were examined for periods of steady IMF B_y and B_z conditions where the SuperDARN radars concurrently observed a high echo occurrence rate (> 500 gridded l-o-s velocities). The propagation delay between the satellite and magnetopause were calculated using the methods of *Weimer et al.* (2003) and *Weimer* (2004). Observations were considered for $B_z < 0$ and $B_y < 0$ on January 21, 2001 at 16:50-16:52 UT, for $B_z < 0$ and $B_y > 0$ on January 20, 2001 at 16:20-16:22 UT, for $B_z > 0$ and $B_y < 0$ on December 01, 2001 at 20:16-20:18 UT and for $B_z > 0$ and $B_y > 0$ on March 11, 2002 at 22:52-22:54 UT. Figure 3.6 shows the convection maps for these 4 combinations of the IMF B_y and B_z polarity. Convection vectors are plotted at observation coordinates to indicate the flow direction and data distribution.

In Figures 3.6 a and b, convection is plotted for periods of IMF $B_z < 0$ for $B_y < 0$ and $B_y > 0$, respectively. Both patterns are two-celled with strong sunward flow in the auroral regions of the plot closed by anti-sunward flow over the polar cap. When $B_y < 0$, the anti-sunward flow is directed from $\sim$ 13 MLT to $\sim$ 05 MLT indicating a dominance of the dawnside cell, whereas for $B_y > 0$, the convection flows from $\sim$ 09 MLT to $\sim$ 20 MLT,

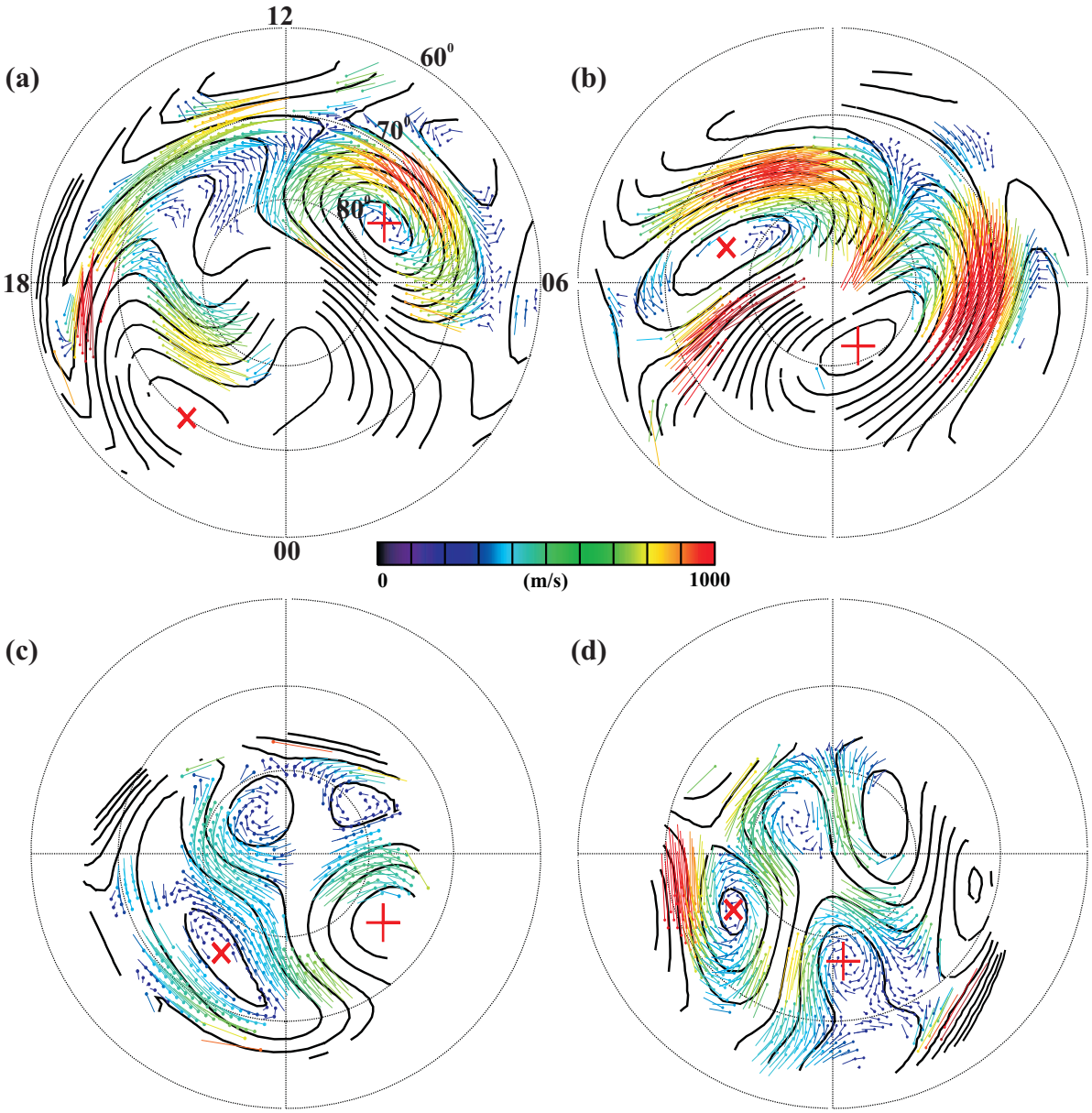

Figure 3.6: Contours of Φ_E with a 6 kV contour spacing determined using SCHA-2 for $K_{max} = 4$ for events and IMF conditions of (a) January 21, 2001 16:50-16:52 UT, $B_z < 0$, $B_y < 0$, (b) January 20, 2001 16:20-16:22 UT, $B_z < 0$, $B_y > 0$, (c) December 01, 2001 20:16-20:18 UT, $B_z > 0$, $B_y < 0$, and (d) March 11, 2002, 22:52-22:54 UT, $B_z > 0$, $B_y > 0$. MLT and MLAT labels in (a) apply to (b), (c), and (d). The plus and cross signs indicate the maxima and minima Φ_E associated with the normal convection pattern.

and the duskside cell dominates. In Figure 3.6c, $B_z > 0$ and $B_y < 0$. The convection pattern is four-celled. The outer dawn and dusk convection foci are centered at $\sim 75°$ MLAT and approximately 04 and 22 MLT, respectively. These cells indicate anti-sunward flow over the polar cap closed by sunward directed flow over the auroral regions. There are two inner

reverse convection cells with foci centered at $\sim 85^\circ$ MLAT and 13 MLT and at 80° MLAT and 08 MLT. The reverse convection cells indicate sunward directed flow along the ~ 10 MLT meridian and a dominance of the reverse dusk cell over the reverse dawn cell. In Figure 3.6d, $B_z > 0$ and $B_y > 0$. The convection pattern is similar to that shown in Figure 3.6c, except the sunward directed flow associated with the two reverse convection cells on the dayside is located just past 12 MLT, indicating a dominance of the reverse dawn cell over the reverse dusk cell.

The convection patterns generated using SCHA-2 illustrated in Figure 3.6 are consistent with known characteristics of plasma circulation for $B_z < 0$ (*Reiff and Burch*, 1985) (see Section 1.4.1) and $B_z > 0$ (*Reiff and Burch*, 1985; *Watanabe and Sofko*, 2009) (see Section 1.4.2), and with data-based models of ionospheric convection (*Heppner and Maynard*, 1987; *Foster et al.*, 1986; *Weimer*, 1995; *Ruohoniemi and Greenwald*, 1996; *Ruohoniemi and Greenwald*, 2005), suggesting the SCHA-2 technique performs well when the IMF is in a quasi-steady state and the SuperDARN coverage is good.

Periods of such good coverage are not typical, particularly at solar minimum. To see how the SCHA-2 technique performs for periods of limited data coverage, consider the event of September 28, 2005 where a stream of fast flow was observed by the Tiger/Unwin radar pair (*Makarevich et al.*, 2009). For the two-minute interval 09:28-09:30 UT, 137 observations are limited to a spherical cap of half-angle $\theta_c = 9^\circ$ centered at magnetic latitude and longitude of -66° and 236°, respectively. Figure 3.7a shows the SCHA-2 convection map generated for $K_{max} = 4$. The flow is primarily westward, with a meridional component near 60° MLAT. There are two peaks in the flow of ~ 1100 m/s and 700 m/s located at 70° and 63° MLAT. These flows are reasonably high, and the question of how accurate they are arises. To determine the ability of the SCHA-2 technique to represent the real convection pattern, a comparison with observations from another instrument should be considered.

In the following Sections, the ability of the SCHA-2 convection mapping technique to map ionospheric convection is examined. SCHA-2 convection maps are compared to the ion drifts concurrently measured by the DMSP satellites, and to convection maps derived using both the merge and FIT techniques.

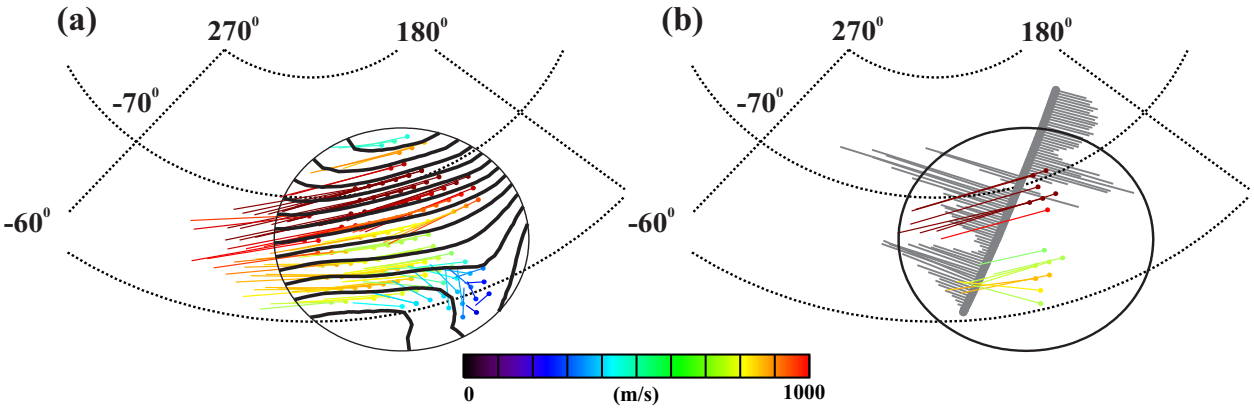

Figure 3.7: (a) SCHA-2 convection for $K_{max} = 4$, $\theta_c = 9°$ on September 28, 2005 for the interval 09:28-09:30 UT. Contours of Φ_E are spaced at 6 kV. (b) Corresponding merged SuperDARN velocities and the DMSP cross-track ion drifts observed at 09:24-09:30 UT (grey).

3.6 Validation by comparison with DMSP ion drifts

In Section 2.5, a comparison showing agreement between SuperDARN l-o-s velocities and the cross-track component of the ion drift observed by the DMSP satellites was discussed (see Figure 2.10). For a subset of those events for the northern hemisphere radars, the slope of the best-fit line to the data and correlation coefficient were $m = 0.74$ and $R = 0.88$, respectively. For this subset, maps of the SuperDARN-derived convection pattern were generated using the FIT technique with constraints from a statistical model and an HMB using $\theta_{FIT} = 30°$ and $K_{max} = 4$ and convection vectors were compared to the two-dimensional ion drift observed by the DMSP satellites during the corresponding interval (see Figure 2.19 and corresponding text). A similar comparison, which is discussed below, was performed based on SuperDARN-derived convection maps generated using the SCHA-2 technique with $\theta_c = 30°$ and K_{max}=6.

Figure 3.8 shows the results for a comparison of the magnitude and azimuth of the convection vectors. For convection azimuth, the points are clustered about the diagonal bisector and the slope of the best-fit line to the data set is $m = 0.78$. The correlation coefficient is somewhat low at $R = 0.55$ due to a number of points indicating opposite directions of the flow. If these points are removed, the slope and correlation coefficient

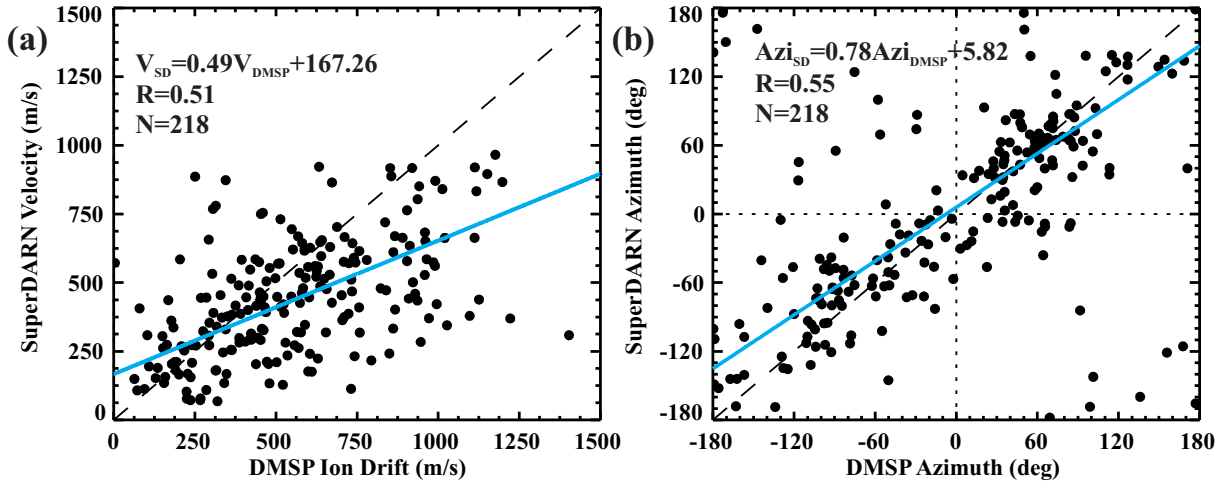

Figure 3.8: Scatter plots of the two-dimensional (a) velocity magnitude and (b) azimuth of the plasma flow calculated from SuperDARN l-o-s velocities using the SCHA-2 technique with K_{max}=6 and DMSP ion drifts. The equation of the best-fit line (blue line), correlation coefficient of the data set, and number of points of comparison are indicated.

increase to $m = 0.88$ and $R = 0.91$. The statistics for the scatter plot of the convection magnitudes are somewhat reduced compared to the plot for azimuth; $m = 0.49$ and $R = 0.51$.

The correlation between data sets in terms of azimuth is improved compared to the original subset of the l-o-s comparison ($m = 0.74$ and $R = 0.88$). However, the comparison in terms of magnitude indicates an overall reduction in the magnitude of the convection determined using the SCHA-2 technique. Similar results were found in the comparison between ion drift vectors observed by the DMSP satellites and the convection vectors determined using the FIT technique (see Section 2.5). It is likely that the reduction in the velocity magnitude is due to gridding of the raw l-o-s velocity and internal processes of the SCHA-2 technique, such as the smoothing introduced by limiting the fit to K_{max}=6.

As was discussed in Section 2.5, a comparison was not performed during intervals of high flow variability, as during such periods the differing spatial and temporal resolutions of the instruments would exaggerate the disagreement that would be observed between data sets. As an example, in Figure 3.7b the DMSP cross-track ion drifts (grey vectors) corresponding to the 2-min convection maps in Figure 3.7a are plotted. Although both instruments indicate a double peaked flow structure, the variability in the flow is more pronounced in the DMSP data. Evaluation of the SCHA-2 technique under periods of variable flow would be better accomplished through comparison between instruments measuring at the same res-

olution. For example, a comparison may be performed between convection calculated from SuperDARN l-o-s velocities using the SCHA-2 and merge techniques.

3.7 Validation by comparison with merged vectors

A comparison was performed over periods of large-scale data coverage and for periods of variable flow over a small spherical cap. For large-scale coverage, the merge technique was applied at two-minute intervals of observation for an event on January 3, 2001 from 01:04 to 01:24 UT, where the IMF was steady at $B_z \sim -7$ nT and $B_y \sim 0$ nT. For this period there are > 800 vectors constraining each map, and the SCHA-2 technique was applied on a spherical cap of $\theta_c = 25^\circ - 30^\circ$ and $K_{max} = 6$. Figure 3.9 shows a scatter plot of the (a) north/south and (b) east/west components of the SCHA-2 versus merged convection comparison. The agreement is excellent in the north/south direction ($R = 0.88$ and $m = 0.85$), and is somewhat reduced in the east/west component ($R = 0.82$ and $m = 0.61$). However, the results may be improved to $R = 0.83$ and $m = 0.68$ if the maps are re-processed with $K_{max} = 8$. Increased values of K_{max} may also be used, but for $K_{max} > 8$, the corresponding convection pattern becomes distorted due to an insufficient number of observations.

An identical comparison was performed for events having a high spatial variability over a localized region. Fast flow streams are frequently observed over the Tiger/Unwin SuperDARN radar pair in the southern hemisphere in the dusk sector. In 2004 and 2005, 18 events were identified during which fast flows were observed by the DMSP satellites and there were overlapping Tiger and Unwin radar observations. From these 18 events, 57 two-minute convection maps were generated using the SCHA-2 technique with $K_{max} = 4$ for a spherical cap size of roughly 10° centered over the region of data. Figure 3.7 shows an example of such an event. Sample merged vectors are indicated in Figure 3.7b by the colored vectors.

Figures 3.9 c and d show a comparison of the SCHA-2 convection versus the corresponding merged vectors. Despite the limited coverage, these events indicate good agreement in both components of the flow with R=0.81 and m=0.71 in the north/south direction and R=0.78 and m=0.69 in the east/west direction.

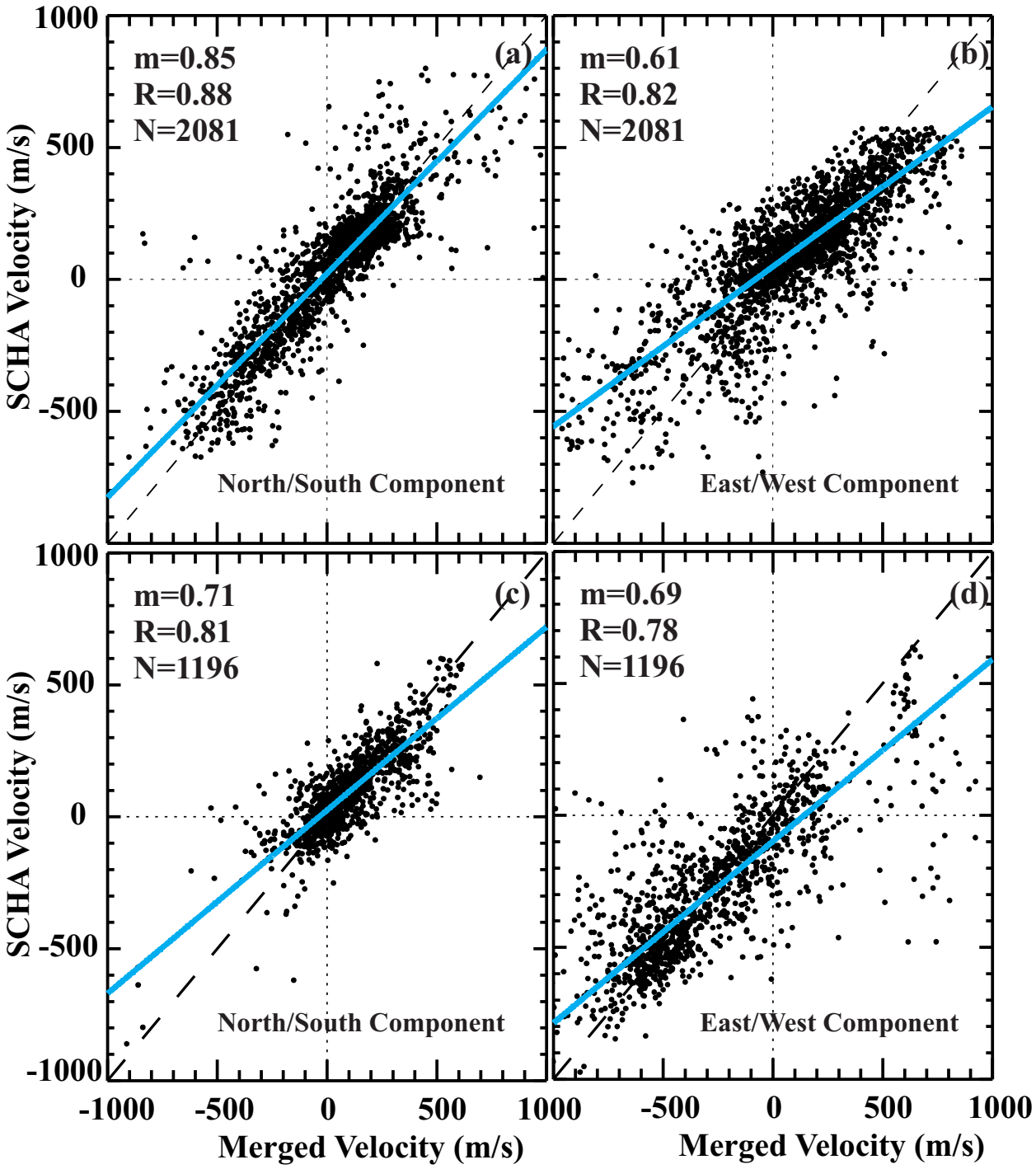

Figure 3.9: Comparison of the (a,c) north/south and (b,d) east/west components of SuperDARN-derived SCHA-2 convection vectors with merged convection vectors for (a,b) good data coverage for K_{max}=6 and (c,d) limited data coverage for K_{max}=4. The slope of the best-fit line (blue line), correlation coefficient, and number of points are indicated.

3.8 Discussion

Currently, the FIT-technique is generally used for generating SuperDARN-inferred convection maps. The fitting is done using a modified spherical harmonic analysis method as described in Section 2.3.3. The relative performance of the FIT and SCHA-2 techniques may be discussed by comparing maps of the convection determined using either technique. All FIT maps generated in this comparison are constrained using a statistical convection model according to the IMF conditions observed by the ACE satellite and using an HMB.

Figure 3.10a shows the observed l-o-s velocities for a 2-minute interval beginning at 22:52 UT on March 11, 2002. During this interval the IMF B_y and B_z were positive and $6 < B_t < 12$ nT. The overplotted potential pattern indicates the statistical model derived by *Ruohoniemi and Greenwald* (1996) for these IMF conditions. The model shows a three celled convection pattern with a reverse convection cell located on the dayside, poleward of 80° MLAT with sunward directed flow approximately aligned along the 14 MLT meridian. The distribution of l-o-s velocities in 3.10a indicate several regions of overlap. In Figure 3.10b, overlapping l-o-s velocities have been combined using the merge technique. Like the model pattern, the merged convection vectors indicate the presence of a reverse convection cell in the high-latitude dayside ionosphere with sunward directed flow approximately aligned along the 14 MLT meridian.

In Figure 3.10c, the FIT-technique was applied with $\theta_{FIT} = 27°$ and $K_{max} = 6$. In the FIT map, convection contours are smoothly closed near the equatorward boundary of the plot. The regular dawnside and duskside convection cells reach maximum and minimum values (red plus and cross) at coordinates of 80° MLAT and 0.2 MLT, and 75° MLAT and 20.2 MLT, respectively. Flow reaches a maximum value of $\sim$ 900 m/s around the equatorward portion of the duskside cell. There are two reverse convection cells centered over 12 MLT with sunward directed flow reaching $>$ 900 m/s approximately aligned along the 10 MLT meridian at $\sim$ 85° MLAT. The general shape of the corresponding SCHA-2 convection map shown in Figure 3.10d has similarly located convection cells, but there are noticeable differences between maps. For example, in the SCHA-2 map, the magnitude of the maximum velocity at the equatorward edge of the duskside convection cell reaches peak

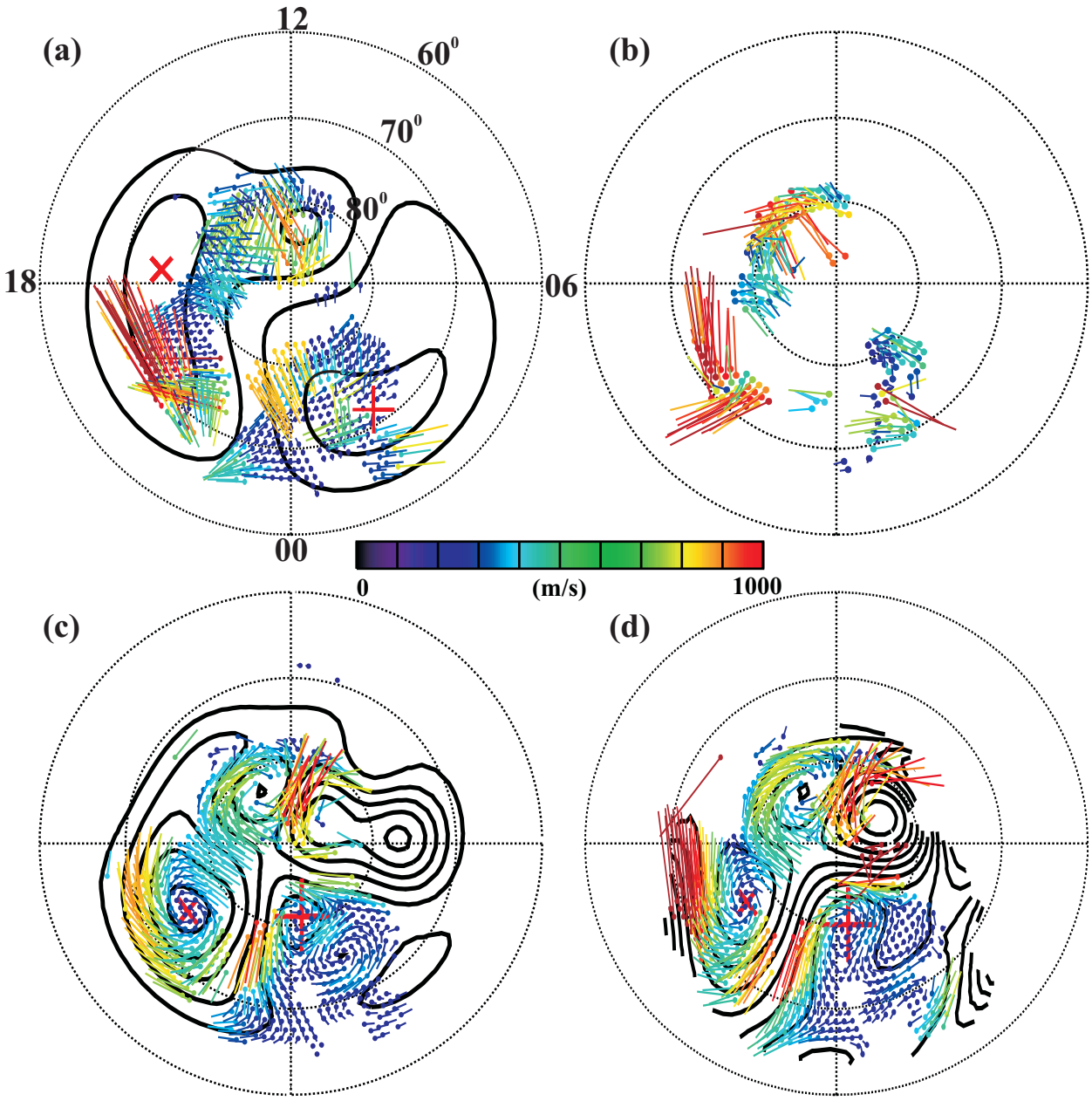

Figure 3.10: Convection maps based on SuperDARN observations (shown in (a)) for an event on March 11, 2002 at 22:52-22:54 UT. Convection was mapped using the (b) merged technique, (c) FIT-technique with $K_{max} = 6$ and $\theta_{FIT} = 27°$, and (d) the SCHA-2 technique with a spherical cap centered over the pole, $K_{max} = 6$, and $\theta_c = 27°$. Contour lines in (a) indicate the statistical model convection pattern (according to *Ruohoniemi and Greenwald* (1996) for IMF $B_y > 0$, $B_z > 0$, and $6 < B_t < 12$ nT) used to constrain the FIT convection map shown in (c). MLT and MLAT coordinate labels in (a) apply to (b), (c), and (d). In (a), (c), and (d), contours represent Φ_E with a 6 kV contour spacing and the plus and cross signs indicate maxima and minima in Φ_E.

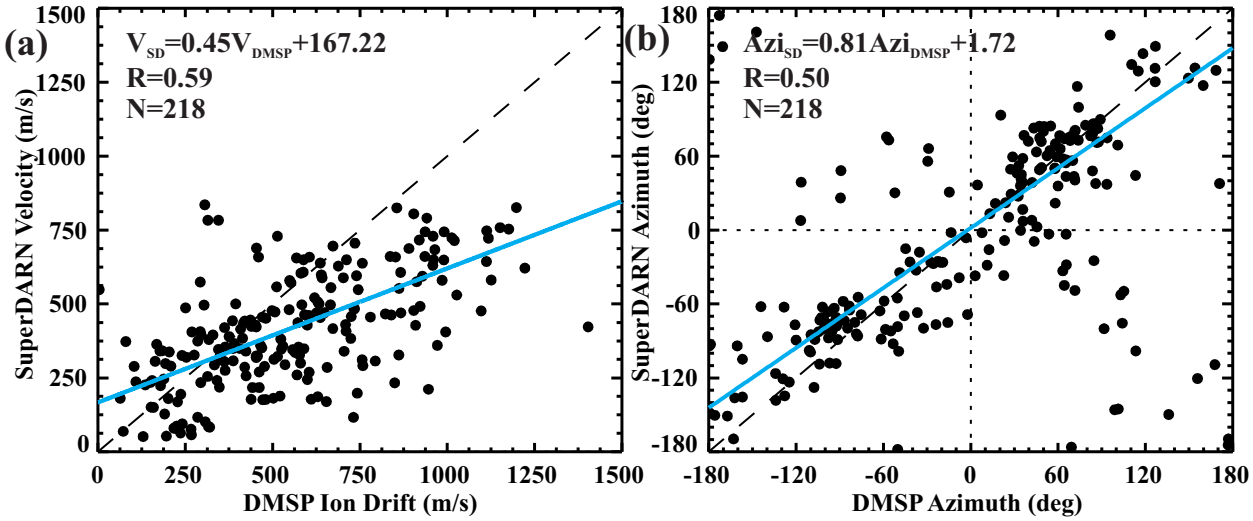

Figure 3.11: Scatter plots of the two-dimensional (a) velocity magnitude and (b) azimuth of the plasma flow calculated from SuperDARN l-o-s velocity vectors using the FIT technique for K_{max}=6 and DMSP ion drifts. The equation of the best-fit line (heavy solid line), correlation coefficient of the data set and number of points of comparison are indicated.

velocities of $>$ 1000 m/s, showing better agreement with the merged map shown in Figure 3.10b and the observed velocities shown in Figure 3.10a. The magnitude and orientation of the sunward directed flow associated with the reverse convection cells agrees with the FIT convection.

Large l-o-s velocities ($>$ 1000 m/s) are observed in the dusk sector in the $70° - 75°$ MLAT band, suggesting the high velocity flow mapped by the SCHA-2 technique better reflects the true flow. This high speed flow channel was likely suppressed by the global fitting of the FIT-technique due to the low-velocity ($<$ 400 m/s) flows observed at adjacent latitudes. These local flows cannot be accommodated into a global solution which satisfies the condition for a zero potential at the low-latitude boundary of the plot. This result remains the same if the convection zone adopted in the FIT approximation is expanded by setting $\theta_{FIT} = 35°$ (not shown).

The performance of the FIT and SCHA-2 technique may be further examined by repeating the comparisons presented in the previous section using the FIT technique and comparing the results. Consider the comparison performed between the convection calculated using the SCHA-2 technique versus the 2-dimensional DMSP ion drift shown in Figure 3.8. Figure 3.11 plots the magnitude and azimuth of the convection calculated using the

FIT technique for K_{max}=6 and the DMSP ion drift. The results of the comparison in terms of magnitude (m=0.45, R=0.59) and azimuth (m=0.81, R=0.50) are almost identical to the previous results where convection was determined using the SCHA-2 technique (m=0.49, R=0.51 for magnitude and m=0.78, R=0.55 for azimuth).

The comparison with merged velocities for periods of good data coverage shown in Figures 3.9 a and b may be repeated using FIT convection vectors, see Figures 3.12 a and b. The results of such work are slopes and correlation coefficients of m=0.76 and R=0.86 in the north/south direction and m=0.63 and R=0.79 in the east/west direction. As with the DMSP comparison, the results of the merged comparison are very similar to those determined using the SCHA-2 technique (m=0.85 and R=0.88 in the north/south direction and m=0.61 and R=0.82 in the east/west direction).

One might expect similarity between results of the DMSP and merged comparisons with convection calculated using both the SCHA-2 and FIT techniques due to the criteria used to select events. For the DMSP comparison, events were chosen where the satellite was roughly centered within a given radar field of view so there were multiple points to evaluate. In the merged comparison, events with overlapping observations were chosen so that merged vectors could be determined. To satisfy these criteria, events were chosen during periods of good data coverage when the sampling region was typically poleward of 70° MLAT. The convection vectors were therefore largely determined by the data, rather than the extra constraints applied in the FIT technique which might otherwise lead to discrepancies. For periods with poor data coverage, and at lower latitudes it is expected that the convection pattern will be different for the FIT and SCHA-2 convection mapping techniques.

In regions lacking sufficient data coverage, the shape of the FIT-determined convection pattern is constrained to follow a pre-determined statistical model (*Ruohoniemi and Greenwald*, 1996; *Ruohoniemi and Greenwald*, 2005; *Shepherd and Ruohoniemi*, 2000). The model is chosen based on the orientation and strength of the IMF B_y and B_z components. Proper choice of statistical model is only possible when the IMF is both stable and can be precisely determined. When the IMF is variable or undergoes rapid changes in polarity, the plasma flow is also in transition and is therefore not likely to match the statistical model convection pattern for particular IMF conditions. Although a statistical model may be used

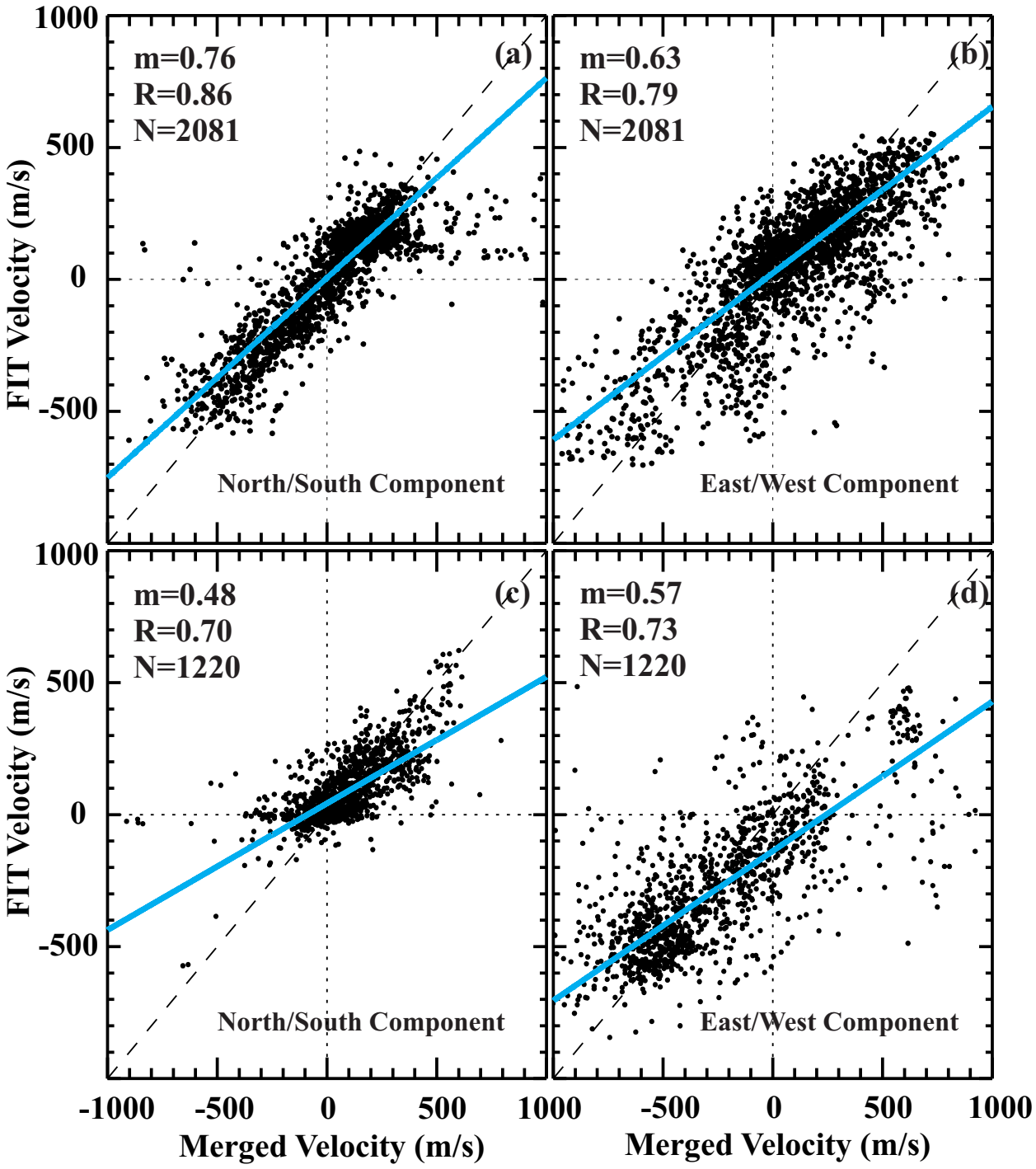

Figure 3.12: Comparison of the (a,c) north/south and (b,d) east/west components of the SuperDARN derived FIT and merged convection vectors for K_{max}=6 for periods of (a,b) good data coverage and (c,d) limited data coverage. The slope of the best-fit line (blue line), correlation coefficient, and number of points are indicated.

with the SCHA technique, it is not necessary, as a spherical cap may be placed directly over the observations without considering regions void of data. In this way, the FIT technique is beneficial in creating global maps of the convection, but is unable to resolve smaller-scale features without distorting the global map. The SCHA technique is better able to resolve structure over localized regions bounded by the extent of the data.

At low latitudes near θ_{FIT}, the stretching procedure employed by the FIT technique constrains the flow to be azimuthal. Therefore θ_{FIT} must be carefully chosen to accurately reflect the low-latitude boundary of the convection pattern. If, for example, the boundary is placed at too high a latitude, then flow that is supposed to cross the boundary of the plot will be rotated by up to $\sim 90^\circ$ in the FIT-mapped convection pattern. For example, the merged convection vectors in Figure 3.10b indicate high velocity flow crossing 70° MLAT nearly perpendicularly in the dusk sector. In the FIT convection map (Figure 3.10c), the corresponding convection vectors are rotated so the flow is nearly parallel to 70° MLAT. Fortunately, such constraints only dominate at the low-latitude boundary of the plot, and may be avoided by the accurate selection of θ_{FIT}. In contrast, the SCHA-2 technique allows flow to cross the boundary of the spherical cap allowing for a more rigorous solution.

For events with poor data coverage, untypical flow, or points close to the low-latitude boundary of the flow, it is likely that discrepancies will develop between the FIT and SCHA-2 convection patterns. Reconsider the event of September 28, 2005 where a stream of fast flows were observed by the Tiger/Unwin SuperDARN radar pair (see Section 3.5) located between 60° and 70° MLAT in the southern hemisphere. Observations were available in a localized region spanning an angular radius of $\sim 10^\circ$. For such events, it is no longer expected that the SCHA-2 and FIT vectors will yield similar results. To demonstrate, consider an example taken at 09:52-09:54 UT. Figure 3.13 shows the input gridded l-o-s velocities and a spherical cap of angular radius $\theta_c = 9^\circ$, which will be used for analysis.

Figure 3.14 a and c show the convection calculated using the FIT and SCHA-2 techniques, respectively. For the FIT comparison, $\theta_{FIT} = 29^\circ$ is chosen to encompass the region of interest, and $K_{max} = 6$. In the SCHA-2 comparison, a spherical cap of $\theta_c = 9^\circ$ is used for a maximum degree-index of $K_{max} = 4$. Note that different values of K_{max} are used for the FIT and SCHA-2 techniques to ensure similar wavelengths are mapped. The flow

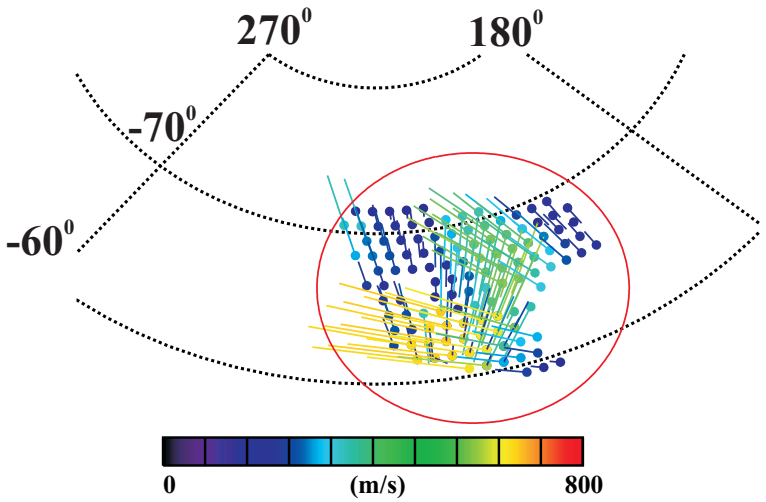

Figure 3.13: Gridded l-o-s velocity from the Tiger/Unwin SuperDARN radar pair on September 28, 2005 for the interval 09:52-09:54 UT. The red circle indicates a spherical cap of angular radius $\theta_c = 9°$ centered over the grid cells.

contours for the FIT map are smoothed in comparison to the corresponding SCHA-2 map. Both techniques indicate flow that is largely azimuthal, but in the SCHA-2 map, there is a north/south component in the flow at the most equatorward portion of the map. To determine how the convection represents the original gridded l-o-s velocities input to the convection mapping algorithm, scatter plots were generated to compare the projection of the convection vector in the l-o-s direction to the gridded l-o-s velocity. Figures 3.14 b and d show the results for the FIT and SCHA-2 convection vectors, respectively. For the SCHA-2 map, there is near-perfect agreement between input and convection velocity. The correlation coefficient is R=0.95, and the slope of the best fit line to the data set is m=0.95. Agreement is also good for the FIT convection map (R=0.91, m=0.86), but there is a cluster of low velocity (<400 m/s) points (shown in red) indicating flow in the opposite direction. Such a cluster of points is not present in the SCHA-2 convection comparison. Conflicting points are located in the most equatorward portion of the map (see Figure 3.15a) where the SCHA-2 convection map indicates flow across the low-latitude boundary and the FIT convection map shows azimuthally aligned flow. Figure 3.15b shows the merged vectors calculated for this event. In the region of disagreement, merged vectors also indicate flow having a north/south component. Given the magnitude of the l-o-s and merged vectors for this event, it is unlikely that the velocity represents E-region scatter, but further investigation is recommended.

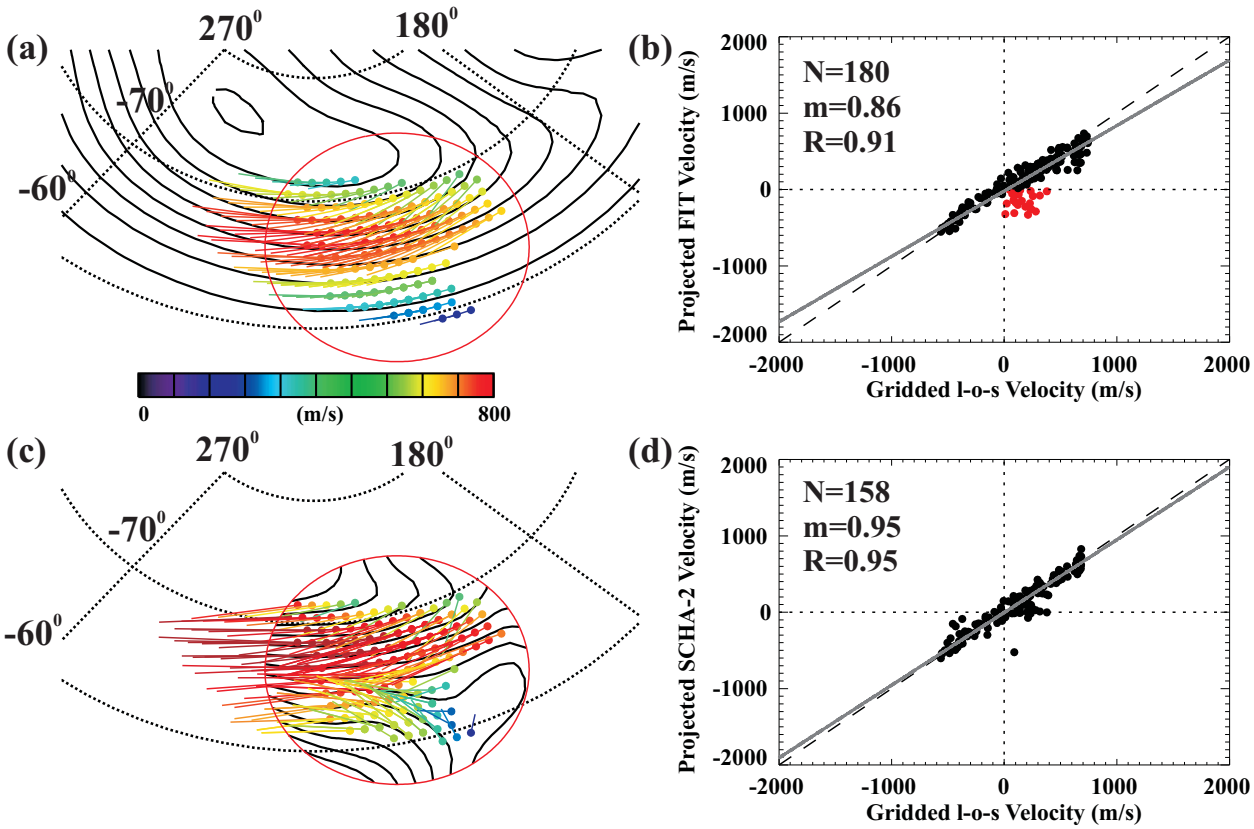

Figure 3.14: (a) FIT convection for $K_{max} = 6$, $\theta_{FIT} = 29°$, and (c) SCHA-2 convection for $K_{max} = 4$, $\theta_c = 9°$ for the event considered in Figure 3.13. Contours in (a) and (c) represent Φ_E with a 6 kV contour spacing. Scatter plot of the (b) FIT and (d) SCHA-2 convection projected in the l-o-s direction versus the input gridded l-o-s velocity for the convection diagrams shown in (a) and (c), respectively. Red dots in (b) indicate a population of results having opposite polarity.

Figures 3.12 c and d show a comparison of the FIT and merged velocities for the 18 events previously considered in Section 3.7 where highly varying flow was observed by a localized cluster of observations. The scatter plots show a slope and correlation coefficient of $m = 0.48$ and $R = 0.70$ and $m = 0.57$ and $R = 0.73$ for the north/south and east/west components of the convection. Results for the east/west component of the flow show reasonable agreement with the results of the SCHA-2 comparison shown in Figure 3.9d in terms of the correlation coefficient (R=0.78 for SCHA-2 convection), but the slope is reduced (from m=0.69 for SCHA-2 convection). This indicates a tendency for the FIT convection to be smoothed compared to the SCHA-2 convection. Results for the north/south component of the flow show poor agreement with the results of the SCHA-2 comparison shown in Figure

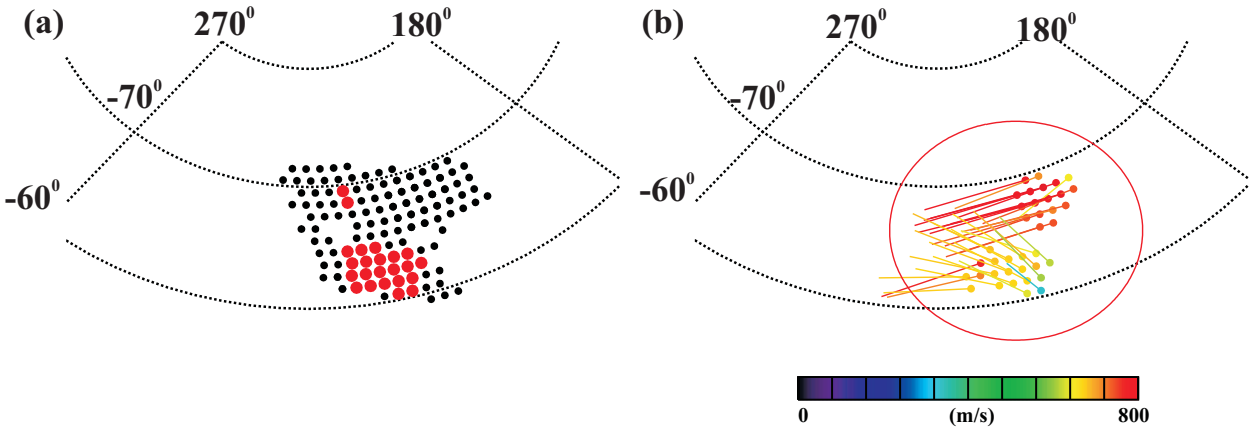

Figure 3.15: (a) Location of grid points for the comparison shown in Figure 3.14. (b) Convection vectors calculated using the merge technique for the event considered in Figure 3.13.

3.9c (m=0.71, R=0.81). The slope of the best-fit line for the FIT comparison indicates that the FIT convection is $\sim \frac{1}{2}$ of the merged convection in the north/south direction due to a large clustering of points near 0 m/s.

Events for this comparison all demonstrate fast plasma flows that are azimuthally aligned according to the DMSP satellite observations of the cross-track ion drift, and the azimuthal alignment imposed through stretching by the FIT-technique is therefore not a large factor in explaining the disagreement between the FIT and SCHA techniques. For these cases, inconsistencies can be explained by the relative difference between the maximum flow speed ($>$ 1000 m/s) and the background flow ($\sim$ 300 m/s). The fast flows are located within only a few degrees of θ_{FIT}, and there must therefore be a large gradient between the zero velocity flow at θ_{FIT} and the maximum flow speed of $>$ 1000 m/s. A high value of K_{max} is necessary to properly map such data. For example, if the comparison is re-done with $K_{max} = 8$ the results improve slightly to $m = 0.54$ and $R = 0.72$ and $m = 0.66$ and $R = 0.74$ for the north/south and east/west components. This example shows that the SCHA-2 technique is better able to resolve flow that is both localized and highly variable as the accuracy of the mapped convection is less dependent on the choice of processing parameters.

The importance of choosing a reasonable low-latitude flow boundary may be illustrated by re-examining the differences between the FIT and SCHA-2 convection. Figure 3.16 shows

a scatter plot of the (a) north/south and (b) east/west components of the FIT and SCHA-2 convection vectors previously compared to the merged vectors in Figures 3.9 a and b and Figures 3.12 a and b.

In the east/west component of the flow, there is good agreement between convection calculated using either technique (m=0.94 and R=0.79). Agreement is worse in the north/south component (R=0.53) as there is a significant portion of points where the FIT-technique had near zero values and the SCHA-2 technique indicated a wide range of values. Such flows correspond to points in the low-latitude region of the plot where the SCHA-2 technique allowed the flow contours to cross the boundaries, whereas the FIT-technique constrained the potential to be zero at the boundary of the plot, thereby forcing the flow to be azimuthally aligned at latitudes near θ_{FIT}.

To test the above hypothesis, the convection was re-calculated using $\theta_{FIT} = \theta_c = 40^\circ$ to prevent the forced azimuthal alignment. Figures 3.16 c and d show the resultant comparison. Agreement is improved in the north/south component of the plot with $R = 0.74$. The grouping of points previously clustered along the y-axis shifts closer to the dashed bisecting line, indicating that the shift in θ_{FIT} has allowed the flow to rotate away from the east/west direction and cross the $\theta = 30^\circ$ circle of co-latitude. Agreement in the east/west direction of the plot has shifted slightly so that $m = 1.10$ and R=0.87, indicating a tendency for the SCHA-2 velocity to be larger than the corresponding FIT velocity. These results suggest there is a strong dependence of the FIT technique on the proper choice of θ_{FIT}, particularly for vectors at low latitudes. The SCHA-2 technique is free of this dependency and therefore provides more consistent convection results.

3.9 Summary and conclusions

In this Chapter, spherical cap harmonic analysis was introduced for mapping ionospheric convection using SuperDARN radar observations. It was shown that

1. The SCHA technique with (SCHA-1) or without (SCHA-2) a zero-potential boundary condition at the border of the convection zone reproduced the expected convection pattern for an arbitrarily generated test pattern that was characterized at a number

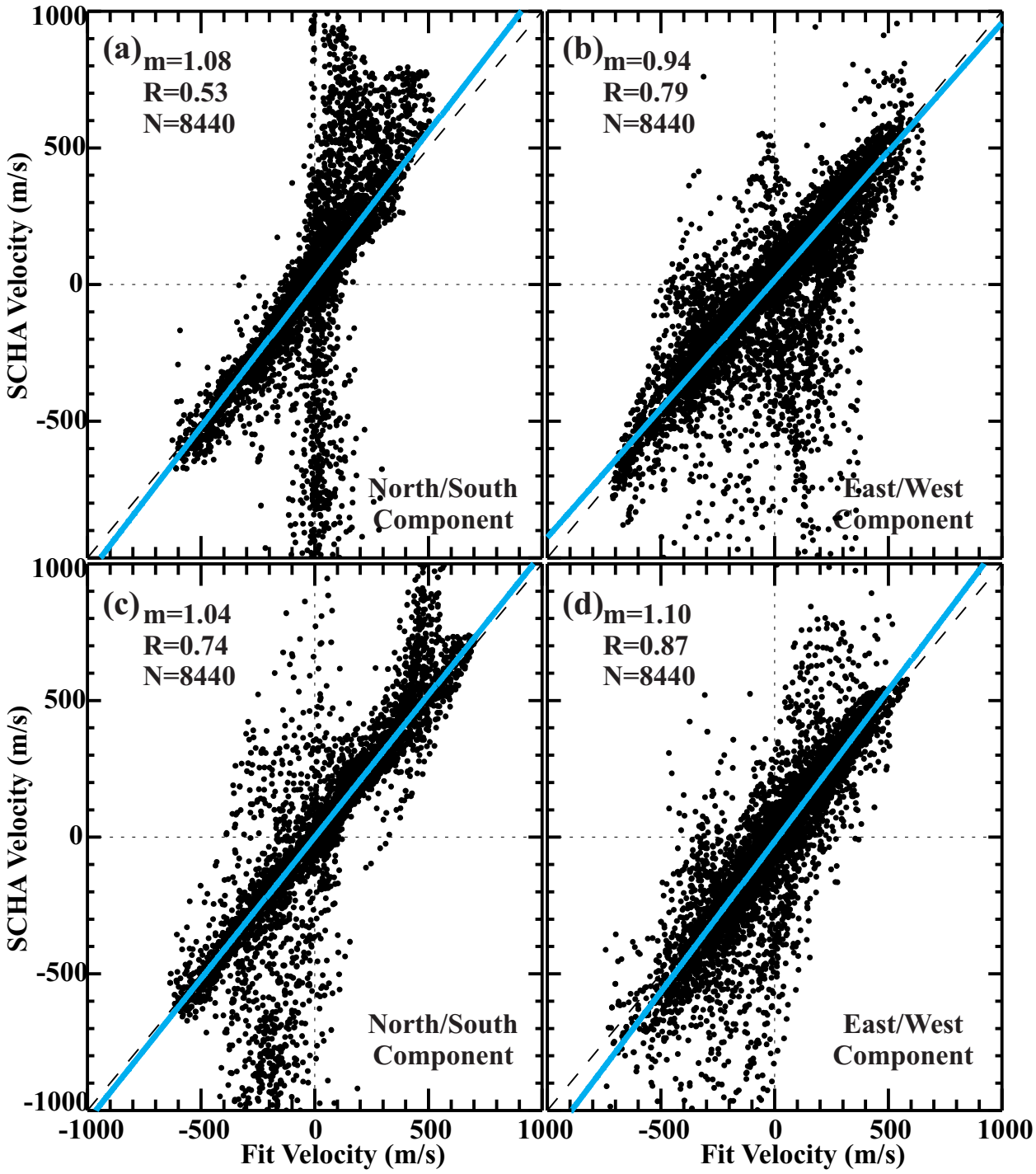

Figure 3.16: (a,c) North/south and (b,d) east/west components of the SCHA-2 versus FIT-based convection. In all plots, $K_{max} = 6$, and $\theta_{FIT} = \theta_c =$ (a,b) 30° and (c,d) 40°.

of pre-selected points distributed either uniformly or at possible locations of radar observations. A more realistic situation was simulated through the addition of noise to both the magnitude and direction of the pre-selected vectors.

2. For periods of good coverage of SuperDARN measurements, the SCHA-2 technique produces convection patterns consistent with expectations for various combinations of IMF B_y and B_z.

3. Convection vectors calculated using SuperDARN measurements and the SCHA-2 convection mapping technique agreed with the DMSP ion drifts for events selected during periods of smooth temporal and spatial variations of the flow. The correlation coefficient and the slope of the best-fit line for a scatter plot of the SCHA-2 convection versus DMSP ion drift were $R = 0.51$ and $m = 0.49$ in terms of convection magnitude and $R = 0.91$ and $m = 0.88$ in terms of convection azimuth.

4. For periods of both good and limited data coverage of SuperDARN measurements, convection vectors inferred by the SCHA-2 technique agreed with the velocity vectors determined using the merge technique. For events with good data coverage the correlation coefficient and the slope of the best-fit line were $R = 0.88$ and $m = 0.85$ for the north/south component and $R = 0.82$ and $m = 0.61$ for the east/west component of the convection vectors. For events with fast plasma flows in localized regions the correlation coefficient and the slope of the best-fit line were $R = 0.81$ and $m = 0.71$ for the north/south component and $R = 0.78$ and $m = 0.69$ for the east/west component of the convection vectors.

5. As a consequence of forcing the potential of the low-latitude boundary of the convection zone to zero, the FIT technique requires flow near the boundary of the plot to be azimuthally directed. Such an assumption requires that the shape and size of the convection zone be known. The SCHA-2 technique is not limited by this constraint, and it is possible to plot convection based solely on measured inputs.

6. The SCHA-2 technique performed comparably to the FIT technique for convection maps over regions of good data coverage during periods of smooth spatial and temporal

variations of the flow. However, for periods of spatially confined and variable flow, the SCHA-2 technique provided a better representation of the convection pattern.

These results indicate that SCHA can be used as a fitting technique for SuperDARN data to produce maps of the ionospheric convection. The SCHA technique may be applied to additional data sets to map convection. In the following Chapter, techniques for applying SCHA for mapping the ionospheric plasma flow based on magnetometer data will be discussed.

Chapter 4

Convection derivation from magnetometer and SuperDARN data

In the previous Chapter a method was developed and reviewed for mapping ionospheric convection using SCHA and SuperDARN measurements. Based on the results of Chapter 3, it was concluded that the SCHA technique is appropriate for convection mapping when measurements are either scattered about the entire high latitude region, or confined to a localized region in space. However, regardless of the fitting technique, as the density of measurements within the mapping region decreases, the reliability of the resulting convection map is reduced. It is therefore worthwhile to consider improving a problematic data set by introducing data from alternate sources, such as magnetometers.

Magnetometer sites span a larger region than the SuperDARN radars, and offer a continuous time series of observations. Magnetometery may therefore be relied on to provide a general overview of the convection pattern. This will be of particular importance where there are gaps in the SuperDARN field of view, or during events where there are drops in the echo occurrence rate. In this Chapter, techniques for mapping the ionospheric convection pattern based on magnetometer measurements or on joint magnetic and radar data sets will be discussed.

4.1 Magnetometers

Originally created in the 1940s by Victor Vacquier, the fluxgate magnetometer has become a popular instrument for observing variations in the intensity of the Earth's magnetic field from ground-based stations and on satellites such as Magsat and Ørsted (*Good*, 2007). One of the earliest fluxgate magnetometers was developed by Paul Serson of the Dominion Observatory

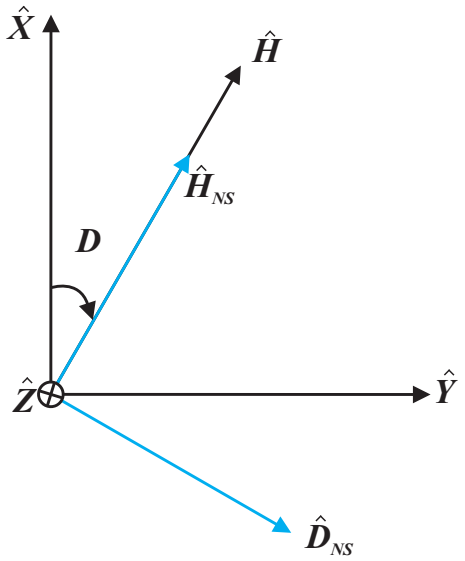

Figure 4.1: Illustration of the XYZ and HDZ coordinate systems viewed from above in a plane tangent to the Earth's surface. $\hat{\boldsymbol{X}}$, $\hat{\boldsymbol{Y}}$, and $\hat{\boldsymbol{Z}}$ point in the geodetic north, east, and vertically downward directions, respectively. $\hat{\boldsymbol{H}}$ points toward magnetic north during magnetically quiet times and deviates during more active periods. The non-standard HDZ coordinate system (blue) has a vector component $\hat{\boldsymbol{H}}_{NS}$ pointing in the magnetic north direction and a component $\hat{\boldsymbol{E}}_{NS}$ pointing in the magnetic east direction.

(*Serson*, 1957). Descriptions of the basic fluxgate magnetometer are available, for example, in *Serson* (1957), *Hargreaves* (1992), *Kivelson and Russell* (1995), *Campbell* (2003), and *Good* (2007).

Magnetometer observations are typically reported in either the XYZ or HDZ coordinate system, see Figure 4.1. Both systems are defined in terms of the geodetic coordinate system (see Appendix A.1). In the XYZ coordinate system, the X-axis is located in a plane tangent to the surface of the Earth pointing toward the pierce-point of the Earth's spin axis in the northern hemisphere. The Z-axis points vertically inward, perpendicular to the plane holding the X-axis, and the Y-axis completes the right handed coordinate system.

In the HDZ coordinate system, H describes the horizontal component of the magnetic field in the XY plane. The angle between the X and H directions is called the declination angle, D. The pointing direction of the H vector depends on the relative strengths of the X and Y contributions to the measured field. During periods of low magnetic activity, H points toward magnetic north. The Z direction is identical to that of the XYZ coordinate systems. In some cases, a non-standard (NS) orthogonal HDZ coordinate system is defined

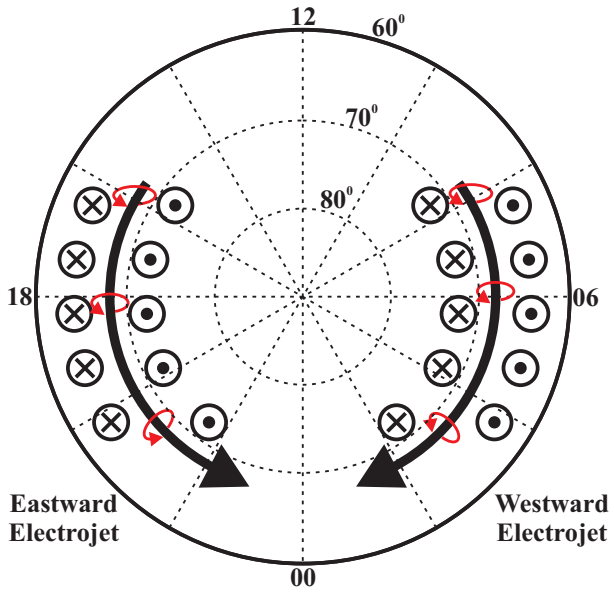

Figure 4.2: A cartoon illustration of the eastward and westward auroral electrojets (black arrows) in the high-latitude ionosphere. Circles with crosses and dots indicate the direction of field-aligned currents flowing into and out of the ionosphere, respectively. Red arrows indicate the direction of the magnetic field associated with the electrojets.

with H_{NS} describing the component of the horizontal field in the direction of the magnetic pole in the northern hemisphere, and D_{NS} describing the component of the horizontal field in the direction perpendicular to H_{NS} toward the east. In the following, magnetic observations have been converted to either the XYZ or standard HDZ coordinate system.

4.1.1 Observing magnetic activity

Variation in the magnetic field observed by a ground-based magnetometer may be indicative of the location of the magnetometer with respect to the ionospheric current system. In Figure 4.2, the black arrows on the duskside and dawnside indicate the directions of the eastward and westward auroral electrojets, respectively. Circles show the direction of FACs flowing into (crosses) and out of (dots) the ionosphere, and the red curved arrows indicate the direction of the magnetic field produced by the electrojet current. Ground-based magnetometers observe positive enhancements in the H-component of the magnetic field when they are located under the eastward electrojet, and reductions when they are located under the westward electrojet. The z-component of the magnetic field can be used to determine if the station is located poleward or equatorward of the electrojet. Under the eastward electrojet, positive variations

in the z-component of the magnetic field indicate the station is located in the R2 FAC region equatorward of the electrojet, and negative variations indicate the station is located in the R1 FAC region poleward of the electrojet. Under the westward electrojet, positive variations indicate the station is located under the R1 FAC region poleward of the electrojet, and negative variation indicates the station is located in the R2 FAC region equatorward of the electrojet.

In addition to observing the variation of the magnetic field, it is desirable to know the magnitude and direction of the perturbation in the magnetic field. The magnetic field perturbation is determined by removing the variation for a quiet period from the measured magnetic field. The quiet level field is determined by first identifying the five quietest days, according to the AE index, in each of the two months most closely surrounding the day of interest. Each component of the magnetometer data for those days are averaged to determine an average magnetic field value Q_i at each time step, δt. For magnetic data used in this study $\delta t = 1$ minute. The average curves are fit with the following Fourier expansion to obtain a function Q describing the quiet level curve

$$Q = \sum_{k=0}^{\infty} \left[a_k \cos(kx) + b_k \sin(kx) \right], \tag{4.1}$$

where a_k and b_k are fitting coefficients to be determined, and x represents the minute of the day, in radians. In practice, the Fourier expansion will be truncated at 4 terms.

Once the quiet level magnetic field is known, the magnetic field perturbation is determined by subtracting the quiet level magnetic field from the observed magnetic field for the day of interest. The quiet level curve is characteristic for a given station, and quiet levels from one station cannot be used for another.

4.1.2 Magnetometer networks and data availability

Magnetometer stations are distributed worldwide in networks operated by various organizations and Universities. Measurements from these and many other stations are available from the SuperMAG data repository operated by the John Hopkins University Applied Physics Laboratory (JHU APL) (*Gjerloev*, 2009). Magnetometer networks located in Canada include

the Canadian Magnetic Observatory System (CANMOS), the Canadian Array for Real-time Investigations of Magnetic Activity (CARISMA), and the Magnetometer Array for Cusp and Cleft Studies (MACCS). Magnetic observatory data from around the world is also available from the International Real-time Magnetic Observatory Network (INTERMAGNET), also available through SuperMAG. Data are collected for all available stations and represented in a single coordinate system with unit vectors pointing in the direction of local magnetic north, local magnetic east, and in the vertical. For analysis purposes, these coordinates were rotated by the local declination angle D, determined from the IGRF magnetic field model, to a geocentric coordinate system. Data are available in 1-minute increments for measurements made in 1997-2008. Figure 4.3 shows the geographic coordinates of the magnetometer stations included in the SuperMAG data repository.

4.2 Review of mapping electrodynamic parameters from magnetometer data

The magnetic field variations observed by ground-based magnetometers may be attributed to sources internal and external to the Earth. The external source of magnetic perturbations is normally modeled on a surface in the ionosphere where a current flows in the form of the eastward and westward electrojet. When the current varies (e.g., due to particle precipitation) the associated magnetic field fluctuates, inducing an electromotive force in the ground which drives an internal current creating an internal source of magnetic field perturbations.

Techniques have been developed to use observations of the perturbation magnetic field from ground-based magnetometers to globally map electric fields, plasma velocity, and current systems in the ionosphere. These techniques range in complexity, with the simplest representation involving a rotation of the measured perturbation magnetic field vector by 90° counter clockwise to determine the convection direction (*Friis-Christensen and Wilhjelm*, 1975; *Friis-Christensen et al.*, 1975; *Clauer and Friis-Christensen*, 1988; *Benkevitch*, 2006). Using this technique, the direction of the convection is known, but the convection magnitude may only be represented in nT, instead of the desired units of m/s. In *Benkevitch* (2006), agreement between the convection direction determined through such a rotation and

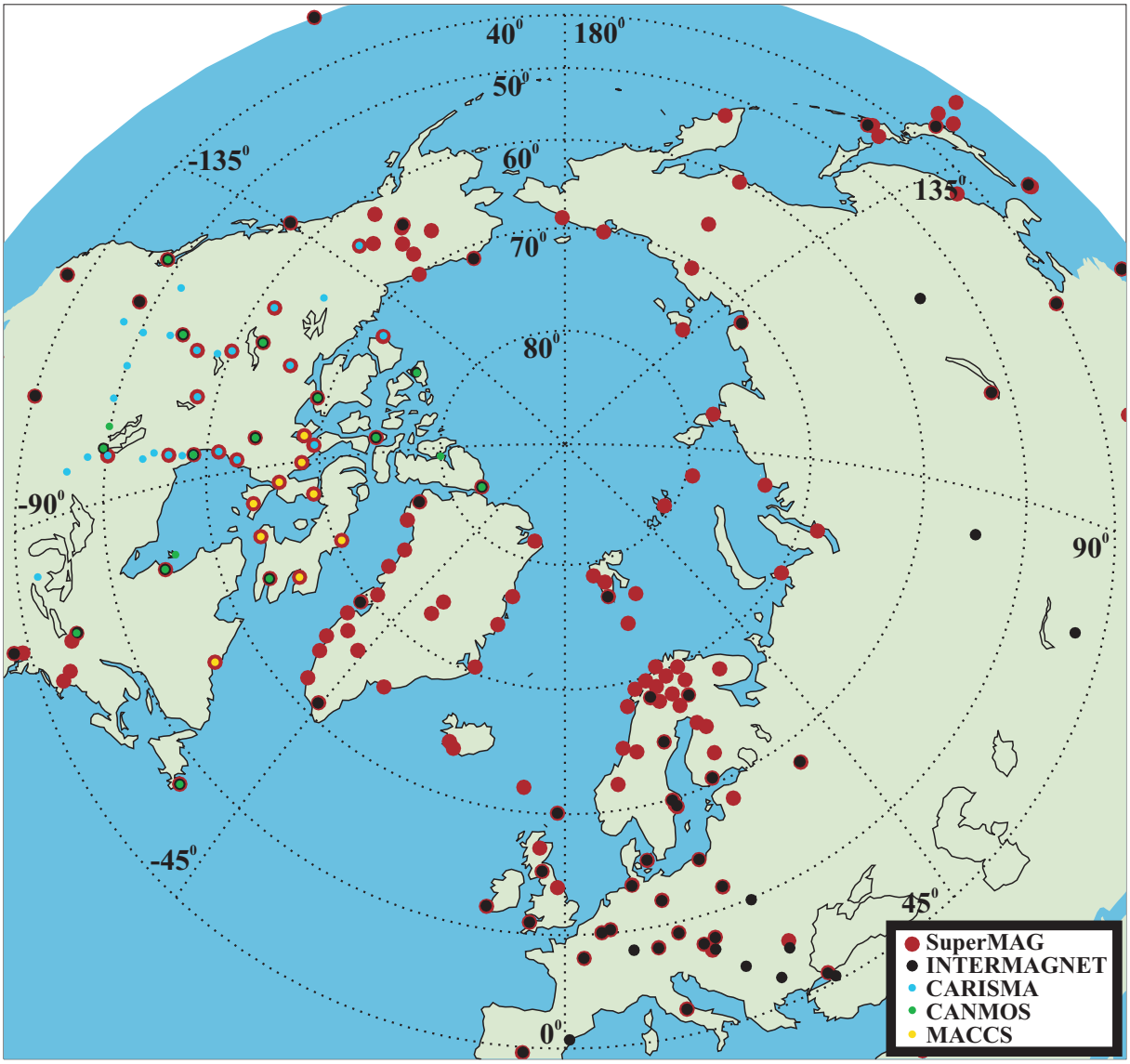

Figure 4.3: Geographic locations of magnetometer sites available from the SuperMAG data repository. INTERMAGNET, CARISMA, CANMOS, and MACCS magnetometer stations are also indicated.

the convection direction derived using the SuperDARN FIT technique with constraints from a statistical model and HMB was examined. *Benkevitch* (2006) showed that the convection azimuth was within reasonable agreement (within $\pm 45°$) for 57% of the $> 75,000$ points of comparison considered over five 1-day periods. *Boteler and van Beek* (1993) and *Boteler and van Beek* (1999) discuss the equivalent overhead current technique. In this simplified approach, the equivalent current system is represented by an infinitely long line current located 100 km above the Earth's surface.

In this section, two more advanced mathematical techniques for mapping electrodynamic properties will be presented. The Assimilative Mapping of Ionospheric Electrodynamics (AMIE) technique will be presented first followed by an equivalent current method combined with the Kamide-Richmond-Matsushita (KRM) technique.

4.2.1 AMIE technique

The AMIE technique provides a procedure for mapping electrodynamic quantities in the high-latitude region using both statistical models and a variety of direct and indirect observations from ground-based and satellite instruments (*Richmond and Kamide*, 1988; *Richmond*, 1992; *Lu et al.*, 2001). Mapped parameters include the electrostatic potential (Φ_E), electric field ($\mathbf{E}$), height-integrated horizontal electric current density ($\mathbf{J}_\perp$), field-aligned current density ($\mathbf{J}_\parallel$), and magnetic perturbation field ($\Delta\mathbf{B}$). For a given time interval, each parameter is expanded as a series of basis functions (*Richmond and Kamide*, 1988; *Haines*, 1999)

$$\Phi_E(\theta,\phi) = \sum_{k=0}^{\infty}\sum_{m=-k}^{k} a_{km}\Phi_{E,km}(\theta,\phi) \tag{4.2}$$

$$\mathbf{E}(\theta,\phi) = \sum_{k=0}^{\infty}\sum_{m=-k}^{k} a_{km}\mathbf{E}_{km}(\theta,\phi) \tag{4.3}$$

$$\mathbf{J}_\perp(\theta,\phi) = \sum_{k=0}^{\infty}\sum_{m=-k}^{k} a_{km}\mathbf{J}_{\perp km}(\theta,\phi) \tag{4.4}$$

$$\mathbf{J}_\parallel(\theta,\phi) = \sum_{k=0}^{\infty}\sum_{m=-k}^{k} a_{km}\mathbf{J}_{\parallel km}(\theta,\phi) \tag{4.5}$$

$$\Delta\mathbf{B}(h,\theta,\phi) = \sum_{k=0}^{\infty}\sum_{m=-k}^{k} a_{km}\Delta\mathbf{B}_{km}(h,\theta,\phi), \tag{4.6}$$

where θ, ϕ, and h represent co-latitude, longitude and altitude in the geomagnetic coordinate system (see Appendix A.2), a_{km} are constant coefficients to be solved, and the remaining terms represent basis functions. The first four parameters are mapped at some reference altitude, whereas the perturbation magnetic field is height-dependent and cannot be simply

mapped along the magnetic field lines (*Richmond*, 1992). The basis functions Φ_{km} are chosen to be a mathematically complete set to represent any electrostatic potential for the high latitude region (poleward of co-latitude $\theta_0 = 34°$) and to be continuous between the equator and θ_0. *Richmond and Kamide* (1988) show these conditions are satisfied by defining $\Phi_{E,km}$ as

$$\Phi_E = \sum_{k=0}^{\infty} \sum_{m=-k}^{k} a_{km} \Phi_{km}(\theta, \phi) \tag{4.7}$$

$$= \begin{cases} \sum_{k=0}^{\infty} \sum_{m=-k}^{k} a_{km} K_{km_1} P_{n_k(m)}^{|m|}(\cos\theta) f_m(\phi) & : \quad 0 \le \theta < \theta_0 \\ \sum_{k=0}^{\infty} \sum_{m=-k}^{k} a_{km} K_{km_2} \left[\tan^m\left(\frac{\theta}{2}\right) + \cot^m\left(\frac{\theta}{2}\right)\right] f_m(\phi) & : \quad \theta_0 < \theta \le \frac{\pi}{2} \end{cases} \tag{4.8}$$

where K_{km_1} and K_{km_2} are normalization constants which ensure $\Phi_E(\theta, \phi)$ is continuous at θ_0, $P_{n_k(m)}^{|m|}(\cos\theta)$ are the Associated Legendre Functions of integer order m and non-integer degree $n_k(m)$, and $f_m(\phi)$ is given by

$$f_m(\phi) = \begin{cases} \sqrt{2}\cos(m\phi) & : \quad m < 0 \\ 1 & : \quad m = 0 \\ \sqrt{2}\sin(m\phi) & : \quad m > 0 \end{cases} \tag{4.9}$$

Basis functions in equations (4.3), (4.4), and (4.5) are related to $\Phi_E(\theta, \phi)$ through

$$\mathbf{E}(\theta, \phi) = -\nabla \Phi_E(\theta, \phi) \tag{4.10}$$

$$\mathbf{J}_{\perp}(\theta, \phi) = \bar{\bar{\Sigma}} \cdot \mathbf{E}(\theta, \phi) \tag{4.11}$$

$$\mathbf{J}_{\parallel}(\theta, \phi) = \nabla \mathbf{J}_{\perp}(\theta, \phi) \tag{4.12}$$

(*Richmond and Kamide*, 1988; *Haines*, 1999), where $\bar{\bar{\Sigma}}$ represents the height-integrated conductance tensor (see Section 1.2.2). Coefficients a_{km} are determined by a least-squares fit to both observations and statistical models of the desired parameters.

The Hall (Σ_H) and Pedersen (Σ_P) conductances needed to solve equations (4.11) and (4.12) are based on a statistical conductance model (e.g., *Hardy et al.*, 1987; *Fuller-Rowell*

and Evans, 1987). The statistical conductance model for a specific period can be improved through modifications based on, for example, incoherent scatter radar observations of the electron density, satellite observations of precipitating particles (e.g., DMSP), and optical measurements from satellites (e.g., NOAA, UARS) (*Richmond and Kamide*, 1988).

The remaining basis functions $\Delta\mathbf{B}_{km}(h,\theta,\phi)$ are found from $\mathbf{J}_{\perp km}(\theta,\phi)$ and $\mathbf{J}_{\parallel km}(\theta,\phi)$ as well as a contribution from an induced Earth current. In these calculations, the magnetic field is assumed to be radially directed. *Richmond and Kamide* (1988) (and references therein) estimate the assumption of a purely vertical magnetic field introduces a difference of up to 10% from the results of a tilted field. Contributions from magnetospheric currents such as the ring current are also neglected.

The induced internal current source is evaluated by assuming a conducting layer located at 250 km below the Earth's surface under a perfectly insulating layer (*Richmond and Kamide*, 1988). *Richmond and Kamide* (1988) argue that any errors due to this assumption are diminished by the relative magnitude and importance of the contribution of the ionospheric current over the current induced in the ground.

To determine the electrodynamic parameters in equations (4.2)-(4.6), the AMIE procedure can use statistical models of the ionospheric convection to constrain the fit in regions not constrained by data, although this is not necessary (*Lu et al.*, 2001). The convection models used by AMIE include the Millstone Hill model (*Foster et al.*, 1986), Heppner and Maynard model (*Heppner and Maynard*, 1987; *Rich and Maynard*, 1989), Weimer model (*Weimer*, 1995), and IZMIRAN model (*Papitashvili et al.*, 1994). *Lu et al.* (2001) show that the choice of statistical model has little influence over regions well covered by data.

Combining measurements from multiple instruments makes AMIE an attractive method for mapping electrodynamic properties. In practice, convection maps are generated using magnetometer data in combination with statistical models while other data sets, such as the SuperDARN radar data set, are often ignored.

The AMIE method is limited in that it is designed to calculate electrodynamic properties over the entire hemisphere, which requires a large number of measurements reasonably spread throughout the hemisphere, particularly the high-latitude region. In the more realistic case where observations are irregularly spaced, the convection is adequately constrained

over the region of observation, but merely replicates model results over regions of sparse measurement, making it impossible to track anything other than a general overview of the convection over time. Another method will therefore be discussed for determining electrodynamic properties from magnetometer data which involves the application of equations developed in the KRM technique to an equivalent current system mapped using either a spherical elementary current system (SECS) or SCHA-2 approach.

4.2.2 Equivalent current and the KRM technique

In the KRM method, the ionospheric current system and associated electric field are determined using ground-based observations of the perturbation magnetic field in combination with a conductance model (*Kamide et al.*, 1981). *Kamide et al.* (1981) discuss how the full ionospheric current density **J** cannot be determined by ground-based measurements alone.

By the Helmholtz theorem, any vector field is comprised of both a curl-free (cf) and a divergence-free (df) component. The horizontal ionospheric current **i** on the surface of a spherical shell may then be written as

$$\mathbf{i} = \mathbf{i}_{cf} + \mathbf{i}_{df}, \tag{4.13}$$

where $\mathbf{i}_{cf}$ and $\mathbf{i}_{df}$ represent the curl-free and divergence-free components of **i**, respectively. It then follows that the current density **J** is written as

$$\mathbf{J} = \mathbf{J}_{cf} + \mathbf{J}_{df}. \tag{4.14}$$

Magnetic field-aligned current density ($\mathbf{J}_{\parallel}$) is given by *Kamide et al.* (1981)

$$\mathbf{J}_{\parallel} = \nabla \cdot \mathbf{i} = \nabla \cdot \mathbf{i}_{cf}, \tag{4.15}$$

and $\mathbf{i}_{cf}$ acts to close the field-aligned currents. By Fukushima's theorem (*Fukushima*, 1971), the current system represented by $\mathbf{J}_{\parallel}$ and $\mathbf{i}_{cf}$, or equivalently $\mathbf{J}_{\parallel}$ and $\mathbf{J}_{cf}$, produces no observable effects on the ground. It follows that the current system represented by $\mathbf{J}_{df}$ is a horizontal sheet current which produces the same magnetic field on the ground as the real

current system (*Kamide et al.*, 1981; *Vanhamäki and Amm*, 2007). Such a current system will be defined as the equivalent current system described by the equivalent current density $\mathbf{J}_{eq}$. It follows that $\nabla \times \mathbf{J}$ is given by

$$\nabla \times \mathbf{J} = \nabla \times \mathbf{J}_{eq}. \tag{4.16}$$

The ionospheric electric field ($\mathbf{E}$) is related to the above system of equations by relating $\mathbf{E}$ to the electrostatic potential (Φ_E) by

$$\mathbf{E} = -\nabla \Phi_E \tag{4.17}$$

through Ohm's law in the form

$$\mathbf{J} = \Sigma_P \mathbf{E} + \Sigma_H \left(\hat{\boldsymbol{r}} \times \mathbf{E} \right), \tag{4.18}$$

where $\hat{\boldsymbol{r}}$ is the unit vector in the radial direction. Combination of equations (4.16)-(4.18) yields a second order differential equation in terms of Φ_E (*Vanhamäki and Amm*, 2007)

$$\Sigma_H \nabla^2 \Phi_E + \nabla \Sigma_H \cdot \nabla \Phi_E + \left(\nabla \Sigma_P \times \nabla \Phi_E \right)_{\hat{\boldsymbol{r}}} = \left(\nabla \times \mathbf{J}_{eq} \right)_{\hat{\boldsymbol{r}}}. \tag{4.19}$$

Therefore, if $\mathbf{J}_{eq}$, Σ_H, and Σ_P are known, Φ_E may be found from equation (4.19). The electric field and current system may be solved using equations (4.17), (4.18), and (4.15).

The assumptions made by this technique include an electrostatic electric field, equipotential field lines, and radially directed magnetic field lines. Contributions from ionospheric winds, the ring current, and the magnetopause current are neglected. Such assumptions are reasonably valid in the high-latitude region, but break-down at lower latitudes. The KRM solution is therefore only valid for describing the high-latitude ionosphere.

This method requires that the equivalent current density $\mathbf{J}_{eq}$ first be obtained from ground-based measurements of the perturbation magnetic field. The method of determining $\mathbf{J}_{eq}$ is not explicitly discussed in *Kamide et al.* (1981). Examples in *Kamide et al.* (1981) are presented based on an equivalent current system previously determined in *Matsushita*

(1975) using a SHA approach. In the next sections the spherical elementary current system (SECS) SCHA-2 techniques will be introduced as examples of how $\mathbf{J}_{eq}$ might be determined.

Spherical elementary current system

Amm (1997), *Amm and Viljanen* (1999), and *Vanhamäki et al.* (2003) introduce the SECS method for determining $\mathbf{J}_{eq}$. Using Helmholtz's theorem, they show the ionospheric current density $\mathbf{J}$ may be uniquely constructed by a superposition of curl-free ($\mathbf{J}_{cf}$) and divergence-free ($\mathbf{J}_{df}$) spherical elementary current systems (SECS) distributed about the ionosphere. Each SECS is described in its own spherical coordinate system (r', θ', ϕ') using equations

$$\mathbf{J}_{df}(r', \theta', \phi') = \frac{I_{0,df}}{4\pi r'} \cot\left(\frac{\theta'}{2}\right) \hat{\boldsymbol{\phi}}', \qquad \text{and} \tag{4.20}$$

$$\mathbf{J}_{cf}(r', \theta', \phi') = \frac{I_{0,cf}}{4\pi r'} \cot\left(\frac{\theta'}{2}\right) \hat{\boldsymbol{\theta}}', \tag{4.21}$$

where and $I_{0,df}$ and $I_{0,cf}$ are scaling factors to be determined. The spherical coordinate system for each SECS is centered about the SECS pole, defined as the axis to the (r', θ', ϕ') coordinate system where $\theta' = 0$. The poles of the SECS are distributed about the ionosphere at coordinates (θ_0, ϕ_0) in the (r, θ, ϕ) coordinate system at a radial distance $r' = R_I$ from the center of the Earth, where R_I is the radius of the ionosphere, which is assumed to exist in a thin layer at 100 km altitude. Figure 4.4 illustrates the curl-free and divergence-free elementary current systems. Note that the SECSs described by $\mathbf{J}_{cf}$ are associated with the FAC flowing radially inward or outward from the SECS poles and therefore produces no magnetic effect below the ionosphere. Therefore, for the case of a perturbation magnetic field observable from the ground only, $\mathbf{J}$ cannot be determined (*Fukushima*, 1971). Instead, the equivalent current density $\mathbf{J}_{eq}$, equivalent to $\mathbf{J}_{df}$, may be determined.

To determine the ground magnetic effect of $\mathbf{J}_{df}$, the vector potential $\mathbf{A}(\mathbf{r}')$ below the ionosphere is determined, and the magnetic field is expressed as $\mathbf{B} = \nabla \times \mathbf{A}$. For $r < R_I$, the magnetic field due to $\mathbf{J}_{df}$ flowing at $r = R_I$ is given by (see *Amm and Viljanen* (1999)

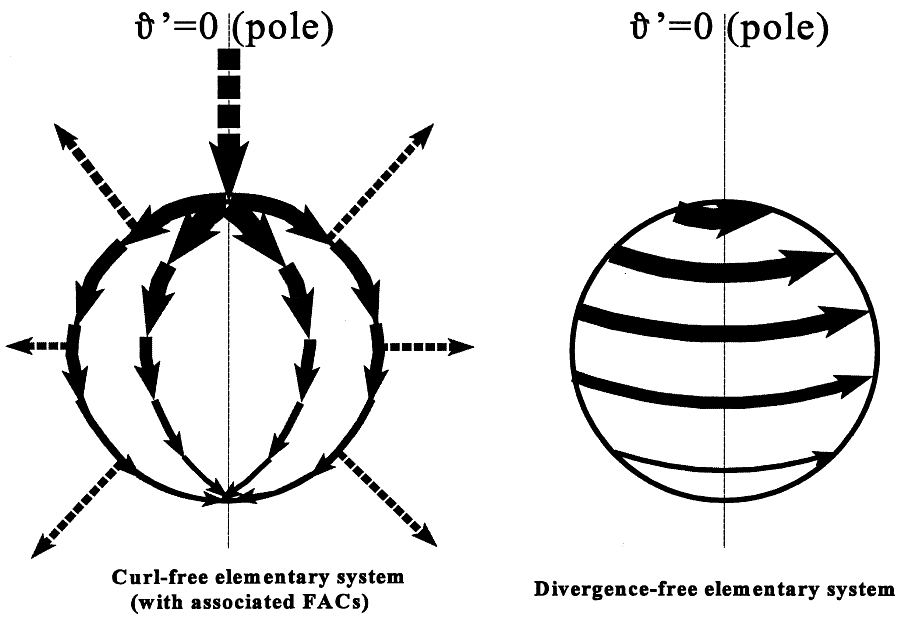

Figure 4.4: (a) Curl-free and (b) divergence-free spherical elementary current systems (*Amm and Viljanen*, 1999).

for a full derivation)

$$B_{r'}(r,\theta') = \frac{\mu_0 I_{0,df}}{4\pi r}\left(\frac{1}{\sqrt{1-\frac{2r\cos\theta'}{R_I}+\left(\frac{r}{R_I}\right)^2}}-1\right), \tag{4.22}$$

$$B_{\theta'}(r,\theta') = -\frac{\mu_0 I_{0,df}}{4\pi r\sin\theta'}\left(\frac{\frac{r}{R_I}-\cos\theta'}{\sqrt{1-\frac{2r\cos\theta'}{R_I}+\left(\frac{r}{R_I},\right)^2}}+\cos\theta'\right), \qquad \text{and} \tag{4.23}$$

$$B_{\phi'}(r,\theta) = 0. \tag{4.24}$$

Equations (4.22) and (4.23) only represent the external ionospheric contributions to the magnetic field. Internal contributions may be represented by placing a second layer of SECS in the ground (*Vanhamäki et al.*, 2003).

The scaling factors $I_{0,df}$ are determined as follows (*Amm and Viljanen*, 1999). Consider n measurements of the observed magnetic field disturbance $\Delta\mathbf{B}$ on the ground irregularly spaced at coordinates (r_k, θ_k, ϕ_k),$k = 1 \ldots n$. Place poles of m elementary current systems

at coordinates (r_l, θ_l, ϕ_l),$l = 1 \ldots m$. Next, solve

$$\mathbf{T} \cdot \mathbf{I} = \mathbf{Z}, \tag{4.25}$$

where $\mathbf{Z}$ is a $(2n \times 1)$ vector of the observed quantities of $B_{r'}$ and $B_{\theta'}$, $\mathbf{I}$ is an $(m \times 1)$ vector of scaling factors, and $\mathbf{T}$ is a $(2n \times m)$ matrix of the θ and ϕ components of the ground magnetic effect of the elementary current systems, where the pole of element T_{kl} is located at r_l for observation r_k. The vector $\mathbf{I}$ may be solved using any matrix technique. However, since the system is underdetermined $(n < m)$, $\mathbf{T}$ is poorly conditioned, and *Amm and Viljanen* (1999) therefore recommend using singular value decomposition to obtain the matrix solution.

Spherical cap harmonic analysis technique

Haines and Torta (1994) introduce a method for determining $\mathbf{J}_{eq}$ based on the magnetic field perturbation determined using SCHA-2 (*Haines*, 1985a; *Haines*, 1988).

Consider the surface of a spherical Earth of radius R_E on which the magnetic field ($\mathbf{B}$) and magnetic scalar potential (Φ_B) are measured. In the atmosphere, the magnetic field is source-free because the atmosphere is non-conducting so no electric currents flow there

$$\mathbf{B} = -\nabla \Phi_B. \tag{4.26}$$

The geomagnetic potential is harmonic and satisfies the Laplace equation

$$\nabla^2 \Phi_B = 0. \tag{4.27}$$

The geomagnetic potential may be determined using the normal method of separation of variables for sources internal and external to the surface of the Earth. For internal sources, Φ_B and $\frac{d\Phi_B}{dr}$ must go to zero as the radial distance r from the center of the Earth approaches infinity, and there will be a $\frac{1}{r}$ dependence of Φ_B on r. For external sources, both Φ_B and $\frac{d\Phi_B}{dr}$ must be finite within the sphere and there will be a direct dependence between Φ_B and r.

The geomagnetic potential, separated for internal and external sources, is represented by a series expansion using spherical cap harmonics (*Haines*, 1985a; *Haines*, 1988)

$$\begin{aligned}\Phi_B(r,\theta,\phi) &= R_E \sum_{k=0}^{K^i_{max}} \sum_{m=0}^{k} \left(\frac{R_E}{r}\right)^{n_k(m)+1} \left[g^i_{km}\cos(m\phi) + h^i_{km}\sin(m\phi)\right] P^m_{n_k(m)}(\cos\theta) \\ &\quad + R_E \sum_{k=0}^{K^e_{max}} \sum_{m=0}^{k} \left(\frac{r}{R_E}\right)^{n_k(m)} \left[g^e_{km}\cos(m\phi) + h^e_{km}\sin(m\phi)\right] P^m_{n_k(m)}(cos\theta), \end{aligned} \tag{4.28}$$

where θ and ϕ are the geocentric co-latitude and longitude in the spherical cap coordinate system. The function $P^m_{n_k(m)}(cos\theta)$ is the Associated Legendre Function of non-integer degree k and order m, and $K^{i,e}_{max}$ is the maximum degree index (see Section 3.1). The fitting coefficients $g^{i,e}_{km}$ and $h^{i,e}_{km}$ are constants which must be determined to describe $\Phi_B(r,\theta,\phi)$ over the entire spherical cap. Superscripts i and e indicate whether the indexed variable is for internal or external sources.

The radial ($\hat{\boldsymbol{r}}$), co-latitudinal ($\hat{\boldsymbol{\theta}}$), and longitudinal ($\hat{\boldsymbol{\phi}}$) components of the magnetic field may be derived by substituting the potential given by equation (4.28) into equation (4.26). The magnetic field components are easily found:

$$\begin{aligned} B_r &= -\sum_{k=0}^{K^i_{max}} \sum_{m=0}^{k} (n_k(m)+1) \left(\frac{R_E}{r}\right)^{n_k(m)+2} \left[g^i_{km}\cos(m\phi) + h^i_{km}\sin(m\phi)\right] P^m_{n_k(m)}(\cos\theta) \\ &\quad + \sum_{k=0}^{K^e_{max}} \sum_{m=0}^{k} n_k(m) \left(\frac{r}{R_E}\right)^{n_k(m)-1} \left[g^e_{km}\cos(m\phi) + h^e_{km}\sin(m\phi)\right] P^m_{n_k(m)}(\cos\theta), \end{aligned} \tag{4.29}$$

$$\begin{aligned} B_\theta &= -\sum_{k=0}^{K^i_{max}} \sum_{m=0}^{k} \left(\frac{R_E}{r}\right)^{n_k(m)+2} \left[g^i_{km}\cos(m\phi) + h^i_{km}\sin(m\phi)\right] \frac{dP^m_{n_k(m)}(\cos\theta)}{d\theta} \\ &\quad + \sum_{k=0}^{K^e_{max}} \sum_{m=0}^{k} \left(\frac{r}{R_E}\right)^{n_k(m)-1} \left[g^e_{km}\cos(m\phi) + h^e_{km}\sin m\phi\right] \frac{dP^m_{n_k(m)}(\cos\theta)}{d\theta}, \end{aligned} \tag{4.30}$$

$$\begin{aligned} B_\phi &= \sum_{k=0}^{K^i_{max}} \sum_{m=0}^{k} \left(\frac{R_E}{r}\right)^{n_k(m)+2} \left[g^i_{km}\sin(m\phi) - h^i_{km}\cos(m\phi)\right] \frac{mP^m_{n_k(m)}(\cos\theta)}{\sin\theta} \\ &\quad + \sum_{k=0}^{K^e_{max}} \sum_{m=0}^{k} \left(\frac{r}{R_E}\right)^{n_k(m)-1} \left[g^e_{km}\sin(m\phi) - h^e_{km}\cos(m\phi)\right] \frac{mP^m_{n_k(m)}(\cos\theta)}{\sin\theta}. \end{aligned} \tag{4.31}$$

To determine the fitting coefficients, measurements from each magnetometer station are transformed into the geocentric coordinate system with measurement components in the $\hat{\boldsymbol{r}}$, $\hat{\boldsymbol{\theta}}$, and $\hat{\boldsymbol{\phi}}$ directions. Coefficients $g_{km}^{i,e}$ and $h_{km}^{i,e}$ are determined by minimizing the equation

$$\chi^2 = \sum_{i=1}^{3N} \left(B_{measured} - B_{calculated}\right)_i^2 , \tag{4.32}$$

where N is the total number of magnetometer stations, $B_{measured}$ represents each of the three components of the magnetic field measured at each magnetometer station, and $B_{calculated}$ is the magnetic field calculated using equation (4.29), (4.30), or (4.31). The minimization is performed using singular value decomposition. The above technique can also be applied to find the perturbation magnetic field $\Delta\mathbf{B}$.

The methods of *Haines and Torta* (1994) (summarized below) are used to determine the equivalent current using the $g_{km}^{i,e}$ and $h_{km}^{i,e}$ coefficients to describe $\Delta\mathbf{B}$. This method assumes there are external and internal sources of magnetic perturbations.

External currents originate from a surface within the ionosphere located at some radius $R_2 = R_E + h_2$ whereas the internal currents are modeled by a surface within the upper few 100 km of the Earth at radius $R_1 = R_E - h_1$. Typically, $h_2 \sim 110$ km and $h_1 \sim 400$ km (*Haines and Torta*, 1994). The geomagnetic potential may be described in each region as described below.

For some radius $r > R_2$ the source of the magnetic perturbation is entirely internal:

$$\Phi_{B,2} = R_E \sum_{k=0}^{K_{max}^i} \sum_{m=0}^{k} \left(\frac{R_E}{r}\right)^{n_k(m)+1} \left[g_{km}^{i\star}\cos(m\phi) + h_{km}^{i\star}\sin(m\phi)\right] P_{n_k(m)}^m(\cos\theta), \tag{4.33}$$

whereas, for $R_1 < r < R_2$ there are both internal and external sources and the potential is defined according to equation (4.28). For $r < R_1$ the sources are entirely external:

$$\Phi_{B,1} = R_E \sum_{k=0}^{K_{max}^e} \sum_{m=0}^{k} \left(\frac{r}{R_E}\right)^{n_k(m)} \left[g_{km}^{e\star}\cos(m\phi) + h_{km}^{e\star}\sin(m\phi)\right] P_{n_k(m)}^m(\cos\theta). \tag{4.34}$$

Note that new coefficients $g_{km}^{i,e\star}$ and $h_{km}^{i,e\star}$ have been introduced to describe the potential $\Phi_{B,1}$ and $\Phi_{B,2}$. These coefficients may be defined in terms of the $g_{km}^{i,e}$ and $h_{km}^{i,e}$ coefficients,

which have already been found in mapping the magnetic field perturbations so that $\Phi_{B,1}$ and $\Phi_{B,2}$ may be fully described in terms of known parameters. This is accomplished by assuming continuity of the vertical field at each of the R_1 and R_2 boundaries, implying

$$\left.\frac{\partial \Phi_{B1}}{\partial r}\right|_{r=R_1} = \left.\frac{\partial \Phi_B}{\partial r}\right|_{r=R_1}, \qquad \text{and} \tag{4.35}$$

$$\left.\frac{\partial \Phi_{B2}}{\partial r}\right|_{r=R_2} = \left.\frac{\partial \Phi_B}{\partial r}\right|_{r=R_2}. \tag{4.36}$$

By substituting equations (4.28), (4.33), and (4.34) into equations (4.35) and (4.36), $g_{km}^{i,e\star}$ and $h_{km}^{i,e\star}$ are solved as

$$g_{km}^{i\star} = g_{km}^{i} - \frac{n_k(m)}{n_k(m)+1}\left(\frac{R_2}{R_E}\right)^{2n_k(m)+1} g_{km}^{e}, \tag{4.37}$$

$$h_{km}^{i\star} = h_{km}^{i} - \frac{n_k(m)}{n_k(m)+1}\left(\frac{R_2}{R_E}\right)^{2n_k(m)+1} h_{km}^{e}, \tag{4.38}$$

$$g_{km}^{e\star} = g_{km}^{e} - \frac{n_k(m)+1}{n_k(m)}\left(\frac{R_E}{R_1}\right)^{2n_k(m)+1} g_{km}^{i}, \qquad \text{and} \tag{4.39}$$

$$h_{km}^{e\star} = h_{km}^{e} - \frac{n_k(m)+1}{n_k(m)}\left(\frac{R_E}{R_1}\right)^{2n_k(m)+1} h_{km}^{i}. \tag{4.40}$$

The equivalent current density of the external sources J_{eq}^{e} is determined by considering the behavior of the tangential component of the field. From Maxwell's equations, the magnetic field $\mathbf{B}$ is described in terms of the current density $\mathbf{J}$ and the electric field $\mathbf{E}$

$$\nabla \times \mathbf{B} = \mu_0 \mathbf{J} + \mu_0 \varepsilon_0 \frac{\partial \mathbf{E}}{\partial t}. \tag{4.41}$$

By assuming $\mathbf{B}$ is radially directed (approximately true in the high-latitude ionosphere) and steady state ($\frac{\partial E}{\partial t} = 0$), the equation reduces to

$$\nabla \times \mathbf{B} = \mu_0 \mathbf{J}_{eq}, \tag{4.42}$$

where $\mathbf{J}_{eq}$ is the current density flowing on a spherical shell perpendicular to $\hat{\boldsymbol{r}}$. Rearranging

equation (4.42)

$$\begin{aligned}\mathbf{J}_{eq} &= \frac{1}{\mu_0}\nabla \times \mathbf{B} \\ &= \frac{1}{\mu_0}\hat{\boldsymbol{r}} \times -\left(\nabla \Phi_B\right), \end{aligned} \tag{4.43}$$

where, since the current flows on a surface, $\nabla = \nabla_r = \hat{\boldsymbol{r}}$ has been used in the cross product, and $\mathbf{B}$ has been substituted according to equation (4.26).

At $r = R_2$, the external contribution to the perpendicular current density for external sources is (*Stratton*, 1941; Section 1.13).

$$\begin{aligned}\mathbf{J}^e_{eq} &= -\frac{1}{\mu_0}\hat{\boldsymbol{r}} \times \boldsymbol{\nabla}_s(\Phi_{B,2} - \Phi_B)|_{r=R_2} \\ &= -\frac{1}{\mu_0}\left[\frac{1}{r}\frac{\partial(\Phi_{B,2} - \Phi)}{\partial\theta}\hat{\boldsymbol{\phi}} - \frac{1}{rsin\theta}\frac{\partial(\Phi_{B,2} - \Phi)}{\partial\phi}\hat{\boldsymbol{\theta}}\right]\Bigg|_{r=R_2}, \end{aligned} \tag{4.44}$$

where the surface gradient (∇_s) has been taken because the vertical magnetic field is constrained to be continuous through current layers. Substitution of $\Phi_{B,2}$ and Φ_B lead to a solution for the equivalent current for external sources:

$$J^e_{eq\theta} = \frac{1}{\mu_0}\sum_{k=0}^{K^e_{max}}\sum_{m=0}^{k}\frac{2n_k(m)+1}{n_k(m)+1}\left(\frac{R_2}{R_E}\right)^{n_k(m)-1}\left[g^e_{km}\sin(m\phi) - h^e_{km}\cos(m\phi)\right]\frac{mP^m_{n_k(m)}(cos\theta)}{sin\theta} \tag{4.45}$$

$$J^e_{eq\phi} = \frac{1}{\mu_0}\sum_{k=0}^{K^e_{max}}\sum_{m=0}^{l}\frac{2n_k(m)+1}{n_k(m)+1}\left(\frac{R_2}{R_E}\right)^{n_k(m)-1}\left[g^e_{km}cos(m\phi) + h^e_{km}sin(m\phi)\right]\frac{dP^m_{n_k(m)}(cos\theta)}{d\theta}. \tag{4.46}$$

Similarly, at $r = R_1$, the equivalent current density for internal sources is given by

$$\begin{aligned}\mathbf{J}^i_{eq} &= -\frac{1}{\mu_0}\hat{\boldsymbol{r}} \times \nabla_s(\Phi_B - \Phi_{B,1})|_{r=R_1} \\ &= -\frac{1}{\mu_0}\left[\frac{1}{r}\frac{\partial(\Phi_B - \Phi_{B,1})}{\partial\theta}\hat{\boldsymbol{\phi}} - \frac{1}{rsin\theta}\frac{\partial(\Phi_B - \Phi_{B,1})}{\partial\phi}\hat{\boldsymbol{\theta}}\right]|_{r=R_1} \end{aligned} \tag{4.47}$$

and equivalent current in the $\hat{\boldsymbol{\theta}}$ and $\hat{\boldsymbol{\phi}}$ directions of the internal sources are given by

$$J^i_{eq\theta} = \frac{1}{\mu_0}\sum_{k=0}^{K^i}\sum_{m=0}^{k}\frac{2n_k(m)+1}{n_k(m)}\left(\frac{R_E}{R_1}\right)^{n_k(m)+2}\left[-g^i_{km}sin(m\phi) + h^i_{km}cos(m\phi)\right]\frac{mP^m_{n_k(m)}(cos\theta)}{sin\theta} \tag{4.48}$$

$$J^i_{eq\phi} = -\frac{1}{\mu_0}\sum_{k=0}^{K^i}\sum_{m=0}^{k}\frac{2n_k(m)+1}{n_k(m)}\left(\frac{R_E}{R_1}\right)^{n_k(m)+2}\left[g^i_{km}cos(m\phi)+h^i_{km}sin(m\phi)\right]\frac{dP^m_{n_k(m)}(cos\theta)}{d\theta}. \quad (4.49)$$

Discussion of technique

Both the SCHA-2 and SECS techniques are similar in that they are able to map $\mathbf{J}_{eq}$ based on a limited number of magnetometer stations over a localized region of measurement. In Section 3.2, it was shown that the mapping resolution of the SCHA-2 technique is dependent on the size of the spherical cap, the distribution of observations, and the maximum value of K_{max} that can map a given region. For an irregular distribution of observations, resolution is limited by the least dense region of measurement within the mapping region.

Amm and Viljanen (1999) argues that the SECS technique is more adaptable than the SCHA-2 technique as the mapping resolution of the SECS technique is determined by the number and spacing of divergence-free SECS, which may vary over the region of interest. Although SECS may be arbitrarily spaced over the region of interest, *Vanhamäki et al.* (2003) suggest that the spacing between SECS be smaller than $\frac{1}{2}$ the spacing between magnetometers, and the area within which the SECS are placed not exceed the area of observation by more than a few degrees. *Amm and Viljanen* (1999) suggest placing more poles over a region of dense measurements and fewer poles over a more sparse region so more complex features are illustrated when the density of measurements allows it. We argue that a convection map generated with a resolution that varies across the map is misleading, and therefore impractical. For example, consider a complicated feature which spreads across the entire region of interest. Over a region of dense measurement, the higher resolution map will be able to represent the full complexity of the convection, whereas over the region of low resolution the features will be artificially smooth. To the untrained eye, the change in mapping resolution may be attributed to the convection pattern, rather than the mapping algorithm. In practice, it will be more useful to use a uniform distribution of poles in the SECS approach based on limitations determined from the least dense region of measurement in the mapping region. We therefore argue that the SCHA-2 and SECS techniques are comparable. The SCHA-2 method will be used for mapping electrodynamic properties to be consistent with

methods previously developed for use in this Thesis. A full comparison of the SCHA-2 and SECS mapping techniques is suggested as a topic of future research.

4.2.3 Mapping convection based on $\mathbf{J}_{eq}$ using the SCHA-2 technique

The equivalent current system describes the direction of the equivalent convection by rotating the $\mathbf{J}_{eq}$ vectors described by equations (4.45), (4.46), (4.48), and (4.49) by 180°, see Figure 4.6 to follow. The magnitude of the equivalent convection vectors is given in units of (A/km^2) rather than (m/s).

Provided the ionospheric equivalent current $\mathbf{J}_{eq}$, and the Hall (Σ_H) and Pedersen (Σ_P) conductance are known, or can be represented by a model, the electrostatic potential Φ_E can be determined by solving the second order differential equation (see Section 4.2.2)

$$\Sigma_H \nabla^2 \Phi_E + \nabla \Sigma_H \cdot \nabla \Phi_E + (\nabla \Sigma_P \times \nabla \Phi_E)_{\hat{\boldsymbol{r}}} = (\nabla \times \mathbf{J}_{eq})_{\hat{\boldsymbol{r}}} \,. \tag{4.19}$$

The right hand side of equation (4.19) is known and can be expanded as

$$(\nabla \times \mathbf{J}_{eq})_{\hat{\boldsymbol{r}}} = \frac{1}{r \sin\theta} \left[\frac{\partial}{\partial \theta} \left(\sin\theta J^e_{eq\phi} \right) - \frac{\partial J^e_{eq\theta}}{\partial \phi} \right], \tag{4.50}$$

where $J^e_{eq\theta}$ and $J^e_{eq\phi}$ are given by equations (4.45) and (4.46), and r represents the radius of the external ionospheric source of $\mathbf{J}_{eq}$ (typically ∼100 km). The left hand side of equation (4.19) is entirely dependent on Φ_E and the Hall and Pedersen conductances, which will be derived from the Hardy conductance model based on the K_p value of the event of interest (*Hardy et al.*, 1985; *Hardy et al.*, 1987).

In Section 3.1, it was shown that the electrostatic potential on a spherical cap having angular radius θ_c centered at coordinates (θ_N, ϕ_N) is represented by a series expansion of Legendre polynomials (see equation (3.1))

$$\Phi_E(\theta, \phi) = \sum_{k=0}^{K_{max}} \sum_{m=0}^{k} [A_{km} \cos(m\phi) + B_{km} \sin(m\phi)] P^m_{n_k(m)}(\cos\theta), \tag{4.51}$$

where θ and ϕ represent the co-latitude and longitude in the spherical cap coordinate system. The fitting coefficients A_{km} and B_{km} are determined by first substituting equation (4.51) into equation (4.19) and minimizing the difference between the left and right hand sides of the equation. The following equations are necessary for the expansion of the left hand side of equation (4.19):

$$\begin{aligned}\nabla\Sigma_{P,H} &= \frac{1}{r}\frac{\partial\Sigma_{P,H}}{\partial\theta}\hat{\boldsymbol{\theta}} + \frac{1}{r\sin\theta}\frac{\partial\Sigma_{P,H}}{\partial\phi}\hat{\boldsymbol{\phi}} \\ &= \nabla\Sigma_{P,H\theta}\hat{\boldsymbol{\theta}} + \nabla\Sigma_{P,H\phi}\hat{\boldsymbol{\phi}} \end{aligned} \tag{4.52}$$

$$(\nabla\Sigma_P \times \nabla\Phi_E)_{\hat{\boldsymbol{r}}} = \nabla\Sigma_{P\theta}\nabla\Phi_{E\phi} - \nabla\Sigma_{P\phi}\nabla\Phi_{E\theta}, \tag{4.53}$$

$$\begin{aligned}\nabla\Phi_E &= \frac{1}{r}\frac{\partial\Phi_e}{\partial\theta}\hat{\boldsymbol{\theta}} + \frac{1}{r\sin\theta}\frac{\partial\Phi_E}{\partial\phi}\hat{\boldsymbol{\phi}} \\ &= \frac{1}{r}\sum_{k=0}^{K_{max}}\sum_{m=0}^{k}(A_{km}\cos(m\phi) + B_{km}\sin(m\phi))\frac{dP}{d\theta}\hat{\boldsymbol{\theta}} \\ &\quad + \frac{1}{r\sin\theta}\sum_{k=0}^{K_{max}}\sum_{m=0}^{k}(-A_{km}\sin(m\phi) + B_{km}\cos(m\phi))mP\hat{\boldsymbol{\phi}} \\ &= \nabla\Phi_{E\theta}\hat{\boldsymbol{\theta}} + \nabla\Phi_{E\phi}\hat{\boldsymbol{\phi}} \end{aligned} \tag{4.54}$$

$$
\begin{aligned}
\nabla^2\Phi_E &= \frac{1}{r^2\sin\theta}\frac{\partial}{\partial\theta}\left[\sin\theta\frac{\partial\Phi_E}{\partial\theta}\right]+\frac{1}{r^2\sin^2\theta}\frac{\partial^2\Phi_E}{\partial\phi^2} \\
&= \frac{1}{r^2\sin\theta}\frac{\partial}{\partial\theta}\left[\sin\theta\sum_{k=0}^{K_{max}}\sum_{m=0}^{k}\left(A_{km}\cos(m\phi)+B_{km}\sin(m\phi)\right)\frac{dP}{d\theta}\right] \\
&\quad +\frac{1}{r^2\sin^2\theta}\frac{\partial}{\partial\phi}\left[\sum_{k=0}^{K_{max}}\sum_{m=0}^{k}\left(-A_{km}\sin(m\phi)+B_{km}\cos(m\phi)\right)mP\right] \\
&= \frac{1}{r^2\sin\theta}\left[\cos\theta\sum_{k=0}^{K_{max}}\sum_{m=0}^{k}\left(A_{km}\cos(m\phi)+B_{km}\sin(m\phi)\right)\frac{dP}{d\theta}\right. \\
&\quad \left.+\sin\theta\sum_{k=0}^{K_{max}}\sum_{m=0}^{k}\left(A_{km}\cos(m\phi)+B_{km}\sin(m\phi)\right)\frac{d^2P}{d\theta^2}\right] \\
&\quad -\frac{1}{r^2\sin^2\theta}\sum_{k=0}^{K_{max}}\sum_{m=0}^{k}\left(A_{km}\cos(m\phi)+B_{km}\sin(m\phi)\right)m^2P \\
&= \sum_{k=0}^{K_{max}}\sum_{m=0}^{k}\left(A_{km}\cos(m\phi)+B_{km}sin(m\phi)\right)\left[\frac{\cos\theta}{r^2\sin\theta}\frac{dP}{d\theta}+\frac{1}{r^2}\frac{d^2P}{d\theta^2}-\frac{m^2}{r^2\sin^2\theta}P\right] \qquad (4.55)
\end{aligned}
$$

where the notation $P = P_{n_k(m)}(\cos\theta)$ has been used.

After substituting equations(4.55)-(4.53) into the left-hand side of equation (4.19), the only unknown variables to be solved are the fitting coefficients A_{km} and B_{km}, which are determined through a minimization of the difference between the right and left hand sides of equation (4.19) using the familiar method of singular value decomposition. Once the fitting coefficients A_{km} and B_{km} are known, the electrostatic potential, and therefore the electric field and velocity may be described across the entire spherical cap. Using this technique, the convection is determined in the desired units of m/s.

4.3 Mapping convection based on magnetometer data

For the case of magnetometer-derived convection maps, electrostatic potential will be represented through contours limited to a region of constraint determined using the masking algorithm described in Section 3.2. There are generally fewer inputs used to generate magnetometer-derived convection maps. To clearly illustrate the convection flow, vectors will be plotted in a grid with a grid spacing of 1.5° of latitude within the entire region of constraint.

Three types of magnetometer-derived convection vectors will be considered. The simplest convection pattern is derived by rotating the measured perturbation magnetic field by 90° counter-clockwise, and describing the magnitude of the convection in units of nT. There is no separation of the internal and external magnetic field sources and the convection is only defined in the direct region surrounding the measurements. Convection maps generated using this technique will be referred to as perturbation convection maps. The second is determined by first finding the equivalent current by separating the internal and external source contributions to the perturbation magnetic field and fitting the data using SCHA-2 (see equations (4.45) and (4.46)). The equivalent current system is rotated by 180° to describe the magnitude of the convection in units of A/km^2. Convection maps generated using this technique will be referred to as equivalent convection maps. Finally, the KRM technique is used to determine the convection based on the equivalent current density inferred using the SCHA-2 technique and a conductance model. Convection maps generated using this technique will be referred to as conductance-based convection maps. Unlike the perturbation and equivalent convection mapping techniques, which only determine the direction of the convection, the conductance-based convection mapping technique is able to determine the full convection vector. The differences between the perturbation, equivalent, and conductance-based convection vectors will be discussed in this Section.

4.3.1 Comparison of perturbation, equivalent, and conductance-based convection

Consider the magnetic perturbation measured on January 20, 2001 at 13:30 UT, when the IMF B_z was steady at ∼-5 nT. Figure 4.5 shows the perturbation convection vectors. Figures 4.6 a and b illustrate the equivalent and conductance-based convection patterns. The equivalent convection shown in 4.6a was combined with the Hall and Pedersen conductance determined from the Hardy model for $K_p = 2$ to generate the ionospheric convection pattern shown in 4.6b.

In Figures 4.6 a and b, a spherical cap centered over the north geographic pole was considered with $\theta_c = 40°$ and $K_{max} = 3$. More complicated flow structures could be mapped

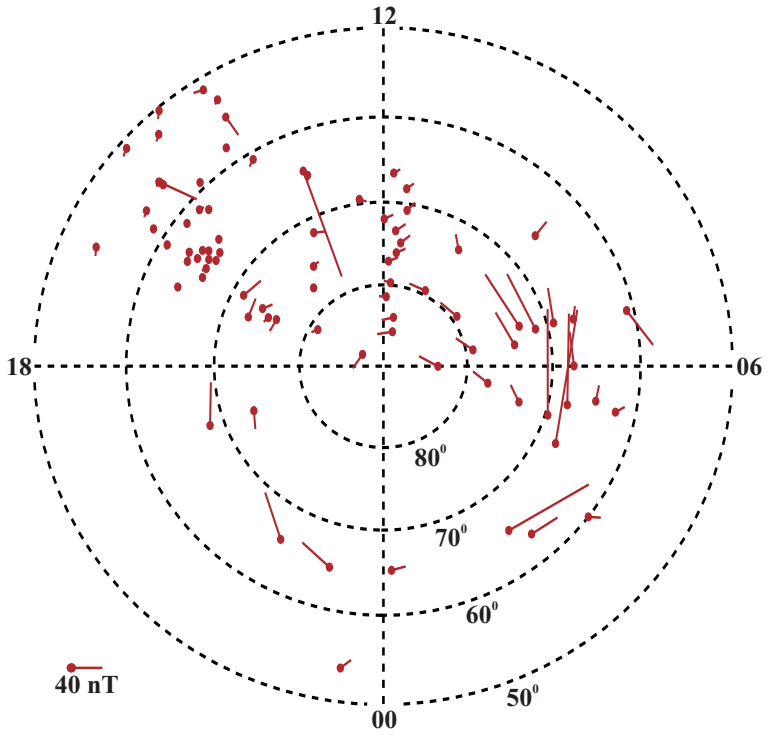

Figure 4.5: Vector plot of the perturbation magnetic field, rotated by 90° counter clockwise, in the AACGM coordinate system for a two-minute interval beginning at 13:30 UT on January 20, 2001.

using a higher fitting degree, but this is not supported by the low density of magnetometer stations. Calculations were performed in the geographic coordinate system and converted to AACGM coordinates for plotting. Convection contours are plotted across the entire spherical cap with regions eliminated by the masking algorithm shown in grey.

Both convection patterns shown in Figures 4.6 a and b indicate a two-celled pattern with anti-sunward flow over the polar cap. In (a), the anti-sunward convection flow is aligned along the noon-midnight meridian with convection vortices centered at 80° MLAT and approximately 05 and 18 MLT. In (b) the anti-sunward convection flow is aligned along the 10-22 MLT meridian with convection vortices centered at 72° MLAT and 03 and 15 MLT. The equivalent convection pattern does not include contributions from the ionospheric conductance, which explains the difference.

In an attempt to evaluate differences in the directions of the equivalent convection pattern shown in (a) and the conductance-based convection pattern in (b), the convection direction was compared to the convection pattern derived by an alternate data set and

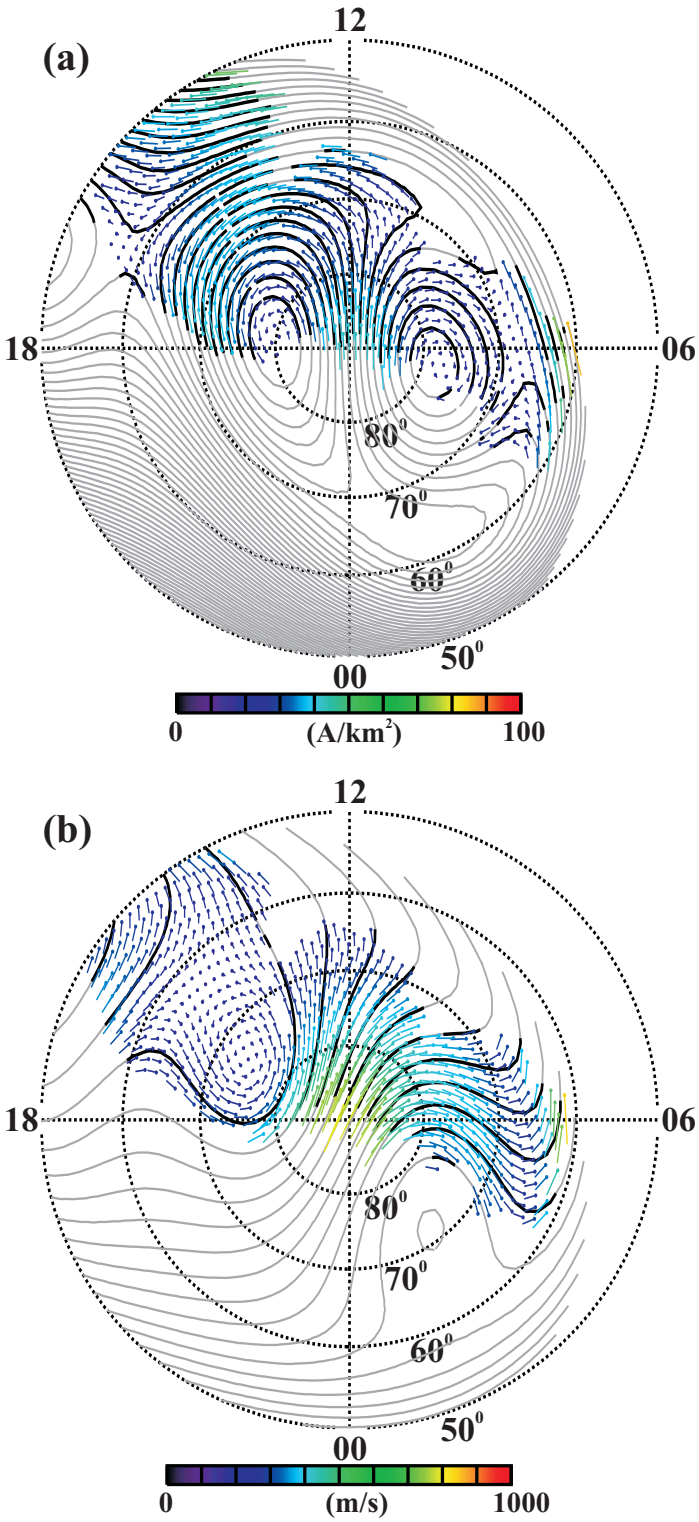

Figure 4.6: Contour plots of the (a) equivalent and (b) conductance-based convection. Black contour lines indicate those regions over which the contours are well constrained by the data. Over the region of constraint (see text) vectors showing the (a) equivalent and (b) conductance-based convection are plotted with a grid spacing of 1.5°. All plots are in the AACGM coordinate system.

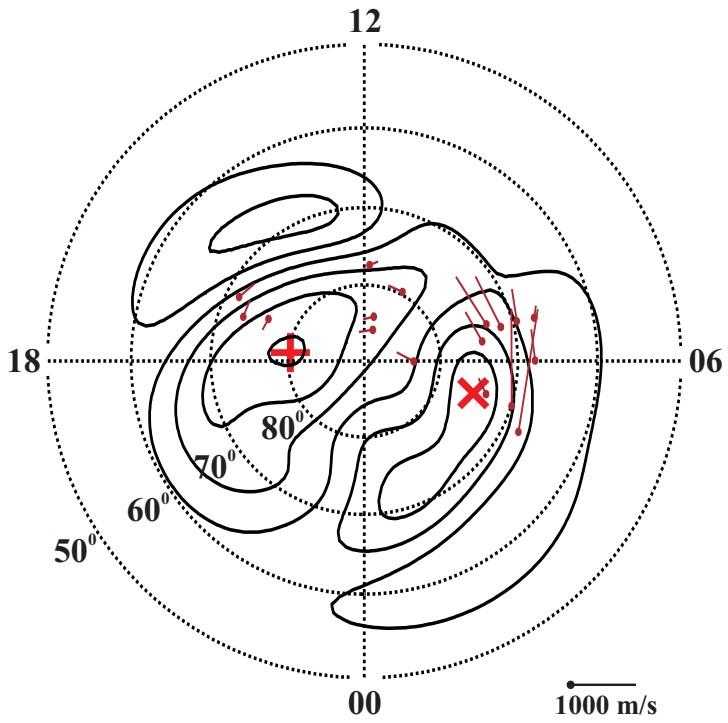

Figure 4.7: Contours of the electrostatic potential (6 kV spacing) derived using the SuperDARN FIT technique with constraints from a statistical model and HMB for a two-minute interval on January 20, 2001 beginning at 13:30 UT. The plus and cross signs indicate the maximum and minimum of the potential. Magnetic field perturbation vectors used in the comparison are plotted in red.

technique. Similar to *Benkevitch* (2006), the convection patterns shown in Figure 4.6 were compared with convection derived using the SuperDARN FIT technique. To generate the SuperDARN convection plot, gridded l-o-s velocities were considered for all available northern hemisphere SuperDARN radars and processed with $K_{max} = 6$ and $\theta_{FIT} = 40°$ with constraints from both a statistical model and an HMB. Figure 4.7 shows the SuperDARN convection pattern for the same period considered in Figure 4.6. The inner two convection cells represent the standard two-cell convection pattern typical for periods of southward IMF, with anti-sunward flow over the polar cap approximately aligned along the 10-22 MLT meridian. The normal dawn and duskside convection vortices are centered at 70° MLAT and 02 MLT and 80° MLAT and ∼18 MLT, respectively. The locations of the dawn and dusk convection vortices, and the orientation of the flow indicate better agrement between the SuperDARN-inferred convection pattern and the conductance-based convection pattern over the equivalent convection pattern.

Comparisons were performed at the coordinates of magnetometer stations provided (1) the magnetometer station produced a measurement, (2) the magnetometer station was within 160 km of at least 6 SuperDARN gridded l-o-s velocities, (3) the magnitude of the perturbation vector was > 15 nT to exclude noise, and (4) the magnitude of the FIT convection velocity was at least 50 m/s. For the example illustrated in Figures 4.5-4.7, these constraints limit the comparison to 17 vectors centered over the region of constraint, see red vectors in Figure 4.7.

A large scale comparison was performed between the direction of the perturbation, equivalent, and conductance-based convection patterns with the SuperDARN-inferred FIT convection pattern. Convection maps were generated at two-minute intervals for January 23, 2000, January 20 and 21, 2001, June 09, 2001, and July 15, 2001. Events were selected during periods of good data coverage for magnetic activity levels ranging from $K_p = 0$ to $K_p = 6$. To ensure well constrained convection maps, the data set was limited to events having at least 300 SuperDARN gridded l-o-s velocities. In addition, events were limited to periods where 0° magnetic longitude (close to the Kapuskasing radar station) was between 7 and 12 MLT to ensure the SuperDARN radar network was approximately centered over the dayside MLT sector so that convection cells would be adequately constrained.

Figure 4.8 shows the distribution of the scatter of the azimuth of the (a) perturbation, (b) equivalent, and (c) conductance-based convection vectors against the azimuth of the SuperDARN convection vectors determined by the FIT technique. Although a significant amount of scatter lies away from the diagonal bisector for the perturbation convection plot, the correlation coefficient is R=0.70 and the slope of the best-fit line to the data set is m=1.00. Scatter for the equivalent convection azimuth also lies close to the diagonal bisector, but correlation is reduced (R=0.47, m=0.75), see Figure 4.8c. Figure 4.8e shows a scatter plot of the azimuth of the conductance-based convection versus the direction of the SuperDARN convection. In this case, scatter is more spread out (R=0.36, m=0.51).

Figure 4.8 shows histograms of the azimuthal difference between the (b) perturbation, (d) equivalent, and (f) conductance-based convection vectors and the convection vectors determined using the SuperDARN FIT technique. There are $> 16,000$ points of comparison. The distributions have been normalized according to the maximum number of points ob-

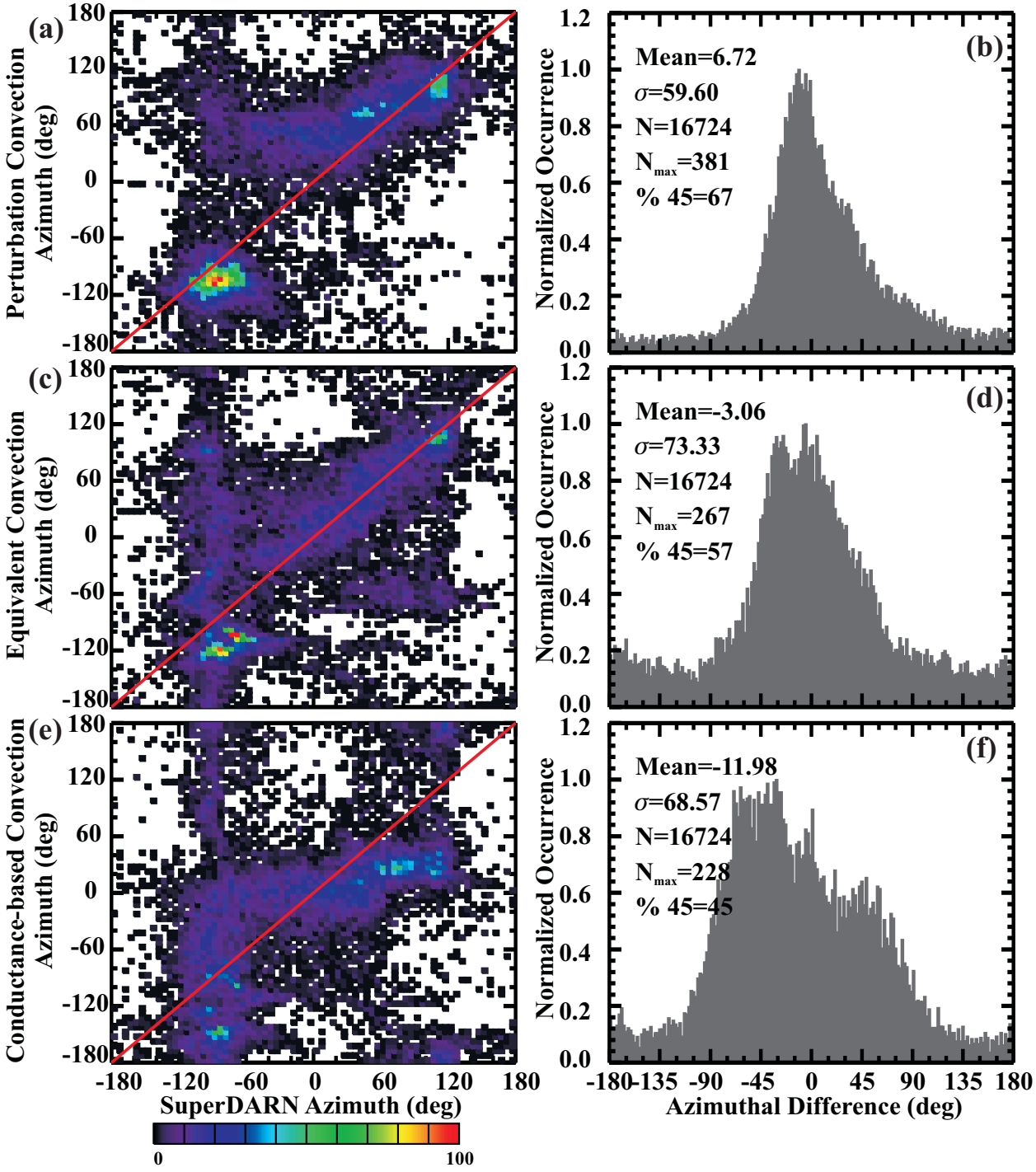

Figure 4.8: Scatter plots of the azimuth of the (a) perturbation convection (c) equivalent convection, and (e) conductance-based convection against the SuperDARN convection for multiple events (see text). Red lines in (a,c,e) indicate the bisector of perfect agreement. Histograms of the azimuthal difference between convection derived using the SuperDARN FIT technique and the (b) perturbation (d) equivalent, and (f) conductance-based convection. The mean, standard deviation, number of points, and maximum of the distribution are indicated, as well as the percent of points with azimuthal differences of less than ±45°.

served in a single bin. The distribution for the perturbation convection peaks at $-11°$. The distribution for the equivalent convection is double peaked with maximum values at $-5°$ and $-25°$. The distribution for the conductance-based convection has a maximum value at $-31°$. For the perturbation distribution, 67% of comparisons had azimuthal differences with magnitudes of $< 45°$ compared to 57% and 45% for the equivalent and conductance-based convection comparisons. The results of the perturbation comparison are better than the 57% found by *Benkevitch* (2006), whereas the results of the equivalent convection are comparable to *Benkevitch* (2006), and the conductance-based convection comparison are somewhat lower.

The conductance-based convection maps are dependent on K_p level to determine which Hardy conductance values are applied to determine the convection. In Figure 4.9 the events considered to generate Figure 4.8 were separated according to the K_p index associated with the interval. Although the days chosen spanned a variety of K_p levels ranging from 0 to 6, the constraints applied to the data set limited those events to K_p=2, 3, and 4. For K_p=2, the distributions for the perturbation convection is single peaked with a maximum at $-1°$. The equivalent convection distribution is wider with a maximum at $-29°$. The histogram for the conductance-based convection is double peaked with maximum values at $-51°$ and $39°$. For the perturbation, equivalent, and conductance-based convection 56%, 53%, and 47% of points lie within $\pm 45°$, respectively. For K_p=3, the perturbation distribution has a peak at $-5°$, and 71% of points have azimuthal differences within $\pm 45°$. The distribution for the equivalent convection is similar with a peak at $-7°$ and 67% of points within $\pm 45°$. The conductance-based distribution is multi-peaked with its highest peak at $-27°$ and 54% of points within $\pm 45°$. For K_p=4, the perturbation and equivalent convection distributions are wider and the conductance-based convection distributions becomes single-peaked compared to the K_p=3 distributions. The percentage of points within $\pm 45°$ rises to 73% for the perturbation distribution, and drops to 51% and 36% for the equivalent and conductance-based distributions.

Both the perturbation and equivalent convection patterns show reasonable agreement with the SuperDARN-inferred convection pattern, but are unable to provide estimates of the magnitude of the convection. To generate conductance-based convection patterns, models of

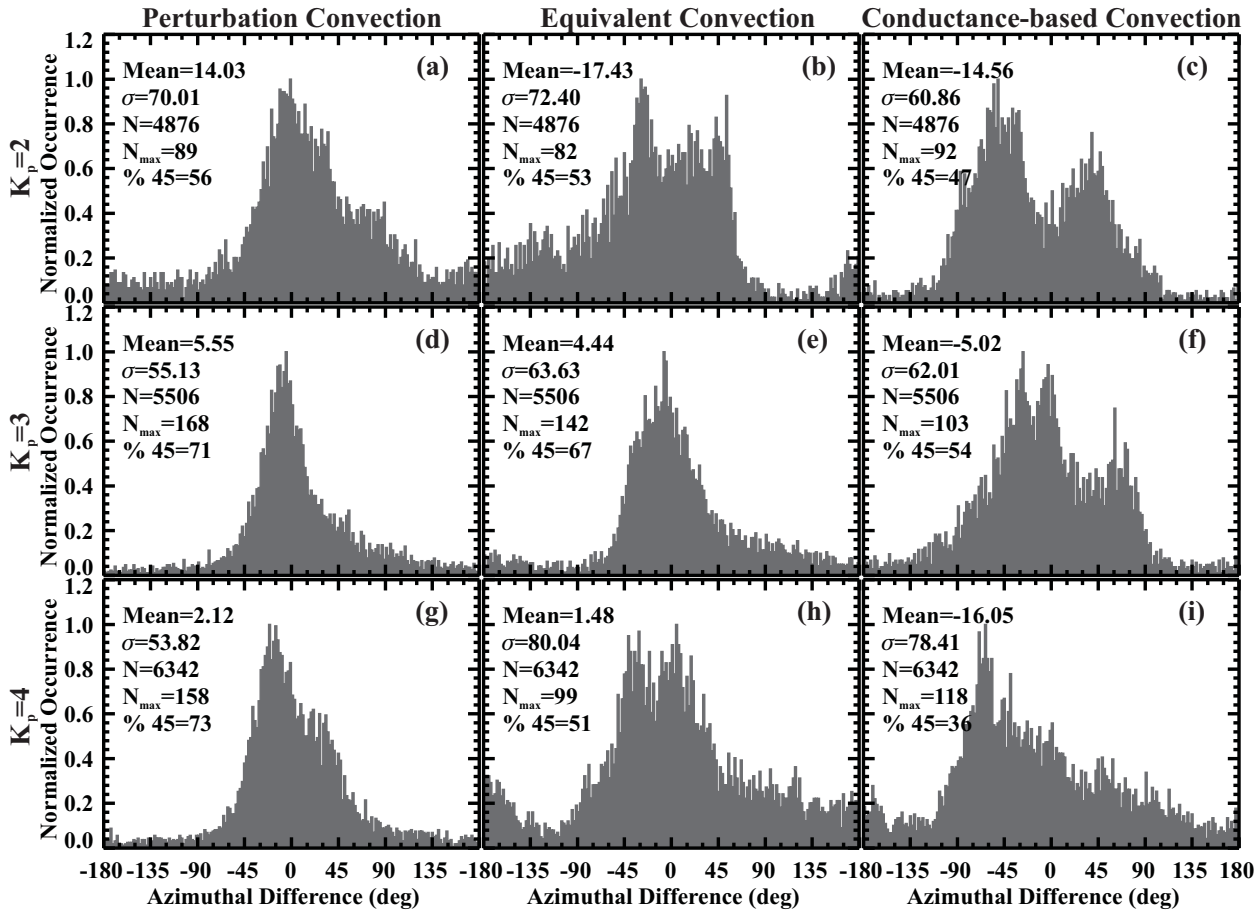

Figure 4.9: The same as the histograms shown in Figure 4.8, but for K_p values of (a,b,c) 2, (d,e,f) 3, and (g,h,i) 4.

the conductance and the KRM equations are applied to determine both the magnitude and direction of the ionospheric plasma flow. However, the distributions for the conductance-based convection pattern (which was based on data from < 100 magnetometers) indicates a lower percentage of points showing reasonable agreement with the SuperDARN-inferred convection pattern (which was derived from > 300 measurements), particularly for larger K_p. These results suggest that although magnetometers can be used to map convection, the low number of stations available means the resultant maps are not well constrained and it is difficult to make comparisons with maps made from a large data set like SuperDARN.

The disadvantage of using magnetometer data to generate maps of the global convection pattern is the large spacing between stations. Magnetometers are not able to achieve the same kind of spatial resolution as the SuperDARN radars. This may be a serious problem during periods of $B_z > 0$ when there are multiple convection cells, the size of which may be

smaller than can be resolved by the magnetometers. For this reason, it will be more useful to use magnetometer data to supplement the SuperDARN data set, rather than to generate maps of the magnetometer-derived convection pattern. Such attempts will be discussed in the following section.

4.4 Technique for combining SuperDARN and magnetometer data sets for mapping the ionospheric convection pattern

Before magnetometer and SuperDARN data sets are merged to generate joint convection maps, it must be established that the SuperDARN and magnetometer instruments characterize the same phenomenon. As was previously shown in Section 4.2.2, the ionospheric current density $\mathbf{J}$ can be broken into curl-free and divergence-free components such that $\mathbf{J} = \mathbf{J}_{cf} + \mathbf{J}_{df}$. It was further shown that the equivalent current system $\mathbf{J}_{eq}$ derived from ground-based magnetometers represents the divergence-free portion of $\mathbf{J}$ such that $\mathbf{J}_{eq} = \mathbf{J}_{df}$, where $\mathbf{J}_{eq}$ is a horizontal sheet current producing the same magnetic field on the ground as $\mathbf{J}$.

In the high-latitude ionosphere, field-aligned currents flow radially into or out of the ionosphere. Electric fields in the plane perpendicular to the magnetic field ($\mathbf{E}_\perp$) associated with the inward or outward flowing FACs are oriented away from or toward the inflow or outflow point, respectively. Positive electric charges drift in the direction of $\mathbf{E}_\perp$, opposite to the drift of electrons, forming the Pedersen current ($\mathbf{J}_p$). Electrons drift in the $\mathbf{E}_\perp \times \mathbf{B}$ direction whereas ions are stationary, forming the Hall current ($\mathbf{J}_h$). In the case of uniform conductance, $\mathbf{E}_\perp$ is purely divergent or convergent so that $\mathbf{J}_p$ is purely curl-free ($\mathbf{J}_p = \mathbf{J}_{cf}$) and $\mathbf{J}_h$ is purely divergence-free ($\mathbf{J}_h = \mathbf{J}_{df}$).

For the case of uniform ionospheric conductance, the equivalent current system constructed from magnetometer data given by $\mathbf{J}_{eq} = \mathbf{J}_{df}$ is therefore due to the Hall current. Since the SuperDARN radars measure the $\mathbf{E}_\perp \times \mathbf{B}$ component of the plasma drift, which is associated with the Hall current, the best agreement between SuperDARN and magnetome-

ter convection is expected on the dayside where the conductance is more uniform due to the dominance of solar radiation.

Describing how the SuperDARN and magnetometer data sets may be merged to create a joint convection map requires a better understanding of how the fitting coefficients are determined for the SuperDARN and magnetometer data sets separately. For this purpose, consider observations of some arbitrary parameter $f(r, \theta, \phi)$ scattered across a spherical cap or radius r which varies in terms of co-latitude (θ) and longitude (ϕ) with respect to the spherical cap coordinate system

$$f(r, \theta, \phi) = \sum_{k=0}^{\infty} \sum_{m=0}^{k} A_{km} c(r, \theta, \phi) + B_{km} d(r, \theta, \phi), \tag{4.56}$$

where k and m are the integer degree-index and order of the function, and A_{km} and B_{km} are constant fitting coefficients which are determined from the data set and $c(r, \theta, \phi)$ and $d(r, \theta, \phi)$ are basis functions.

To model $f(r, \theta, \phi)$ at any coordinate on the sphere, physical measurements (f_i) must be substituted into equation (4.56) to solve for the fitting coefficients. Consider, for example, N observations of some measured quantity f. An equation may be written for each measurement f_i located at coordinate (r_i, θ_i, ϕ_i)

$$f_i(r, \theta, \phi) = \sum_{k=0}^{K_{max}} \sum_{m=0}^{k} A_{km} c_{km}(r_i, \theta_i, \phi_i) + B_{km} d_{km}(r_i, \theta_i, \phi_i), \tag{4.57}$$

where the summation over k has been limited to some maximum degree K_{max}, and there are $(K_{max} + 1)^2$ possible fitting coefficients. Expanding this over all points, an array of N equations may be written as follows

$$\begin{aligned}
f_1 &= A_{00} c_{00_1} + \cdots + A_{K0} c_{K0_1} + A_{11} c_{11_1} + B_{11} d_{11_1} + A_{21} c_{21_1} + B_{21} d_{21_1} + \cdots \\
f_2 &= A_{00} c_{00_2} + \cdots + A_{K0} c_{K0_2} + A_{11} c_{11_2} + B_{11_2} d_{11} + A_{21} c_{21_2} + B_{21} d_{21_2} + \cdots \\
&\cdots\cdots\cdots

be written in matrix form as

$$\begin{pmatrix} f_1 \\ f_2 \\ \vdots \\ f_N \end{pmatrix} = \begin{pmatrix} c_{00_1} & \cdots & c_{K0_1} & c_{11_1} & d_{11_1} & c_{21_1} & d_{21_1} & \cdots \\ c_{00_2} & \cdots & c_{K0_2} & c_{11_2} & d_{11_2} & c_{21_2} & d_{21_2} & \cdots \\ \vdots & \ddots & \vdots & \vdots & \vdots & \vdots & \vdots & \ddots \\ c_{00_N} & \cdots & c_{K0_N} & c_{11_N} & d_{11_N} & c_{21_N} & d_{21_N} & \cdots \end{pmatrix} \cdot \begin{pmatrix} A_{00} \\ \vdots \\ A_{K0} \\ A_{11} \\ B_{11} \\ A_{21} \\ \vdots \end{pmatrix},$$

or in a more compact notation as

$$\overline{\overline{\mathbf{F}}} = \overline{\overline{\mathbf{CD}}} \cdot \overline{\overline{\mathbf{AB}}} \tag{4.58}$$

where $\overline{\overline{\mathbf{F}}}$ represents an $N \times 1$ matrix of the measured quantities, $\overline{\overline{\mathbf{CD}}}$ is an $N \times (K_{max}+1)^2$ matrix representing functions of r, θ, and ϕ, and $\overline{\overline{\mathbf{AB}}}$ is a $(K_{max}+1)^2 \times 1$ matrix of the A_{km} and B_{km} fitting coefficients. For large data sets ($N >> (K_{max}+1)^2$), a method such as singular value decomposition is used to solve the coefficients by minimizing the difference between the measured and modeled parameters at known coordinates.

For deriving the ionospheric convection pattern based on $N = N_{SD}$ SuperDARN gridded l-o-s velocities, equation (4.58) may be written as

$$\overline{\overline{\mathbf{F}}}_{SD} = \overline{\overline{\mathbf{CD}}}_{SD} \cdot \overline{\overline{\mathbf{AB}}}_{SD}, \tag{4.59}$$

where $\overline{\overline{\mathbf{F}}}_{SD} = v_{los}$, and $c(r,\theta,\phi)$ and $d(r,\theta,\phi)$ are given by (see Section 2.3.3 and Section 3.1)

$$c(r,\theta,\phi) = \frac{m\sin(m\phi)}{rB\sin\theta} P^m_{n_k(m)}(\cos\theta)\cos\gamma + \frac{\cos(m\phi)}{rB}\frac{dP^m_{n_k(m)}(\cos\theta)}{d\theta}\sin\gamma \tag{4.60}$$

$$d(r,\theta,\phi) = \frac{-m\cos(m\phi)}{rB\sin\theta} P^m_{n_k(m)}(\cos\theta)\cos\gamma + \frac{\sin(m\phi)}{rB}\frac{dP^m_{n_k(m)}(\cos\theta)}{d\theta}\sin\gamma \tag{4.61}$$

where γ is the azimuth of the l-o-s velocity, and B is the magnitude of the Earth's magnetic field.

The velocity matrix in equation (4.59) does not need to be limited to observations from the SuperDARN instrument. Data from complementary instruments measuring velocity may

be merged with the SuperDARN l-o-s velocities to create a joint data set. For example, in Section 2.2 it was shown that DMSP ion drifts agree with SuperDARN l-o-s velocities, and it was concluded that the data sets may be merged.

For deriving the ionospheric convection pattern based on $N = 3N_{MAG}$ measurements of the three-dimensional magnetic field from ground-based magnetometers, equation (4.58) may be written as

$$\overline{\overline{\mathbf{F}}}_{MAG} = \overline{\overline{\mathbf{CD}}}_{MAG} \cdot \overline{\overline{\mathbf{AB}}}_{MAG}, \tag{4.62}$$

where $\overline{\overline{\mathbf{F}}}_{MAG}$ is given by equation (4.50), and it can be shown that

$$\begin{aligned} c(r,\theta,\phi) &= \Sigma_H \cos(m\phi) \left[\frac{\cos\theta}{r^2 \sin\theta} \frac{dP}{d\theta} + \frac{1}{r^2} \frac{d^2P}{d\theta^2} - \frac{m^2}{r^2 \sin^2\theta} P \right] \\ &\quad + (\nabla\Sigma_{H\theta} + \nabla\Sigma_{P\phi}) \frac{\cos(m\phi)}{r} \frac{dP}{d\theta} - (\nabla\Sigma_{H\phi} - \nabla\Sigma_{P\theta}) \frac{m \sin(m\phi)}{r \sin\theta} P \end{aligned} \tag{4.63}$$

$$\begin{aligned} d(r,\theta,\phi) &= \Sigma_H \sin(m\phi) \left[\frac{\cos\theta}{r^2 \sin\theta} \frac{dP}{d\theta} + \frac{1}{r^2} \frac{d^2P}{d\theta^2} - \frac{m^2}{r^2 \sin^2\theta} P \right] \\ &\quad + (\nabla\Sigma_{H\theta} + \nabla\Sigma_{P\phi}) \frac{\sin(m\phi)}{r} \frac{dP}{d\theta} + (\nabla\Sigma_{H\phi} - \nabla\Sigma_{P\theta}) \frac{m \cos(m\phi)}{r \sin\theta} P, \end{aligned} \tag{4.64}$$

where the notation $P = P^m_{n_k(m)}(\cos\theta)$ has again been used, and $\nabla\Sigma_{P,H\theta}$ and $\nabla\Sigma_{P,H\phi}$ are given by equation (4.52).

In equations (4.59) and (4.62), the fitting coefficients $\overline{\overline{\mathbf{AB}}}_{SD}$ and $\overline{\overline{\mathbf{AB}}}_{MAG}$ are both used to describe the electrostatic potential (see equations (3.1) and (4.51)). Provided the same value of K_{max} is used to describe the $\overline{\overline{\mathbf{AB}}}_{SD}$ and $\overline{\overline{\mathbf{AB}}}_{MAG}$ matrices, then $\overline{\overline{\mathbf{AB}}}_{SD}$=$\overline{\overline{\mathbf{AB}}}_{MAG}$=$\overline{\overline{\mathbf{AB}}}$, and equations (4.59) and (4.62) can be combined to create a joint data set described by the matrix equation

$$\begin{pmatrix} \overline{\overline{\mathbf{F}}}_{SD} \\ \overline{\overline{\mathbf{F}}}_{MAG} \end{pmatrix} = \begin{pmatrix} \overline{\overline{\mathbf{CD}}}_{SD} \\ \overline{\overline{\mathbf{CD}}}_{MAG} \end{pmatrix} \cdot \left(\overline{\overline{\mathbf{AB}}} \right), \qquad \text{or} \tag{4.65}$$

$$\overline{\overline{\mathbf{F}}}_J = \overline{\overline{\mathbf{CD}}}_J \cdot \overline{\overline{\mathbf{AB}}}, \tag{4.66}$$

where $\overline{\overline{\mathbf{F}}}_J$ represents an $(N_{SD} + 3N_{MAG}) \times 1$ matrix of measured SuperDARN and magne-

tometer values, $\overline{\overline{\mathbf{CD}}}_J$ is an $(N_{SD} + 3N_{MAG}) \times (K_{max} + 1)^2$ matrix representing functions of r, θ, and ϕ, and $\overline{\overline{\mathbf{AB}}}$ is a $(K_{max} + 1)^2 \times 1$ matrix of the A_{km} and B_{km} fitting coefficients.

Upon applying these techniques, it was found that the magnetometer data did not contribute to the overall convection map. Closer examination of the data set revealed that $\overline{\overline{\mathbf{F}}}_{MAG}$ and $\overline{\overline{\mathbf{CD}}}_{MAG}$ were several orders of magnitude smaller than $\overline{\overline{\mathbf{F}}}_{SD}$ and $\overline{\overline{\mathbf{CD}}}_{SD}$. Figure 4.10 shows a histogram of the ratio of velocity (described by $\overline{\overline{\mathbf{F}}}_{SD}$) to $(\nabla \times \mathbf{J}_{eq})$ (described by $\overline{\overline{\mathbf{F}}}_{MAG}$) for the events considered in Section 4.3.1. The distribution peaks at 1950 $\frac{(m/s)}{(A/km^2)}$. The reason for the difference can be seen by considering the units of the SuperDARN and magnetometer terms. Velocity and $(\nabla \times \mathbf{J}_{eq})$ are determined in units of (m/s) and (A/km^2), respectively. Based on analysis of units alone, the conversion of (A/km^2) to (m/s) involves multiplication by a conversion factor

$$\alpha = \frac{h}{B\Sigma} \tag{4.67}$$

$$\simeq \frac{10^5 m}{(10\frac{V \cdot s}{km^2}) \cdot (10S)} \tag{4.68}$$

$$\simeq 10^3 \frac{m}{s} \frac{km^2}{A} \tag{4.69}$$

where h is the assumed height of external contributions to $\mathbf{J}_{eq}$, B is the magnitude of the magnetic field near the surface of the Earth, and Σ is the ionospheric conductance. It can be seen that α is a rough approximate of the peak in the ratio shown in Figure 4.10. To balance the joint matrix equation, a weighting factor equal to 1950 $\frac{(m/s)}{(A/km^2)}$ is therefore applied to terms in both $\overline{\overline{\mathbf{F}}}_{MAG}$ and $\overline{\overline{\mathbf{CD}}}_{MAG}$.

The complete algorithm for generating convection maps using the SCHA-2 technique using both SuperDARN and magnetometer measurements will be illustrated by working through an example for a two-minute interval beginning at 14:02 UT on January 20, 2001. The SuperDARN contributions will be considered first. Figure 4.11a shows the location in geocentric coordinates of the 751 SuperDARN points for which gridded l-o-s velocities were available for this event (black circles). The $\overline{\overline{\mathbf{F}}}_{SD}$, $\overline{\overline{\mathbf{CD}}}_{SD}$, and $\overline{\overline{\mathbf{AB}}}$ matrix elements are determined using the methods previously outlined. A spherical cap centered over the pole

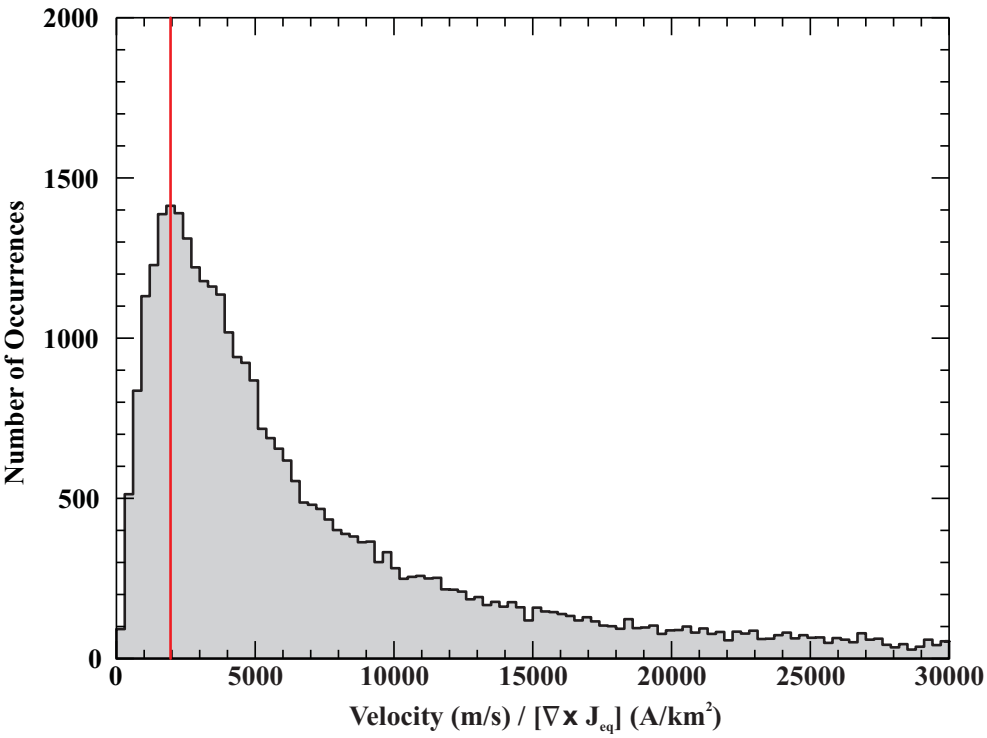

Figure 4.10: Histogram of the ratio of Velocity (m/s) / $[\nabla \times \mathbf{J}_{eq}]$ (A/km^2).

with $\theta_c = 35°$ and $K_{max} = 6$ is used. Figure 4.11b also shows the magnetometer station location of the 83 magnetometers available for the event (grey circles). The perturbation magnetic field is determined in geocentric coordinates for magnetometer stations that are not isolated where a point is defined to be isolated if a circle of radius $\frac{4\theta_c}{K_{max}p}$ contains fewer than p magnetometer stations. There are 26 isolated and 57 non-isolated magnetometer stations. Due to the low density of points the $\overline{\overline{\mathbf{F}}}_{MAG}$, $\overline{\overline{\mathbf{CD}}}_{MAG}$, and $\overline{\overline{\mathbf{AB}}}$ matrix elements are determined using $K_{max} = 3$. Once the SD and MAG matrices have been separately determined, they are merged to create the $\overline{\overline{\mathbf{F}}}_J$, $\overline{\overline{\mathbf{CD}}}_J$, and $\overline{\overline{\mathbf{AB}}}$ matrices. The elements of the coefficients matrix $\overline{\overline{\mathbf{AB}}}$ are found, and the electrostatic potential and convection velocity may be determined within the entire region of constraint.

The light grey shading in Figures 4.11 a and b shows the region of constraint for the SuperDARN-only and merged data sets, respectively. Visual comparison of Figures 4.11 a and b indicates that the region of constraint is only slightly increased with the addition of the magnetometer data set. Contributions from the magnetometer data set therefore serves to shape the convection pattern rather than increase the overall region of constraint.

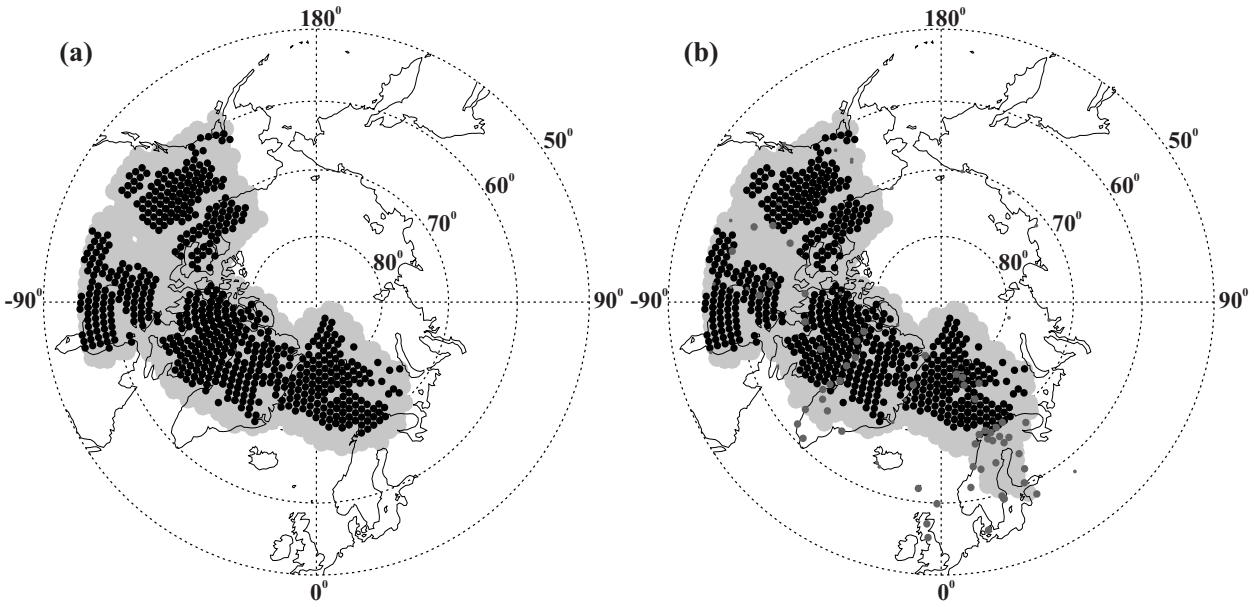

Figure 4.11: (a) Location of SuperDARN grid points and corresponding l-o-s velocities in geocentric coordinates for a two-minute interval beginning at 14:04 UT on January 20, 2001. Light grey shading indicates the region of interest for a spherical cap centered over the pole with $\theta_c = 35°$. (b) Same as (a), with the addition of isolated (small grey dots) and non-isolated (large grey dots) magnetometer stations.

Figure 4.12a shows the convection derived with the SuperDARN velocities shown in Figure 4.11a using the SCHA-2 technique for a spherical cap centered over the pole with $\theta_c = 35°$ and $K_{max} = 6$. Contours for the electrostatic potential and the convection vectors have been converted to the AACGM coordinate system for consistency with previous convection diagrams, and convection vectors have been plotted over the entire region of interest at a grid spacing of 1.5°. During this interval the IMF is in a quasi-steady state with $B_x \simeq -2$ nT, $B_y \simeq 3$ nT, and $B_z \simeq -5$ nT. The convection pattern is two-celled with convection vortices located at $\sim 75°$ MLAT. The dawn and dusk vortices are located at ∼05 and 15 MLT, respectively. There is a strong flow of ∼900 m/s along the dayside portion of the dusk convection cell, and the cross-polar cap flow is anti-sunward at approximately 800 m/s.

Figure 4.12b shows the convection pattern derived using both the SuperDARN gridded l-o-s velocities and the magnetometer perturbation data, the coordinates of which are indicated in Figure 4.11b. The convection pattern also exhibits a two-celled structure. The dawn cell is centered at $\sim 75°$ MLAT and 06 MLT. The duskside cell is centered at 78° and 15 MLT. The convection flow exceeds 1000 m/s along the dayside region of the duskside

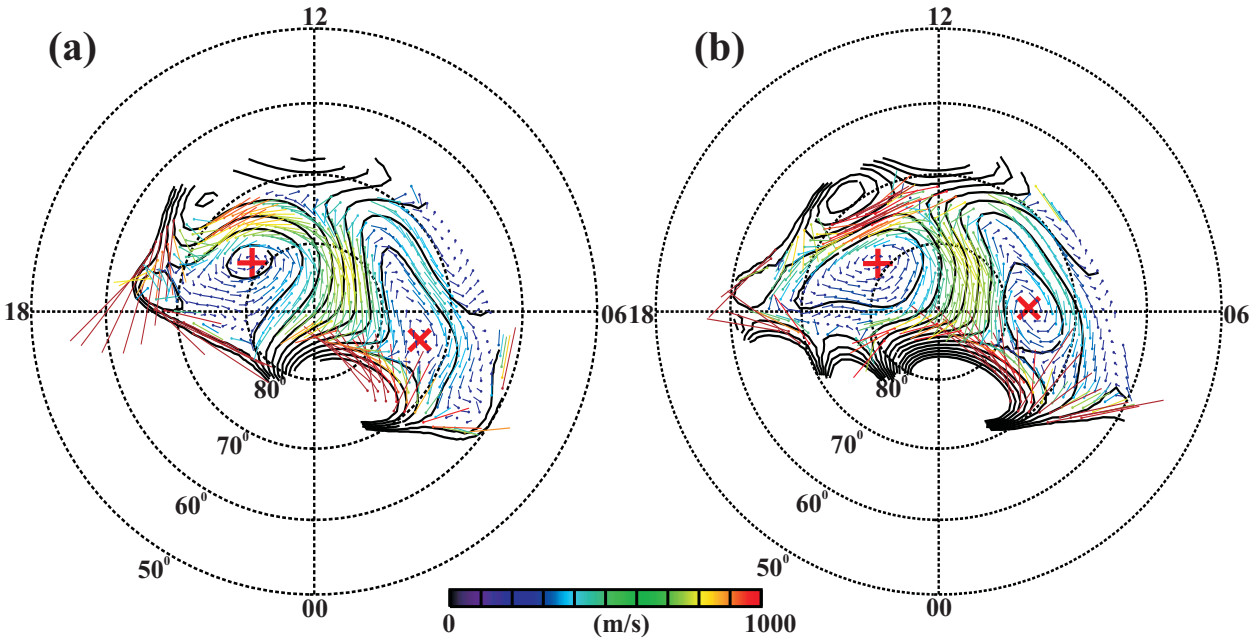

Figure 4.12: Convection patterns derived using (a) SuperDARN l-o-s velocities and (b) SuperDARN l-o-s velocities and magnetometer perturbations using the SCHA-2 technique with $\theta_c = 35°$ and $K_{max} = 6$ for a two-minute interval beginning at 14:04 UT on January 20, 2001. The Φ_E is contoured with a 6 kV spacing and the plus and cross signs indicate the maximum and minimum of the potential.

convection cell, and is anti-sunward over the polar cap with a magnitude of approximately 800 m/s.

There are differences between convection patterns shown in Figures 4.12 a and b. The dawnside convection vortex shifts sunward by one hour of MLT with the addition of the magnetometer data, but the location of the duskside convection cell is not altered. The CPCP changes only slightly from 45.7 kV to 46.1 kV with the addition of the magnetometer data. The magnitude of the convection flow differs by a few 100 m/s in the dayside portion of the dusk convection cell (stronger with the addition of magnetometer data).

To determine how the addition of the magnetometer data set affects convection mapping, it is necessary to compare the plasma flows calculated and measured. The DMSP satellites measure discrete portions of the convection pattern along the satellite path, making it an ideal instrument for comparison. As an example, Figure 4.13 shows the 2D ion drifts measured by DMSP satellite F13 for a 10 minute interval centered over the two-minute interval mapped in Figures 4.12 a and b. The DMSP ion drift indicates anti-sunward polar

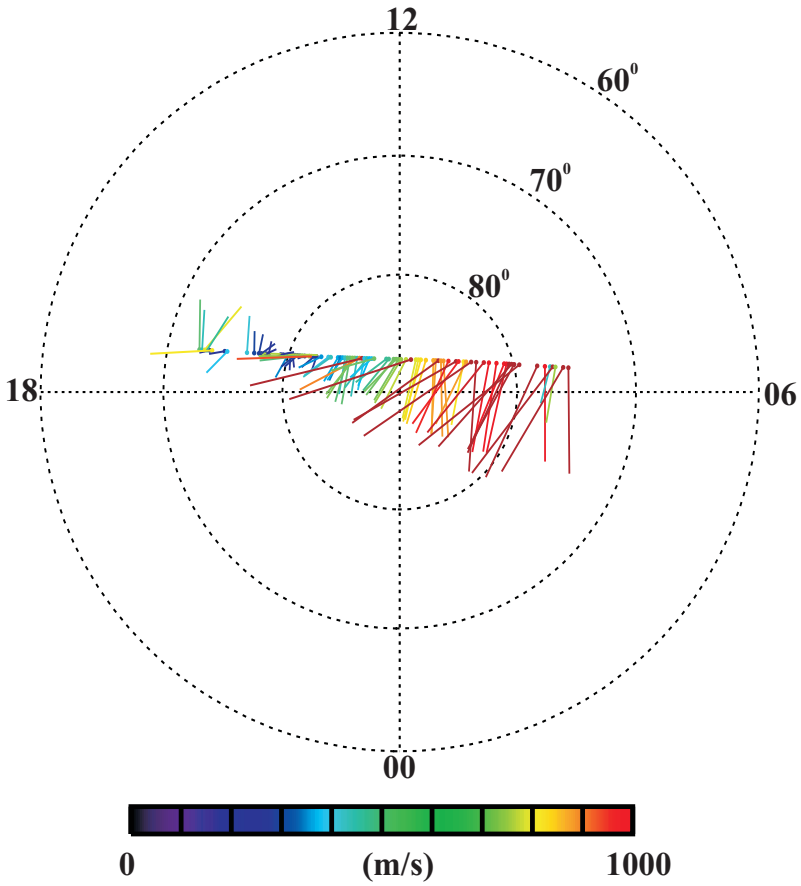

Figure 4.13: Two-dimensional ion drifts observed by DMSP satellite F13 at 13:58-14:08 UT on January 20, 2001.

cap flow reaching upwards of 1000 m/s. Neither the SuperDARN-only or the joint SuperDARN/magnetometer convection plot is able to capture such high flows coincident with the satellite trajectory.

Convection was next determined at the location of the DMSP measurements shown in Figure 4.13 based on the maps shown in Figures 4.12 a and b. Histograms of the difference between the north/south and east/west components of the flow are shown in Figures 4.14 a and b for velocity vectors determined using only the SuperDARN data set and a combination of the SuperDARN and magnetometer data sets, respectively. There is little difference between the mean and standard deviations of the histograms (mean=-78.38 m/s and -85.66 m/s, σ=348.72 m/s and 341.63 m/s). This is likely due to the limited coverage of the magnetometer data set compared to the excellent coverage provided by the SuperDARN radars. It should be noted that if the DMSP data set shown in Figure 4.13 is added to the

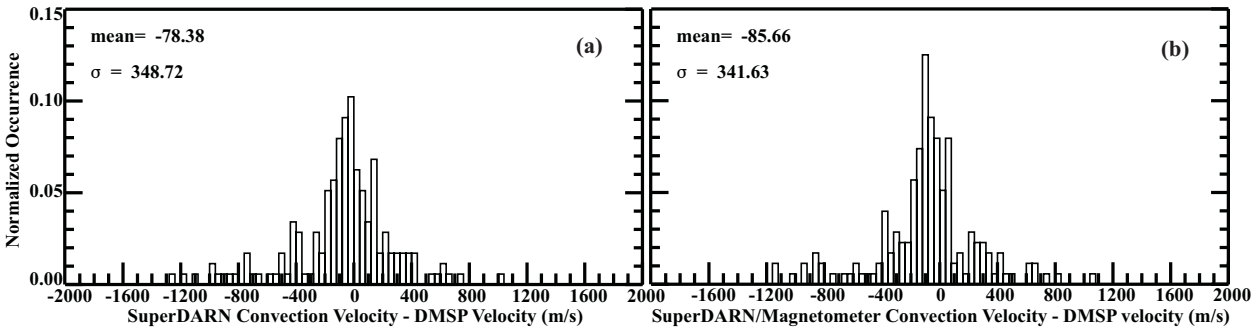

Figure 4.14: Normalized histogram of the difference between the north/south and east/west components of the two-dimension ion drifts observed by DMSP satellite F13 at 13:58-14:08 UT on January 20, 2001 and convection velocity inferred from (a) SuperDARN and (b) SuperDARN and magnetometer data sets.

SuperDARN and magnetometer data set to create a multi-instrument convection map the result (not shown) is a convection map that looks nearly identical to that plotted in Figure 4.12 but with a larger velocities over the polar cap. In addition, the peak of histogram of the difference between velocities shifts closer to zero (mean=-8.79 m/s) and narrows (σ=278.34 m/s).

In the future, a more thorough analysis of the effects of adding magnetometer data to generate convection maps will be performed with data sets having either more sparse SuperDARN coverage or better magnetic coverage (see Section 6.2.3). Convection maps processed in the remainder of this work have been generated from joint velocity and magnetometer data sets where the SuperDARN data coverage is extensive.

This particular technique for combining magnetometer and velocity data sets is relatively new and requires some validation. This will be performed by examining the relative strength of the overall convection pattern as characterized by the size of the cross polar cap velocity and CPCP. The velocity may be directly observed by SuperDARN and the CPCP may be calculated using either the FIT or SCHA-2 techniques. In the next Section, another method of assessing the convection strength will be explored by considering the polar cap north (PCN) magnetic index derived from magnetometer measurements. Magnetometer and SuperDARN results will be compared. Results of this assessment have been published in *Fiori et al.* (2009).

4.5 Assessing convection strength through the PCN magnetic index

The polar cap (PC) index was originally introduced to characterize magnetic activity in the polar cap (*Troshichev and Andrezen*, 1988; *Troshichev et al.*, 2006). Subsequent investigations established strong correlations between the PC index and the CPCP and the average anti-sunward convection velocity across the polar cap (*Troshichev et al.*, 1996; *Troshichev et al.*, 2000; *Lukianova et al.*, 2002; *Ridley and Kihn*, 2004). These results imply the index characterizes ionospheric convection. The PC index was first produced for the southern hemisphere based on data from the Vostok magnetometer (MLAT=$-83.4°$), and later for the northern hemisphere using data from the Thule magnetometer (MLAT=$85.4°$).

During periods of southward oriented IMF, the horizontal current pattern is two-celled with sunward directed current over the polar cap region closed by anti-sunward currents at low latitudes in the dawn and dusk sectors (*Vennerstrøm and Friis-Christensen*, 1991). The near-pole stations used to calculate the PC indices are therefore always located in the region of sunward directed current. The magnetic activity associated with this current system is called the DP2 current system; it stretches in the dawn-dusk direction over the pole (*Troshichev and Andrezen*, 1988). The PC index is meant to gauge the strength of fluctuations in the DP2 activity due to changes in the merging electric field.

4.5.1 Calculation of the PC index

Calculation of the PC index begins by finding the magnetic disturbance δF observed at either Thule or Vostok as (*Troshichev et al.*, 2006)

$$\delta F = \delta D \cdot sin\gamma \pm \delta H \cdot cos\gamma, \tag{4.70}$$

where δD and δH are orthogonal and represent the maximum deviation of the component of the magnetic field in the magnetic east and north directions from a quiet level, which is based on an average of quiet intervals over a thirty day period (*Troshichev et al.*, 2006). Angle γ

represents the station mean declination angle (*Troshichev and Andrezen*, 1988; *Troshichev et al.*, 2006)

$$\gamma = \lambda \pm DE + \phi + UT, \tag{4.71}$$

where λ and DE represents the longitude and mean declination angles of the station of interest. For Vostok, $DE = -117°$, and for Thule, $DE = 285°$ (*Troshichev and Andrezen*, 1988). Declination angle is defined as being positive toward the east and the plus (negative) sign in equations (4.70) and (4.71) is used for the southern (northern) hemisphere. Angle ϕ represents the angle between the typical direction of the sunward current over the polar cap and the noon-midnight meridian for the universal time (UT) and season of observation.

To remove diurnal and seasonal oscillations, δF is described by

$$\delta F = \alpha E_m + \beta, \tag{4.72}$$

where E_m represents the merging electric field given by

$$E_m = V_{SW}(B_z^2 + B_y^2)^{\frac{1}{2}} \sin^2 \frac{\Theta}{2}, \tag{4.73}$$

where V_{SW} is the solar wind velocity, B_y and B_z are the y and z components of the IMF, and Θ represents the angle between the IMF and the Earth's dipole axis (*Troshichev and Andrezen*, 1988; *Troshichev et al.*, 2006).

The parameters ϕ from equation (4.71), and α and β from equation (4.72) are determined based on several years of ACE observations of the solar wind for each season (summer, winter, and equinox) and for each UT hour. These parameters are used to calculate the PC index from

$$PC = \xi \frac{\delta F - \beta}{\alpha}, \tag{4.74}$$

where $\xi = 1m/mV$ scales the PC index so that it is dimensionless (*Troshichev et al.*, 2006). Normalizing the PC index with respect to E_m indicates that, unlike other indices which

measure substorm or auroral activity, the PC index is a measure of the coupling of the solar wind with the magnetosphere.

4.5.2 Previous characterizations of the convection strength using the PC index

The aim of this study is to investigate the relationship between the PCN magnetic index and the average cross-polar cap convection velocity (CPCV) and the CPCP. This is to extend earlier comparisons by *Troshichev et al.* (1996), *Troshichev et al.* (2000), and *Lukianova et al.* (2002), which involved limited $\mathbf{E}\times\mathbf{B}$ drift data sets obtained from the EXOS-D and DMSP satellites. Although these studies demonstrated clear relationships between both the CPCP and CPCV with the PC index, the quantitative conclusions drawn did not agree.

Troshichev et al. (1996) and *Ridley and Kihn* (2004) determine the relationship between the CPCP and the PC index. *Troshichev et al.* (1996) found a linear relationship of

$$CPCP = 8.78 + 19.35 \cdot (PC), \tag{4.75}$$

based on six months of observations spanning summer and winter months and PC indices of -1 to 6. *Ridley and Kihn* (2004) determined the CPCP from magnetometer measurements processed using AMIE, and found linear relationships of

$$CPCP = 38.20 + 16.22 \cdot (PC) \qquad \text{(summer)}, \tag{4.76}$$

$$CPCP = 27.12 + 15.50 \cdot (PC) \qquad \text{(winter)}, \tag{4.77}$$

for summer and winter months for PC indices ranging from -2 to 8. At PC=0, the results of *Ridley and Kihn* (2004) are ∼20-30 kV larger than the results of *Troshichev et al.* (2006). This difference narrows to ∼7-20 kV at PC=3 and ∼5-11 at PC=6.

Troshichev et al. (2000) and *Lukianova et al.* (2002) examine the relationship between the CPCV and the PC index. For the northern hemisphere, *Troshichev et al.* (2000) obtained

the relationship

$$E = \left[9.00 + 4.50 \cdot PCN - 0.17 \cdot PCN^2\right] \times 1.7, \tag{4.78}$$

where E is electric field in mV/m, and the factor of 1.7 scales observations from DMSP satellite (∼840 km) to ionospheric altitudes. *Lukianova et al.* (2002) extended these results by concentrating on periods of high magnetic activity and found

$$E = \left[6.0 + 3.0 \cdot PCN - 0.06 \cdot PCN^2\right] * 1.7, \tag{4.79}$$

where the factor of 1.7 is similarly applied. More recently, *Ridley and Kihn* (2004) compared the PCN index and the polar cap electric field inferred from magnetometer data by applying the AMIE technique. These authors observed a linear relationship between the PCN index and electric field and reported different relationships for the summer and winter months:

$$E = 29.69 + 5.79 \cdot PCN \qquad \text{(winter)} \tag{4.80}$$

$$E = 48.52 + 5.20 \cdot PCN \qquad \text{(summer)} \tag{4.81}$$

These relationships are significantly different from those reported earlier in equations (4.78) and (4.79). Equations (4.80) and (4.81) predict very high (>40-75 mV/m) polar cap electric fields for low magnetic activity (PCN < 4), whereas *Troshichev et al.* (2000) and *Lukianova et al.* (2002) report lower electric fields which saturate at ∼40-50 mV/m for higher magnetic activities. *Ridley and Kihn* (2004) hypothesized that the seasonal effect could be partially due to uncertainty in the ionospheric conductance in their AMIE derivations and suggested making a more thorough comparison of the PCN index with electric field data collected using a 'conductance independent source', such as SuperDARN.

The relationship between the PCN index and ionospheric convection is further investigated through comparison first with the CPCV directly observed by the Rankin Inlet (RKN) SuperDARN radar and then with the CPCP and CPCV determined through mapping observations from all available northern hemisphere SuperDARN radars using the FIT technique. Observations are divided into summer and winter periods to examine the seasonal

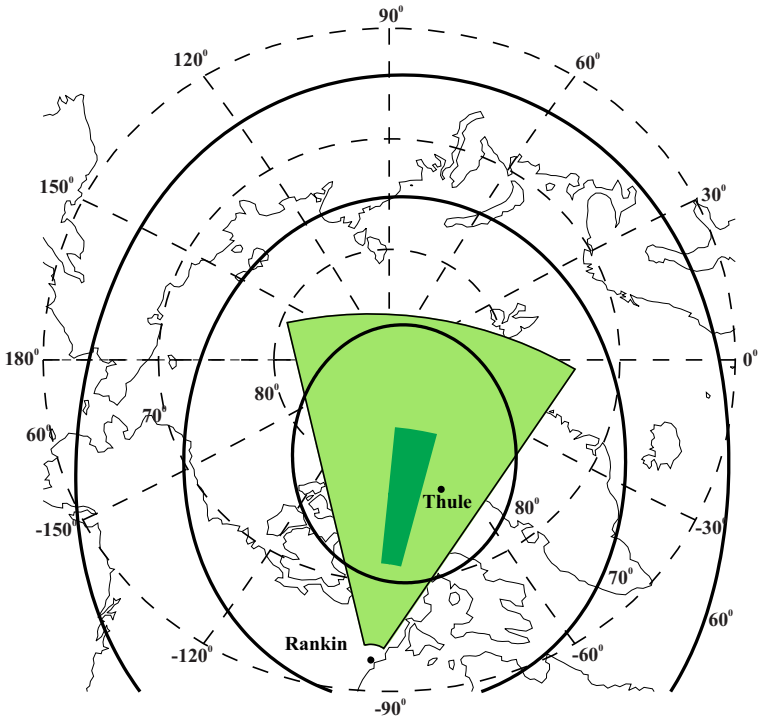

Figure 4.15: Location and field of view of the Rankin Inlet HF radar (light shading) and the Thule magnetometer. The dark shading shows the beam/gates of the radar data used in this study as described in the text. Heavy lines represent AACGM latitudes of 60°, 70°, and 80°, respectively.

dependence of the results.

4.5.3 Geometry of observations and radar data handling

Figure 4.15 shows the field of view of the RKN radar located at a geographic latitude and longitude of 62.82°N and 93.11°W, respectively. The radar central beams are oriented toward the magnetic pole making it convenient to monitor the cross-polar cap convection in the noon and midnight sectors for which the flows are predominantly meridional. Here, focus will be placed on observations in the noon sector where the conductance is more uniform and not strongly affected by injections of energetic particles from the magnetotail.

Also shown in Figure 4.15 is the location of the Thule magnetic observatory (77.47°N, 69.33°W). The observatory zenith corresponds to beam 11 and gate 39 of the Rankin radar. RKN observations over Thule are of primary interest in the first part of this study as it is natural to compare radar and magnetometer data collected from the same location. Unfor-

tunately, insufficient radar data have been accumulated over Thule. For this reason, Rankin data were considered for the central region (beams 6-9, range gates 20-50) indicated by the darker shading in Figure 4.15. The RKN velocity within the region of interest is represented by the median value of the top 50% of all velocity values for each radar scan. Such a limitation helps to eliminate low velocity magnitudes caused by both ground scattered echoes and cross-polar cap flows with significant azimuthal components.

For the first comparison, the CPCV observed by the RKN radar was compared to the PCN index at 1-min increments for summer (June 2007; July 2006, 2007; August 2006, 2007) and winter (January 2007; November 2006, 2007) months. For the purpose of this research, events were limited to observations in the 10 MLT sector when the RKN radar was most closely aligned along the anti-sunward convection flow across the polar cap for a typical two-cell convection pattern. The data set was further filtered to periods of IMF $B_z < -1$ nT and near-zero B_y to ensure that the convection pattern was two-celled with anti-sunward flow approximately aligned along 10 MLT and that the PCN index could be accurately determined.

The second comparison performed was between both the CPCP and CPCV and the PCN index. In this approach, the average convection velocity over the polar cap is estimated by dividing the CPCP by the distance along a spherical shell between the foci of the convection cells. Contributions from the RKN radar help to close the gap in data coverage over the polar cap typical for SuperDARN observations in the past. This approach has its own difficulties as the overall SuperDARN echo occurrence rates are not great for the entire period of the RKN operation, and individual convection maps have limited numbers of points. For example, occasions with > 300 points on a single convection map are quite rare. To select data with the best possible coverage, the SuperDARN data base for 2006-2008 was manually searched to locate periods when at least 200 points were available, the points were reasonably spread over the throat region, the two-cell convection pattern was obviously in effect, and the location of the convection foci seemed to be reliably determined. In total, 1170 two-minute intervals were identified for summer (June-August) and winter (November-January) months during which time vortices in the convection flow were well constrained by SuperDARN observations in the northern hemisphere.

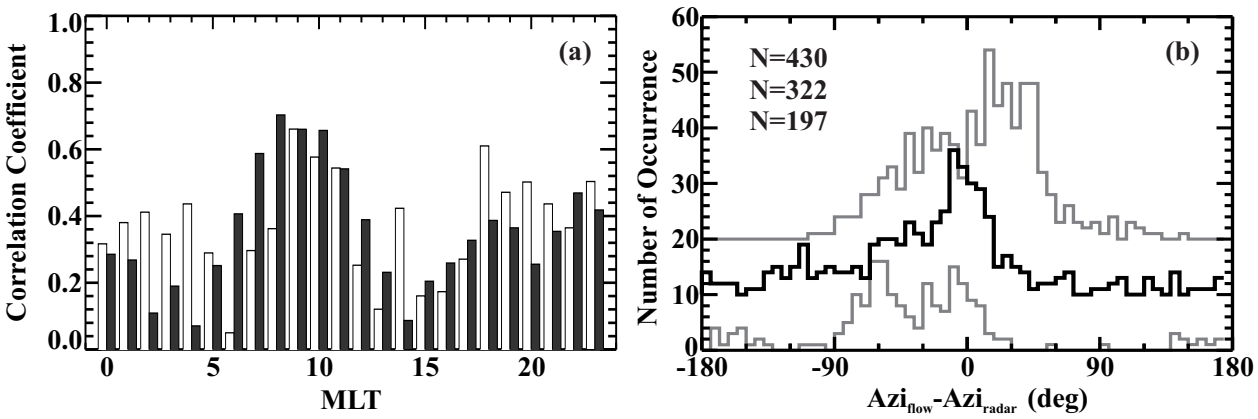

Figure 4.16: (a) Correlation coefficients between the PCN 1 min index and the Rankin median l-o-s velocity for the summer (white) and winter (black) months for measurements in the central beam/gate region of interest. (b) Distribution of the difference in azimuth between the convection vector and the radar line of sight for observations in the 09 (bottom), 10 (middle), and 11 (top) MLT sectors.

4.5.4 Results and Discussion

To justify the selection of the 10 MLT sector for comparison, two analyses have been performed. First, the correlation coefficient between the RKN velocity and the PCN index were determined for each MLT sector for periods of $PCN > 0$. Figure 4.16a shows the correlation coefficients obtained for summer and winter months. For both the summer and winter months, the correlation peaks once a few hours before noon, and again near midnight. This is consistent with the expectation that the radar beams would align with the cross-polar cap flow during these periods. In general, correlation is better for the noon peak than for the midnight peak, and for the winter months than for the summer months.

Figure 4.16a indicates that the best correlation occurs in the hours before noon. To determine the pre-noon MLT sector in which the radar beams best aligns with the cross-polar cap flow, the convection direction was compared with the radar beam azimuth in each region. Convection maps were generated using observations of all SuperDARN radars and applying the FIT-technique for all two-minute intervals for winter months. Then, the azimuth of the convection vector located in the central region of the RKN radar (average of beam 7-8, gate 35) was compared with the azimuth of the radar look direction. To maintain reliability, only convection maps with > 250 points were considered.

Figure 4.16b shows histograms of the difference between the azimuth of the convection flow direction and the radar look-direction when RKN was located in the 09 MLT (bottom), 10 MLT (middle) and 11 MLT (top) sectors. For the 09 and 11 MLT sectors the distribution is double peaked. Peaks are located near 0° and either −60° (09 MLT) or −30° (11 MLT). This suggests that in the 09 and 11 MLT sectors a portion of the flow is observed along the radar l-o-s, but for a significant period of the time, the flow is also observed to be L-shell aligned. The distribution in the 10 MLT sector is single peaked with a maximum near 0°, suggesting the radar l-o-s is aligned with the convection flow and the radar observes the full convection vector. For this reason, further analysis will be performed on RKN data collected in the 10 MLT sector.

Figure 4.17 summarizes the findings of *Fiori et al.* (2009). Scatter plots were generated of the CPCP and CPCV versus PCN index. The grey filled circles indicate scatter for the (a,b) CPCP determined using the FIT technique and for the (c,d) CPCV measured by the RKN radar in the central beam/gate region. Scatter of the CPCV determined by the FIT technique is not shown. To emphasize trends in the relationship between variables, the scatter was binned according to the PCN index in bins of width 0.33. For each bin, the average RKN CPCV, convection CPCV and its standard deviation were determined, provided there were at least 10 measurements within the bin. These average values and their standard deviations are shown in Figure 4.17 using colored filled circles and lines. Figures 4.17 a and b show the average CPCP (blue) for (a) summer and (b) winter months. Figures 4.17 c and d indicate the average CPCV measured by RKN (red) and determined from convection maps (green) for the (c) summer and (d) winter months.

The average velocity derived by the two independent methods (l-o-s observations and convection maps) agree, although not entirely, for PCN values of 1-3. More significant differences in the typical velocities, obtained by the two methods, were found for small PCN values of less than ∼1. To explain these differences, it should be pointed out that although the central beam/gate region is expected to be aligned along the convection throat at 10 MLT, this will not necessarily be true at all times. For small PCN values, the merging electric field is small and the conditions in the ionosphere are weakly disturbed. For such conditions, the convection cells shrink in size, and the RKN radar might monitor flows with

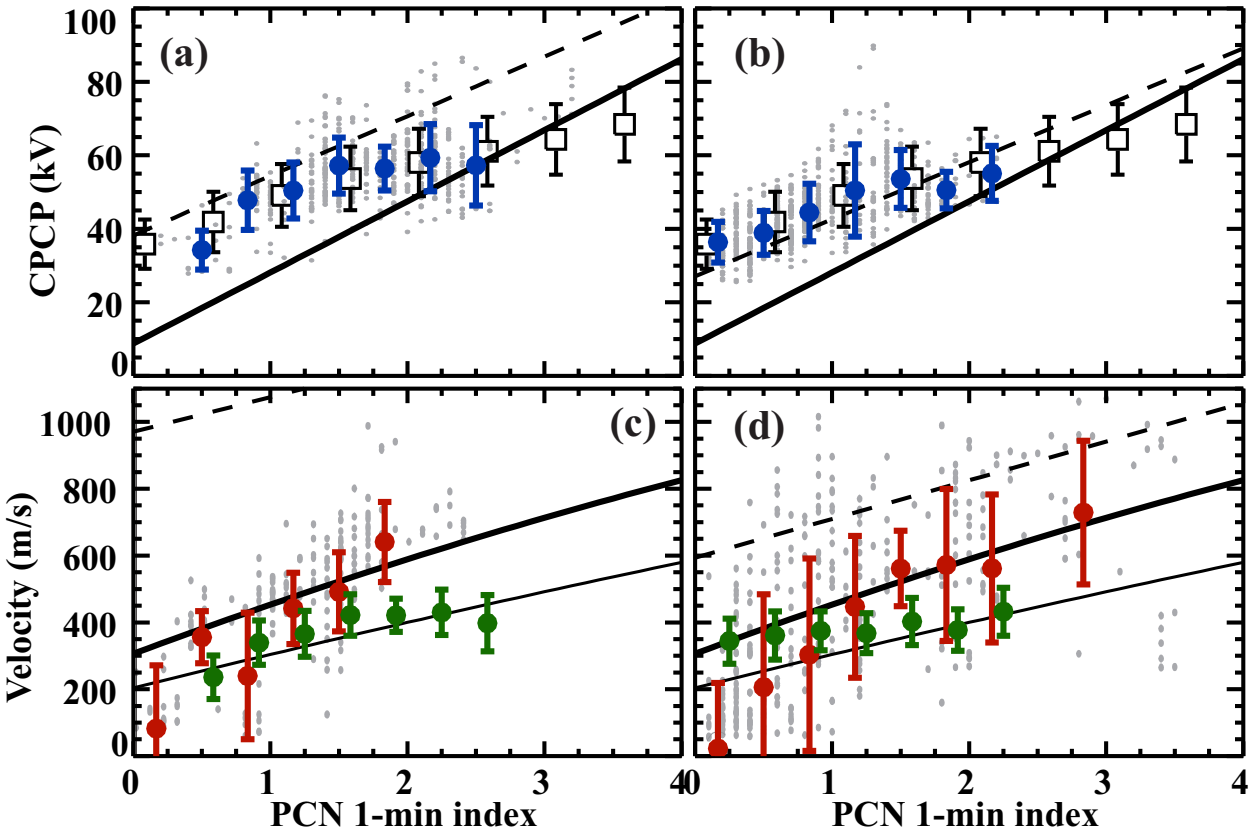

Figure 4.17: Scatter plots of the (a,b) cross-polar cap potential and (c,d) RKN l-o-s velocity at 10 MLT for $B_z < -1$, $|B_y| < 2$, and $|B_z| > |B_y|$ versus the PCN 1 min index for the (a,c) summer and (b,d) winter months. The relationship between the CPCP and PCN 1 min index as derived by *Troshichev et al.* (1996) (black line), *Ridley and Kihn* (2004) (dashed line), *Khachikjan et al.* (2008) (black squares), and as derived from the FIT technique (blue circles) are indicated. The relationship between the flow across the polar cap and PCN 1 minute index in the (c) summer and (d) winter months as derived by *Troshichev et al.* (2000) (heavy black line), *Lukianova et al.* (2002) (thin black line), and *Ridley and Kihn* (2004) (dashed line), and the SuperDARN-inferred velocity measured by the RKN radar (red circles) and determined using the FIT technique (green circles) are indicated.

significant azimuthal components, not stretched along the magnetic meridian. In this case, even sunward polarity of the flow can be detected for IMF $B_z < 0$, especially if the B_y component is large.

To show how previously reported relationships between average CPCV or CPCP and PCN compare to the scatter plots, the appropriate empirical dependencies from *Troshichev et al.* (1996), *Troshichev et al.* (2000), *Lukianova et al.* (2002), and *Ridley and Kihn* (2004) are plotted in Figure 4.17. To present the results of the above papers in terms of the velocity, and not the electric field, a constant magnetic field value of 0.5×10^{-4} T was applied. Note

that *Troshichev et al.* (1996) did not sort data according to season. Also presented in Figures 4.17 a and b is the subset of the *Khachikjan et al.* (2008) measurements of the CPCP (black squares and bars) collected for the period of January 31-February 10, 2002.

For both summer and winter months, observations of the CPCP (blue filled circles) are close to those reported by *Khachikjan et al.* (2008) (black squares), within experimental errors. Predictions of the CPCP by *Ridley and Kihn* (2004) for both seasons also agree with the SuperDARN measurements with larger differences during the summer months for $PCN > 2$. The line by *Troshichev et al.* (1996) lies somewhat below the SuperDARN points for small PCNs but agrees with them at large PCNs.

The empirical lines by *Troshichev et al.* (2000) and *Lukianova et al.* (2002) for the average CPCV lie somewhat away from both SuperDARN sets of points, but within the standard deviations of the SuperDARN data. The empirical lines by *Ridley and Kihn* (2004) are significantly above both the SuperDARN measurements and the trends from *Troshichev et al.* (2000) and *Lukianova et al.* (2002). For both the summer and winter months, SuperDARN shows best agreement with observations of *Lukianova et al.* (2002).

The following circumstances should be considered in attempting to understand disagreements in Figures 4.17 c and d. Observations with drift meters on satellites are limited as high-quality data are not readily available (*Troshichev et al.*, 2000; *Lukianova et al.*, 2002). The statistics referenced here include 200-300 points. For these measurements, only the cross-track component of the ion drift was considered for satellites passing approximately perpendicular to the noon-midnight meridian. SuperDARN observations show that flows can deviate significantly from a well-defined two-cell convection pattern with strictly anti-sunward flow over the polar cap. Estimates of the transpolar flow velocities using the AMIE technique also have limitations, largely based on the reliability of the ionospheric conductance model applied; substorm periods are very difficult to handle properly using this method.

Year-round observations by the RKN radar and the entire SuperDARN network allowed the question of the seasonal variation of the CPCV-PCN relationship to be addressed. It was shown that the slopes of the best linear fit lines for the RKN data in the central beams were about the same for the winter and summer observations. Similar slopes were also inferred

from the CPCV data for the summer observations (see red versus green circles in Figure 4.17c for $PCN > 0.5$). Despite some summer-winter differences, data presented in this study do not show significant seasonal differences. This implies that the AMIE modeling by *Ridley and Kihn* (2004) are noticeably affected by the choice of conductance model.

Data presented in Figures 4.17a-d indicate that as the PCN index increases, both the CPCP-PCN and CPCV-PCN dependencies show signs of saturation for $PCN > 2$. This contrasts with *Troshichev et al.* (1996) and *Ridley and Kihn* (2004) who did not find any saturation effect in the CPCP data obtained from satellite measurements of the ion drift. To better characterize the CPCV-PCN and CPCP-PCN dependencies, observations during periods with $PCN > 4$ are highly desirable. Since the publication of *Fiori et al.* (2009), such a study has been performed.

4.5.5 Examination of the CPCP saturation effect as a function of the PCN magnetic index

The comparison between CPCP and PCN has been expanded to include periods of increased magnetic activity by examining a wide range of events in 2000 and 2001 during the most recent solar maximum. Various parameters, including the UT time of observation, IMF B_z, PCN index, and number of observations were considered to select 4-minute intervals for generating convection maps to ensure a wide range of events were included in the data set. In total, 4605 intervals were selected. The FIT technique was used to map the observed l-o-s velocities with constraints using a statistical model and an HMB, $K_{max} = 6$, and θ_{FIT} between 50° and 66° MLAT, depending on the distribution of measurement coordinates.

Figure 4.18a shows a scatter plot of the CPCP determined using the FIT technique versus the PCN index. Blue circles indicate the mean and standard deviation of points in bins of 0.33 PCN. For $PCN < 3$ there is a linear relationship between the CPCP and the PCN index, which agrees with results reported in the previous sections. However, as the PCN index increases, the rate of increase of the CPCP slows, indicating a saturation of the CPCP at ~ 80 kV. This saturation is possibly due to limitations of the FIT technique. For example, forcing the convection to zero at θ_{FIT} prevents the convection foci from shifting to more

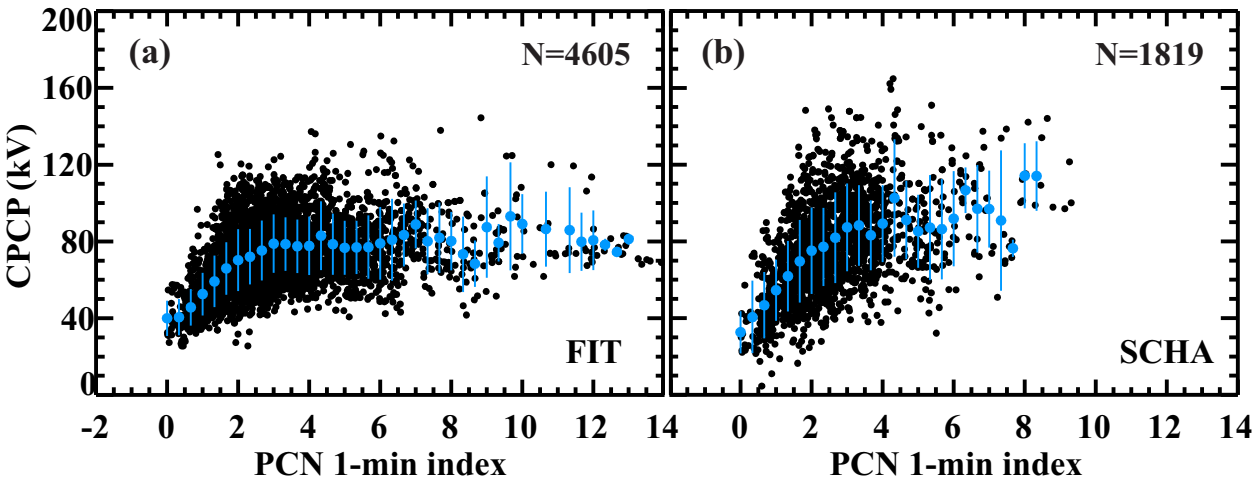

Figure 4.18: CPCP determined using the (a) FIT and (b) SCHA-2 technique versus PCN index for N convection maps. Blue circles and lines indicate the mean and standard deviation of the scatter binned in increments of 0.33 PCN. Events in (b) come from a subset of those used in (a) where the CPCP was well constrained by data.

equatorward locations, thereby limiting the maximum separation between convection cells, and limiting the maximum CPCP that may be obtained. To evaluate if such a constraint is important, the CPCP for the events shown in Figure 4.18a were also determined using the SCHA-2 technique.

Of the 4605 intervals analyzed, 1819 were identified for which the convection vortices were sufficiently constrained by data so that the CPCP could be reliably determined using the SCHA-2 technique. Figure 4.18b shows a scatter plot of the SCHA-derived CPCP versus PCN. For $PCN < 4$, there is a linear relationship between the CPCP and the PCN. For $PCN > 4$, the CPCP determined using the SCHA-2 technique is not limited to 80 kV, but there are not enough data points to observe a clear relationship between the CPCP and PCN.

Figure 4.19a shows scatter plots of the SCHA-2 versus the FIT-derived CPCP. The correlation coefficient ($R = 0.85$) indicates excellent agreement between data sets. There is a tendency for the CPCP to be larger when determined using the SCHA-2 technique compared to the FIT technique, and the slope of the best-fit line to the data set is $m = 1.30$.

Figure 4.19b shows the CPCP-PCN relationships derived using the FIT technique (black), the SCHA-2 technique (grey), and reported by *Troshichev et al.* (1996) (grey) and by *Ridley and Kihn* (2004) for the summer (red) and winter (blue) months. The FIT and

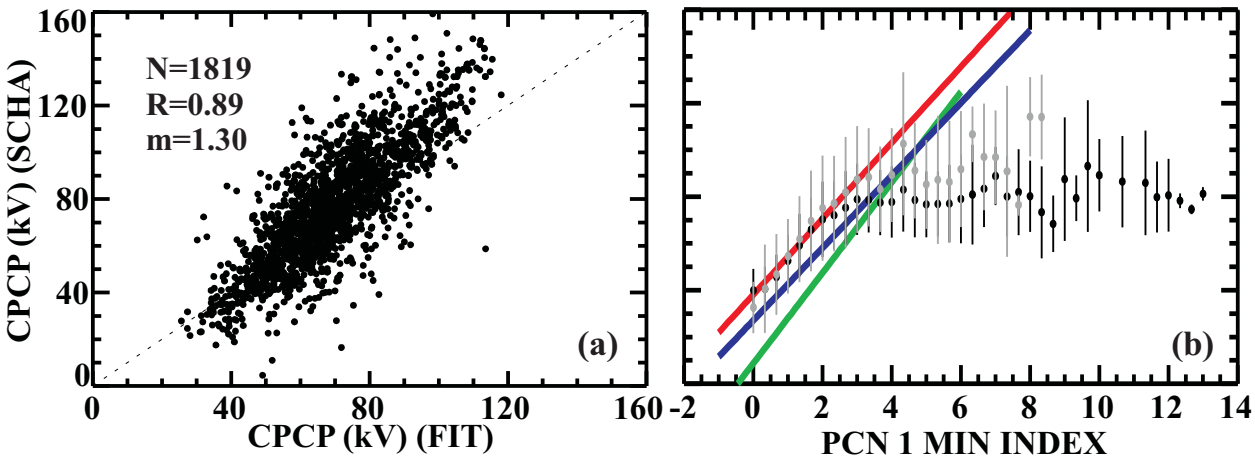

Figure 4.19: (a)CPCP determined using the SCHA-2 technique versus CPCP determined using the FIT technique for a subset of events from Figure 4.18a where the CPCP was well constrained by data. The correlation coefficient (R) and slope of the best-fit line to the data (m) are indicated. (b) Black and grey filled circles and lines indicate the mean and standard deviations of the CPCP calculated using the FIT and SCHA-2 techniques plotted in Figure 4.18 (a) and (b). The green line shows the relationship derived by *Troshichev et al.* (1996). The red and blue lines show the relationships derived by *Ridley and Kihn* (2004) for the summer and winter months, respectively.

SCHA-2 are nearly identical for $PCN < 4$, and there is a linear increase from 40 to 80 kV. As PCN increases above 4, the FIT-derived CPCP saturates at 80 kV. For $4 < PCN < 7$, the SCHA-derived CPCP shows signs of saturation at a slightly higher level of 90-100 kV. For $PCN > 7$, saturation is somewhat less clear due to a reduction in the number of data points and the more erratic shifting of the CPCP to minimum and maximum values of 70 to 110 kV. There is excellent agreement between both the FIT and SCHA-derived CPCP with the results of *Ridley and Kihn* (2004) for the summer months prior to the saturation, as the red line passes through or near the center of all the filled circles. The blue line showing the relationship derived by *Ridley and Kihn* (2004) for the winter months also shows reasonable agreement prior to saturation as it passes within one standard deviation of the mean values derived using the FIT and SCHA-2 techniques. The results of *Troshichev et al.* (1996) show worse agreement. None of the past relationships indicate a saturation of the CPCP for increasing PCN.

As the PCN index increases, the number of SuperDARN echoes is reduced and it is less likely that convection vortices are well constrained so that the CPCP may be accurately

described. In such cases the location of the convection vortices, and the magnitude of the electrostatic potential at the vortices mapped using the FIT technique are largely influenced by the statistical models added to constrain the data. The largest possible value of the CPCP for the statistical model convection maps for a convection zone bounded at $\theta_{FIT} = 60°$ MLAT is 75 kV, which nearly coincides with the saturation point of the FIT derived CPCP. These results suggest that for high PCN when the number of vectors decreases, the ionospheric convection pattern derived with the FIT-technique is highly dependent on, and even limited by, the statistical model used to constrain the fit. For convection mapped using the SCHA-2 technique, the convection is not well constrained due to the reduced number of observations, explaining the loss of data as PCN increases. These results suggest that the addition of a complementary data set would contribute to constraining the convection so that the CPCP may be accurately determined using either the FIT or SCHA-2 techniques, without the influence of a statistical model.

4.5.6 Conclusions of the conductance-based convection assessment

In this section, the PCN index was assessed as a measure of ionospheric convection across the polar cap by comparing it with convection measurements made using the SuperDARN radars. For $PCN < 4$ it was shown that

1. The velocity estimated from the Rankin Inlet Doppler measurements increases with the PCN index. The correlation coefficient between the velocity and PCN index depends on the magnetic local time of measurement, maximizing to ∼0.6-0.7 in the midnight and noon sectors when the radar field-of-view is roughly oriented along the noon-midnight meridian. In the 10 MLT sector the dependence is approximately linear for $PCN < 2$, but the rate of velocity increase slows as the PCN index increases above 2, possibly indicating the onset of saturation.

2. The slope for the linear part of the average velocity-PCN dependence was found to be ∼2 times larger as compared to previous publications by *Troshichev et al.* (2000), *Lukianova et al.* (2002), and *Ridley and Kihn* (2004). However, if the RKN data for $PCNs < 1$ are not considered (observations for low PCNs are expected to occur

during periods of anti-sunward flows with significant azimuthal flow components) than the slopes for the RKN data become comparable to those from previous publications.

3. The cross-polar cap average velocity estimated from the cross-polar cap potential divided by the distance between the two-cell convection foci shows a linear increase with the PCN index for values between 0 and ∼2. The slope of the best fit line agrees with previous publications, particularly for summer months.

4. The observed relationships between the PCN index and the cross-polar cap velocity derived from both line-of-sight observations and from the cross-polar cap potential did not show significant differences between summer and winter months.

5. The cross-polar cap potential determined from 1170 convection maps (involving polar cap Rankin Inlet radar data) also increases with the PCN magnetic index. The dependence can be approximated by a linear function for $PCN < 2$. For larger PCNs, the rate of increase slows down and the onset of the saturation effect is evident.

For an increased data set with $PCN < 10 - 14$ it was shown that

1. The cross-polar cap potential determined from 4605 convection maps for $0 < PCN < 14$ using the SuperDARN FIT-technique indicated a linear relationship for $PCN < 4$. As PCN increased above 4, the CPCP saturated at 80 kV.

2. For 1819 events where the convection was well constrained, it was shown that there is a linear relationship between the FIT and SCHA-derived CPCP with a correlation coefficient of $R = 0.85$ for $0 < PCN < 4$. There is a tendency for the CPCP derived using the SCHA-2 technique to be larger than the CPCP derived using the FIT technique. For $PCN > 4$, there is some evidence of saturation at 90-100 kV, but the effect is not obvious due to a reduction in the number of data points.

These results suggest that the PCN magnetic index is adequate in assessing the strength of the convection strength for $PCN < 4$. At higher PC values, the relationship is less clear.

4.6 Summary and conclusions

In this Chapter, magnetometers were introduced as an instrument for mapping the ionospheric convection pattern. Three different techniques of convection mapping were discussed. The simplest method involves rotating the observed perturbation magnetic field by 90° counter clockwise to determine the direction of the ionospheric convection. Maps generated by this technique were labeled perturbation convection maps. Equivalent convection maps were generated by determining the equivalent current due to external sources using SCHA-2 and rotating the resultant vectors by 180°. The equivalent convection pattern was next combined with the Hardy conductance model to determine the conductance-based convection pattern. All three methods are able to determine the pointing direction of the convection, but only the conductance-based convection maps provide velocity magnitudes in units of (m/s).

Perturbation, equivalent, and conductance-based convection maps were compared to convection maps generated using the SuperDARN FIT technique with contributions from a statistical model and an HMB following the methods of *Benkevitch* (2006). It was found that for magnetic activities of K_p=2-4, the perturbation, equivalent, and conductance-based convection maps all showed reasonable agreement between SuperDARN and magnetometer results. The best agreement was found for the perturbation convection map. Based on these results, it was concluded that the technique used to derive the conductance-based convection maps is not properly constrained by the low number of magnetometer stations available (<100) and that convection can not be reliably mapped based on magnetometer stations alone. It was suggested that magnetometer data could be used for convection mapping through combining the SuperDARN and magnetometer data sets to make a joint convection map.

A technique for merging velocity and magnetometer data sets was presented. The addition of magnetometer data did not cause dramatic changes to the overall convection pattern. Instead, adjustments were made to the convection pattern, which was reflected in the location of the vortices of the convection cells, and the magnitude of both the flow speed

and the CPCP. These changes, although small, indicate that the addition of magnetometer data to the SuperDARN data set adds constraints to the resultant convection map.

The PCN magnetic index was examined for assessing the strength of the convection pattern through a comparison to the CPCP and CPCV determined from SuperDARN measurements. It was determined that the PCN magnetic index is able to predict the strength of the convection for PCN<3. However, as the PCN index increases above 3, saturation of the CPCP determined by SuperDARN makes the relationship less clear. As PCN increases, the SuperDARN data set is reduced and the location and strength of the maximum and minimum potential is not well constrained. In such a case, applying a statistical model to constrain the map will potentially limit the value of the CPCP determined.

Constraining the convection with measurements from a complementary data set provides a better description of the convection over regions containing data, but does not necessarily allow the convection pattern to be resolved over the entire high-latitude region. Generating joint convection maps is, however, useful in filling out convection maps where there are gaps in the SuperDARN data, or where it is necessary to define parameters such as the CPCP, which is dependent on accurate knowledge of the location of the convection vortices. Such applications will be implemented in the next Chapter to study the convection response to a southward turning of the IMF.

Chapter 5

Response of ionospheric convection inferred from magnetometer and radar data to sharp southward IMF turnings

In Chapter 1 it was shown that ionospheric plasma circulation is driven by electric fields established through the interaction of the IMF with the Earth's magnetic field. Understanding the structure of the convection pattern as a function of the IMF therefore provides important information on solar wind-magnetosphere-ionosphere coupling.

When the IMF is in a quasi-steady state and southward, the ionospheric plasma flow follows a well-known two-cell pattern. This pattern is driven by reconnection processes at the front-side magnetosphere and in the magnetotail. When the IMF is northward, the convection pattern is more complicated; there are often multiple convection cells driven by interchange reconnection processes (see Section 1.1). Although steady state convection patterns are well described, the evolution of the pattern between states is not well understood. As the IMF changes, it is likely that various driving sources superimpose to produce the resultant convection pattern. Whether or not this expectation is correct needs to be verified. In this respect, cases where the IMF quickly changes its orientation from northward to southward are of particular interest.

This Chapter investigates the reconfiguration of the convection pattern following a sharp southward turning of the IMF from stable northward to stable southward B_z. Investigations in the past have been made using either measurements of the geomagnetic field (ground-based magnetometers) or the plasma drift (ground-based radars or satellites). In this study, both magnetic field (ground-based magnetometers) and ionospheric drift (SuperDARN radars) measurements will be combined and examined.

5.1 Review of previous work

Identifying the ionospheric effects due to an IMF transition is a complex problem. To confidently state whether or not a reaction observed in the ionosphere is an effect of the IMF transition one must determine

1. The expected signatures of an IMF transition
2. The expected spatial scale of the ionospheric response and adequacy of observational means to detect the signatures
3. Estimates of the disturbance propagation time from satellite measurements of the solar wind taken between the Sun and the Earth

It is expected that the arrival of the transition would be followed (within tens of minutes) by an overall intensification of the two-cell convection pattern and a flow reversal over the dayside polar cap with sunward directed flow changing to anti-sunward directed flow. The expected effects of a southward IMF transition therefore depend on the coordinates (MLAT and MLT) of observations with respect to the ionospheric convection pattern, and the instrument used to make the measurements. Stations for current magnetometer networks are concentrated at auroral oval latitudes, and magnetometers are therefore expected to detect enhanced magnetic field perturbations in response to the transition. The SuperDARN radars should see changes in the ionospheric convection pattern at all MLATs and in all MLT sectors. More drastic changes should be observed at high latitudes where the convection is expected to reverse from sunward to anti-sunward directed flow.

Changing the intensity of the ionospheric convection driver is not instantaneous. In the ionosphere, ion motion is dependent on collisions with neutral particles that are not sensitive to the external electric and magnetic fields (*Kelley*, 1989). Following an IMF transition, inertial forces, caused by collisions between ions and neutral particles, drive convection according to the pre-existing pattern of plasma flow, leading to a delay in the formation of a new pattern. *Ruohoniemi and Greenwald* (1998) and *Hairston and Heelis* (1995) refer to this phenomenon as the flywheel effect. Even if the delay time for propagation of the transition

from a satellite where it is observed to the ionosphere can be accurately determined, which is a formidable task by itself, inertial effects (such as the flywheel effect) might cause a delay in the detection of the response. The relative strength of the typical two-celled $B_z < 0$ convection pattern compared to the weaker multi-celled $B_z > 0$ convection pattern would suggest a longer delay in the convection reconfiguration associated with a northward transition compared to a southward transition (*Ruohoniemi and Greenwald*, 1998).

Thus far, publications on the restructuring of the convection pattern in response to a sudden transition in the IMF B_z component are somewhat contradictory. Differences center around two major focuses of investigation: (1) identifying whether the reconfiguration process initiates either locally on the dayside or globally, and (2) describing the duration of the restructuring process.

With respect to the first focus of investigation, two scenarios have been identified to describe the response of the ionospheric convection pattern to a sudden southward turning of the IMF. In the first scenario, the ionospheric response begins at the dayside cusp region and propagates toward the nightside (*Lockwood et al.*, 1986; *Cowley and Lockwood*, 1992; *Saunders et al.*, 1992). Under the second scenario, the entire high-latitude ionosphere responds simultaneously to the IMF transition in all MLT sectors (*Ridley et al.*, 1998; *Ruohoniemi and Greenwald*, 1998; *Shepherd et al.*, 1999; *Huang et al.*, 2000; *Nishitani et al.*, 2002; *Lu et al.*, 2002).

5.1.1 Scenario 1: Dayside-to-nightside progression of the response

Lockwood et al. (1986) made observations of the plasma velocity at two separate locations near 14 MLT using the EISCAT radar during a single IMF transition event. At both locations they observed enhancements in the velocity magnitude approximately 11 minutes after a southward IMF turning. The enhancement onset was observed at slightly different times for each of the two locations, suggesting an eastward propagation of ~ 1 km/s moving away from the noon sector. *Saunders et al.* (1992) made similar conclusions by correlating oscillations in the IMF B_z with the Y-component of the magnetic field observed at four magnetometer

stations. During a one hour period, seven IMF transitions were observed, with the magnetic field fluctuating between ±7 nT. Oscillations with similar time-scales were observed in the magnetometer data. The magnetometer response was observed to have a 5 minute delay for stations in the 08-12 MLT sector and a 10-15 minute delay in the 06-08 and 12-14 MLT sectors. The offset in the onset time observed at each station suggested motion away from 10 MLT at ∼5 km/s which then slowed to ∼2 km/s. *Cowley and Lockwood* (1992) observed an expansion of flow away from noon at ∼5 km/s, and a 15 minute delay in the establishment of a new convection pattern.

Lockwood et al. (1986) and *Cowley and Lockwood* (1992) (and references therein) observed that during a period of prolonged northward IMF the plasma flow was slower and the convection pattern was contracted compared to cases of northward IMF. The arrival of southward oriented magnetic field lines stimulated dayside reconnection causing magnetic flux tubes to move equatorward, causing the rapid expansion of the open/closed field line boundary to lower latitudes. The newly opened field lines are dragged anti-sunward, explaining the anti-sunward progression of the convection response.

Using SuperDARN, *McWilliams et al.* (2001a) and *McWilliams et al.* (2001b) show that regardless of the orientation of the convection pattern, the initial convection response to a southward IMF turning following a prolonged period of northward IMF occurs close to noon. Following the southward turning, a patch of high-power radar backscatter was observed to propagate from noon to 18 MLT over a period of 30 minutes, corresponding to an average speed of 0.87 km/s.

5.1.2 Scenario 2: Simultaneous response across all MLT sectors

Contrary to Scenario 1, descriptions of Scenario 2 have been made either on plasma drift measurements made by SuperDARN or through convection maps generated using both the FIT and AMIE convection mapping techniques. Perturbations of the magnetic field observed by ground-based magnetometers have also been used to identify the ionospheric signature of a southward turning in the IMF. *Huang et al.* (2000) studied magnetic traces for magne-

tometers over a time interval containing several northward and southward transitions and observed that the deviation in the magnetic field increased for southward turnings, and decreased for northward turnings. *Huang et al.* (2000) reported that the primary change of the convection pattern for different orientations of the IMF B_z was the location of the convection foci and the magnitude of the overall convection flow. Flows were enhanced for southward IMF and weaker for northward IMF. For a single southward turning, *Nishitani et al.* (2002) determined that the onset observed by cusp and several polar cap magnetometers was simultaneous, indicating an immediate response of the transition wavefront over the polar cap. *Lu et al.* (2002) observed a similar simultaneous response based on measurements from magnetometer chains located at 00, 05, and 20 MLT. They also reported that the time to reach a maximum perturbation was dependent on latitude, being faster at higher latitudes than at lower latitudes.

Measurements of the SuperDARN l-o-s velocity also suggest a global and simultaneous ionospheric response to a southward IMF transition. *Ruohoniemi and Greenwald* (1998) examined the l-o-s velocity measured by four northern hemisphere radars at beam/gate cells separated in latitude near 11, 12, 19, and 21 MLT. Near noon, the IMF transition was observed as a flow reversal from sunward to anti-sunward flow over a period of two minutes. Away from noon, the transition onset was observed as a rapid enhancement in the magnitude of the l-o-s velocity. The transition onset was observed simultaneously (within 2 minutes) at all locations. *Shepherd et al.* (1999) showed a similar simultaneous response (within 30 seconds, based on the scan times of individual radars) based on the l-o-s velocity for beam/gate cells spread over 7 hours of MLT. *Nishitani et al.* (2002) considered range-time-intensity (RTI) plots for the Saskatoon and Stokkseyri radars in the northern hemisphere and the Halley and Syowa South radars in the southern hemisphere for a single southward turning. The ionospheric response to the IMF transition was identified as a change in the polarity or magnitude of the l-o-s velocity, or in the latitudinal location of the ionospheric echoes. Based on these parameters, the transition onset was simultaneously observed by all four radars. *Lu et al.* (2002) considered the RTI plot of a single SuperDARN radar and observed that the time of the transition onset, as indicated by a change in the velocity polarity, was consistent with the onset observed at several magnetometer stations. In addition, they observed that

the rate at which the velocity increased in magnitude (following the southward turning) varied in latitude, being faster at higher latitudes than at lower latitudes.

The SuperDARN-inferred convection maps also show an immediate and global convection response to a southward transition in the IMF. *Ruohoniemi and Greenwald* (1998) generated convection maps for a single southward turning event using the FIT-technique. To avoid biasing of the results, they used a fixed statistical model indicating a weak two-cell pattern throughout the duration of the transition. They observed a flow change from sunward to anti-sunward directed flow near noon and the emergence of a single duskside convection cell (a gap in observations made identification of a dawnside convection cell unreliable), consistent with a transition from a typical $B_z > 0$ to $B_z < 0$ convection pattern. *Shepherd et al.* (1999) generated convection maps for another southward turning event, concentrating on the dayside ionosphere where there were enough observations to reasonably constrain a plot using the standard FIT technique. After the transition they observed an enhancement in the overall velocity magnitude at all MLTs where ionospheric scatter was detected.

Ridley et al. (1998) studied the effects of IMF transitions on ionospheric plasma flow by examining convection patterns generated using the AMIE technique based on magnetometer data for transitions in both the IMF B_y and B_z. For all transition events, they observed an instantaneous reconfiguration of the ionospheric convection pattern at the time of the transition onset across the entire high-latitude region, rather than a gradual change spreading out from the cusp, as described in Scenario 1. *Ridley et al.* (1998) explained that the entire ionosphere reacts within a matter of seconds to the IMF electric field mapped down to the cusp. *Lu et al.* (2002) agrees with these results for a separate event analyzed using the AMIE method, observing no propagation in the location of the convection foci and no evolution of the convection pattern following the immediate reconfiguration after the transition.

Yu and Ridley (2009) examined the ionospheric response to the IMF by considering both the magnetic perturbation observed on the ground and the high-latitude convection pattern simulated using the Block Adaptive-Tree Solar-wind Roe-Type Upwind Scheme (BATS-R-US) magnetohydrodynamic (MHD) code to simulate a southward turning. They observed a change of polar cap convection from sunward to anti-sunward simultaneously (within 2 minutes) in the noon and midnight sectors. There was no propagation of the convection foci

associated with the convection reconfiguration. For magnetic perturbations at locations distributed in both MLT and MLAT, there was an immediate enhancement of the H component of the magnetic field corresponding to the arrival of the transition at the ionosphere. Maximum perturbations were reached first at higher latitudes than lower latitudes and at local noon than on the nightside. Their results show a fast onset followed by a slower evolution to the final convection state.

Ridley et al. (1998) suggest that a simultaneous (within 2 minutes) global response indicates that the electric field driven by the IMF is mapped down to the ionosphere by a magnetosonic wave traveling at the Alfvén speed. *Shepherd et al.* (1999) suggest the amount of field line draping may be responsible for the differences in the convection response in Scenario 1 and 2. Increased field line draping would cause reconnection to occur over a larger region causing the reconfiguration of the convection pattern to follow Scenario 2 rather than Scenario 1.

5.1.3 Duration of the reconfiguration process

Published results on the second focus of investigation into the restructuring process, which deals with the duration of the reconfiguration, are more consistent for both magnetometer and radar results. To accurately describe the reconfiguration of the ionospheric convection pattern, it is necessary to know when the transition wavefront arrives at the ionosphere.

It is difficult to determine exactly when the effect of the IMF transition observed by satellites will be detected in the Earth's ionosphere. Established methods may be used to determine propagation time for the IMF perturbation wavefront to travel from the satellite to the magnetopause (for example, *Weimer et al.*, 2003; *Weimer*, 2004), but propagation to the ionosphere is less clear. *Lu et al.* (2002) observed an ionospheric onset 7 minutes after the transition wavefront was calculated to reach the magnetopause which agrees with the 5-9 minute delay (with an error of ± 3 minutes) observed by *Huang et al.* (2000). Based on simulations, *Yu and Ridley* (2009) predicted a $\sim 2.3 - 4$ minute delay.

Some research indicates there is a delay from the time the transition wavefront reaches the ionosphere to the time a response is observed in the convection pattern. *Ruohoniemi and Greenwald* (1998) observed a 12-14 minute delay from the time a southward turning

was expected in the ionosphere and the time of the response in the convection pattern. *McWilliams et al.* (2001a) and *McWilliams et al.* (2001b) observed a 15-30 minute delay. *Hairston and Heelis* (1995) attempt to determine the response time based on observations from consecutive passes of the DMSP satellites. They observed a delay between the time it took the transition to first reach and then be observed in the ionosphere. The delay was 17-25 minutes for southward turnings and 28-44 minutes for northward turnings. Both *Ruohoniemi and Greenwald* (1998) and *Hairston and Heelis* (1995) attribute a delay in the convection reconfiguration to the flywheel effect.

Huang et al. (2000) reported that it took 10-20 minutes after the initial convection response for the convection pattern to fully reconfigure to a steady state pattern. *Ridley et al.* (1998) observed that, on average, the plasma flow took 12-13 minutes to completely reconfigure to a new steady state. *Nishitani et al.* (2002) observed that the afternoon convection cell formed immediately after the arrival of the IMF transition, but that the initial reconfiguration was followed by a 25 minute period over which time the convection pattern intensified to a final steady state.

Based on this summary of the previously observed response of the ionospheric convection pattern to a quick southward turning of the IMF B_z, it is possible that inconsistencies arise from considering magnetometer and SuperDARN data separately. In this Chapter, we consider simultaneous radar and magnetometer observations and map the convection using both the SuperDARN and ground-based magnetometer data. Our goal is to attain a more comprehensive picture of the phenomenon. Two events will be examined in detail.

5.2 Investigation of two B_z transition events

A southward transition event was defined by a sudden (<5 min) turning of the IMF from at least +5 to -5 nT immediately preceded and followed by a period of relatively stable IMF B_z. Events were chosen provided data were available for the ACE satellite, magnetometers, and SuperDARN, and > 500 SuperDARN measurements were available in the majority of

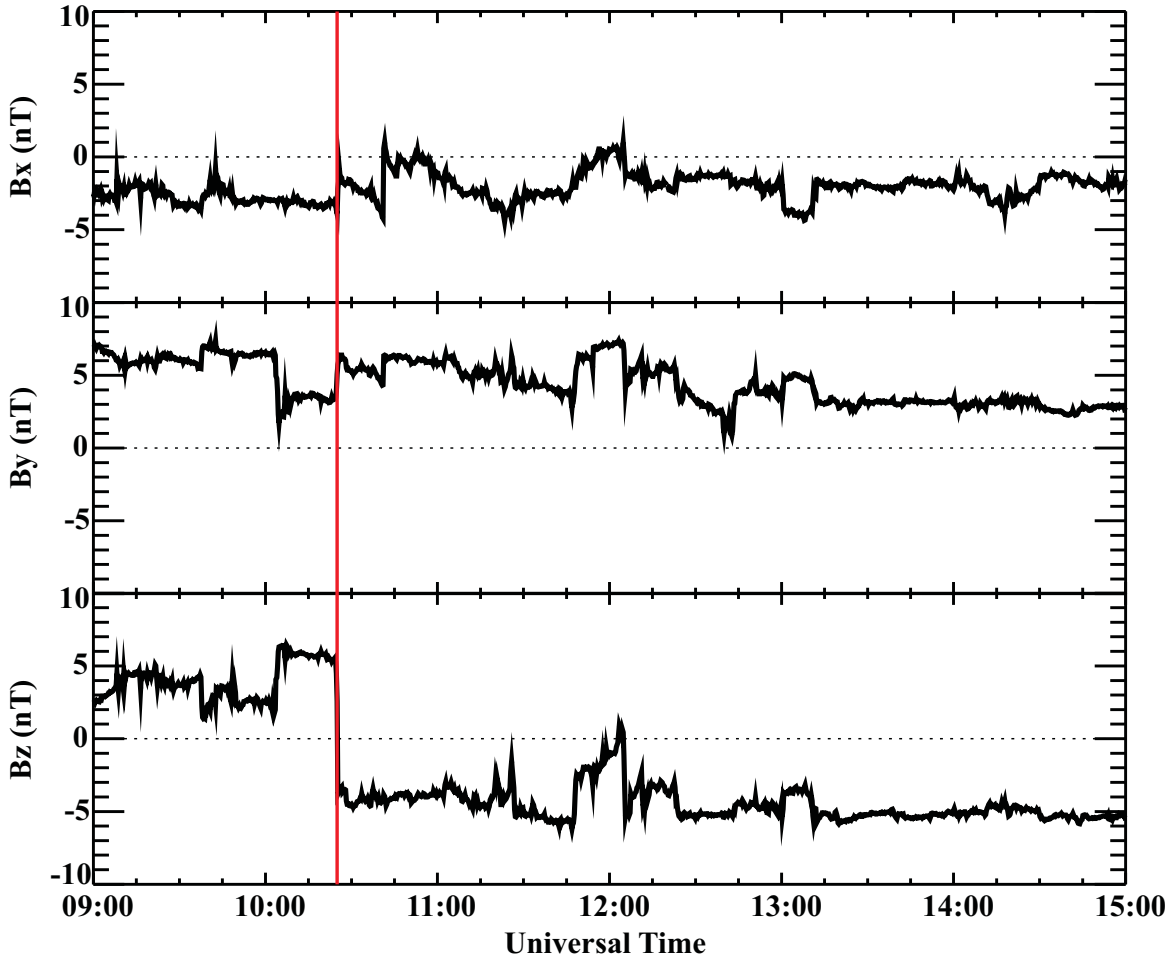

Figure 5.1: IMF B_x, B_y, and B_z on January 20, 2001. A sharp southward turning in the IMF is indicated by a vertical red line.

2-minute intervals within a 6 hour window surrounding the southward turning. The event was required to occur in the late afternoon to ensure the radar data satisfactorily constrained the convection vortices on the dayside. Based on these criteria, two events were selected for analysis; January 20, 2001 and November 02, 2001.

5.2.1 January 20, 2001

Figure 5.1 shows the IMF B_x, B_y, and B_z measured by the ACE satellite on January 20, 2001. The vertical red line at 10:25 UT indicates a sharp southward transition in the IMF B_z, accompanied by comparatively small changes in the B_x and B_y components. Using the Weimer technique (*Weimer et al.*, 2003; *Weimer*, 2004), the delay time for propagation of the IMF from the location of the ACE satellite to the magnetopause was calculated to be 88

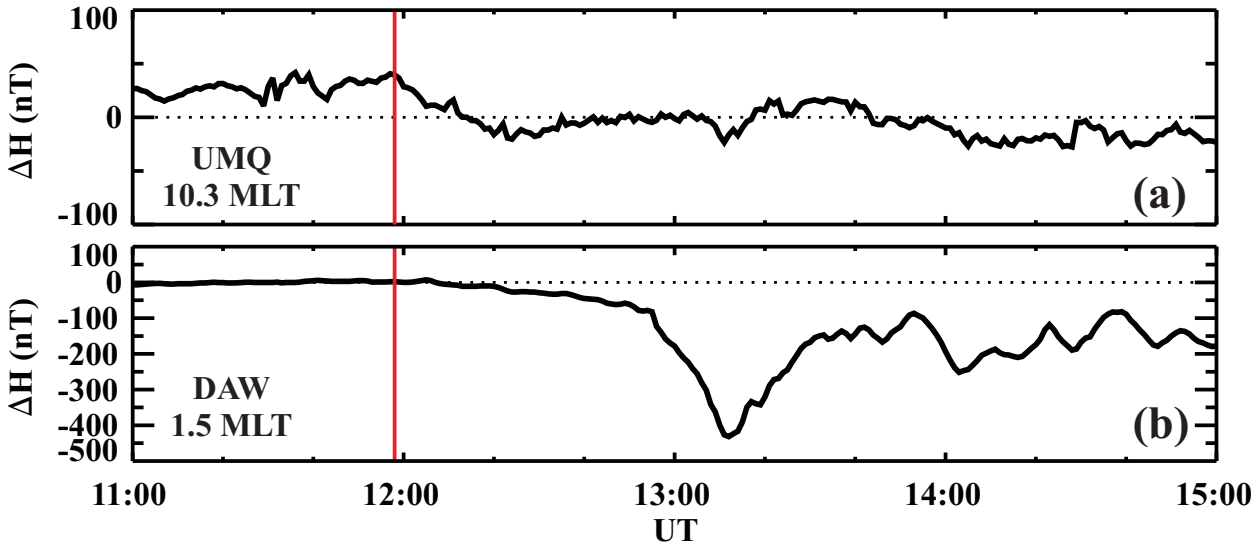

Figure 5.2: Line plots of the perturbation in the H component of the magnetic field for a station location near (a) noon and (b) midnight. The site code and station MLT are indicated in the bottom left corner of each plot. A vertical red line shows the expected ionospheric onset of the southward transition indicated in Figure 5.1.

minutes. Accounting for a delay of ~ 5 minutes for propagation between the magnetopause and the high-latitude ionosphere (which will be later verified by measurement), the southward transition is expected to affect the ionosphere at ~11:58 UT.

Response observed by magnetometers

Line plots of the perturbation in the H component of the magnetic field (ΔH) were generated for all magnetometer stations. The quiet level for determining ΔH was calculated as described in Section 4.1.1 using the average of the 5 quietest days in January and in February, according to the AE index: January 1, 2, 6, 18, 30, and February 3, 4, 5, 16, 25.

Figures 5.2 a and b show sample magnetometer traces of the perturbation magnetic field typically seen for stations located near noon and midnight, respectively. The vertical red lines mark the expected ionospheric onset time of the transition wavefront, hereafter referred to as the 'expected onset'. On the dayside, ΔH changes from 40 nT to -10 nT, beginning at the expected onset. On the nightside, the perturbation magnetic field begins a gradual depression starting 7 minutes after the expected onset. In general, the observed ionospheric onset of the transition wavefront, hereafter referred to as the 'ionospheric onset', is generally seen as a marked enhancement in the magnitude of ΔH, sometimes accompanied

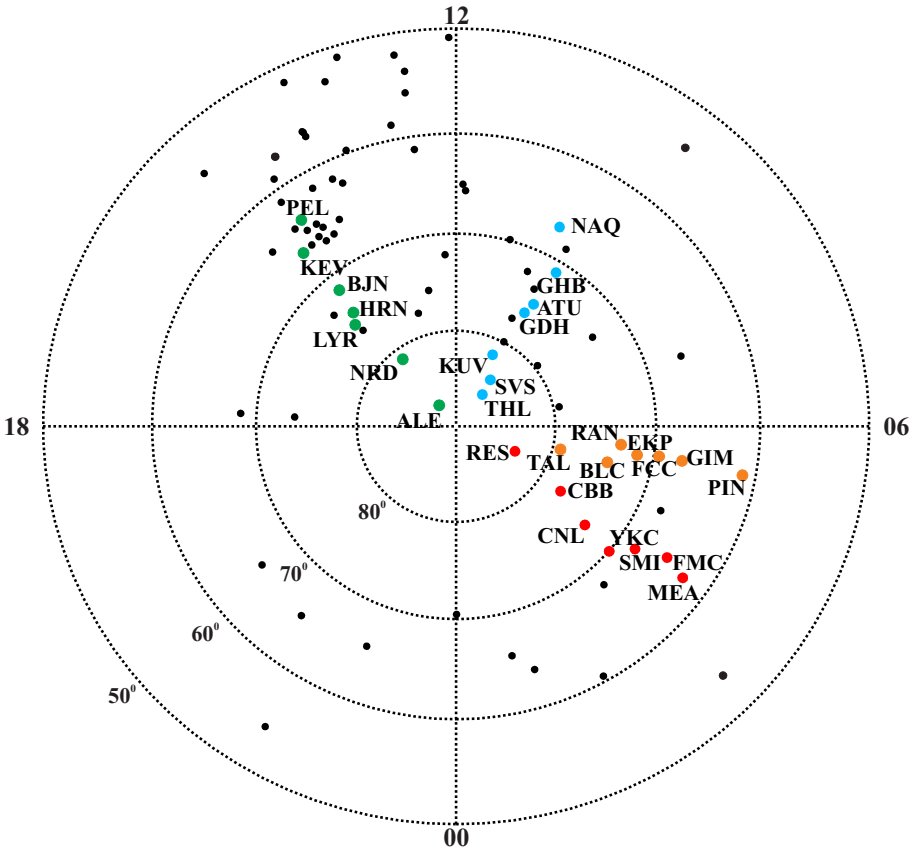

Figure 5.3: Location of magnetometer stations available for the January 20, 2001 event in MLAT/MLT coordinates at 12:00 UT. The green, blue, orange, and red filled circles indicate magnetometer stations approximately aligned along the 14, 10, 05, and 03 MLT meridians.

by a change in polarity. The size and duration of the enhancement varies from station to station.

The progression of the ionospheric onset was examined by considering ΔH for magnetometers distributed in MLT. Figure 5.3 plots the locations of magnetometer stations in MLAT/MLT coordinates at 12:00 UT. Green, blue, orange, and red filled circles in Figure 5.3 show magnetometer stations approximately aligned with the 14, 10, 05, and 03 MLT meridians. Line plots for these specific stations are shown in Figure 5.4.

At CNL, YKC, SMI, and FMC (64.5° to 73.3° MLAT) the ionospheric onset is accompanied by an enhancement in ΔH to more negative values, consistent with the location of the stations with respect to the westward electrojet. At FMC, the ionospheric onset is observed at the time of the expected onset, whereas there are 6 and 8 minute delays for SMI and YKC, respectively.

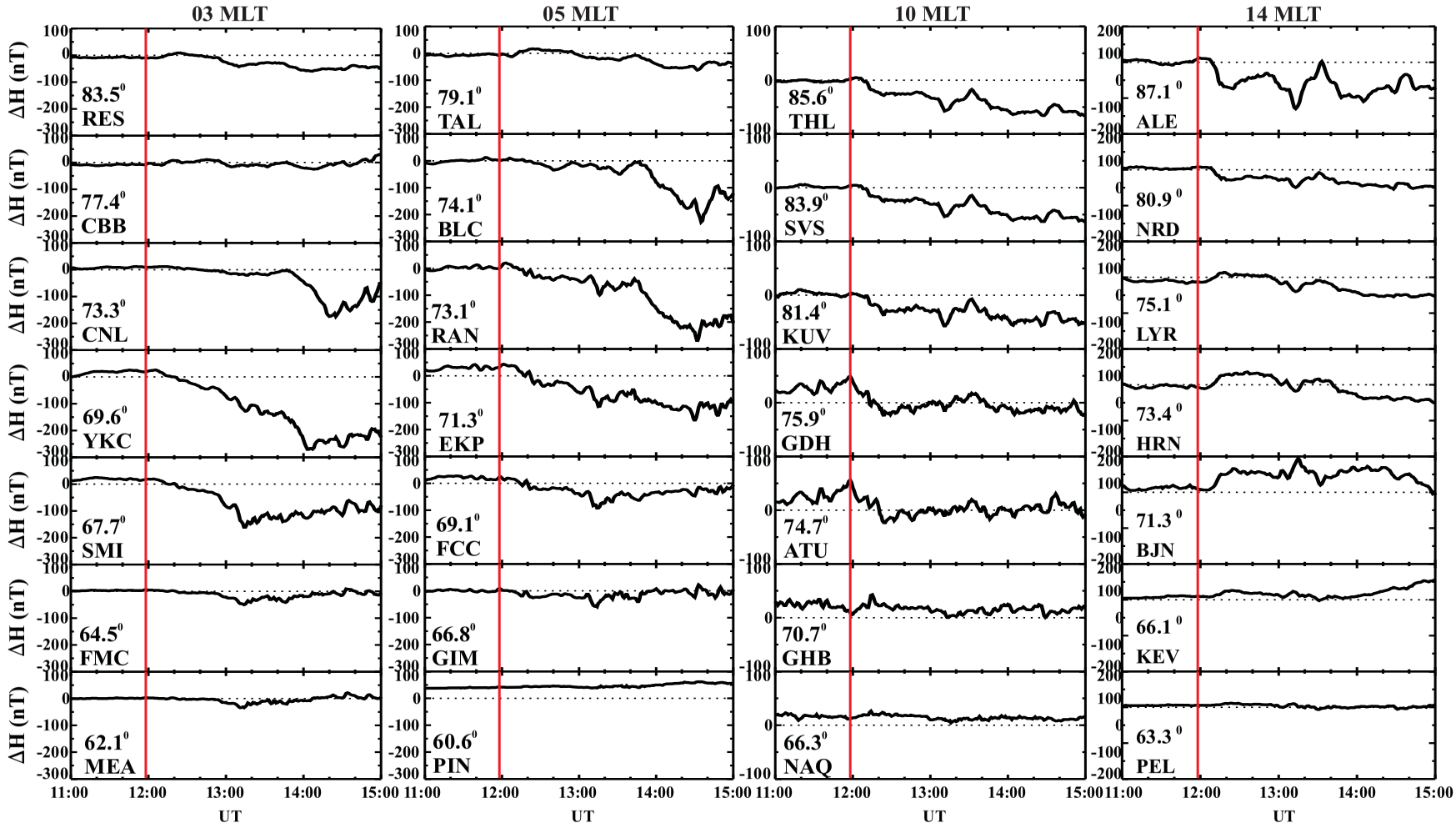

Figure 5.4: Line plots of ΔH for stations approximately aligned with the 03, 05, 10, and 14 MLT meridian at 12:00 UT on January 20, 2001. Stations are sorted by descending latitude. The site identification code and the station MLAT are indicated in the bottom left corner of each plot. A vertical red line shows the expected onset of the southward transitions indicated in Figure 5.1.

At 05 MLT the ionospheric onset is marked by an enhancement in ΔH to more negative values at the BLC, RAN, EKP, FCC, and GIM sites (66.8° to 74.1° MLAT). There is no delay from the expected onset for the GIM station. Delays of 1, 3, 5, 8, and 10 minutes are observed at FCC, EKP, RKN, BLC, and TAL, respectively. The maximum ΔH is first observed at the lowest latitude stations and then at successively higher latitudes for both the 03 MLT and 05 MLT stations. Along the 10 MLT meridian, the ΔH measured at THL, SVS, KUV, GDH, ATU, and GHB (74.7° to 85.6° MLAT) also enhanced to more negative values in association with the southward turning with delays of 0 minutes for the ATU and GDH stations, 1 minute for the KUV and GHB stations, 8 minutes for the THL station and 9 minutes for the SVS station.

Unlike the previous MLT sectors, stations along the 14 MLT meridian are located under the eastward electrojet and, with the exception of the most poleward stations, the ionospheric response is expected to be an enhancement in ΔH to more positive values. There are clear reactions to the southward turning observed at ALE, NRD, LYR, HRN, BJN, and KEV (66.1° to 87.1° MLAT) by an increase in ΔH. The delay in the response time varies from 5-6 minutes at HRN and LYR to 9-12 minutes at the remaining stations.

Response observed by SuperDARN radars

Figure 5.5 plots the location and field-of-view of the 8 northern hemisphere SuperDARN radars considered for the January 20, 2001 event. The black, orange, yellow, dark blue, green, light blue, red, and purple points represent grid cells for which plots of the l-o-s velocity were generated (Figure 5.5) for the Goose Bay, Saskatoon, Stokkseyri, Kapuskasing, Kodiak, Prince George, Hankasalmi, and Pykkvibaer radars, respectively. Vectors in Figure 5.5 indicate the direction of positive flow (away from the radar). The ionospheric onset is expected to manifest in the SuperDARN data as a marked change in the observed magnitude or direction of the velocity.

Figure 5.6 shows line plots of the gridded l-o-s velocity observed at coordinates indicated in Figure 5.5 for a period spanning from 11 to 14 UT. Due to changing observational conditions, echoes are not continuously observed at many individual grid points for prolonged periods of time, and there are gaps in the data not seen in the magnetometer plots.

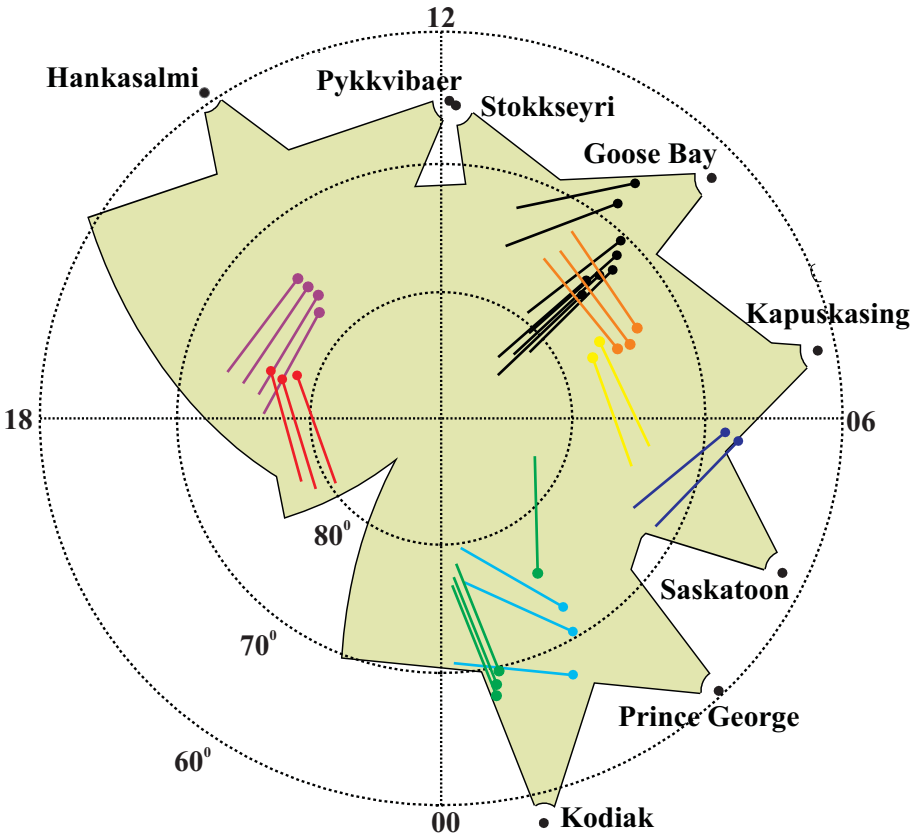

Figure 5.5: Location and field of view (green shading) of the SuperDARN radars for the January 20, 2001 event in MLAT/MLT coordinates at 12:00 UT. Colored vectors indicate the location of grid points and corresponding l-o-s velocities sampled for this event and the direction of positively oriented flow.

The first column in Figure 5.6 corresponds to grid cells in the 02 MLT sector. The Prince George radar observes an increase in the magnitude of the velocity to more negative values, ∼10-15 minutes after the southward turning. According to the sample vectors plotted in Figure 5.5 (light blue), this corresponds to an increase in the magnitude of the flow across the polar cap. In the 69.5° and 70.5° MLAT grid cells, the Kodiak radar observes a change from positive to negative velocities beginning five minutes after the expected onset. At 70.5° MLAT, the change in polarity is accompanied by an increase in the magnitude of the velocity. There is a small enhancement in the velocity at 68.5° MLAT, but no change in polarity.

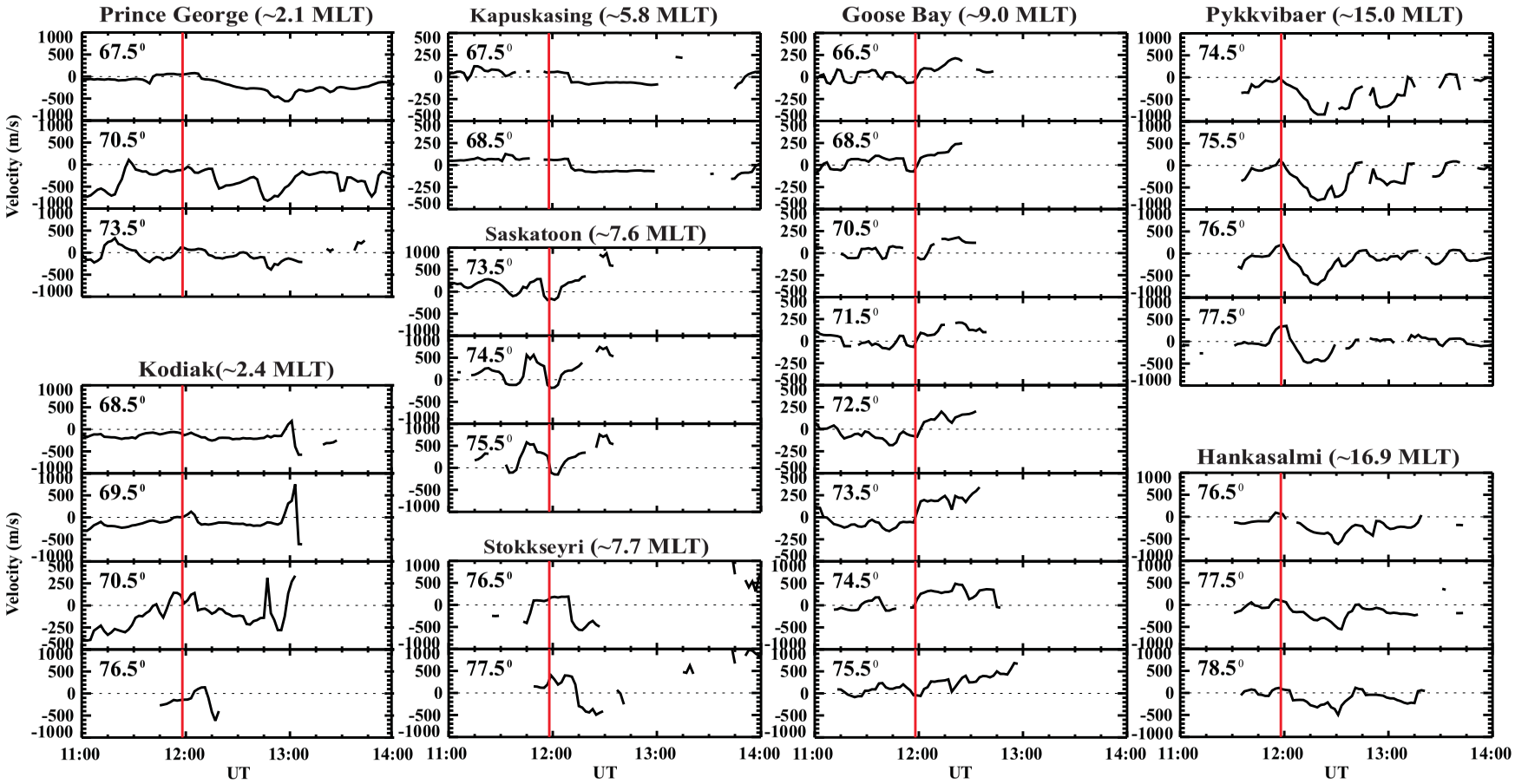

Figure 5.6: Line plots of the gridded l-o-s velocity observed by the Prince George, Kodiak, Kapuskasing, Saskatoon, Stokkseyri, Goose Bay, Pykkvibaer, and Hankasalmi radars for grid cells located at the MLATs and MLTs indicated for an event on January 20, 2001. A vertical red line shows the expected onset of the southward turnings indicated in Figure 5.1.

Data for Kapuskasing, Saskatoon, and Stokkseyri radars in the second column of Figure 5.6 represent observations for the 05-08 MLT sectors. Line plots for the Kapuskasing radar indicate a change in the velocity polarity, without a corresponding change in magnitude, $\sim$ 10 minutes after the expected onset. The flow reversal corresponds to a sudden flip from plasma moving first away from and then toward the Kapuskasing radar at $\sim 68^{\circ}$ MLAT near 06 MLT (see dark blue vectors in Figure 5.5). At Saskatoon, the plasma flow changes from -200 m/s approximately 5 minutes after the initial southward turning to +600 m/s $\sim$30 minutes later. Stokkseyri radar observations show a similar change in polarity beginning 5-10 minutes after the expected onset from velocities of +200 m/s to -600 m/s. Results plotted for the Saskatoon and Stokkseyri radars show the same reaction, but with opposite polarity, due to the opposite pointing direction of the radars. Data for the Saskatoon and Stokkseyri radars indicate a reversal from flow moving from 12 MLT toward 06 MLT prior to the transition to flow moving from 06 MLT toward 12 MLT approximately 5-10 minutes after the transition.

The third column in Figure 5.6 shows the l-o-s velocity observed by the Goose Bay radar in grid cells aligned along $\sim$ 09 MLT. For all latitudes the grid cells indicate a reversal in the velocity polarity and an increase in the magnitude of the velocity from -100 m/s to +500 m/s beginning at the expected onset passing through 0 m/s after 1-3 minutes. According to the Goose Bay radar, the ionospheric response is closely followed by a rotation of flow across the polar cap from sunward to anti-sunward directed flow. These observations are in agreement with descriptions given for the Saskatoon and Stokkseyri radars, but occur 5-10 minutes sooner.

The final column in Figure 5.6 plots the velocity observed by the Pykkvibaer and Hankasalmi radars in the late afternoon at 15-17 MLT (purple and red vectors in Figure 5.5, respectively). Both stations indicate a change from positive to negative velocity accompanied by an increase in velocity magnitude beginning at the time of the initial southward turning. The rate of increase is the largest for these stations compared to stations at other MLTs. Observations at Pykkvibaer and Hankasalmi correspond to flow pointing toward the radar in the anti-sunward direction prior to the expected onset and away from the radar (in the sunward direction) within 5 minutes of the expected onset.

Table 5.1: Delay in the response observed by SuperDARN for the January 20, 2001 event.

Radar	**Number of Observations**	**Delay (minutes)**
Prince George	41	11
Kodiak	39	11
Kapuskasing	9	11
Saskatoon	18	5
Stokkseyri	7	9
Goose Bay	20	2
Pykkvibaer	21	3
Hankasalmi	16	7

In response to the arrival of the transition wavefront, the gridded l-o-s velocities plotted in Figure 5.6 changed in polarity or increased in magnitude (or both). Similar trends were observed for additional grid cells not plotted in Figure 5.6. Table 5.1 lists the total number of grid cells for which a response was clearly identified, and the average delay between the expected and ionospheric onset times.

With the help of the vectors plotted in Figure 5.5, the line plots in Figure 5.6 may be used to infer the configuration of the general convection pattern. Observations from the Kodiak and Prince George radars indicate anti-sunward flow across the polar cap which becomes sunward at more equatorward latitudes. With a delay ranging from 15 to 20 minutes after the transition onset, the magnitude of the flow enhances. Measurements from the Kapuskasing, Saskatoon, Stokkseyri, and Goose Bay radars indicate a change in polarity associated with the transition, passing through 0 m/s within 5 minutes of the expected onset. The orientation of the flow suggests that prior to the transition, the grid cells are located on a dawnside reverse convection cell, and 5 minutes after the expected onset, the grid cells reflect plasma flow typical of the dawnside cell of the Dungey convection pattern. Observations made by the Pykkvibaer and Hankasalmi radars suggest the grid cells are first located under a duskside reverse convection cell and then under a Dungey convection cell. Although the convection response is observed near the expected onset, it takes several minutes for the convection pattern to restructure and the flow to reverse. Observations on the dayside support the restructuring of the ionospheric convection pattern from a typical multi-celled convection pattern having sunward directed flow over the polar cap (often observed for

periods of northward IMF) to a two-celled convection pattern having anti-sunward directed flow over the polar cap, more typical for periods of southward IMF.

Figures 5.7 a,c and b,d map the convection pattern determined from SuperDARN gridded l-o-s velocities using the FIT and SCHA-2 techniques, respectively. Figure 5.7 a,b shows the convection pattern determined for the two-minute interval beginning at 11:52 UT, 8 minutes prior to the expected onset when the IMF is northward at 5 nT. These maps were processed with $K_{max} = 6$ and $\theta_{FIT} = \theta_c = 24°$. Both FIT and SCHA-2 plots indicate a multi-celled convection pattern with a clearly mapped dawnside convection cell. The vortex of the dawnside convection cell is located near midnight, and the entire convection cell is compressed on the nightside ionosphere. In the FIT map the dawnside cell stretches into the duskside sector with high-latitude flow directed from dawn-to-dusk at midnight poleward of 80° MLAT. The SCHA-2 map shows a convection cell confined to the dawnside and convection flow is directed sunward in the region poleward of 80° at midnight, consistent with observations of the gridded l-o-s velocities from the Kodiak and Prince George radar, see Figure 5.6. The contradicting flow in the FIT map is explained by the influence of the statistical model used to constrain the gap in data in the 18-24 MLT region. The duskside convection cell is not well constrained and has not been mapped by the SCHA-2 technique. The red cross in the FIT map indicates an estimated location of the duskside convection vortex based on contributions from a statistical model.

Both techniques map reverse convection cells on the dayside. The FIT map clearly shows the complete dawnside reverse convection cell poleward of 80° MLAT in the 10-12 MLT sector with low-velocity flow (∼300 m/s) directed sunward over the polar cap region. In the SCHA-2 convection pattern, the dawnside reverse convection cell is located in the $75° - 80°$ MLAT and 08-10 MLT region; the plasma flow is directed across the polar cap with magnitudes of 400-500 m/s on the nightside reaching 600-700 m/s on the dayside. Measurements from the Goose Bay, Saskatoon, and Stokkseyri radars all reflect flow characteristic of the reverse convection cell, and it is therefore likely that the location of the convection cell plotted by the SCHA-2 technique is correct. Due to the large number of observations on the dayside, it is unlikely that the discrepancies between the FIT and SCHA-2 techniques regarding the dawnside reverse convection cell are due to the application of a

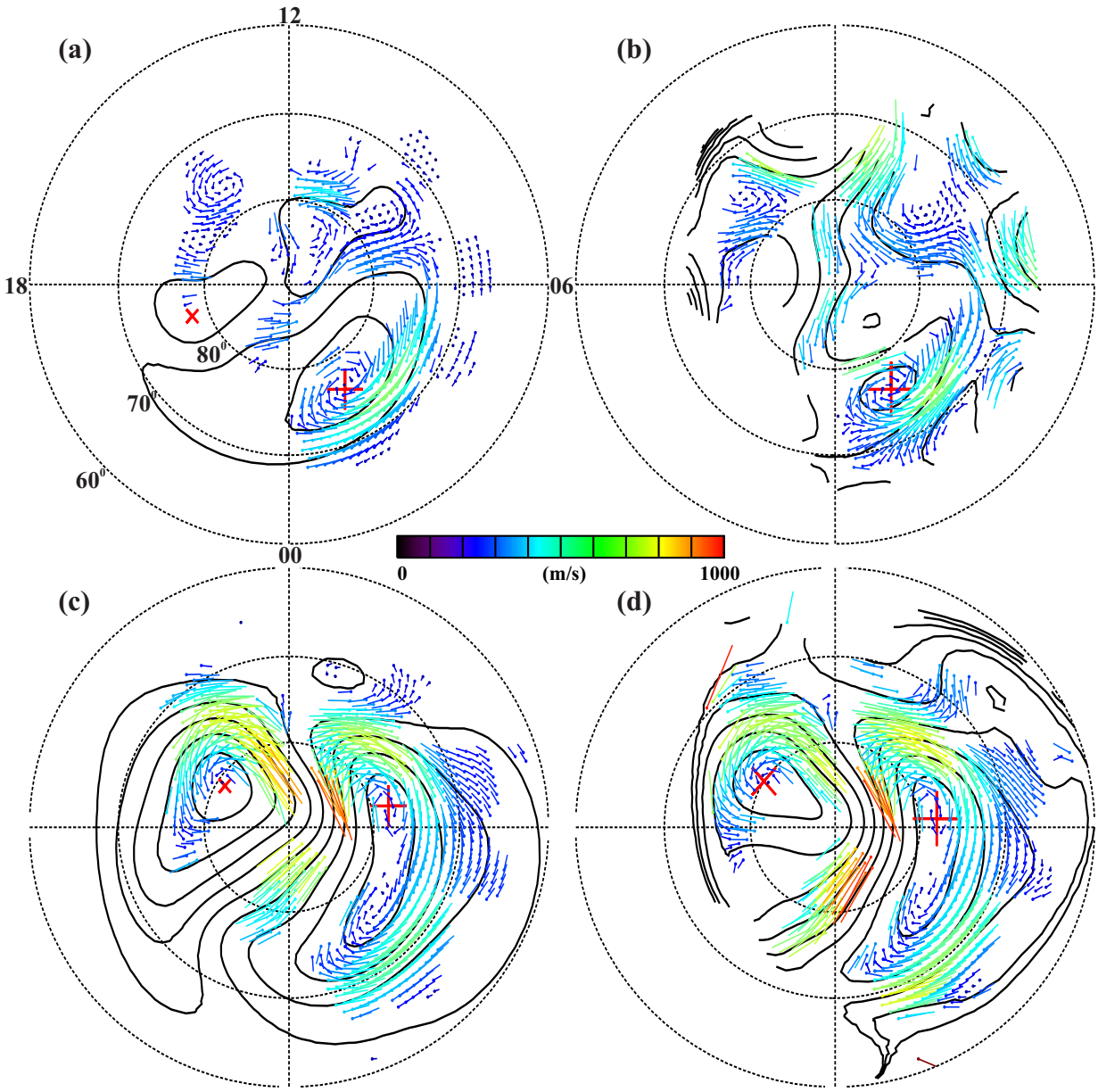

Figure 5.7: Convection patterns determined from SuperDARN gridded l-o-s velocities using the (a,c) FIT technique with contributions from a statistical model and HMB, and (b,d) SCHA-2 technique for the two-minute interval beginning at (a,b) 11:52 UT and (c,d) 12:26 UT on January 20, 2001. All convection maps were processed with $K_{max} = 6$ and (a,b) $\theta_{FIT} = \theta_c = 24°$ and (c,d) $\theta_{FIT} = \theta_c = 35°$. Contours show the electrostatic potential Φ_E with a 6 kV spacing. The plus and cross signs indicate the maximum and minimum Φ_E, respectively.

statistical model. Instead, the more poleward location of the reverse convection cell, and reduction in the velocity magnitude for the FIT technique, are likely due to the compression of the convection pattern on the dayside by the HMB.

Figure 5.7 c,d maps the convection pattern for a two-minute interval beginning at 12:26 UT, 28 minutes after the arrival of the transition wavefront, when the IMF is directed southward at -5 nT. Both the FIT and SCHA-2 maps indicate a two-celled convection pattern typical for periods of southward IMF. The convection foci of the dawn and dusk convection cells are similarly located, and the CPCP measured between the convection foci are similar ($CPCP_{FIT}$=55.5 kV and $CPCP_{SCHA}$=49.6 kV). Although the direction of the plasma flow is roughly the same in both maps, the magnitude of the velocity is different. For example, the magnitude of the anti-sunward flow associated with the duskside convection cell reaches peak values of $>$ 850 m/s in the FIT map and 800 m/s in the SCHA-2 map. In contrast, the SCHA-2 map indicates velocities 200-300 m/s larger than those reported by the FIT map in the 00-02 MLT sector poleward of 80° MLAT. Reduced FIT convection is likely due to a dominance of the statistical model and a data gap in the dusk sector.

5.2.2 November 02, 2001

Figure 5.8 shows the IMF B_x, B_y, and B_z components measured by the ACE satellite for a second event on November 02, 2001. Vertical red lines at 11:07 UT and 11:11 UT indicate a sharp southward transition from 7 nT to -6 nT. Throughout the interval the B_y and B_z components are comparatively stable, but there are sharp changes in the B_y component in association with the southward transition.

Using the Weimer technique (*Weimer et al.*, 2003; *Weimer*, 2004), and accounting for a ∼5 minute delay in traveling from the magnetosphere to the ionosphere, the propagation delay time between the satellite and ionosphere was found to be 70 minutes at the time of the southward transitions. The southward transition at 11:07 UT is therefore expected to reach the ionosphere at ∼12:17 UT. From this point on only the initial transition will be referenced.

Response observed by magnetometers

For this event, the magnetometer and radar stations were similarly located to those mapped in Figure 5.3 due to the similarity in the ionospheric arrival time of the two events.

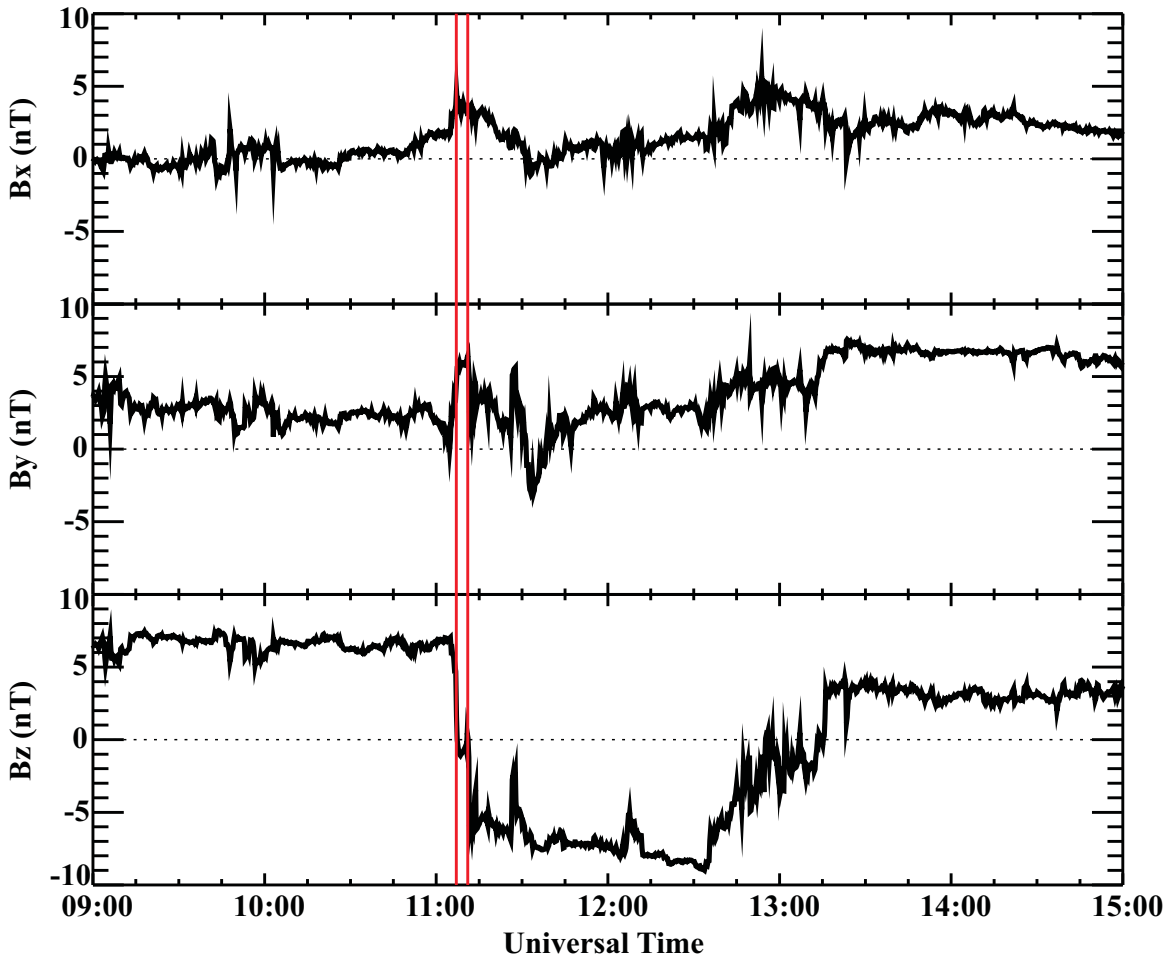

Figure 5.8: IMF B_x, B_y, and B_z on November 02, 2001. Sharp southward turnings in the IMF are indicated by vertical red lines.

Figure 5.9 shows line plots of ΔH for stations approximately aligned along the 03, 05, 10, and 14 MLT meridians. Quiet level was determined based on magnetic measurements made on October 7, 17, 18, 24, and 26, 2001 and on November 3, 27, 28, 29, and 30, 2001.

The first column in Figure 5.9 indicates stations approximately located in the 03 MLT sector under the westward electrojet. At the ionospheric onset the ΔH at RES and CBB stations (77.4° to 83.5° MLAT) increases, whereas the ΔH at YKC, SMI, FMC, and MEA stations (62.1° to 69.6° MLAT) begin a gradual decrease. Responses are delayed by 10 minutes from the expected onset at the RES and CBB stations, and 11, 15, and 17 minutes for the FMC, SMI, and MEA stations, respectively. The maximum ΔH is first observed at the lowest latitude stations, and then at successively higher latitudes.

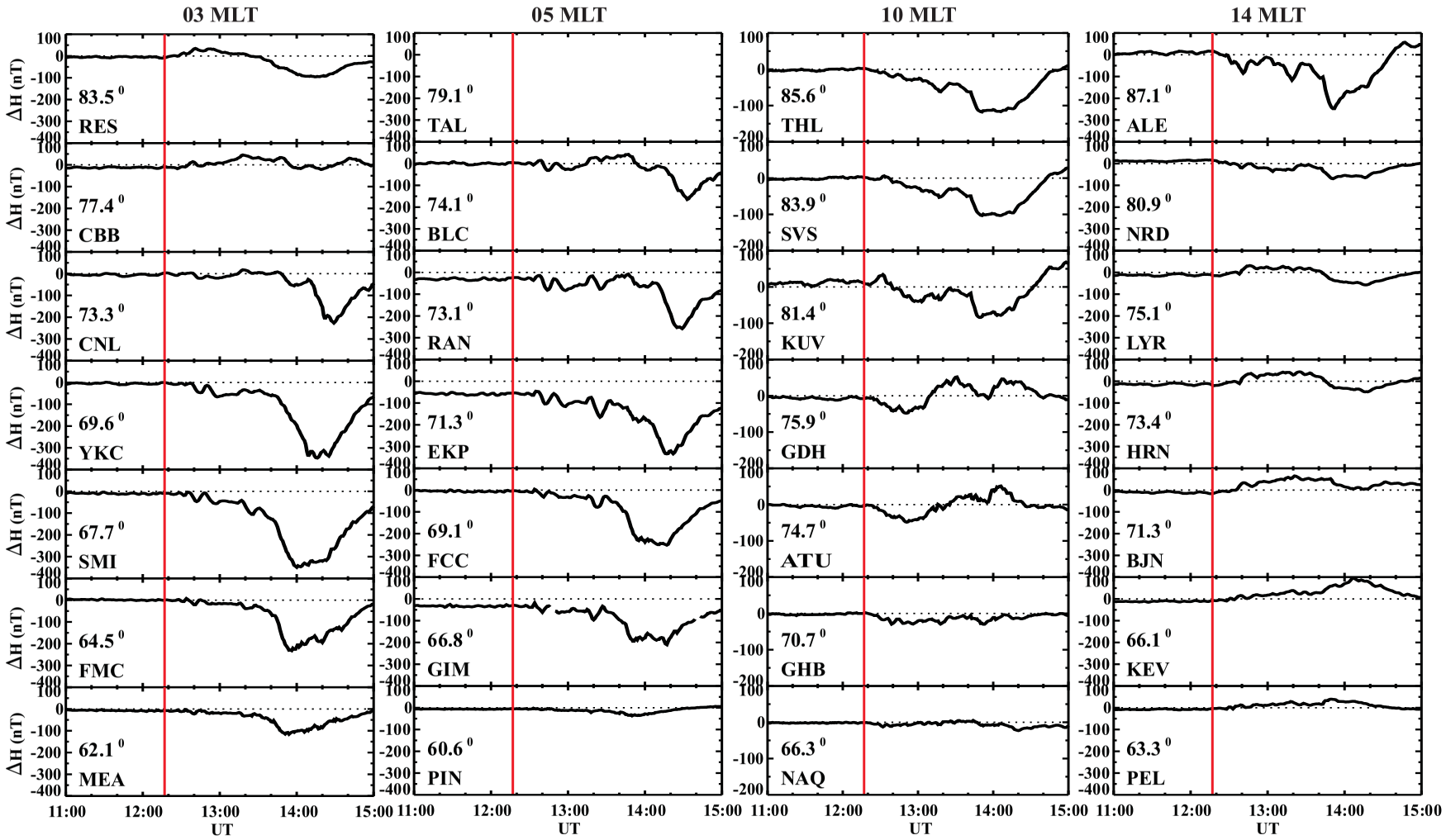

Figure 5.9: Line plots of ΔH for stations approximately aligned with the 03, 05, 10, and 14 MLT meridians at 12:00 UT on November 02, 2001. Stations are sorted by descending latitude. The site identification code and the station MLAT are indicated in the bottom left corner of each plot. Vertical red lines show the expected onset of the southward transitions indicated in Figure 5.8.

Stations located at 05 MLT (second column) are also located under the westward electrojet. Data were not available for the TAL station. The ionospheric onset is marked by a decrease at BLC, RAN, EKP, FCC, GIM, and PIN (60.6° to 74.1° MLAT). Responses were observed with a delay of 10 minutes at BLC, 16 minutes at RAN, and 17 minutes at both FCC and GIM stations. There is a trend of increased delay in the arrival of the maximum magnetic perturbation with increasing latitude.

Along the 10 MLT meridian, the southward transition is marked by a decrease in the THL, SVS, KUV, GDH, ATU, and GHB stations (70.7° to 85.6° MLAT). There was a delay of 0-4 minutes at the THL, KUV, ATU, and GHB stations, 7 minutes at the GDH station, and 16 minutes at the SVS station.

The final column in Figure 5.9 shows ΔH observed along the 14 MLT meridian under the eastward electrojet. The ionospheric response is seen in ΔH as a decrease at ALE and NRD and an increase at LYR, HRN, BJN, KEV, and PEL (63.3° to 87.1° MLAT). The ionospheric onset was delayed from the expected onset by 1 minute at ALE and HRN, 3 minutes at NRD, 6 minutes at LYR, and 11 minutes at KEV and PEL. In general, the strength of the reaction decreases with decreasing latitude.

Response observed by SuperDARN radars

Figure 5.10 plots the location and field-of-view of the 7 northern hemisphere SuperDARN radars considered for the November 02, 2001 event. The black, orange, yellow, light blue, green, red, and purple vectors correspond to grid cells considered from the Goose Bay, Saskatoon, Stokkseyri, Prince George, Kodiak, Hankasalmi, and Pykkvibaer radars, respectively. Figure 5.11 shows line plots of the flow observed at the grid cells indicated in Figure 5.10.

Observations for the Kodiak radar are located within the $\sim$ 02 MLT sector (green vectors). According to the line plots in Figure 5.11, there is a change in the velocity from $\sim$ 500 m/s to -500 m/s beginning 10-15 minutes after the expected onset and passing through 0 m/s after 5-10 minutes. This corresponds to flow moving first sunward and then anti-sunward over the polar cap. Grid cells for the Prince George radar are located in the 03 MLT sector (light blue vectors), and indicate flow changing from $<$ 100 m/s to -400 m/s

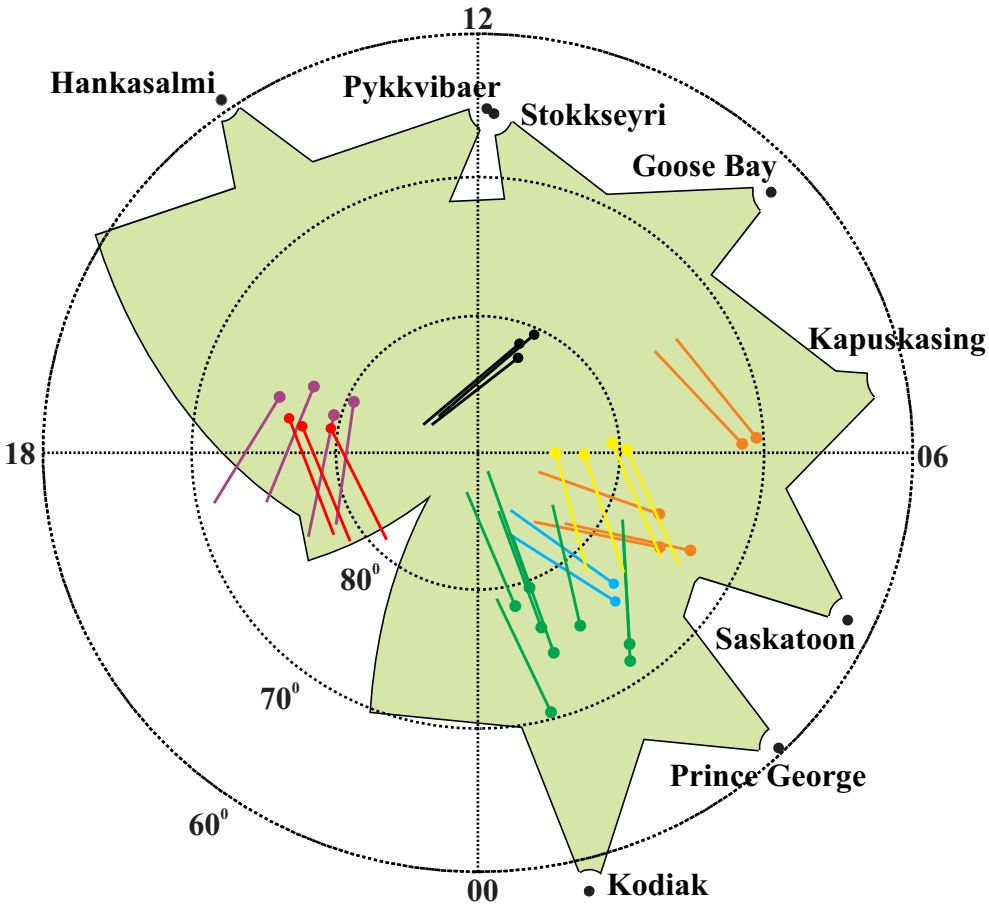

Figure 5.10: Location and field of view (green shading) of the SuperDARN radars for the November 02, 2001 event in MLAT/MLT coordinates at 12:00 UT. Colored vectors indicate the location of grid points and corresponding l-o-s velocities sampled for this event and the direction of positively oriented flow.

beginning ∼5 minutes after the expected onset. The direction of the flow observed at Kodiak and Prince George agree.

Grid points for the Saskatoon radar (orange vectors) are located between the 04 and 06 MLT meridians. The first two plots for the Saskatoon radar correspond to the two vectors located just past 06 MLT. They indicate an increase in the velocity magnitude (to more positive values) beginning approximately 10 minutes after the expected onset. Such observations correspond to flow moving away from the radar toward 12 MLT. The lower three line-plots correspond to the three orange vectors located closer to the 04 MLT meridian. In these plots, there is a reversal in the polarity of the velocity from < 100 m/s to up to -500 m/s. The change in the velocity begins 5-10 minutes after the transition onset with the

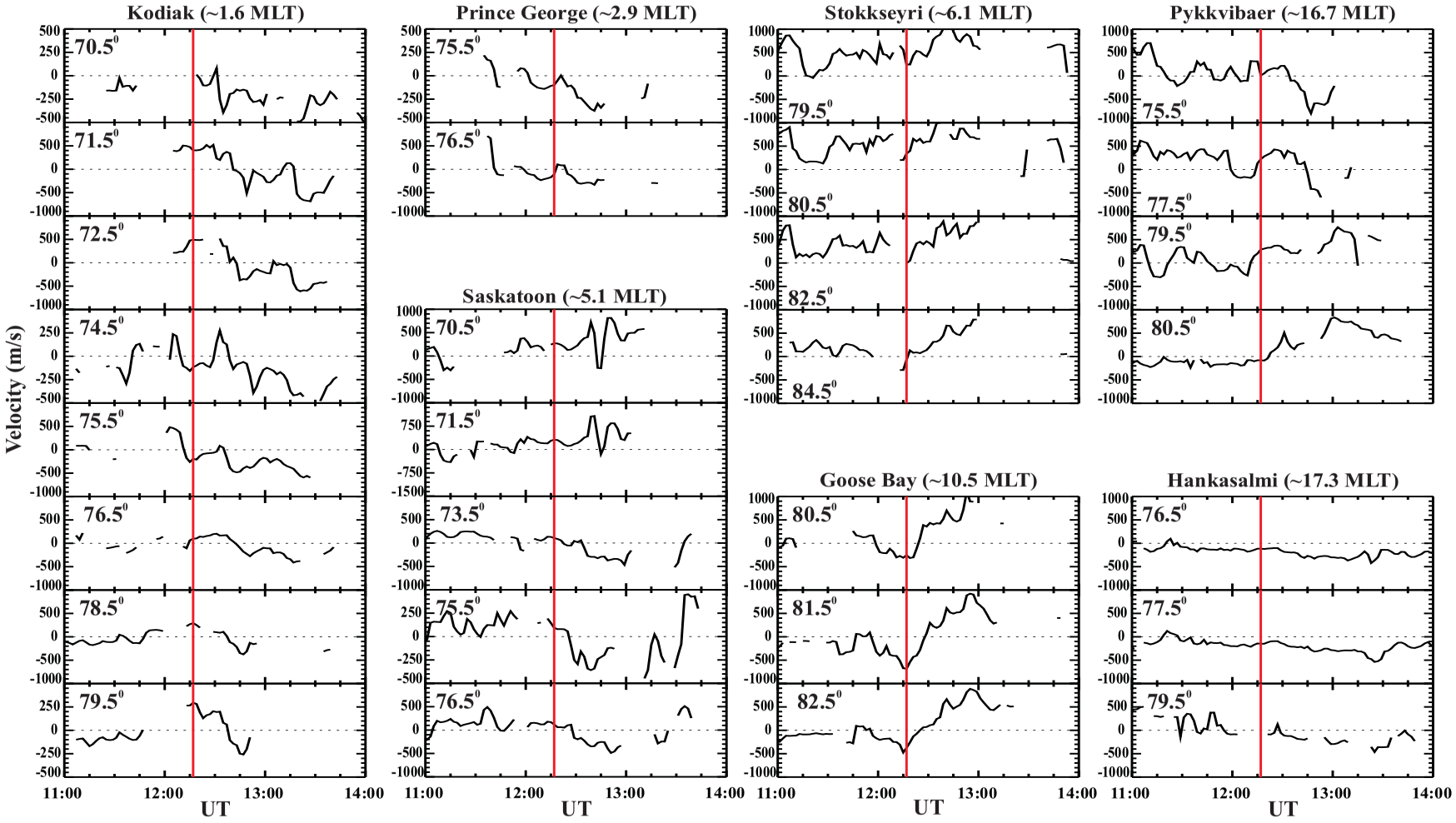

Figure 5.11: Line plots of the gridded l-o-s velocity observed by the Prince George, Kodiak, Kapuskasing, Saskatoon, Stokkseyri, Goose Bay, Pykkvibaer, and Hankasalmi radars for grid cells located at the MLATs and MLTs indicated for an event on November 02, 2001. Vertical red lines show the expected onset of the southward turnings indicated in Figure 5.8.

velocity passing through 0 m/s approximately 2 minutes later. Figure 5.10 indicates that the l-o-s component of the flow at grid cells sampled for these plots is aligned in the meridional direction. As such, the plasma flow associated with activity in the line plots indicates a rotation from plasma moving first toward, and then away from the magnetic pole.

Line plots in the third column of Figure 5.11 are for the Stokkseyri and Goose Bay radars, located in the high-latitude region of the 06 MLT sector (yellow vectors) and 10 MLT sector (black vectors), respectively. The Stokkseyri radar indicates flow moving away from the radar in the anti-sunward direction which increases in magnitude beginning at the expected onset. At 10 MLT poleward of 80° MLAT, the Goose Bay radar observes a large change in the velocity from -500 m/s to 1000 m/s beginning at the expected onset and passing through 0 m/s 5 minutes later.

The Pykkvibaer and Hankasalmi radars are approximately co-located along the 17 MLT meridian. The Pykkvibaer radar shows two different features. For flow at 75.5° and 77.5° MLAT the ionospheric onset, indicated by a reversal from 200-300 m/s to <-500 m/s, is delayed 10 minutes from the expected onset. Flow reverses from moving first away from and then toward 12 MLT along the $\sim 76°$ magnetic meridian. For flow at a slightly higher latitude of 79.5° MLAT, there does not appear to be any clear reaction to the transition onset. However, at 80.5° MLAT, the flow increases from -100 m/s to 500 m/s over 13 minutes, beginning 4 minutes after the expected onset. This motion corresponds to a reversal of the flow which moves first toward 12 MLT along the 80.5° meridian and than away from 12 MLT.

In response to the arrival of the transition wavefront, the gridded l-o-s velocities plotted in Figure 5.6 changed in polarity or increased in magnitude (or both). Table 5.2 indicates the average delay observed for each radar.

Observations for the Kodiak, Prince George, and Goose Bay radars are consistent with the reversal of plasma flowing over the polar cap in the sunward direction prior to the transition and the anti-sunward direction after the transition, consistent with the establishment of the dawnside cell of the Dungey convection pattern. Flow observed by both the Stokkseyri and Saskatoon radars support this conclusion. The Kodiak, Prince George, and Goose Bay radars contradict in their estimation of the time delay between the expected and ionospheric

Table 5.2: Delay in the response observed by SuperDARN for the November 02, 2001 event.

Radar	**Number of Observations**	**Delay (minutes)**
Prince George	3	5
Kodiak	36	16
Saskatoon	17	11
Stokkseyri	19	1
Goose Bay	18	2
Pykkvibaer	15	7
Hankasalmi	7	9

onset: 15-25, 1-2, and ~ 5 minutes for Kodiak, Prince George, and Goose Bay, respectively. The opposing direction of the most poleward and equatorward plasma flow observed by the Pykkvibaer radar suggests counter-clockwise directed flow, characteristic of the duskside reverse convection cell. After the ionospheric onset the flow reverses. As with the January 20, 2001 event, observations on the dayside support the restructuring of the ionospheric convection pattern from a multi-celled convection pattern during the period of northward IMF prior to the arrival of the southward turning to a two-cell convection pattern.

Figure 5.12 shows convection maps determined using the (a,c) FIT and (b,d) SCHA-2 convection mapping techniques based on SuperDARN data. In Figures 5.12 a and b convection is mapped with $K_{max} = 6$ and $\theta_{FIT} = \theta_c = 31^\circ$ for the two-minute interval beginning at 12:06 UT, 10 minutes prior to the expected onset when the IMF is northward at 8 nT. Both maps show multi-celled convection patterns with a Dungey-like dawnside convection cell with vortex located in the 05 MLT sector and $\sim 78^\circ$ MLAT. The FIT-technique maps an additional duskside cell with vortex approximately centered on the 18 MLT meridian poleward of 80° MLAT. Although plasma flow in this region is similar in the SCHA-2 map, a convection cell has not been mapped. A pair of reverse convection cells are mapped on the dayside using both the FIT and SCHA-2 techniques. The vortex of the duskside reverse convection cell is located in the 14 MLT sector at 78° MLAT in both maps. The vortex of the dawnside reverse convection cell is located in the 10 MLT sector at $\sim 75^\circ$ MLAT for the FIT map and near the magnetic pole for the SCHA-2 map. Although the exact location of the dawnside vortex varies between maps, both show a reverse convection system with sunward directed flow over the polar cap.

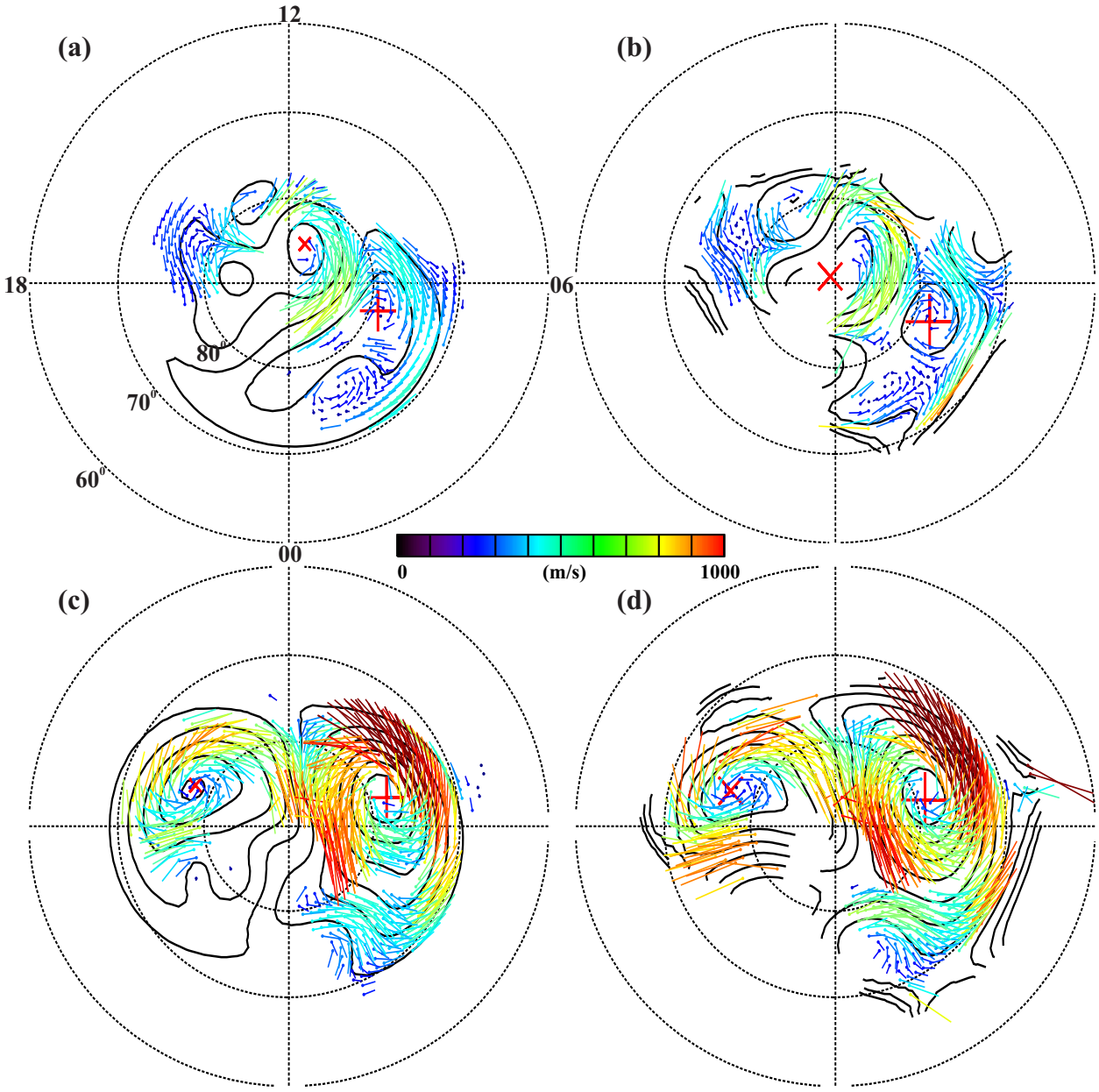

Figure 5.12: Convection patterns determined from SuperDARN gridded l-o-s velocities using the (a,c) FIT technique with contributions from a statistical model and HMB, and (b,d) SCHA-2 technique for the two-minute interval beginning at (a,b) 12:08 UT and (c,d) 12:42 UT on January 20, 2001. All convection maps were processed with $K_{max} = 6$ and (a,b) $\theta_{FIT} = \theta_c = 31°$ and (c,d) $\theta_{FIT} = \theta_c = 34°$. Contours represent electrostatic potential Φ_E with a 6 kV spacing. The cross and plus signs indicate the maximum and minimum Φ_E, respectively.

Line-plots for the Kodiak, Prince George, Saskatoon, Stokkseyri, Goose Bay, and Hankasalmi radars shown in Figure 5.11 and the three most poleward sampled grid cells of the Pykkvibaer radar are consistent with the maps plotted in Figure 5.12. In the 75.5° grid cell, the Pykkvibaer radar observes a component of the convection flow directed away from the radar (away from 12 MLT) along 75.5° MLAT, which is not observed in the convection pattern. This observation was used to identify a possible duskside reverse cell centered within the Hankasalmi/Pykkvibaer points of observation which is not shown in the FIT convection map. According to the FIT and SCHA-2 maps, this convection vortex is actually located at ∼14 MLT.

Figures 5.12 c and d map the convection pattern for the two-minute interval beginning at 12:42 UT, 24 minutes after the expected onset, when the IMF is -6 nT. Both the FIT and SCHA-2 maps indicate almost identical two-cell convection patterns. The dawnside and duskside convection foci are similarly located and the CPCP are $CPCP_{FIT}$=65.3 kV and $CPCP_{SCHA}$=64.3 kV. Although the direction of the plasma flow is roughly the same in both maps, there are differences in terms of the magnitude of the velocity within the duskside convection vortex. The FIT convection map shows plasma flows of 400-700 m/s in the dawn-to-dusk direction on the nightside portion of the convection vortex where the SCHA-2 map shows magnitudes of 800-1000 m/s. Line-plots for all radars shown in Figure 5.11 agree with the convection patterns plotted in Figure 5.12.

5.2.3 Summary of the response observed by magnetometers

For two events, the response of the perturbation magnetic field to a southward transition of the IMF was examined. Measurements of the perturbation magnetic field were organized by MLAT for the 03, 05, 10, and 14 MLT sectors. For both events, the ionospheric onset of the transition wavefront was observed as a marked increase or decrease to the perturbation magnetic field, sometimes accompanied by a change in polarity. The size and duration of the enhancement varied from station to station. Stations at the most equatorward latitudes in a given MLT sector showed little-to-no fluctuation in the perturbation magnetic field. In the 03, 05, and 10 MLT sectors the increase in magnitude was observed by a drop to more negative values. In the 14 MLT sector, with the exception of the two stations poleward of 80°,

the increase in magnitude was observed by a rise to more positive values. The ionospheric response to the transition was observed at higher latitudes for the 10 and 14 MLT sectors than for the 03 and 05 MLT sectors, corresponding to the more poleward location of the auroral oval on the dayside (see Figure 1.7).

For the January event, the shortest delays were observed in the 10 MLT sector (0-1 minute) and the longest delay were observed in the 14 MLT sector (9-12 minutes). For the November event, shorter delays were observed in the 10 and 14 MLT sector than the 03 and 05 MLT sector.

Plots of ΔH in the 03 and 05 MLT sectors follow a specific pattern characteristic of substorm activity. ΔH is initially near zero, indicating little activity, and then drops to more negative values corresponding to the onset of the substorm expansion phase. The perturbation magnetic field peaks after a few hours before returning to zero, corresponding to the substorm recovery phase.

Figures 5.13 a and b show the AE index and Pi2 pulsations for the Meanook magnetometer located at 62.1° in the 03 MLT sector (at 12:00 UT) for the January and November events, respectively. For the January event, the AE index begins a gradual increase 12 minutes after the expected onset, enhancing from near zero values at 12:10 UT to ∼100 nT at 12:54 UT. At 12:54 UT the AE index sharply increases, reaching a peak value of ∼ 500 nT at 13:13 UT, 75 minutes after the initial southward turning. Pi2 pulsations are relatively small until 12:47 UT, 7 minutes prior to the enhancement observed in the AE index. These results indicate the onset of the substorm expansion phase at ∼12:50 UT.

For the November event, the AE index begins a gradual increase from near zero values starting at 12:24 UT, 7 minutes after the transition onset, with a sharper increase beginning at 13:05 UT. The peak AE index is reached at 13:50 UT, 93 minutes after the expected onset. Pi2 pulsations pick up at 12:20 UT, 4 minutes before the gradual increase observed by the AE index, become stronger at∼13:30, peaking after 14:15 UT. These results suggest the onset of the substorm expansion phase occurs between 13:00 UT and 13:30 UT.

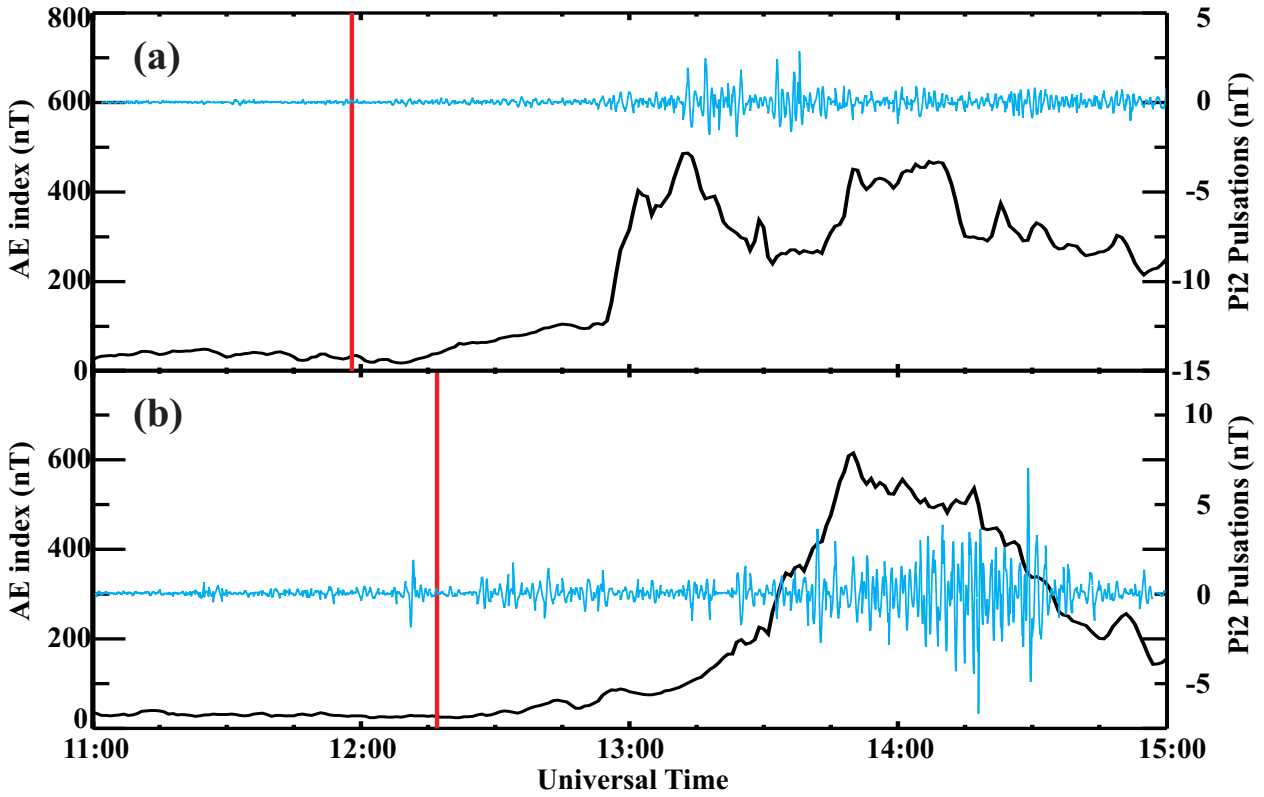

Figure 5.13: AE index (black) and Pi2 pulsations (blue) observed by the Meanook magnetometer station for the (a) January 20, 2001, and (b) November 02, 2001 events. Vertical red lines indicate the ionospheric onset of the southward turnings indicated in Figure 5.1 and Figure 5.8.

5.2.4 Summary of the response observed by SuperDARN

For both events, gridded l-o-s velocities from the northern hemisphere SuperDARN radars were examined for a response to the southward turning of the IMF. The ionospheric onset of the transition wavefront was observed in the gridded l-o-s velocity data as an enhancement in the magnitude of the measured velocity sometimes accompanied by a flow reversal, or as an independent flow reversal without an enhancement in the velocity, consistent with the findings of *Ruohoniemi and Baker* (1998). By examining the position of the radar grid cells sampled and convection maps generated using the FIT and SCHA-2 techniques, the general convection response was inferred. For both the January and November events, a Dungey convection cell was observed on the nightside throughout the entire event. Flow within the cell enhanced 15-20 minutes after the expected onset. Dayside measurements reflected the presence of two reverse convection cells with sunward-directed flow over the polar cap prior

to the onset. Within 5 minutes of onset, grid-cells located over the dawnside reverse cell saw a flow reversal resulting in anti-sunward flow over the polar cap.

Line-plots for the SuperDARN radars were generated for the 02, 06-09, and 17 MLT sectors for the January event and the 02, 03, 04, 06, 10, and 17 MLT sectors for the November event. For the January event, the delay in the ionospheric response observed in individual grid cells varied from 0-5 minutes in the 09 and 15 MLT regions, 5-10 minutes in the 07 and 17 MLT regions, and 10-15 minutes in the 02 and 06 MLT regions for the January 20, 2001 event. These results indicate the ionospheric onset observed by the SuperDARN radars is observed first in the late morning sector and last in the early morning sector. For the November event, the delay times are 0-5 minutes in the 06 and 11 MLT sectors, 5-10 minutes in the 03, 16, and 17 MLT sectors, and 10-20 minutes in the 02 and 07 MLT sectors. The shortest delays were observed in the late morning and the longest delays were observed in the early morning.

5.2.5 Progression of the response observed in both magnetometer and SuperDARN data

To determine the MLT and MLAT dependence of the ionospheric onset of the southward transition wavefront, line plots of ΔH and the gridded l-o-s velocity were expanded to include all available data. Results were only recorded if the data set examined was roughly continuous over a two hour window centered over the expected onset, and a clear change in the trend of the data was observed.

Figures 5.14 a and c show the ionospheric onset observed in the ΔH by magnetometers for the January 20, 2001 and November 02, 2001 events where 142 and 157 magnetometer traces were examined and 38 and 26 events were identified as having clear transition onsets, respectively. The red (blue) dots indicate line plots for which the perturbation magnetic field enhanced to more positive (negative) values. Horizontal lines indicate the expected onset time predicted based on observations from the ACE satellite. The expected onset corresponds to the initial ionospheric response observed by magnetometers, confirming the predicted onset time.

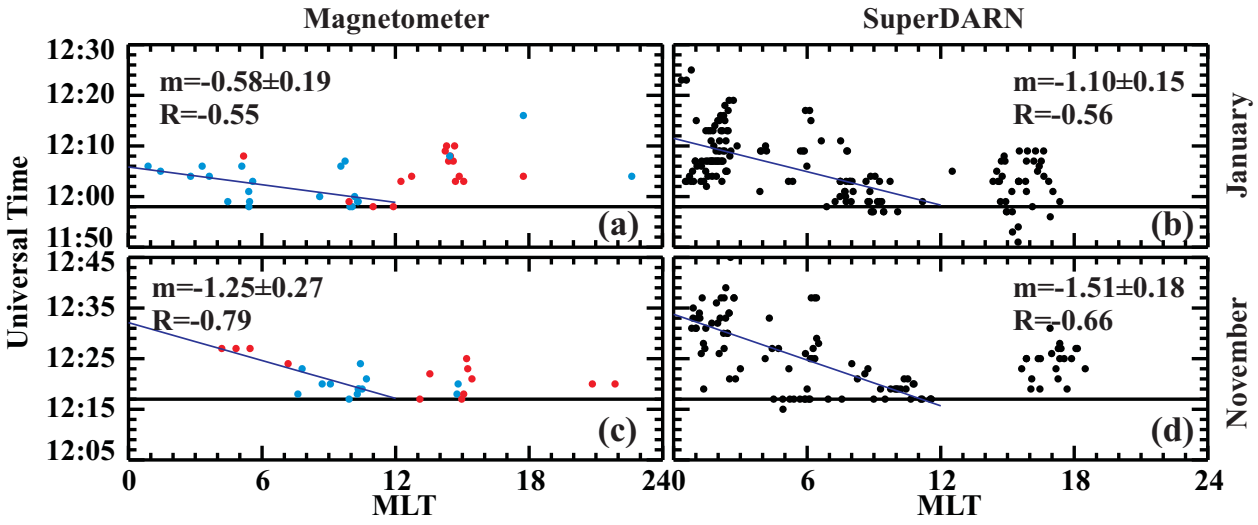

Figure 5.14: Ionospheric onset time of the southward transition wavefront in terms of MLT as determined by (a,c) ΔH from ground-based magnetometers and (b,d) SuperDARN gridded l-o-s velocity for the (a,b) January 20, 2001 and (c,d) November 02, 2001 events. Red (blue) filled circles in a and c indicate changes in ΔH to more positive (negative) values. Horizontal lines plotted at (a,b) 11:58 UT and (c,d) 12:17 UT indicate the expected onset time. Additional lines show the best-fit line to the data set.

The correlation coefficient (R) and best-fit line to the data (having slope m) were determined for data in the [0,12] MLT range. Figures 5.14 a and c indicate there is an MLT dependence of the transition onset time based on magnetometer measurements (R=-0.55 and R=-0.79). For both events, the ionospheric response is first observed between 10 and 12 MLT at the expected onset time, and then progresses toward the nightside. This effect is more strongly observed on the dawnside opposed to the duskside. According to the best-fit line for the January event, the ionospheric response reaches 00 MLT by 12:06 UT, 08 minutes after the initial onset. For the November 02, 2001 event, the best-fit line to the data indicates a dayside-to-nightside progression which reaches midnight 15 minutes after the initial onset. For the January and November events, the rate of change of the transition onset was m^{-1}=-1.72 MLT/min and m^{-1}=-0.80 MLT/min, respectively. At 70° MLAT, this corresponds to a motion of 16.4 km/s and 7.6 km/s, respectively. For both events, the transition onset was generally identified by an enhancement in ΔH to more negative values prior to 12 MLT, and to more positive values after 12 MLT, consistent with enhancements of the westward and eastward electrojets.

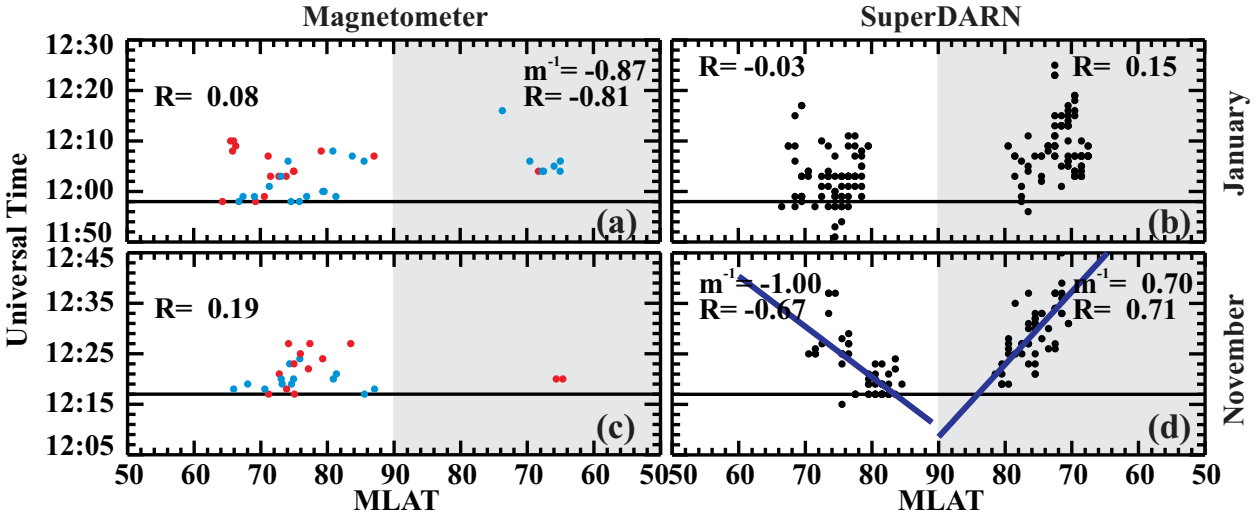

Figure 5.15: Ionospheric onset time of the southward transition wavefront in terms of MLAT as determined by (a,c) ΔH and (b,d) SuperDARN gridded l-o-s velocity for the (a,b) January 20, 2001 and (c,d) November 02, 2001 events. Data is separated for the dayside (10 MLT $\pm$ 6 MLT) and nightside (22 MLT $\pm$ 6 MLT) (grey shading). Red (blue) filled circles in a and c indicate changes in ΔH to more positive (negative) values. Horizontal lines plotted at (a,b) 11:58 UT and (c,d) 12:17 UT indicate the expected onset time. Additional lines show the best-fit line to the data set.

SuperDARN data also indicate a correlation between the ionospheric onset and the MLT location of observation (R=-0.56 and R=-0.66)(Figures 5.14 b and d). Transition onsets were clearly identified in the velocity measurements at 171 and 116 grid points. For the January event, the ionospheric response is first observed between 08 and 11 MLT at the expected onset time. As time progresses, the ionospheric onset is observed closer to midnight, reaching 00 MLT after 5-20 minutes according to the spread of the data, or 13 minutes according to the best-fit line. The best-fit line for the November data indicates a delay of 17 minutes between the time the response is observed near noon and at midnight. The rate of change of the observed response was -0.91 MLT/min and -0.66 MLT/min for the January and November events, respectively. At 70° MLAT, this corresponds to a progression away from noon at a rate of 9.0 km/s and 6.6 km/s, respectively.

The MLAT of measurement coordinates was examined for dependencies with the ionospheric onset time (see Figure 5.15). Data was separated for the dayside and nightside. Although the best-fit line to the MLT diagram suggests an initial onset of 12 MLT, the spread in the data suggests an onset nearer to 10 MLT. The dayside and nightside were

therefore defined as 10 MLT ± 6 MLT and 22 MLT ± 6 MLT. Based on magnetometer data, there is no correlation between MLAT and the ionospheric onset time; correlation is low on the dayside (R=0.08 and R=0.19), and there is an insufficient number of points on the nightside. The SuperDARN data set is much larger, and there appears to be a trend of increasing delay away from the high-latitude region poleward of 80° MLAT. The trend is unclear for the January event (R=0.03 on the dayside and R=0.15 on the nightside). The low correlation is due to the overlapping of points between 12:00 UT and 12:18 UT that is not obvious in the diagram. For the November event, there is a good correlation on both the dayside (R=0.67) and the nightside (R=0.70). The slope of the best-fit line to the data indicates an equatorward progression of $m^{-1} = 1.00°$ MLAT/min (1.9 km/s) on the dayside and $m^{-1} = 0.70°$ MLAT/min (1.3 km/s) on the nightside.

5.2.6 Response of the CPCP determined using a joint velocity and magnetometer data set

Thus far, the evolution of the plasma flow observed at various magnetic latitudes in different MLT sectors has been examined. The next step is to study the response of the ionospheric convection pattern as a whole. The overall strength of the convection pattern in response to changes in the IMF may be determined by examining the CPCP throughout each transition event. Convection maps were generated in two-minute intervals based on the average gridded l-o-s velocity measured by SuperDARN, DMSP measurements for a six-minute interval centered over the two-minute interval, and the average magnetometer perturbation based on the techniques described in Section 4.4 using the SCHA-2 technique with $K_{max} = 6$ and $\theta_c = 35°$. Vortices of the dawn and dusk cell of the two-cell component of the convection pattern having anti-sunward flow over the polar cap were identified.

Figure 5.16a shows the MLT location of the dawn (black) and dusk (blue) convection vortices for the January 20, 2001 event. Gaps in the plots indicate periods where the map was insufficiently constrained by data so that one or both convection foci could not be reliably mapped. Prior to the initial southward transition, the dawnside convection vortex was located at 02 MLT. At the southward turning the dawnside vortex shifted westward to

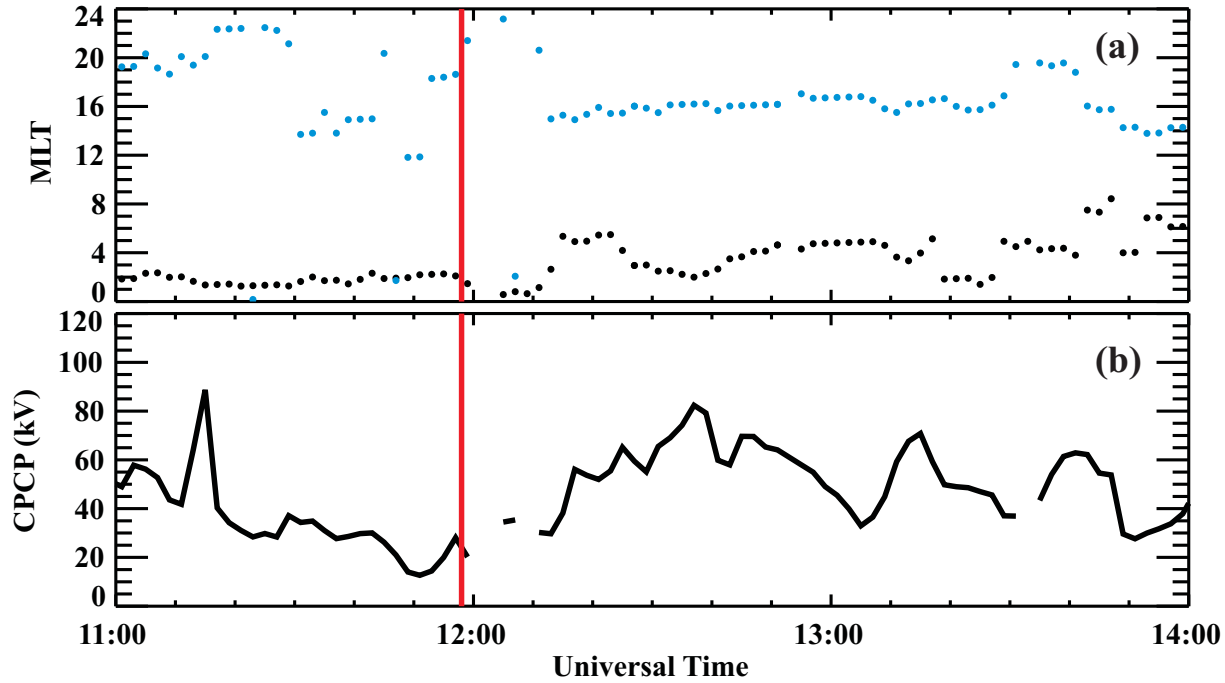

Figure 5.16: (a) MLT location of the dawn (black) and dusk (blue) convection vortices and (b) CPCP measured between vortices on January 20, 2001. Convection patterns were determined using the SCHA-2 technique based on SuperDARN, DMSP, and magnetometer observations with K_{max}=6 and $\theta_c = 35°$. The red vertical lines indicate the expected onset of the transition wavefront.

01 MLT over a period of six minutes, and then reversed and moved eastward to settle at ∼ 04 MLT approximately 16 minutes after the southward transition. At 13:16 UT, the vortex shifted from 04 to 01 MLT over 8 minutes where it remained until 13:38 UT. The location of the duskside convection vortex was more variable. After the southward transition, the location of the vortex stabilized at ∼16 MLT, with some variation after 13:40 UT.

Figure 5.17a shows the MLT location of the dawn and dusk convection vortices for the November 02, 2001 event. Prior to 12:17 UT, when the IMF was northward, the dawnside convection cell was located close to midnight. Approximately 16 minutes after the expected onset, the convection vortex shifted eastward to 05 MLT. As with the January event, the location of the duskside convection cell was more erratic prior to the expected onset of the southward transition. However, at the expected onset, the duskside convection cell began an eastward motion from 20 MLT at 12:16 UT to 16 MLT 19 minutes later. The duskside convection cell remained near 16 MLT until ∼13:40 UT when it began a gradual shift toward 19 MLT.

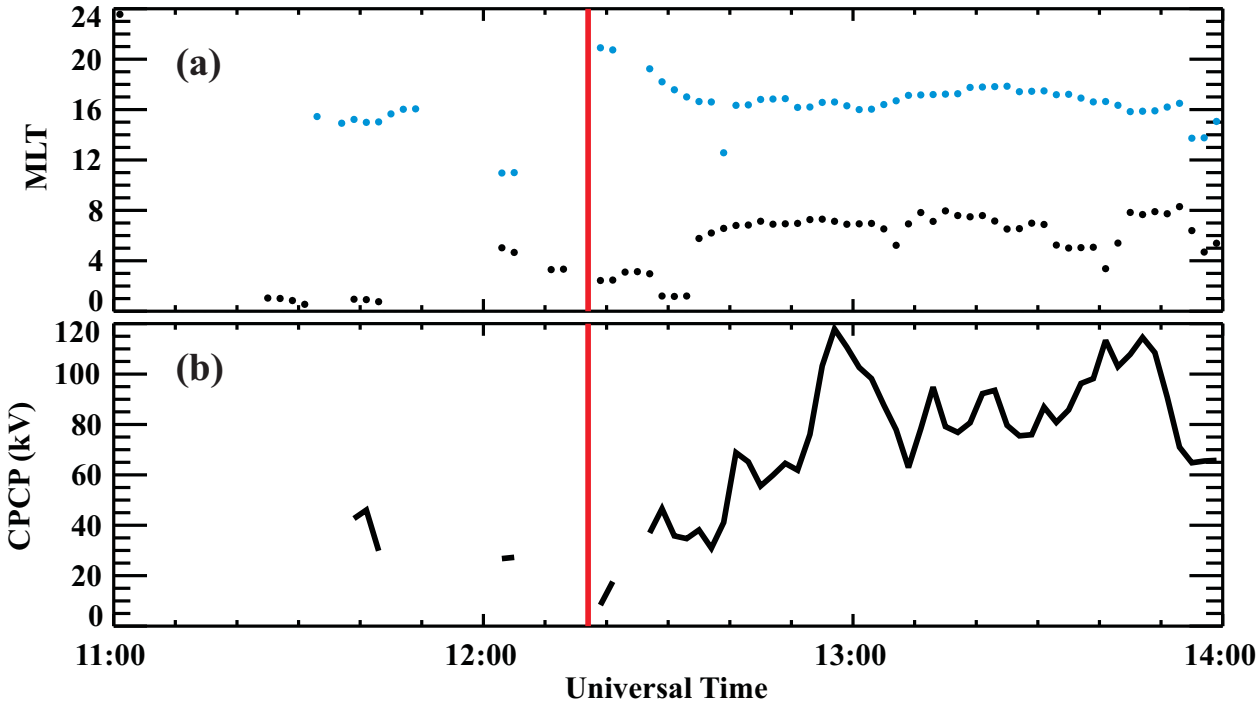

Figure 5.17: Same as Figure 5.16, but for the November 02, 2001 event.

There are similarities in the motion of the dawnside and duskside convection vortices for the January and November events. For periods of northward IMF, the dawnside convection foci was located close to midnight. The southward transition marked an eastward progression of the vortex, which reached a steady position close to 06 MLT. For the January event, the motion of the dawnside convection vortex from 01 to 05 MLT over 14 minutes following the southward transition corresponds to an average eastward propagation of 6.9 km/s at 70° MLAT. For the November event, the transition from 02 to 06 MLT over a 16 minute interval corresponds to an average eastward propagation of 6.0 km/s. For both events, the location of the duskside convection cell was highly variable for periods of northward IMF prior to the transition. For $B_z > 0$, the vortex was located closer to midnight than for periods of $B_z < 0$, where the convection vortex seemed to settle near 16 MLT for both cases.

Figure 5.16b shows the magnitude of the CPCP measured between the dawn and duskside convection vortices for the January 20, 2001 event. During the period of northward IMF, the CPCP was < 40 kV. The CPCP began a gradual enhancement just prior to the expected onset reaching 82.4 kV in the 12:36-12:38 UT interval.

Figure 5.17b shows the CPCP for the November 02, 2001 event. Unlike the January event, there are large gaps in the plot where the convection could not be reliably determined due to gaps in the data. During the period of northward IMF prior to 12:17 UT, the CPCP appeared to be < 40 kV. The expected onset marks the start of an increase in the CPCP which peaked at 117.9 kV in the 12:56-12:58 UT interval.

Based on the statistical model of *Ruohoniemi and Greenwald* (1996), the southward transitions studied here would correspond to a change in the CPCP from 27 kV to 57 kV for the January event, and 14 kV to 62 kV for the November event. Although both events showed an instantaneous response, as seen by the start of an increase in the magnitude of the CPCP, there was a delay in the time to reach a maximum value. For the January event the CPCP increased from 20.2 kV to 68 kV over a 38 minutes, and for the November event the CPCP increased from 8.3 kV to 117.9 kV over 43 minutes.

5.2.7 Analysis of the residual convection pattern

Changes in the ionospheric convection pattern are better visualized by considering the residual of the convection pattern. *Lu et al.* (2002) created such maps for a southward turning event based on magnetometer data and the AMIE convection mapping technique. They created a base convection pattern over a 12 minute interval of steady northward IMF and subtracted the base pattern from the following maps over the transition period. They observed the instantaneous (< 3 min) development of a two-cell convection pattern following the southward turning. The foci of the emerging dusk and dawn convection cells snapped to their final locations following the ionospheric onset of the transition with no indication of the dayside-to-nightside propagation indicated by Scenario 1 of the convection reconfiguration described in Section 5.1. *Ridley et al.* (1998) similarly examined residual convection maps for a number of northward and southward turning events based on magnetometer data. They also observed an instantaneous development of a two-celled convection pattern which enhanced with time, without any propagation of the dawn or dusk convection foci. By examining the value of the residual CPCP, they determined that the convection pattern took $\sim$17 (13) minutes to reach a final steady state for a northward (southward) transition.

Residual convection maps were generated for both the January and November events discussed above using a joint velocity and magnetometer data set (Figure 5.18 and 5.19, respectively). Red shading in Figure 5.18 and 5.19 highlight the emergence of a dawnside residual convection cell. The first map in Figure 5.18 shows the base convection pattern for the January event. The base pattern is an average of 5 two-minute convection maps from 11:42-11:52 UT. Prior to the ionospheric onset of the southward IMF transition, the residual convection patterns are unstructured (not shown), similar to the maps shown for 11:58, 12:00, and 12:02 UT. A positive cell initially forms at 12:04 UT with a vortex approximately centered at 01 MLT and 70° MLAT. The positive cell increases in size and shifts both poleward and eastward over the next 4 intervals. At 12:14 UT, a second vortex becomes visible at 07 MLT and 75° MLAT. This vortex marks the maximum of the dawnside convection cell, which is clearly observed in the 12:16 and 12:18 UT intervals. After 12:14 UT, the location of the convection vortex remains constant, but the convection cell itself continues to evolve, becoming stronger and more defined.

The base plot in Figure 5.19 for the November event is taken over 5 two-minute intervals beginning at 12:02 UT. The ionospheric onset of the southward transition is a two-stage process with sharp transitions at 12:17 UT and 12:21 UT. In this example, two positive dawnside vortices of equal magnitude develop at 12:22 UT just poleward of 70° MLAT centered near 03 MLT and 07 MLT. The motion of the dawnside positive cells marks the emergence of the dawnside cell of a typical two-cell convection pattern 4-6 minutes after the initial 12:17 UT transition. In the next interval, the nightside vortex disappears, and between 12:24 UT and 12:30 UT the dayside vortex shifts to $\sim$ 10 MLT and to 75° MLAT. By 12:34 UT the dawnside convection cell reaches a steady location at 09 MLT and $\sim$ 75° MLAT where it remains in the following two intervals.

According to Figure 5.17a, the dawnside convection vortex is located near midnight ($<$ 04 MLT) between 12:18 UT and 12:32 UT, which contradicts the dayside location of the vortex to the residual convection cell. The SCHA-2 convection maps used to generate the statistics in Figure 5.17a indicate vortices in both the dawn and afternoon sectors throughout the interval. The cell closer to midnight is slightly stronger (by $<$ 3 kV) and was therefore selected to represent the location of the convection vortex in Figure 5.17. Based on the

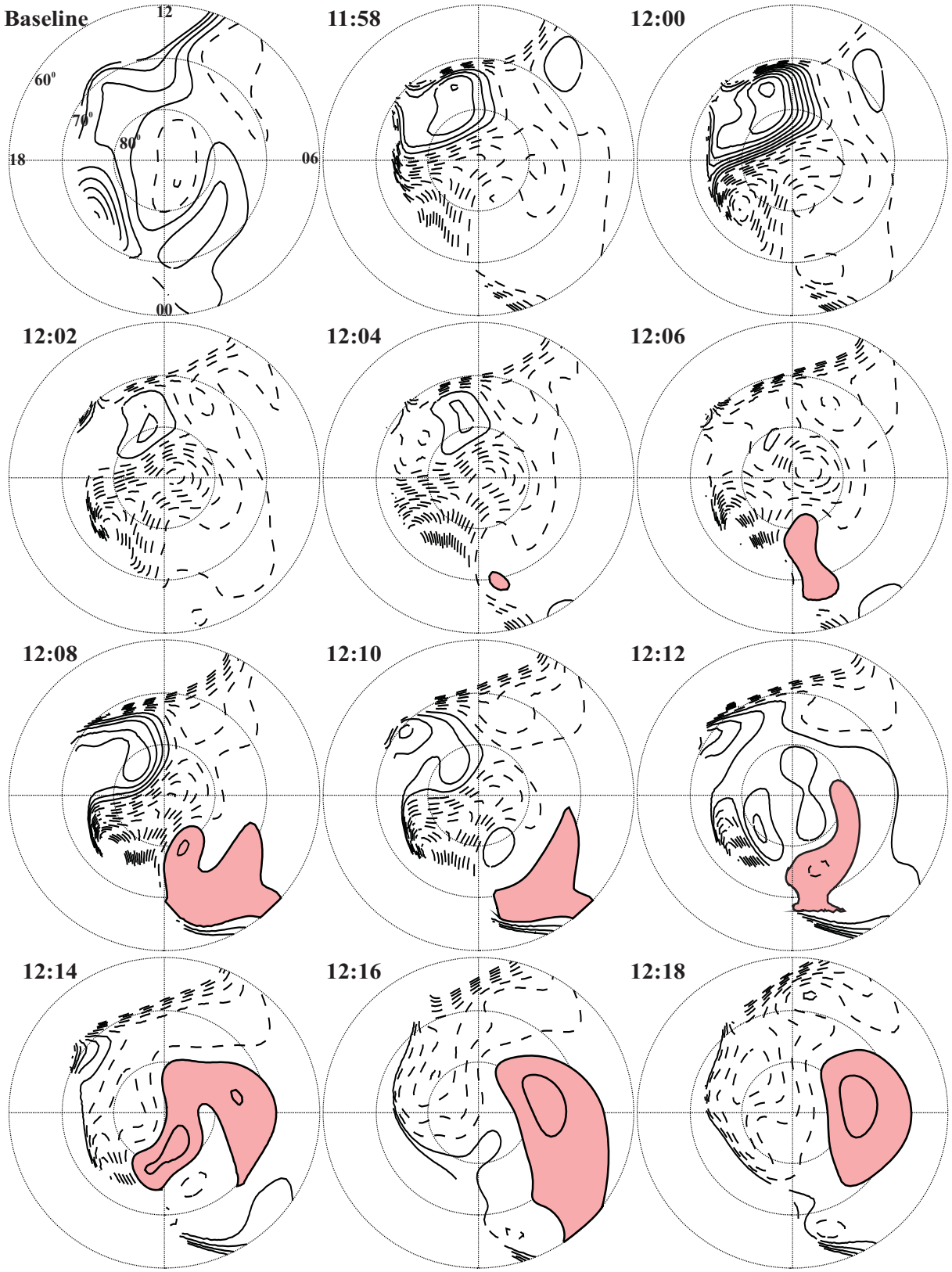

Figure 5.18: Base and residual convection patterns for the January 20, 2001 event. The expected onset occurs at ∼11:58 UT. Solid (dashed) contours indicate negative (positive) residuals and are spaced at 6 kV intervals.

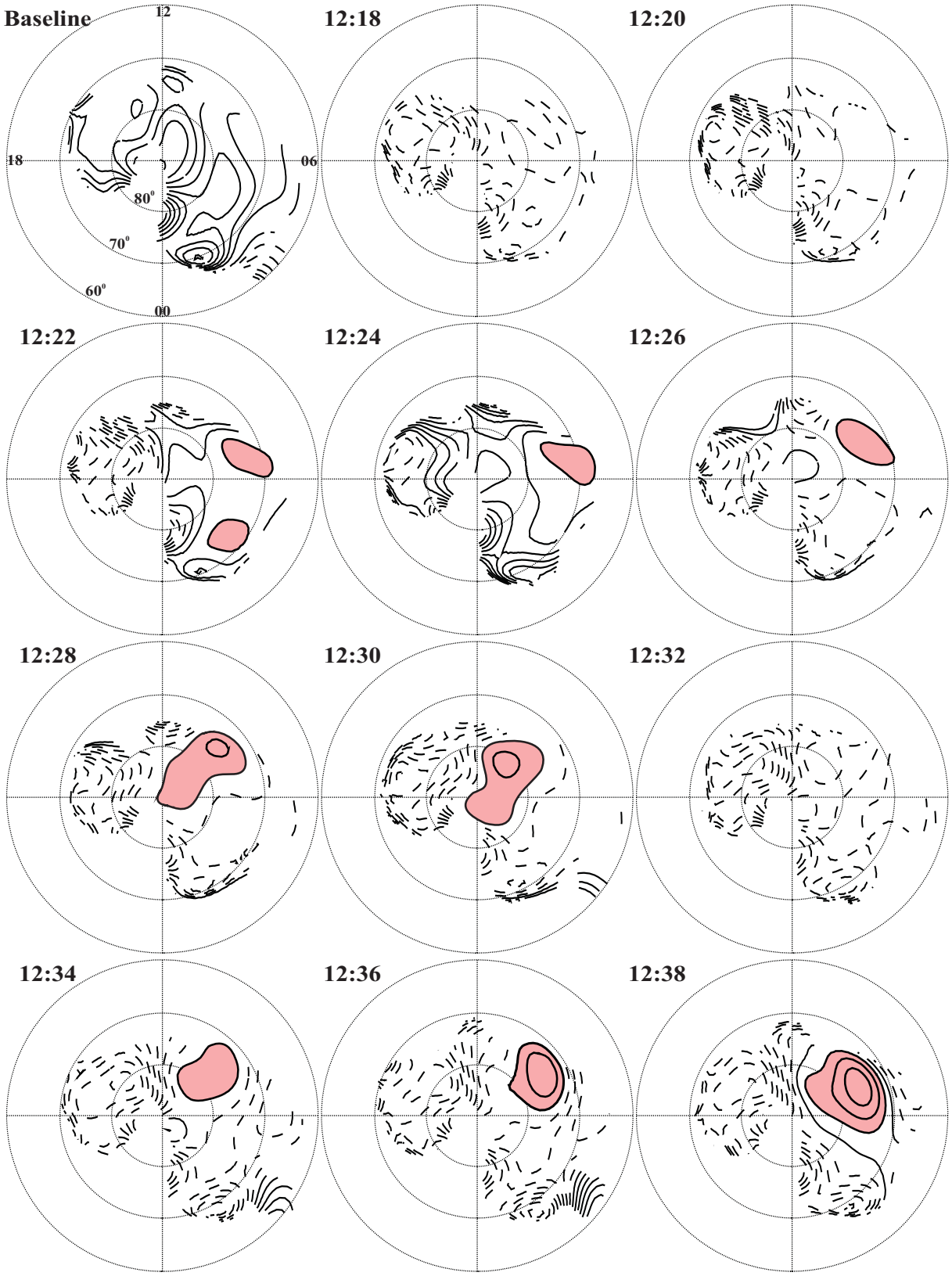

Figure 5.19: Base and residual convection patterns for the November 02, 2001 event. The expected onset occurs at ∼12:17 UT. Solid (dashed) contours indicate negative (positive) residuals and are spaced at 6 kV intervals.

residual diagram, it is evident that the sunward motion of the convection cell is much faster than predicted by the vortex information alone. However, neither plot indicates a settling of the dawnside vortex to a final location until 12:34 UT.

The residual convection pattern clearly shows that the two-cell convection pattern typical for periods of southward IMF develops over a period of time. After the transition, the dawnside vortex takes 4-6 minutes to form, and then 10-12 minutes to move to a final location. For the January event, the dawnside vortex initially formed near midnight and moved sunward. For the November event, the dawnside vortex immediately formed on the dayside and the movement toward a final location was less dramatic than for the January event.

5.3 Discussion

The focus of this work has been to examine the restructuring of the plasma flow after a sudden southward turning in the IMF B_z by identifying the ionospheric region where the reconfiguration begins, and inferring the duration of the restructuring process. Simultaneous radar and magnetometer measurements and maps of the ionospheric convection pattern have been examined. Through comparing the results observed with those cited in past literature, the following picture of the convection reconfiguration emerges.

5.3.1 Progression of the ionospheric response

Descriptions of the reconfiguration process in past literature disagree over whether the initial ionospheric response occurs on the dayside near noon and progresses toward midnight (Scenario 1), or occurs simultaneously across the entire convection zone (Scenario 2). To examine discrepancies between scenarios, the ionospheric response observed by individual magnetometer stations and SuperDARN radar grid cells was examined.

The ionospheric response to the expected arrival of the transition wavefront was observed as an increase in the magnetic field perturbation or velocity, sometimes accompanied by a change in polarity, consistent with the observations of *Lockwood et al.* (1986), *Cowley and Lockwood* (1992), *Saunders et al.* (1992), *Ruohoniemi and Greenwald* (1998), *Shepherd*

et al. (1999), *Huang et al.* (2000),*Lu et al.* (2002), and *Nishitani et al.* (2002). Depending on the location of individual SuperDARN and magnetometer measurements, a delay was observed between the expected onset and the time the ionospheric response was first observed. Based on magnetometer data the response ranged from 0-18 minutes for the January event and 0-10 minutes for the November event, in agreement with the 11 minute delay observed by *Lockwood et al.* (1986) for two stations at 14 MLT, and the 05-15 minute delays observed by *Saunders et al.* (1992) in the 06-14 MLT sectors. The spread in the SuperDARN data was greater with delays of ∼0-30 minutes observed. *Huang et al.* (2000) reported delays of 5-9 minutes, which is consistent with the average spread of the SuperDARN data shown in Figures 5.14 b and d. For both magnetometer and SuperDARN data, the shortest delays were observed within two hours of 10 MLT with delay time increasing toward midnight. The corresponding dayside-to-nightside progression of the ionospheric response was 9.0-16.4 km/s for the January event and 6.6-7.6 km/s for the November event, faster than the 1-5 km/s reported in the literature (*Lockwood et al.*, 1986; *Cowley and Lockwood*, 1992; *Saunders et al.*, 1992; *McWilliams et al.*, 2001b; and *McWilliams et al.*, 2001a).

Lockwood et al. (1986) observed an initial response that occurred at the 10 MLT sector instead of the 12 MLT sector. They explain this by the tilt of the convection pattern with respect to the noon-midnight meridian, so that the throat of the convection flow follows the 10-22 MLT meridian. Based on the pattern of convection shown in Figure 5.7 and Figure 5.12, our results are consistent with this explanation. It might also be noted that for these events, the tilt angle (α) of the IMF wavefront, as calculated using the methods of *Weimer et al.* (2003) and *Weimer* (2004) was $\alpha_x = 60^\circ$ (55°), $\alpha_y = 26^\circ$ (-26°) and $\alpha_z = 14^\circ$ (-22°) in the GSM coordinate system for the January (November) event. For both events, α_x indicates the wavefront hits the magnetopause in the 10 MLT sector. For the event discussed in *McWilliams et al.* (2001a) and *McWilliams et al.* (2001b), the IMF was similarly skewed toward the morning sector, but they observed an initial response to a southward turning closer to 12 MLT.

Figure 5.20 shows a two-dimensional representation of the delay between the expected and ionospheric onsets based on a SuperDARN/magnetometer data set. For the January event, observations along the 10 MLT meridian are observed before those near the 12 MLT

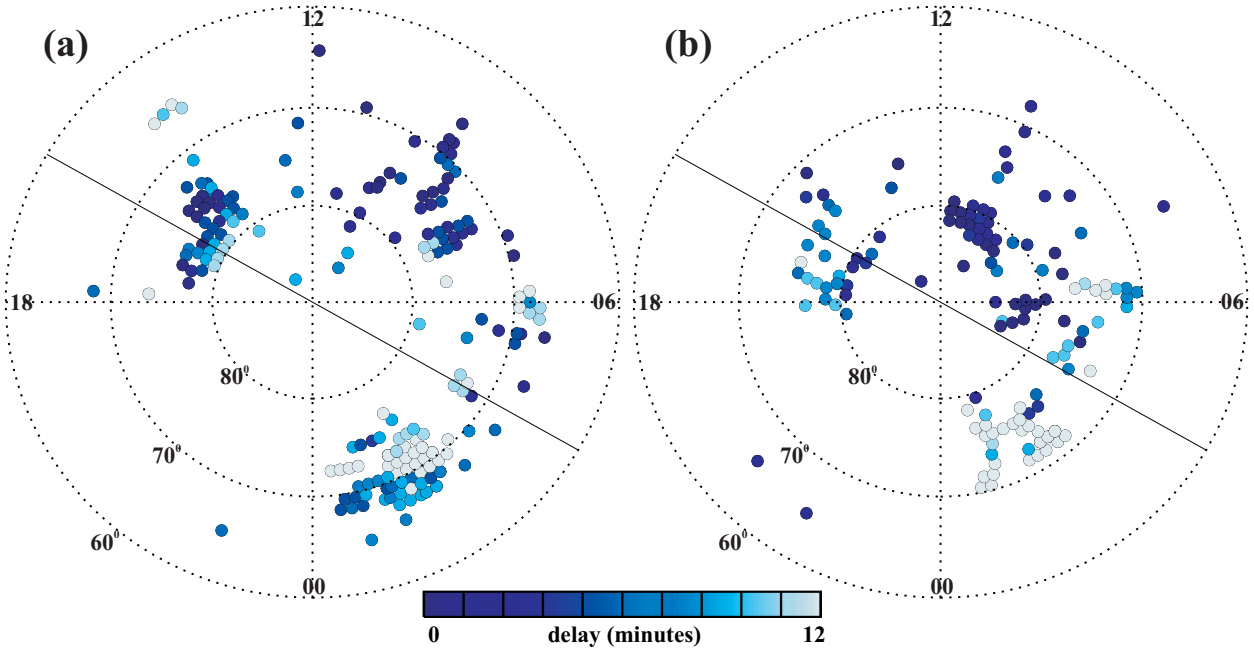

Figure 5.20: Delay between the expected and ionospheric onset in MLT/MLAT AACGM coordinates, as reported by magnetometer and SuperDARN instruments for (a) January 20, 2001 and (b) November 02, 2001.

meridian. For the November event, there is a cluster of points located in the 10-12 MLT region at 80° MLAT which indicate short delay times. It is difficult to resolve the actual location of the initial response as points are not as well distributed at lower latitudes.

The delay observed in Figure 5.20 b shows an equatorward progression of the ionospheric response in the 08 MLT sector for the November event. Similar trends are noted in Figure 5.15 on the nightside for the January event and on both the dayside and nightside for the November event. Such observations are based on SuperDARN measurements and involve an equatorward propagation from latitudes as high as 85° at the expected onset to latitudes of 66° MLAT on both the dayside and the nightside. This effect was only observed in the SuperDARN data set. The question arises as to whether the progression is a true phenomenon or originates from the limited latitudinal band of echo detection and temporal shifts in the band location.

Figure 5.21 and Figure 5.22 show range-time-intensity plots of the l-o-s velocity observed by the Kodiak radar in beams 12 and 05 for the January and November events, respectively. For the January event, the echo occurrence band expands equatorward after the expected onset from 68.5° MLAT at 12:18 UT to 65° MLAT at 12:22 UT, a rate of

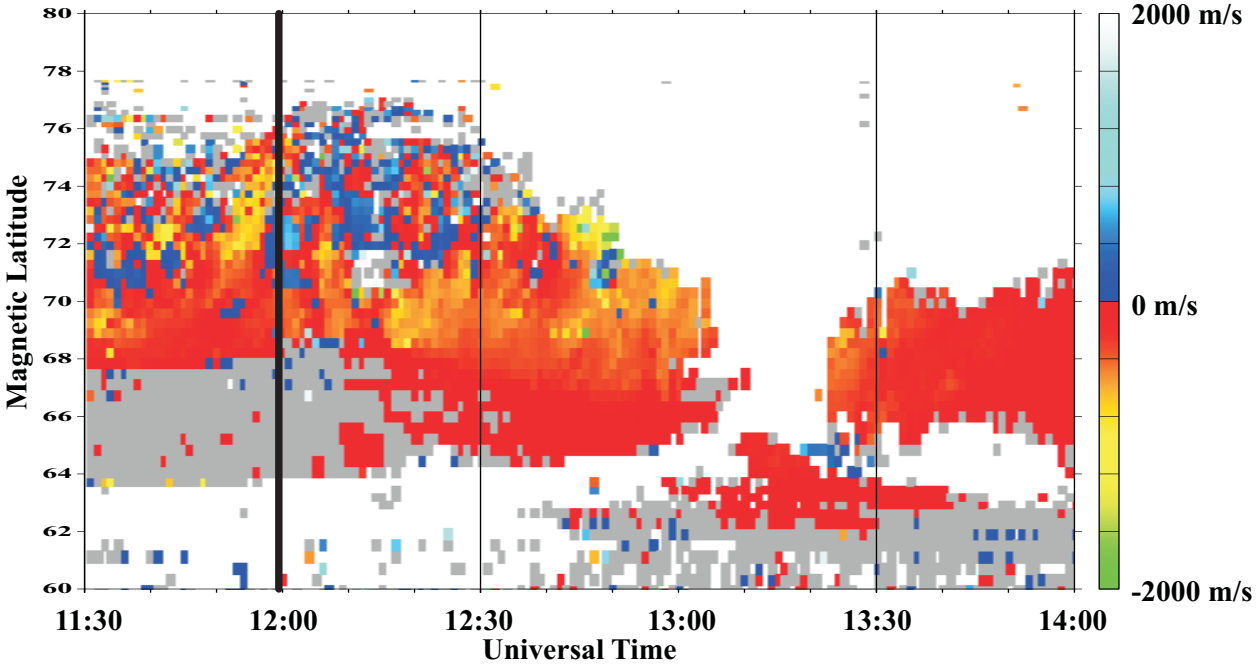

Figure 5.21: RTI plot of the Kodiak l-o-s velocity in beam 12 for January 20, 2001. A heavy black line marks the expected onset.

0.875 MLAT/min. For the November event the echo occurrence band expands from 71.5° at 12:18 UT to 69.5° 6 minutes later, corresponding to a rate of 0.33 MLAT/min which is much slower than the equatorward progression of 0.7-1.00 MLAT/min inferred from SuperDARN velocities. Although the rates do not agree, it is likely that part of the progression effect can be attributed to an expansion in the overall SuperDARN radar field-of-view. *Nishitani et al.* (2002) observed a similar equatorward expansion in the overall echo band at a rate of 3.8 km/s (2.1 MLT/min) in the echo occurrence observed on the dayside by the Saskatoon radar, and attributed the effect to a shift of the cusp to more equatorward latitudes. For this event a similar effect was not observed in the ionospheric echoes of the dayside radars, despite the large occurrence of velocity measurements in the cusp region.

The observed dayside-to-nightside increase in the onset delay time is consistent with the first scenario of ionospheric reconfiguration (*Lockwood et al.*, 1986; *Cowley and Lockwood*, 1992; *Saunders et al.*, 1992). This dayside-to-nightside progression contradicts the results of *Lu et al.* (2002) and *Nishitani et al.* (2002) which describe Scenario 2 of the convection configuration and observed simultaneous responses across the entire high-latitude region in both magnetometer and SuperDARN data sets, and *Ruohoniemi and Greenwald* (1998)

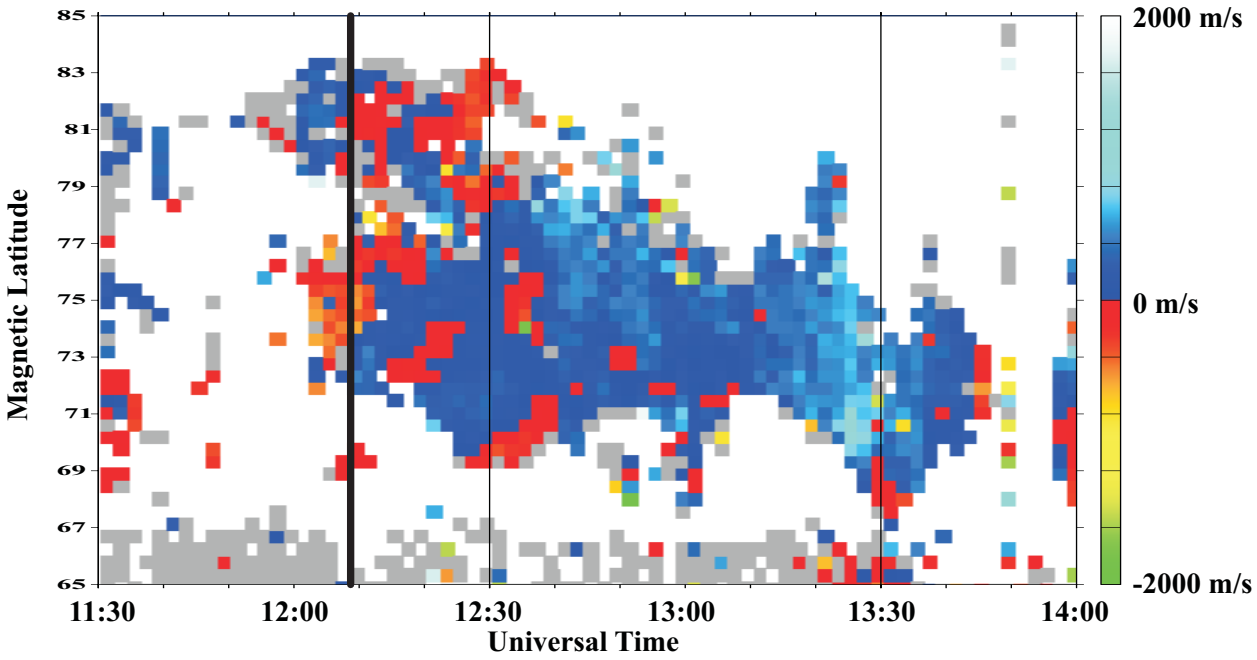

Figure 5.22: RTI plot of the Kodiak l-o-s velocity in beam 05 for November 02, 2001. A heavy black line marks the expected onset.

and *Shepherd et al.* (1999) who observed a simultaneous (within two minutes) response in SuperDARN l-o-s velocities distributed in MLT. It should be noted that conclusions from past literature describing Scenario 1 are based on limited data sets, as opposed to those describing Scenario 2. It is therefore significant that both events from this study, which contain a large number of observations, follows the first scenario of convection reconfiguration.

5.3.2 Duration of the reconfiguration process

Duration of the ionospheric reconfiguration process can be broken into 2 parts: (1) the delay between the expected onset and motion of the dawn and dusk convection cells, and (2) the overall enhancement of the convection pattern.

Prior to the IMF transition, convection was multi-celled, with the two-celled component of the pattern compressed on the nightside and reverse convection cells on the dayside. Approximately 4-6 minutes after the expected onset, the dawnside convection vortex shifted from 01-02 MLT to 05-06 MLT over 14-16 minutes. For the November event, the dawnside vortex simultaneously formed both in the early morning sector and on the dayside 04-06 minutes after the expected onset, and then remained on the dayside undergoing small cor-

rections to its location until a final position was reached after 08-10 minutes. These results agree with *Cowley and Lockwood* (1992), *Hairston and Heelis* (1995) *Ridley et al.* (1998), *Huang et al.* (2000), and *Nishitani et al.* (2002) who reported delays ranging from 10 to 25 minutes from the initial onset for the convection pattern to reach its final configuration. The convection vortices do not appear to 'snap' to their final positions as was reported by *Ridley et al.* (1998), *Lu et al.* (2002), and *Yu and Ridley* (2009).

Both the January and November events show similar trends in the CPCP in response to the change in polarity of the IMF B_z. The sudden transition from northward to southward IMF was marked by an immediate increase in the CPCP. This is in agreement with *Shepherd et al.* (1999), *Huang et al.* (2000), and *Nishitani et al.* (2002) who observed enhancements in the convection pattern associated with the ionospheric onset of a southward transition. Although the initial response was immediate, 38-43 minutes elapsed before the CPCP reached a peak value, whereas the IMF transition occurred over a period of < 5 minutes. The 4-6 minute delay in the formation of the dawnside convection cell observed in the residual plots contradicts the immediate CPCP increase shown in Figures 5.16 and 5.17. The immediate reaction of the CPCP is likely driven by activity on the dayside which coincided with the expected onset of the transition wavefront. Although the response is immediately recognized in the CPCP, the global convection pattern does not immediately change, and the delay in the observed initial formation of the two-cell convection pattern typically observed for periods of southward IMF could be due to inertial effects, such as the flywheel effect discussed in *Ruohoniemi and Baker* (1998) and *Hairston and Heelis* (1995).

5.3.3 Process of reconfiguration

Freeman (2003) explains that the two scenarios of the convection response to a southward turning previously described in the literature are similar. Both involve a convection reconfiguration having an average reconfiguration time of 10-15 minutes. Under the first regime, which he calls the 'Cowley and Lockwood paradigm', the convection pattern immediately reconfigures to a two-celled pattern and the convection foci move azimuthally away from noon toward midnight. The convection enhances over the reconfiguration period. Under the second 'Ridley et al. paradigm', the convection pattern immediately reconfigures to its final

two-celled state, and enhances over the reconfiguration period without a propagation of the convection foci. *Freeman* (2003) states that velocity-time (or equivalently magnetic field-time) studies of the ionospheric response to IMF transitions are too subjective. *Freeman* (2003) proposes models describing each of the two scenarios and demonstrates that the convection determined following these models are consistent with the two paradigms described. *Freeman* (2003) proposes that Scenario 2 is actually a special case of Scenario 1 in which the convection foci jump to their final locations.

Observations of the convection reconfiguration for the events described in this thesis do not fully agree with either Scenario 1 or Scenario 2. Magnetometer and SuperDARN results do suggest a dayside-to-nightside progression of the convection response, consistent with the first part of Scenario 1. However, there was not an associated dayside-to-nightside progression of the convection foci. Observations here suggest the convection foci progress from the nightside, where they are located during the period of northward IMF, toward the dayside. This contrasts with Scenario 2 where the convection foci immediately jump to their final locations. After the observed progression, the convection strength enhances, in agreement with Scenario 2. Based on the partial agreement observed between Scenario 1 and 2, we are inclined to agree with *Freeman* (2003) that the two proposed scenarios of convection reconfiguration overlap.

Shifting of the convection foci from the nightside to the dayside in the residual convection patterns is a significant observation as it is consistent with motion suggested by the statistical models of *Ruohoniemi and Greenwald* (2005) and the more recent model of *Pettigrew et al.* (2010). In this study the IMF changed from IMF B_y=3 nT and IMF B_z=5 nT to IMF B_y=5 nT and IMF B_z=-5 nT for the January event and IMF B_y=5 nT and IMF B_z=7 nT to IMF B_y=5 nT and IMF B_z=-7 nT for the November event. The *Ruohoniemi and Greenwald* (2005) and *Pettigrew et al.* (2010) models indicate an expected shift in the dawnside convection foci from 03 MLT to 05 MLT for $5 \leq B_T \leq 10$ nT. For the events discussed here, the observed shift was from 01 MLT to 07 MLT (January) and 03 MLT to 09 MLT (November). Discrepancies could be attributed to filtering procedures used in creating the statistical models. Both *Ruohoniemi and Greenwald* (2005) and *Pettigrew et al.* (2010) require the IMF conditions persists for at least 36 minutes for data to be included in the

statistical model. Under these circumstances, data associated with all IMF transitions would be disregarded. This being said, one would expect the dawn and dusk convection foci to be located where anticipated by the statistical model when the convection is in a quasi-steady state 30 minutes prior to and after the IMF transition. Looking at the locations of the dawn and duskside foci plotted in Figures 5.16 and 5.17, one can see that when the IMF is in a quasi-steady state prior to the transitions, the dawnside convection cells are located at 02 and 01 MLT for the January and November events, respectively. After the transition the foci settle at 04 and 06 MLT. These results are in closer agreement with *Ruohoniemi and Greenwald* (2005) and *Pettigrew et al.* (2010).

To understand the reconfiguration of the high-latitude plasma flow, a time line of the observed responses has been constructed, see Figure 5.23. Coincident with the expected arrival of the transition wavefront a dayside-to-nightside progression was observed in both magnetometer and SuperDARN data lasting 13-17 minutes, and the CPCP began to increase, peaking after 38-43 minutes. Approximately 4-6 minutes after onset, the dawnside convection cell began an eastward motion from a location near noon, eventually settling near 06 MLT.

Based on these results, the convection reconfiguration can be described as a two-stage process. The first stage (Stage 1) lasts ∼18 minutes. Within this time, the ionospheric response is observed across the entire high-latitude region, beginning on the dayside. The reverse convection cells typical for periods of northward IMF are over-powered and absorbed into the two-cell convection pattern and the dawnside and duskside convection cells shift sunward to a final location at ∼06 and 17 MLT, respectively. In the second stage (Stage 2), which lasts approximately 25 minutes, the overall strength of the convection increases, as is evident by enhancements in the CPCP and the magnitude of the plasma flow.

Overall enhancements in the convection velocity and CPCP have been observed in association with substorm related processes. *Provan et al.* (2004) generated maps of the average convection pattern based on 67 individual substorms (by epoch analysis) for periods of southward IMF (∼-2 nT). They show that the substorm growth phase lasts 18-20 minutes and is characterized by enhancements in the anti-sunward flow over the polar cap and an equatorward motion of the radar backscattering region, ending at the substorm expansion onset. The expansion onset is followed by an immediate suppression of plasma flow on the

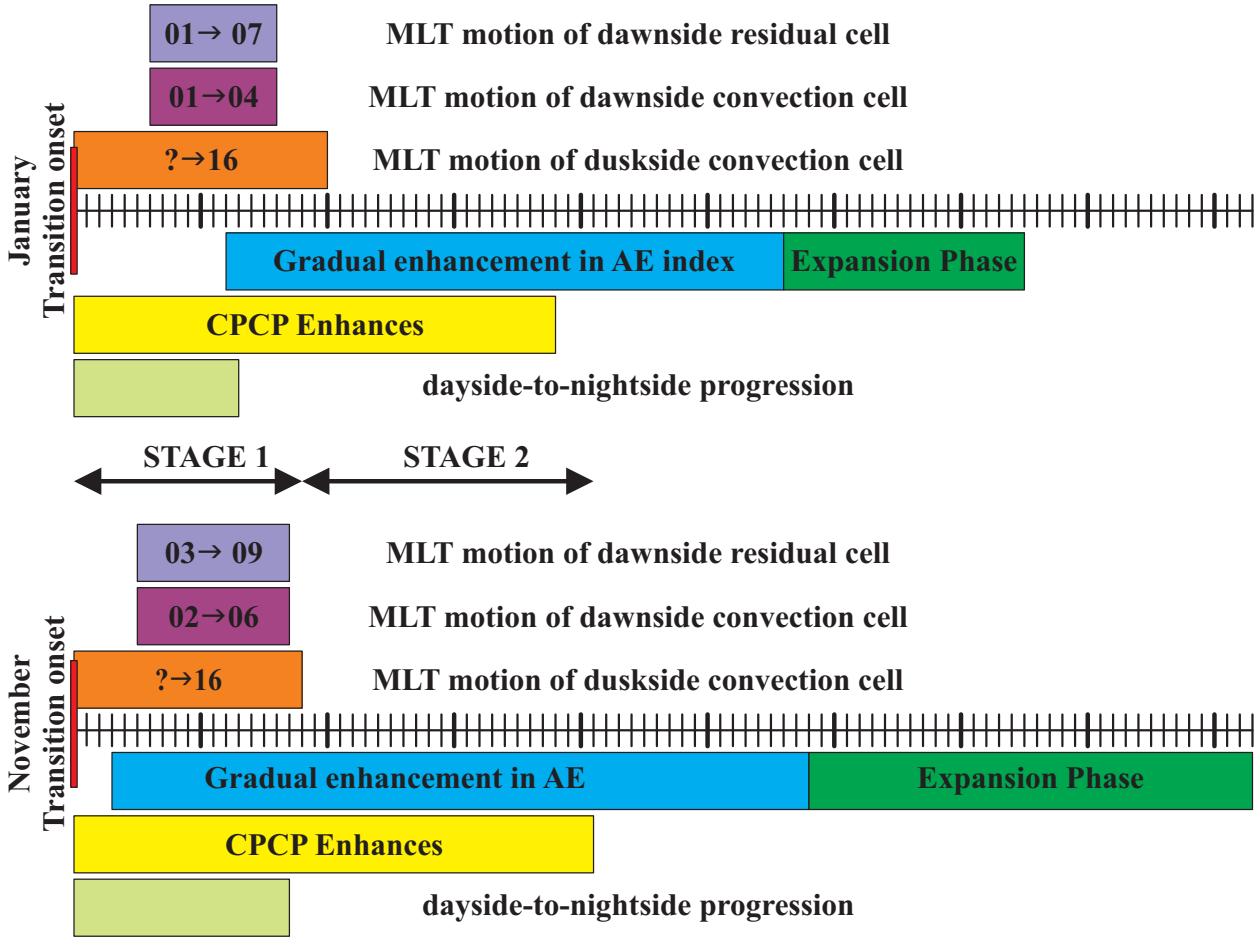

Figure 5.23: Time line of the magnetometer, SuperDARN, and convection response to a sudden southward transition in the IMF for events on (top) January 20, 2001 and (bottom) November 02, 2001.

nightside, a subsequent overall intensification of the flow, and an enhancement of the CPCP. The CPCP quickly increased from 40 kV two minutes prior to the expansion onset to 75 kV, 14 minutes later. For the events in this study, the expansion onset began 56 minutes (January) and 43-73 minutes (November) after the transition onset, well after an enhancement in the CPCP and an equatorward expansion of the radar backscatter region were observed to begin, and after the completion of both Stage 1 and Stage 2 of the reconfiguration process. The significant delay between the transition onset and the expansion onset, and the low magnitude of the AE index (<60 nT) prior to the expansion onset (which implies the transitions do not occur during the recovery phase of a previous substorm) suggests the observed response to the southward turning is not due to the energy transfer (magnetosphere

to ionosphere) associated with the expansion onset. However, based on the evaluation of *Provan et al.* (2004), the substorm growth phase is expected to begin during Stage 2, and although it is likely that the observed effects to the southward transition are directly driven by the solar wind-magnetosphere-ionosphere interaction rather than the observed substorm, contributions from a substorm related process cannot be entirely ruled out for the events selected in this study.

The idea of a two-stage convection response is consistent with observations by *Nishitani et al.* (2002). According to their results, the first stage of the response is the immediate formation of the convection foci. In the second stage, the overall convection pattern intensifies over a period of 25 minutes. Our two-stage process is similar, except we observed a delay of 4-6 minutes in the initial formation of the convection foci. We propose that the reconfiguration process observed by *Nishitani et al.* (2002) is the same process observed here with a delay of 0 minutes in the formation of the convection cells. This 0 minute delay is probably related to the relative magnitude of the transition response observed by magnetometer stations. The reason for the differences are possibly related to the relative magnitude of the IMF B_z before and after the transition. For the January event the IMF B_z changes from +5 nT to -5 nT and for the November event the change is from +7 nT to -6 nT, whereas the event described in *Nishitani et al.* (2002) involved a more sizeable transition from +6 nT to -19 nT.

The reconfiguration process described here can be explained by considering how details of the IMF are communicated between the solar wind, magnetosphere, and ionosphere. *Cowley and Lockwood* (1992) describe the transfer of information in the magnetosphere-ionosphere system using an open flux tube concept. In the high-latitude region the ionospheric plasma flow is driven by electric fields established by the interaction of the IMF and the Earth's magnetosphere, which is largely parameterized by the orientation of the IMF. When the IMF is southward, reconnection occurs on the front-side magnetosphere and open magnetic field lines are driven anti-sunward across the polar cap, which causes anti-sunward flow across the polar ionosphere. Open magnetic field lines eventually reconnect in the magnetotail creating closed field lines which are driven toward the Earth and into the front-side magnetosphere. The corresponding electric fields in the magnetosphere are mapped into the auroral ionosphere and drive plasma sunward. The high-latitude ionosphere can therefore

be thought of as containing three interconnected electrical circuits located over the (1) polar cap (corresponding to anti-sunward directed flow) and (2) the dawnside and (3) duskside auroral zones (corresponding to sunward directed flow). The combination of flow in these regions leads to the familiar two-cell convection pattern that has been referenced throughout this work.

Based on this description, *Cowley and Lockwood* (1992) points out that the convection in the coupled magnetosphere-ionosphere system is dependent on two driving forces. The first driving force is the dayside reconnection rate which directly drives the cross-polar cap flow and is strongest when the IMF is directed southward. The second driving force is magnetotail reconnection which drives the auroral return flow and is in general delayed from the IMF driving the front-side reconnection. The delay between front-side and magnetotail reconnection can be accounted for by the time it takes open flux tubes to travel between reconnection points. For a solar wind speed of roughly 300-400 km/s (approximately true for both the January and November events) and approximating the magnetopause location at 8 R_e sunward of the Earth and a magnetotail neutral line between 50 and 100 R_e on the nightside, the delay time is 15-38 minutes, in agreement with estimates by *Cowley and Lockwood* (1992). *Cowley and Lockwood* (1992) estimate the transfer of information from the magnetotail neutral point to the ionosphere at $\sim$10 minutes, based on a return speed of 1000 km/s (Alfven speed). Using a magnetotail neutral point of 50-100 R_e, we find the delay to be $\sim$5-10 minutes, making the total delay between front-side reconnection and an ionospheric response in the auroral zone roughly 20-48 minutes.

The two-stage reconfiguration process identified can be explained by the open flux tube model. In Stage 1, the arrival of the southward oriented IMF at the magnetopause corresponds to increased reconnection on the front-side magnetosphere leading to an injection of open magnetic field lines which travel along the direction of noon-midnight flow (in this case the 10/22 MLT meridian) toward the nightside. The open magnetic field lines travel through the polar magnetosphere and into the magnetotail where reconnection occurs. Stage 1 lasts $\sim$18 minutes. Recalling that the expected onset was calculated by assuming a 5 minute travel time between the magnetopause and ionosphere, a rough estimate of the delay between the dayside reconnection and the expected ionospheric response is 23 minutes, which falls

within the estimated range of 20-48 minutes. Stage 1 involves the complete transformation of information from the front-side reconnection point, across the polar cap, to the magnetotail reconnection point, and back to the ionosphere. Stage 2 of the reconfiguration process begins once the IMF transition is communicated to the ionosphere from the magnetotail following reconnection at the magnetotail neutral point. There is an overall enhancement of the convection pattern until a steady state is reached.

Using the open flux transportation model, one might expect the dayside-to-nightside progression to be limited to the axis of noon-midnight flow. However, Figure 5.20 shows that the dayside-to-nightside progression is also seen in the distribution of points in the 68°-80° MLAT region. One might also expect that the dawn and dusk cells of the two-cell convection pattern would not move sunward until the start of Stage 2. The open flux transportation model is simplified, whereas in reality the polar and auroral circuits are electrically linked so that changes to the cross-polar flow are projected to auroral latitudes.

5.4 Summary and conclusions

In this Chapter, the reconfiguration of the ionospheric convection pattern associated with a southward turning of the IMF was studied using SuperDARN and magnetometer measurements. The following points can be made:

1. The ionospheric onset of the southward turning of the IMF was indicated by an enhancement in the perturbation magnetic field. The delay in the observation of such enhancements with the expected arrival time of the transition wavefront was shortest ($<$ 1 minute) at 10 MLT and largest (9-12 minutes) at 14 MLT. Enhancements were observed at auroral latitudes in the 03 and 05 MLT sectors, but at higher latitudes in the 10 and 14 MLT sectors. In general, the magnitude of the maximum perturbation decreased with decreasing latitude.

2. The ionospheric onset of the southward transition was indicated by an increase in the SuperDARN velocity magnitude and/or a reversal in the direction of the velocity. Grid cells located on the nightside more often observed magnitude enhancements without

associated direction reversals. The delay between the expected arrival time of the ionospheric onset and a response varied from 0 to 20 minutes, with shorter delays observed in the 09-15 MLT region and longer delays closer to 02 MLT.

3. For both magnetometer and SuperDARN data sets, the initial onset was observed near noon and was coincident with the expected arrival time of the transition wavefront. The ionospheric response to the southward transition then propagated toward the nightside, reaching midnight 8 and 17 minutes later for the January and November events, respectively. The dayside-to-nightside progression is consistent with the first scenario of ionospheric reconfiguration.

4. Convection maps generated using the SCHA-2 technique showed that prior to the southward transition, the vortex of the dawnside convection cell was located close to midnight. After the southward transition, the vortex of the dawnside cell shifted eastward from 01-02 MLT and settled at 05-06 MLT within 14-16 minutes. The location of the vortex of the duskside convection cell was erratic during periods of northward IMF, but settled at 16 MLT within $\sim$16 minutes of the southward transition.

5. For periods of northward IMF, the CPCP was < 40 kV. A southward transition in the IMF was immediately marked by an increase in the CPCP which reached a peak value after $\sim$40 minutes. The potential increase was slow for the first $\sim$15 minutes and more rapid afterwards.

6. We suggest that convection reconfiguration following a southward turning of the IMF is a two-stage process. In the first stage, the transition wavefront impinges on the front-side magnetosphere near noon, dragging open field lines across the polar cap and into the magnetotail. Newly formed closed magnetic field lines return to the Earth communicating the IMF transition to ionosphere after 20-48 minutes. Stage-1 processes include a dayside-to-nightside progression of the ionospheric onset over the polar cap and the shift of the two-cell convection pattern from the nightside to the dayside. In Stage 2 the entire convection pattern enhances.

Chapter 6

Conclusions and suggestions for future research

In this thesis, spherical cap harmonic analysis techniques were developed to produce high-latitude ionospheric convection patterns from ground-based SuperDARN HF radar and magnetometer data. A validation of the new method of convection mapping was performed. The SCHA technique was combined with other approaches to (1) investigate the relationship between the average transpolar flow velocity and CPCP to the magnetometer-based PCN magnetic index, and (2) study the high-latitude convection response to a sharp transition in the IMF B_z from stable positive to stable negative values.

6.1 Conclusions

Conclusions are made on each of the objectives of this thesis separately.

6.1.1 Spherical cap harmonic analysis of SuperDARN observations for generating maps of ionospheric convection

1. Previous work (*Drayton et al.*, 2005) showed that SuperDARN l-o-s velocities reasonably agree with DMSP ion drifts for regions of smooth spatial and temporal variations. However, in this thesis, it was shown that convection vectors derived using the FIT mapping technique are reduced in magnitude compared to direct measurements of the ion drift made by the DMSP satellite. This reduction was attributed to internal processes of the FIT technique, such as the addition of a statistical convection model

to constrain regions void of observations, and forcing the convection and electrostatic potential to zero at the pre-determined boundary of the convection zone. Such actions are necessary in the FIT-technique to obtain a global solution to the convection pattern regardless of the data distribution, but compromise the accurate depiction of convection over more localized regions.

2. A spherical cap harmonic analysis (SCHA) method was introduced as a new technique for mapping the ionospheric convection pattern based on SuperDARN plasma velocity measurements. Two methods were developed for mapping convection with (SCHA-1) and without (SCHA-2) applying a zero-potential constraint at the boundary of the convection zone. The SCHA-1 and SCHA-2 techniques were shown to reproduce expected convection patterns regardless of whether the arbitrarily generated test pattern was characterized at points either uniformly distributed across the high-latitude region or at the possible location of radar observations.

3. Using real measurements for periods of good SuperDARN data coverage, the SCHA-2 technique produced convection maps that were consistent with expectations for various orientations of the IMF B_y and B_z.

4. During periods of smooth temporal and spatial variations of the flow, convection vectors determined using the SCHA-2 technique were shown to reasonably agree with DMSP ion drift vectors. As an additional test, convection vectors derived using the SCHA-2 technique were compared to velocity vectors determined using the SuperDARN merge technique. Events were selected for two cases: (1) where SuperDARN measurements were both numerous and widespread, and (2) where SuperDARN measurements were limited to a localized region of fast flow. For both cases, convection vectors inferred using the SCHA-2 and merge techniques were shown to agree.

5. The SCHA-2 and FIT techniques were shown to produce comparable results for convection maps generated over regions of good data coverage during periods of smooth spatial and temporal variations of the flow. However, the SCHA-2 technique provided a better representation of the convection flow for localized regions of variable plasma flow.

Based on these results it can be concluded that both the SCHA-1 and SCHA-2 techniques are suitable for mapping the ionospheric convection pattern based on SuperDARN velocity data.

6.1.2 Deriving convection patterns from magnetic perturbation data

1. It was shown that the SCHA-2 technique as applied to ground-based magnetometer data is similar to the SECS approach and is expected to produce comparable results in terms of equivalent currents. The SCHA-2 method was expanded to derive the electric field and plasma velocity patterns solely from magnetic perturbations recorded on the ground under the assumption that the conductivity distribution is known.

2. Perturbation, equivalent, and conductance-based convection vectors were determined based solely on magnetometer data and compared to convection vectors derived from SuperDARN data based on the FIT technique. For K_p=2-4, all three convection estimates showed reasonable agreement with the SuperDARN-inferred convection vectors. The perturbation convection map showed the best agreement; processing the data using the SCHA-2 technique did not improve the agreement.

Based on these results, it can be concluded that magnetometer data can be used to produce convection maps. However, for the current station coverage (<100 stations), and the available models of conductivity distribution, the quality of the inferred maps does not provide significant improvement over the perturbation vectors. Magnetometer data would be best used in combination with the SuperDARN data set to create a joint convection map.

6.1.3 Deriving convection patterns based on both magnetometer and radar data

An SCHA-based technique was developed for combining magnetometer and velocity data sets to infer a global convection pattern. For a single event having excellent radar coverage, it was shown that the addition of magnetometer data to the SuperDARN data set had little

influence on the resulting convection pattern. A more comprehensive study, especially for periods of low or moderate radar coverage is left for future work.

6.1.4 PCN magnetic index, CPCP and average velocity of transpolar flows

Comparison of the PCN magnetic index to the cross polar cap velocity (CPCV) measured by the Rankin Inlet SuperDARN radar and to the CPCV and CPCP calculated from SuperDARN-inferred convection maps showed that

1. For a data set where the PCN<4, both the CPCV and CPCP linearly increased with increasing PCN for $0 \leq$ PCN $\leq$3. As PCN increased, the rate of velocity increase slowed, indicating the onset of saturation.

2. For an increased data set with PCN index ranging from 0 to 14, it was shown that the CPCP linearly increased with increasing PCN index for $PCN < 4$. As PCN increased above 4, the CPCP saturated at 80 kV.

3. For a subset of the increased data set, there was a linear relationship between the FIT and SCHA-derived CPCP with a tendency for the SCHA-derived CPCP to be larger. The CPCP calculated using the SCHA-2 technique was shown to increase linearly with increasing PCN index for $PCN < 3$. For larger PCN, there was evidence of saturation at 90-100 kV, but the effect was less obvious than for the FIT-based data set.

Based on these results, it can be concluded that the PCN magnetic index adequately asses the strength of the ionospheric convection for $0 \leq$ PCN ≤ 4.

6.1.5 Magnetometer and radar study of the ionospheric convection response to a sudden southward turning of the IMF

1. The ionospheric onset of the IMF B_z southward turning was observed as an enhancement of the H-component of the perturbation magnetic field for stations spread along

the 03, 05, 10, and 14 MLT sectors. The delay in the observed response from the expected arrival time of the transition wave front was shortest (<1 minute) in the 10 MLT sector (expected sector of IMF impact with magnetopause) and largest (9-12 minutes) in the 14 MLT sector.

2. The ionospheric onset of the IMF B_z southward turning was observed as an increase in the SuperDARN velocity magnitude, or a reversal in the velocity polarity. The delay between the expected arrival time of the transition wave front and the observed response varied from 0 to 20 minutes. The shortest delays were observed in the 09-15 MLT sector, and the longest delays were observed near 02 MLT.

3. For both magnetometer and SuperDARN data sets, the ionospheric response to the arrival of the transition wavefront was shown to propagate from 10 MLT toward the nightside.

4. According to global convection maps generated with the SCHA-2 technique, the dawnside convection vortex shifted eastward (toward noon) from 01-02 MLT and settled at 05-06 MLT after 14-16 minutes from the onset of the ionospheric response. The duskside convection vortex settled at 16 MLT within 16 minutes of the onset. The arrival of the southward transition was marked by an immediate increase of the CPCP from ∼40 kV prior to the transition to a peak value of approximately 60 kV ∼40 minutes later.

5. Analysis of residual convection maps confirmed that the convection vortices do not simply 'snap' to a final position, as claimed in a number of previous studies. It was shown that the dawnside convection vortex first appeared 4-6 minutes after the transition onset and moved toward noon, reaching its final configuration after 8-10 minutes.

Based on the above points, it can be concluded that the convection reconfiguration associated with a southward turning of the IMF is a two-stage process. In the first stage (∼18 minutes), the reverse convection cells associated with the northward IMF break down and the foci of the new Dungey convection pattern are established on the nightside and shift

toward the dayside. The reconfiguration process involves all MLT sectors. In the second stage (∼25 minutes) the overall convection pattern experiences a simple intensification.

6.2 Suggestions for future work

There are several ways in which the work presented can be expanded. Of particular interest is the further improvement of the SCHA-2 technique in the analysis of SuperDARN and magnetometer data. There are several approaches to consider.

6.2.1 Comparison of the SCHA-2 and SECS techniques for mapping ionospheric convection based on SuperDARN measurements

Recently, *Amm et al.* (2010) reported a technique for mapping the ionospheric convection pattern from SuperDARN velocity measurements using a Spherical Elementary Current Systems (SECS) approach. This is an expansion of previously published work where the SECS approach was applied to magnetic data. *Amm et al.* (2010) state that the SECS technique is not limited to a spherical cap (the high-latitude region) and is able to generate convection vectors directly over the region of measurement based entirely on measurements without contributions from a statistical model or boundary conditions. Note that similar statements were made in this thesis regarding the SCHA-2 technique. *Amm et al.* (2010) tested the performance of the SECS technique by comparing convection determined using the SECS technique to convection estimated using the SuperDARN merge technique. They showed that SECS convection vectors had a better agreement with merged vectors than convection vectors determined using the SuperDARN FIT technique.

The SECS and SCHA-2 techniques were discussed in Chapter 4. It was argued that the SECS and SCHA-2 techniques are comparable for generating global-scale maps of the ionospheric convection pattern. It would be highly desirable to test this statement by repeating the comparison performed in *Amm et al.* (2010) using convection vectors calculated with the SCHA-2 technique. A collaborative project with Olaf Amm has been discussed.

6.2.2 Determination of ionospheric convection based on measurements from the Swarm satellite

In 2012 the European Space Agency plans to launch the Swarm satellite mission to provide a survey of the geomagnetic field and a global representation of its variation on time scales from hours to years (*Friis-Christensen et al.*, 2006; *Friis-Christensen et al.*, 2008). The Swarm mission will comprise a side-by-side lower pair of polar orbiting satellites at an altitude of 450 km and a single higher altitude satellite at 530 km. Each satellite will carry a Canadian Electric Field Instrument (EFI) to make continuous observations of the ionospheric plasma drift at a sampling resolution of 16 Hz. Such a resolution corresponds to roughly 20, 000 measurements across the high-latitude region for each satellite, making it possible to examine the plasma flow along the satellite track in detail

The SCHA convection mapping technique will be of particular benefit in mapping measurements from the Swarm satellites over a localized region where the upper and lower satellites cross. Preliminary work on limited data sets has shown that the combination of Swarm and SuperDARN data sets increases both the region of convection constrained by measurements, and the accuracy of the resultant convection maps that could be generated based on data from either instrument alone. An expansion of this work is currently underway.

6.2.3 Evaluating the contribution of magnetometer data to convection mapping

In Chapter 4, a technique for generating global-scale convection maps by combining measurements of the plasma drift and perturbations of the Earth's magnetic field was developed. It was argued that although the magnetometer data set does not contain enough information to create a detailed convection map on its own, it can serve as a constraint to the SuperDARN data set where there are gaps in the data. Examples presented in this thesis came from a data set where there was significant radar coverage, and the effect of adding the magnetometer data set was minimal in the resulting convection maps. Additional events should be considered for data sets where the radar coverage is poor. The quality of convection mapping

can be further improved by adding contributions from magnetometer data from satellites. An excellent data source to be explored is the Iridium satellite project. There are currently >70 Iridium satellites in polar orbits at 780 km in altitude flying in 6 different orbital planes (*Anderson et al.*, 2008). Currently, magnetic data are provided at a resolution of 1 sample every 19.4 s (every 1° MLAT) with occasional periods of high resolution data with 1 sample every 2 s (every 0.1° MLAT)

Future work would involve a detailed analysis of the effect of adding magnetometer data to the SuperDARN data set by comparing convection derived with and without the magnetometer data. To determine whether or not the resultant convection is improved with the addition of magnetometer data, a comparison should be made to a direct measurement of the plasma flow, as might be provided by the DMSP or Swarm satellites.

6.2.4 Potential science topics

Several examples of potential research projects in which the SCHA technique would be advantageous are suggested.

1. Expansion of the IMF transition study: The study of the ionospheric response to transitions in the IMF B_z should be expanded to include more cases. Effects of northward transitions and of the IMF B_y would be interesting topics of investigation.

2. Structure of plasma flows equatorward of the auroral oval: The current statistical convection model does not include measurements at low geomagnetic latitudes. Because of low echo occurrence rates, it would take several years for an appropriate data base to be accumulated. Meanwhile, processing data with SCHA can be performed on a routine basis.

3. Convection patterns within the polar cap: For the current period of low magnetic activity, the majority of SuperDARN echoes are obtained in the polar cap. For such conditions, the FIT technique is inappropriate as it relies on restrictions to the plasma flow at the low-latitude boundary. Development of a regional polar cap convection model is suggested.

4. Geomagnetically induced current hazard assessment: Coronal mass ejections from the sun cause shock-waves in the solar wind. When the enhanced plasma reaches the Earth, there is a temporary enhancement in the magnetopause current, as is evident by a temporary intensification in the magnitude of the magnetic field observed at low-latitude magnetometer stations and can be followed by a geomagnetic storm. Geomagnetic storms induce currents in long conductors such as power systems or pipelines potentially causing damage. Studying the response of the magnetopause current (from ground-based magnetometers) and the ionosphere (from maps of the ionospheric convection inferred from SuperDARN data using SCHA) to sudden storm commencement signatures is suggested.

References

Amm, O., Ionospheric elementary current systems in spherical coordinates and their applications, *J. Geomag. Geoelectr.*, *49*, 947–955, 1997.

Amm, O., and A. Viljanen, Ionospheric disturbance magnetic field continuation from the ground to the ionosphere using spherical elementary current systems, *Earth Planets Space*, *51*, 431–440, 1999.

Amm, O., A. Grocott, M. Lester, and T. K. Yeoman, Local determination of ionospheric plasma convection from coherent scatter radar data using the SECS technique, *J. Geophys. Res.*, *115*(A03304), doi:10.1029/2009JA014832, 2010.

Anderson, B. J., H. Korth, C. L. Waters, D. L. Green, and P. Stauning, Statistical Birkeland current distributions from magnetic field observations by the Iridium constellation, *Ann. Geophys.*, *26*, 671–687, 2008.

Axford, W. I., and C. O. Hines, A unifying theory of high-latitude geophysical phenomena and geomagnetic storms, *Can. J. Phys.*, *39*, 1433–1464, 1961.

Baker, K. B., and S. Wing, A new magnetic coordinate system for conjugate studies at high latitudes, *J. Geophys. Res.*, *94*(A7), 9139–9143, 1989.

Baker, K. B., R. A. Greenwald, J. M. Ruohoniemi, J. R. Dudeney, M. Pinnock, P. T. Newell, M. E. Greenspan, and C.-I. Meng, Simultaneous HF-radar and DMSP observations of the CUSP, *Geophys. Res. Lett.*, *17*(11), 1869–1872, 1990.

Baumjohann, W., and R. A. Treumann, *Basic Space Plasma Physics*, Imperial College Press, 1997.

Bendat, J. S., *Principles and applications of random noise theory*, John Wiley and Sons, New York, 1958.

Benkevitch, L. V., Effects of ionospheric conductance in high-latitude phenomena, Ph.D. thesis, University of Saskatchewan, 2006.

Bhavnani, K. H., and C. A. Hein, An improved algorithm for computing altitude dependent corrected geomagnetic coordinates, *Tech. Rep. PL-TR-94-2310*, "Phillips Laboratory, "Hanscom AFB, MA, USA", 1994.

Blakely, R. J., *Potential theory in gravity and magnetic applications*, Cambridge University Press, Cambridge, UK, 1995.

Boteler, D. H., and G. J. van Beek, Mapping the March 13, 1989 magnetic storm and its effects across N. America, *Proc. Solar-Terrestrial Predictions Workshop, Ottawa, May 18-22*, *3*, 57–70, 1993.

Boteler, D. H., and G. J. van Beek, August 4, 1972 revisited: A new look at the geomagnetic disturbance that caused the l4 cable system outage, *Geophys. Res. Lett.*, *26*(5), 577–580, 1999.

Brandt, S., *Data Analysis: Statistical and Computational Methods for Scientists and Engineers*, 3 ed., Springer, 1998.

Bullard, E. D., The removal of trend from magnetic surveys, *Earth Planet. Sci. Letts.*, *2*(4), 293–300, 1967.

Campbell, W. H., *Introduction to Geomagnetic Fields*, 2nd ed., Cambridge, 2003.

Cerisier, J.-C., and C. Senior, Merge: A FORTRAN program, *Tech. rep.*, Centre d'Étude des Environnements Terrestres et Planétaires, Cent. Nat. de la Rech. Sci., St-Maur, France, 1994.

Chisham, G., I. J. Coleman, M. P. Freeman, and M. Pinnock, Ionospheric signatures of split reconnection X-lines during conditions of IMF $B_z < 0$ and $| B_y | \sim | B_z |$:Evidence for the antiparallel merging hypothesis, *J. Geophys. Res.*, *107*(A101323), doi:10.1029/2001JA009124, 2002.

Chisham, G., T. K. Yeoman, and G. J. Sofko, Mapping ionospheric backscatter measured by the SuperDARN HF radars - Part 1: A new empirical virtual height model, *Ann. Geophys.*, *26*, 823–841, 2008.

Chisham, G., et al., A decade of the Super Dual Auroral Radar Network (SuperDARN): scientific achievements, new techniques and future directions, *Surveys in Geophysics*, *28*(1), 33–109, doi:10.1007/s10712-007-9017-8, 2007.

Clauer, C. R., and E. Friis-Christensen, High-latitude dayside electric fields and currents during strong northward interplanetary magnetic field: Observations and model simulation, *J. Geophys. Res.*, *93*(A4), 2749–2757, 1988.

Cousins, E. D. P., and S. G. Shepherd, A dynamical model of high-latitude convection derived from SuperDARN plasma drift measurements, *J. Geophys. Res.*, *115*(12), doi: 10.1029/2010JA016017, 2010.

Cowley, S. W. H., and M. Lockwood, Excitation and decay of solar wind-driven flows in the magnetosphere-ionosphere system, *Ann. Geophys.*, *10*, 103–115, 1992.

Danskin, D. W., HF auroral backscatter from the E and F regions, Ph.D Thesis, University of Saskatchewan, 2003.

Danskin, D. W., A. V. Koustov, T. Ogawa, N. Nishitani, S. Nozawa, S. E. Milan, M. Lester, and D. Andre, On the factors controlling occurrence of F-region coherent echoes, *Ann. Geophys.*, *20*, 1385–1397, 2002.

Davies, J. A., M. Lester, S. E. Milan, and T. K. Yeoman, A comparison of velocity measurements from the CUTLASS Finland radar and the EISCAT UHF system, *Ann. Geophys.*, *17*(7), 892–902, 1999.

Davies, J. A., T. K. Yeoman, M. Lester, and S. E. Milan, A comparison of F-region ion velocity observations from the EISCAT Svalbard and VHF radars with irregularity drift velocity measurements from the CUTLASS Finland HF radar, *Ann. Geophys.*, *18*(5), 589–594, 2000.

Drayton, R. A., Study of SAPS-like flows with the King Salmon SuperDARN radar, M.Sc. Thesis, University of Saskatchewan, 2006.

Drayton, R. A., A. V. Koustov, M. R. Hairston, and J.-P. Villain, Comparison of DMSP cross-track ion drifts and SuperDARN line-of-sight velocities, *Ann. Geophys.*, *23*(7), 2479–2486, 2005.

Dungey, J. W., Interplanetary magnetic field and auroral zones, *Phys. Res. Lett.*, *6*, 47–48, 1961.

Fejer, B. G., and M. C. Kelley, Ionospheric irregularities, *Reviews of Geophysics*, *18*, 401–454, 1980.

Fiori, R. A. D., A. V. Koustov, D. Boteler, and R. A. Makarevich, PCN magnetic index and average convection velocity in the polar cap inferred from SuperDARN radar measurements, *J. Geophys. Res.*, *114*(A07225), doi:10.1029/2008JA013964, 2009.

Fiori, R. A. D., D. H. Boteler, A. V. Koustov, G. V. Haines, and J. M. Ruohoniemi, Spherical cap harmonic analysis of SuperDARN observations for generating maps of ionospheric convection, *J. Geophys. Res.*, *115*(A07307), doi:10.1029/2009JA015055, 2010.

Foster, J. C., J. M. Holt, R. G. Musgrove, and D. S. Evans, Ionospheric convection associated with discrete levels of particle precipitation, *Geophys. Res. Lett.*, *13*(7), 656–659, 1986.

Freeman, M. P., A unified model of the response of ionospheric convection to changes in the interplanetary magnetic field, *J. Geophys. Res.*, *108*(A1), doi:10.1029/2002JA009385, 2003.

Friis-Christensen, E., and J. Wilhjelm, Polar cap currents for different directions of the interplanetary magnetic field in the Y-Z plane, *J. Geophys. Res.*, *80*(10), 1248–1260, 1975.

Friis-Christensen, E., M. A. McHenry, C. R. Clauer, and S. Vennerstrøm, Ionospheric traveling convection vortices observed near the polar cleft: A triggered response to sudden changes in the solar wind, *Geophys. Res. Lett.*, *15*(3), 253–256, 1988.

Friis-Christensen, E., H. Lühr, and G. Hulot, Swarm: A constellation to study the Earth's magnetic field, *Earth Planets Space*, *58*, 351–358, 2006.

Friis-Christensen, E., H. Lühr, D. Knudsen, and R. Haagmans, Swarm-An Earth observation mission investigating geospace, *Advances in Space Research*, *41*, 210–216, 2008.

Fukushima, N., Electric current systems for polar substorms and their magnetic effect below and above the ionosphere, *Radio Science*, *6*(2), 269–275, 1971.

Fuller-Rowell, T. J., and D. S. Evans, Height-integrated pedersen and hall conductivity patterns inferred from the TIROS-NOAA satellite data, *J. Geophys. Res.*, *91*(A7), 7606–7618, 1987.

Gillies, R. G., G. C. Hussey, G. J. Sofko, R. A. D. Fiori, K. McWilliams, P. Ponomarenko, and J.-P. St-Maurice, Estimation of the index of refraction in the SuperDARN scattering region using interferometry measurments, *J. Geophys. Res.*, *114*(A07305), doi: 10.1029/2008JA013967, 2009.

Gillies, R. G., G. C. Hussey, G. J. Sofko, D. M. Wright, and J. A. Davies, A comparison of EISCAT and SuperDARN F-region measurements with consideration of the refractive index in the scattering volume, *J. Geophys. Res.*, *115*(6), doi:10.1029/2009JA014694, 2010.

Gillies, R. G., G. C. Hussey, G. J. Sofko, P. V. Ponomarenko, and K. A. McWilliams, Improvement of HF coherent radar line-of-sight velocities by estimating the refractive index in the scattering volume using radar frequency shifting, *J. Geophys. Res.*, *116*(1), doi:10.1029/2010JA016043, 2011.

Gjerloev, J. W., A global ground-based magnetometer initiative, *EOS*, *90*, 230–231, 2009.

Good, G. A., *Encyclopedia of Geomagnetism and Paleomagnetism*, chap. History of Instrumentation, pp. 434–438, Encyclopedia of Earth Sciences, Springer, 2007.

Green, D. L., C. L. Waters, and J. W. Gjerloev, The use of spherical cap harmonic analysis in predicting ground magnetic perturbations from ionospheric electric field and conductance models, in *Australian Institute of Physics 17th National Congress*, p. 308, Brisbane, 2006.

Greenwald, R. A., et al., DARN/SuperDARN: A global view of the dynamics of high-latitude convection, *Space Science Reviews*, *71*, 763–796, 1995.

Gustafsson, G., N. E. Papitashvili, and V. O. Papitashvili, A revised corrected geomagnetic coordinate system for epochs 1985 and 1990, *J. Atmos. Terr. Phys.*, *54*(11), 1609–1631, 1992.

Haines, G., *Encyclopedia of Geomagnetism and Paleomagnetism*, chap. Spherical Cap Harmonics, pp. 395–397, Encylopedia of Earth Sciences, Springer, 2007a.

Haines, G. V., Spherical cap harmonic analysis, *J. Geophys. Res.*, *90*(B3), 2583–2591, 1985a.

Haines, G. V., Spherical cap harmonic analysis of geomagnetic secular variation over Canada 1960-1983, *J. Geophys. Res.*, *90*, 12,563–12,574, 1985b.

Haines, G. V., Computer programs for spherical cap harmonic analysis of potential and general fields, *Computers and Geosciences*, *14*(4), 413–447, 1988.

Haines, G. V., Regional magnetic field modelling: a review, *J. Geomag. Geoelectr.*, *42*, 1001–1018, 1990.

Haines, G. V., Everything you wanted to know about AMIE but were afraid to ask, *Internal report*, Natural Resources Canada, GSC Pacific, 1999.

Haines, G. V., Obtaining electric potential and electric fields on the surface of a spherical cap from SuperDARN velocity data using spherical cap harmonic functions, *Internal report*, Natural Resources Canada, 2007b.

Haines, G. V., and J. M. Torta, Determination of equivalent current sources from spherical cap harmonic models of geomagnetic field variations, *Geophys. J. Int.*, *118*, 499–514, 1994.

Hairston, M. R., and R. A. Heelis, Model of the high-latitude ionospheric convection pattern during southward interplanetary magnetic field using de 2 data, *J. Geophys. Res.*, *95*(A3), 2333–2343, 1990.

Hairston, M. R., and R. A. Heelis, Response time of the polar ionospheric convection pattern to changes in the north-south direction of the IMF, *Geophys. Res. Lett.*, *22*(5), 631–634, 1995.

Hamza, A. M., M. Huber, W. Lyatsky, A. V. Kustov, D. André, and G. Sofko, Eastward convection jet at the poleward boundary of the nightside auroral oval, *Geophys. Res. Lett.*, *27*(17), 2809–2812, 2000.

Hardy, D. A., M. S. Gussenhoven, and E. Holeman, A statistical model of the auroral electron precipitation, *J. Geophys. Res.*, *90*(A5), 4229–4248, 1985.

Hardy, D. A., M. S. Gussenhoven, and R. Raistrick, Statistical and functional representations of the pattern of auroral energy flux, number flux, and conductivity, *J. Geophys. Res.*, *92*(A11), 12,275–12,294, 1987.

Hargreaves, J. K., *The Solar-Terrestrial Environment*, Cambridge University Press, Cambridge UK, 1992.

Heppner, J. P., and N. C. Maynard, Empirical high-latitude electric field models, *J. Geophys. Res.*, *92*(A5), 2267–4489, 1987.

Huang, C.-S., D. Murr, G. J. Sofko, W. J. Hughes, and T. Moretto, Ionospheric convection response to changes of interplanetary magnetic field B_z component during strong B_y component, *J. Geophys. Res.*, *105*(A3), 5231–5243, 2000.

Iijima, T., and T. A. Potemra, Large-scale characteristics of field-aligned currents associated with substorms, *J. Geophys. Res.*, *83*(A2), 599–615, 1978.

Kamide, Y., A. D. Richmond, and S. Matsushita, Estimation of ionospheric electric fields, ionospheric currents, and field-aligned currents from ground magnetic records, *J. Geophys. Res.*, *86*(A2), 801–813, 1981.

Kelley, M. C., *The Earth's Ionosphere: Plasma Physics and Electrodynamics*, Academic Press, 1989.

Khachikjan, G. Y., A. V. Koustov, and G. J. Sofko, Dependence of SuperDARN cross polar cap potential upon the solar wind electric field and magnetopause subsolar distance, *J. Geophys. Res.*, *113*(A09214), doi:10.1029/2008JA013107, 2008.

Kivelson, M. G., and C. T. Russell, *Introduction to Space Physics*, Cambridge University Press, Cambridge UK, 1995.

Koustov, A. V., D. W. Danskin, R. A. Makarevitch, and J. D. Gorin, On the relationship between the velocity of E-region HF echoes and E×B plasma drift, *Ann. Geophys.*, *23*(2), 1–9, 2005.

Koustov, A. V., J.-P. St-Maurice, G. J. Sofko, D. Andre, J. W. McDougall, M. R. Hairston, R. A. Fiori, and E. E. Kadochnikov, Validation of the Rankin Inlet PolarDARN radar velocity measurements, *Radio Science*, *44*(RS4003), doi:10.1029/2008RS004045, 2009.

Lacroix, P. J., and D. R. Moorcroft, Ion acoustic HF radar echoes at high latitudes and far ranges, *J. Geophys. Res.*, *106*(A12), 29,091–29,103, 2001.

Lockwood, M., A. P. van Eyken, B. J. I. Bromage, D. M. Willis, and S. W. H. Cowley, Eastward propagation of a plasma convection enhancement following a southward turning of the interplanetary magnetic field, *Geophys. Res. Lett*, *13*(1), 72–75, 1986.

Lu, G., A. D. Richmond, J. M. Ruohoniemi, R. A. Greenwald, M. Hairston, F. J. Rich, and D. S. Evans, An investigation of the influence of data and model inputs on assimilative mapping of ionospheric electrodynamics, *J. Geophys. Res.*, *106*(A1), 417–433, 2001.

Lu, G., T. E. Holzer, D. Lummerzheim, J. M. Ruohoniemi, P. Stauning, O. Troshichev, P. T. Newell, M. Britnacher, and G. Parks, Ionospheric response to the interplanetary magnetic field southward turning: Fast onset and slow reconfiguration, *J. Geophys. Res.*, *107*(A8), doi:10.1029/2001JA000324, 2002.

Lukianova, R., O. Troshichev, and G. Lu, The polar cap magnetic activity indices in the southern (PCS) and northern (PCN) polar caps: Consistency and discrepancy, *Geophys. Res. Lett.*, *29*(18), doi:10.1029/2002GL015179, 2002.

Makarevich, R. A., A. C. Kellerman, Y. V. Bogdanova, and A. V. Koustov, Time evolution of the subauroral electric fields: A case study during a sequence of two substorms, *J. Geophys. Res.*, *90*(A04312), doi:10.1029.2008JA013944, 2009.

Matsushita, S., Morphology of slowly-varying geomagnetic external fields - a review, *Phys. Earth Planet. Inter.*, *10*, 299–312, 1975.

McWilliams, K. A., T. K. Yeoman, , J. B. Sigwarth, L. A. Frank, and M. Brittnacher, The dayside ultraviolet aurora and convection responses to a southward turning of the interplanetary magnetic field, *Ann. Geophys.*, *19*, 707–721, 2001a.

McWilliams, K. A., T. K. Yeoman, and S. W. H. Cowley, Two-dimensional electric field measurements in the ionospheric footprint of a flux transfer event, *Ann. Geophys.*, *18*, 1584–1598, 2001b.

Milan, S. E., T. K. Yeoman, M. Lester, E. C. Thomas, and T. B. Jones, Initial backscatter occurrence statistics from the CUTLASS HF radars, *Ann. Geophys.*, *15*(6), 703–718, 1997.

Milan, S. E., J. A. Davies, and M. Lester, Coherent HF radar backscatter characteristics associated with auroral forms identified by incoherent radar techniques: A comparison of CUTLASS and EISCAT observations, *J. Geophys. Res.*, *104*(A10), 22,591–22,064, 1999.

Nielsen, E., and K. Schlegel, Coherent radar Doppler measurements and their relationship to the ionospheric electron drift velocity, *J. Geophys. Res.*, *90*(44), 3498–3504, 1985.

Nishitani, N., T. Ogawa, N. Sato, H. Yamagishi, M. Pinnock, J.-P. Villain, G. Sofko, and O. Troshichev, A study of the dusk convection cell's response to an IMF southward turning, *J. Geophys. Res.*, *107*(A3), doi:10.1029/2001JA900095, 2002.

Papitashvili, V. O., B. A. Belov, D. S. Faermark, Y. I. Feldstein, S. A. Golyshev, L. I. Gromova, and A. E. Levitin, Electric potential patterns in the northern and southern polar regions parameterized by the interplanetary magnetic field, *J. Geophys. Res.*, *99*(A7), 13,251–13,262, 1994.

Pettigrew, E. D., S. G. Shepherd, and J. M. Ruohoniemi, Climatological patterns of high-latitude convection in the northern and southern hemispheres: Dipole tilt dependencies

and interhemispheric comparisons, *J. Geophys. Res.*, *115*(A07305), doi:10.1029/JA014956, 2010.

Ponomarenko, P. V., J.-P. St-Maurice, C. L. Waters, R. G. Gillies, and A. V. Koustov, Refractive index effects on the scatter volume location and Doppler velocity estimates of ionospheric HF backscatter echoes, *Ann. Geophys.*, *27*(11), 4207–4219, doi:10.5194/angeo-27-4207-2009, 2009.

Press, W. H., S. A. Teukolsky, W. T. Vetterling, and B. P. Flannery, *Numerical Recipes in C: The Art of Scientific Computing*, 2 ed., Cambridge University Press, 1992.

Provan, G., M. Lester, S. B. Mende, and S. E. Milan, Statistical study of high-latitude plasma flow during magnetospheric substorms, *Ann. Geophys.*, *22*, 3607–3624, 2004.

Rees, M. H., and D. Luckey, Auroral electron energy derived from ratio of spectroscopic emissions, 1, model computation, *J. Geophys. Res.*, *79*, 5181–5186, 1974.

Reiff, P. H., and J. L. Burch, IMF B_y-dependent plasma flow and Birkeland currents in the dayside magnetosphere 2. A global model for northward and southward IMF, *J. Geophys. Res.*, *90*, 1595–1609, 1985.

Rich, F. J., and M. Hairston, Large-scale convection patterns observed by DMSP, *J. Geophys. Res.*, *99*(A3), 3827–3844, 1994.

Rich, F. J., and N. C. Maynard, Consequences of using simple analystical functions for the high-latitude convection electric field, *J. Geophys. Res.*, *94*(A4), 3687–3701, 1989.

Richmond, A. D., Assimilative mapping of ionospheric electrodynamics, *Adv. Space Res.*, *12*(6), 59–68, 1992.

Richmond, A. D., and Y. Kamide, Mapping electrodynamic features of the high-latitude ionosphere from localized observations: technique, *J. Geophys. Res.*, *93*(A6), 5741–5759, 1988.

Ridley, A. J., and E. A. Kihn, Polar cap index comparisons with AMIE cross polar cap potential, electric field, and polar cap area, *Geophys. Res. Lett.*, *31*(L07801), doi: 10.1029/2003GL019113, 2004.

Ridley, A. J., G. Lu, C. R. Clauer, and V. O. Papitashvili, A statistical study of the ionospheric convection response to changing interplanetary magnetic field conditions using the assimilative mapping of ionospheric electrodynamics technique, *J. Geophys. Res.*, *103*(A3), 4023–4039, 1998.

Ruohoniemi, J. M., and R. A. Greenwald, Statistical patterns of high-latitude convection obtained from Goose Bay HF radar observations, *J. Geophys. Res.*, *101*(A10), 22,743–21,763, 1996.

Ruohoniemi, J. M., and R. A. Greenwald, The response of high-latitude convection to a sudden southward IMF turning, *Geophys. Res. Lett.*, *25*(15), 2913–2916, 1998.

Ruohoniemi, J. M., and R. A. Greenwald, Dependencies of high-latitude plasma convection: Consideration of interplanetary magnetic field, seasonal, and universal time factors in statistical pattern, *J. Geophys. Res.*, *110*(A09204), doi:10.1029/2004JA010815, 2005.

Ruohoniemi, M., and K. B. Baker, Large-scale imaging of high-latitude convection with Super Dual Auroral Radar Network HF radar observations, *J. Geophys. Res.*, *103*, 20,797–20,811, 1998.

Saunders, M. A., M. P. Freeman, D. J. Southwood, S. W. H. Cowley, M. Lockwood, J. C. Samson, C. J. Farrugia, and T. J. Hughes, Dayside ionospheric convection changes in response to long-period interplanetary magnetic field oscillations: Determination of the ionospheric phase velocity, *J. Geophys. Res.*, *97*(A12), 19,373–19,380, 1992.

Serson, P. H., An electrical recording magnetometer, *Canadian Journal of Physics*, *35*(12), 1387–1394, 1957.

Shepherd, S. G., and J. M. Ruohoniemi, Electrostatic potential patterns in the high-latitude ionosphere constrained by SuperDARN measurements, *J. Geophys. Res.*, *105*(A10), 23,005–23,014, 2000.

Shepherd, S. G., R. A. Greenwald, and J. M. Ruohoniemi, A possible explanation for rapid, large-scale ionospheric responses to southward turnings of the IMF, *Geophys. Res. Lett.*, *26*(20), 3197–3200, 1999.

Sofko, G. J., and A. Walker, Electric field mapping in a dipole field - a tutorial overview, 2006 SuperDARN workshop, Chincoteague, USA, 2006.

Troshichev, O. A., and V. G. Andrezen, Magnetic activity in the polar cap - a new index, *Planet. Space Sci.*, *36*(11), 1095–1102, 1988.

Troshichev, O. A., H. Hayakawa, A. Matsuoka, T. Mukai, and K. Tsuruda, Cross polar cap diameter and voltage as a function of PC index and interplanetary quantities, *J. Geophys. Res.*, *101*(A6), 13,429–13,435, 1996.

Troshichev, O. A., R. Y. Lukianova, V. O. Papitashvili, F. J. Rich, and O. Rasumussen, Polar cap index (PC) as a proxy for ionospheric electric field in the near-pole region, *Geophys. Res. Lett.*, *27*, 3809–3812, 2000.

Troshichev, O. A., A. Janzhura, and P. Stauning, Unified PCN and PCS indices: Method of calculation, physical sense, and dependence on the IMF azimuthal and northward components, *J. Geophys. Res.*, *111*(A05208), doi:10.1029/2005JA011402, 2006.

Vanhamäki, H., and O. Amm, A new method to estimate ionospheric electric fields and currents using data from a local ground magnetometer network, *Ann. Geophys.*, *25*, 1141–1156, 2007.

Vanhamäki, H., O. Amm, and A. Viljanen, One-dimensional upward continuation of the ground magnetic field disturbance using spherical elementary current systems, *Earth Planets Space*, *55*, 613–625, 2003.

Vennerstrøm, S., and E. Friis-Christensen, Comparison between the polar cap index, PC, and the auroral electrojet indices AE, AL, AU, *J. Geophys. Res.*, *96*(A1), 101–113, doi: 10.1029/90JA01975, 1991.

Villain, J. P., R. A. Greenwald, K. B. Baker, and J. M. Ruohoniemi, HF radar observations of E region plasma irregularities produced by oblique electron streaming, *J. Geophys. Res.*, *92*(A11), 12,327–12,342, 1987.

Villain, J.-P., R. André, M. Pinnock, R. A. Greenwald, and C. Hanuise, A statistical study of the Doppler spectral width of high-latitude ionospheric F-region echoes recorded with SuperDARN coherent HF radars, *Ann. Geophys.*, *20*(11), 1769–1781, 2002.

Watanabe, M., and G. J. Sofko, Synthesis of various ionospheric convection patterns for imf B_y-dominated periods: Split crescent cells, exchange cells, and theta aurora formation, *J. Geophys. Res.*, *113*(A09218), doi:10.1029/2007JA012868, 2008.

Watanabe, M., and G. J. Sofko, The interchange cycle - a fundamental mode of magnetic flux circulation for northward interplanetary magnetic field, *Geophys. Res. Lett.*, *36*(L03107), doi:10.1029.2008GL036682, 2009.

Weimer, D. R., Models of high-latitude electric potentials derived with a least error fit of spherical harmonic coefficients, *J. Geophys. Res.*, *100*(A10), 19,595–19,607, 1995.

Weimer, D. R., Correction to - Predicting interplanetary magnetic field (IMF) propagation delay times using the minimum variance technique, *J. Geophys. Res.*, *109*(A12104), doi: 10.1029/2004JA0010691, 2004.

Weimer, D. R., Predicting surface geomagnetic variations using ionospheric electrodynamic models, *J. Geophys. Res.*, *110*(A12307), doi:10.1029/2005JA011270, 2005.

Weimer, D. R., D. M. Ober, N. C. Maynard, M. R. Collier, D. J. McComas, N. F. Ness, C. W. Smith, and J. Watermann, Predicting interplanetary magnetic field (IMF) propagation delay times using the minimum variance technique, *J. Geophys. Res.*, *108*(A1), doi:10.1029/2002JA009405, 2003.

Xu, L., SuperDARN-derived plasma convection: comparison with other data and application to field-aligned current measurements, Ph.D. Thesis, University of Saskatchewan, 2003.

Xu, L., A. V. Koustov, J. Thayer, and M. A. McCready, SuperDARN convection and Sondrestrom plasma drift, *Ann. Geophys.*, *19*(7), 749–759, 2001.

Xu, L., A. V. Koustov, J. S. Xu, R. A. Drayton, and L. Huo, A 2-D comparison of ionospheric convection derived from SuperDARN and DMSP measurements, *Adv. Space Res.*, *42*, 1259–1266, 2008.

Yu, Y., and A. J. Ridley, Response of the magnetosphere-ionosphere system to a sudden southward turning of interplanetary magnetic field, *J. Geophys. Res.*, *114*(A03216), 10.1029/2008JA013,292, 2009.

Appendix A

Coordinate systems

A.1 Geodetic and geocentric coordinate systems

In the geodetic coordinate system the Earth is modeled by an ellipsoid, see Figure A.1a. The semi-major axis (a) is along the equatorial plane and the semi-minor axis (b) is perpendicular in the vertical plane along the spin axis. The World Geodetic System for 1984 (WGS 84) reference ellipsoid with semi-major axis $a = 6378137.0$ m and semi-minor axis $b = 6356752.3142$ m is used. The surface of the ellipse is defined as the equilibrium surface of sea water.

For a point P above the surface of the Earth, latitude (λ_D) is defined as the angle between the equatorial plane and a line which passes through P and crosses the surface of the ellipsoid at right angles. Height (h) is defined as the length of this line above the surface of the ellipsoid. Longitude (ϕ_D) is the angular distance of a vertical plane passing through the center of the ellipsoid and P from a reference plane passing through the former Royal Observatory in Greenwich, UK. In this system the x_D and y_D axes lie in the ecliptic plane such that $y_D = 0$ at the reference meridian. The z_D-axis points perpendicular to the ecliptic plane through the North Pole.

Consider some vector parameter Q measured at point P. The components of Q may be resolved into components in the north, east, and vertical directions. The vertical direction ($\hat{v}_D$) points inward along the line defining latitude as shown. The north direction ($\hat{n}_D$) points toward the north pole perpendicular to $\hat{v}_D$, and the east direction ($\hat{e}_D$) completes a right-handed coordinate system.

In the geocentric coordinate system, the Earth is modeled by a sphere centered at the Earth's center of mass, see Figure A.1b. The z-axis is aligned with the Earth's spin axis, and the x and y axes point at right angles along the equatorial plane. For some point P above the surface of the Earth, latitude (λ) is defined as the angle between the equatorial plane and a line connecting the origin and P. Height (h) is defined as the length of this line

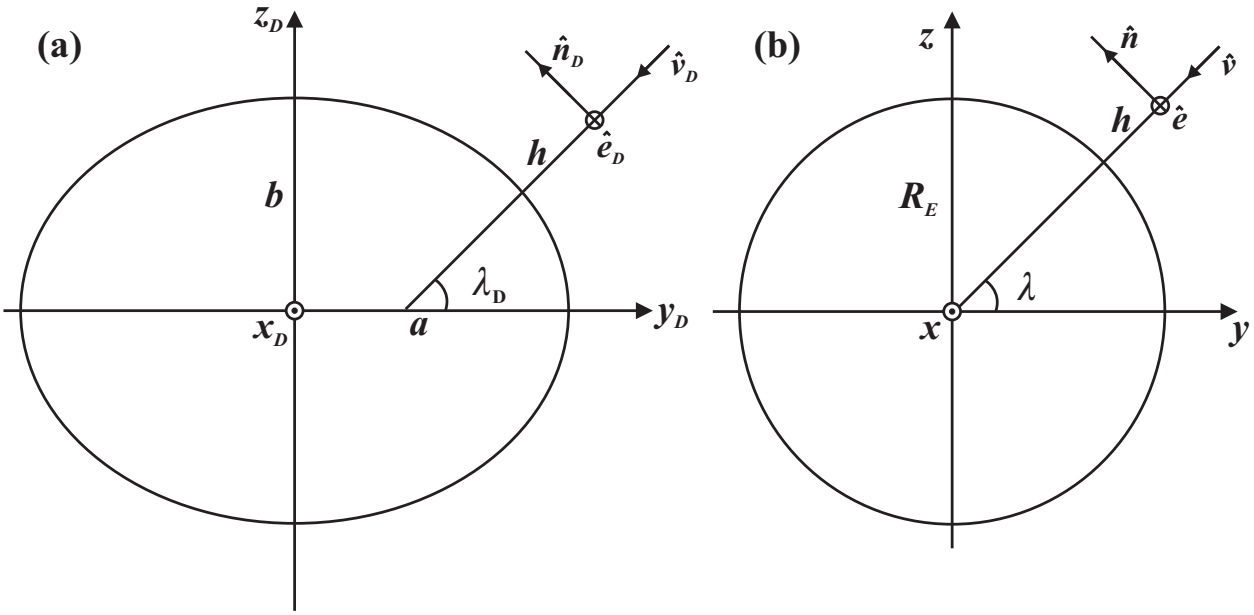

Figure A.1: (a)Representation of the geodetic coordinate system where λ_D is the geodetic latitude, a is the semi-major axis, b is the semi-minor axis, h is height from the surface of the Earth, and $\hat{n_D}$, $\hat{e_D}$, and $\hat{v_D}$ represent unit vectors in the north, east, and vertical directions. (b) Representation of the geocentric coordinate system where λ is the geocentric latitude, R_E is the radius of the Earth, h is height from the surface of the sphere, and $\hat{n}$, $\hat{e}$, and $\hat{v}$ represent unit vectors in the north, east, and vertical directions.

above the surface of the sphere. Longitude (ϕ) is the angular distance between the x-axis and a semi-circle joining the north and south poles through P, measured along the equatorial plane. The x-axis points toward the meridian passing through the former Royal Observatory in Greenwich, UK.

Consider some vector parameter Q measured at point P. The components of Q may be resolved into components in the north, east, and vertical directions. The vertical direction ($\hat{v}$) points radially inward as shown. The north direction ($\hat{n}$) points toward the north pole perpendicular to $\hat{v}$, and the east direction ($\hat{e}$) completes the right-handed coordinate system.

To transform coordinates of a point from the geodetic to the geocentric coordinate system, consider a point P some height h above the surface of a reference ellipsoid with semi-major axis a and semi-minor axis b. The coordinates of P are (λ_D, ϕ_D) in the geodetic coordinate system and (λ, ϕ) in the geocentric coordinate system, see Figure A.2. Geodetic

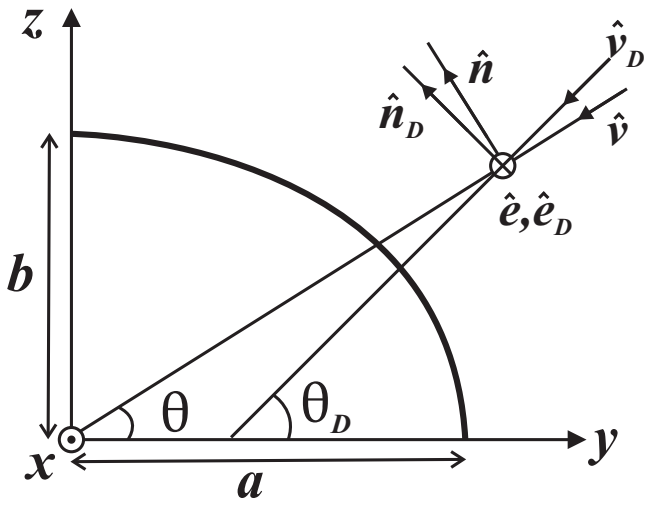

Figure A.2: Transformation from geodetic to geocentric coordinates.

coordinates may be converted to geocentric coordinates x, y, z using the formulas

$$x = \left(\frac{a}{\chi} + h\right) cos\lambda_D cos\phi_D, \tag{A.1}$$

$$y = \left(\frac{a}{\chi} + h\right) cos\lambda_D sin\phi_D, \tag{A.2}$$

$$z = \left(\frac{a(1-e^2)}{\chi} + h\right) sin\lambda, \tag{A.3}$$

where e is the eccentricity of the ellipse given by

$$e^2 = 1 - \frac{b^2}{a^2}, \quad \text{and} \tag{A.4}$$

$$\chi = \sqrt{1 - e^2 sin^2\lambda}. \tag{A.5}$$

The geocentric coordinates r, λ, and ϕ, where $\lambda = 90° - \theta$, are then

$$r = \sqrt{x^2 + y^2 + z^2}, \tag{A.6}$$

$$\lambda = \pi - acos\left(\frac{z}{r}\right), \tag{A.7}$$

$$\phi = atan\left(\frac{y}{x}\right). \tag{A.8}$$

Next, consider some vector measurement at P having components in the $\hat{n_D}$, $\hat{e_D}$, and $\hat{v_D}$ directions in the geodetic system. The $\hat{n_D}$, $\hat{e_D}$, and $\hat{v_D}$ directions may be transformed to the geocentric directions $\hat{n}$, $\hat{e}$, $\hat{v}$ which point as shown. The angle α between similar directions is

$$\alpha = \lambda_D - \lambda, \tag{A.9}$$

The directional unit vectors may be represented using the trigonometric identities

$$\hat{n} = cos\alpha\hat{n_D} - sin\alpha\hat{v_D}, \tag{A.10}$$

$$\hat{e} = \hat{e_D}, \tag{A.11}$$

$$\hat{v} = sin\alpha\hat{n_D} + cos\alpha\hat{v_D}. \tag{A.12}$$

Note that the transformation from geodetic to geocentric coordinates involves a single rotation about the $\hat{e_D}$ unit vector, and $\hat{e}$ and $\hat{e_D}$ therefore point in the same direction.

A.2 Geomagnetic coordinate system

The geomagnetic coordinate system is similar to the geocentric coordinate system. The only difference is a rotation of the geocentric axes x, y, and z to x', y', and z' so that the z'-axis is aligned along the magnetic dipole axis as defined by the International Geomagnetic Reference Field (IGRF) model, and the y' axis points perpendicular to the z axis (*Kivelson and Russell*, 1995). Table A.2 lists the geographic coordinates of the magnetic dipole axis for the years indicated.

For the transformation from geocentric to geomagnetic coordinates, consider a sphere of radius r described by both the geocentric coordinate system x, y, z and the corresponding geomagnetic coordinate system x', y', z' where the z' axis pierces the sphere at some latitude θ and some longitude ϕ measured in the geocentric system. The translation from geocentric to geomagnetic coordinates is equivalent to rotating x, y, z first by an angle ϕ about the z axis and then by an angle $\lambda = \frac{\pi}{2} - \theta$ about the already rotated y axis using the following

Table A.1: Geographic coordinates of the magnetic dipole axis.

Year	Latitude	Longitude
1945	78.47	291.47
1950	78.47	291.15
1955	78.46	290.84
1960	78.51	290.53
1965	78.53	290.15
1970	78.59	289.82
1975	78.69	289.53
1980	78.81	289.24
1985	78.97	289.10
1990	79.13	288.89
1995	79.30	288.59
2000	79.54	288.43

matrix transformation function

$$\begin{pmatrix} x' \\ y' \\ z' \end{pmatrix} = \begin{pmatrix} cos\lambda cos\phi & cos\lambda sin\phi & -sin\lambda \\ -sin\phi & cos\phi & 0 \\ sin\lambda cos\phi & sin\lambda sin\phi & cos\lambda \end{pmatrix} \cdot \begin{pmatrix} x \\ y \\ z \end{pmatrix}.$$

Consider some vector measurement located at point P having north, east, and vertical unit vectors $\hat{n}$, $\hat{e}$, $\hat{v}$ in the geocentric coordinate system. The corresponding components in the geomagnetic coordinate system are then given by

$$\begin{pmatrix} \hat{n'} \\ \hat{e'} \\ \hat{v'} \end{pmatrix} = \begin{pmatrix} cos\lambda cos\phi & cos\lambda sin\phi & -sin\lambda \\ -sin\phi & cos\phi & 0 \\ sin\lambda cos\phi & sin\lambda sin\phi & cos\lambda \end{pmatrix} \cdot \begin{pmatrix} \hat{n} \\ \hat{e} \\ \hat{v} \end{pmatrix}.$$

The radius of the geocentric spherical earth is taken to be $R_E = 6371.2$ km.

A.3 AACGM

When describing phenomena dependent on the Earth's magnetic field, it is convenient to use a magnetic-field dependent coordinate system. The corrected geomagnetic (CGM) coordinate system was developed for this purpose (*Gustafsson et al.*, 1992).

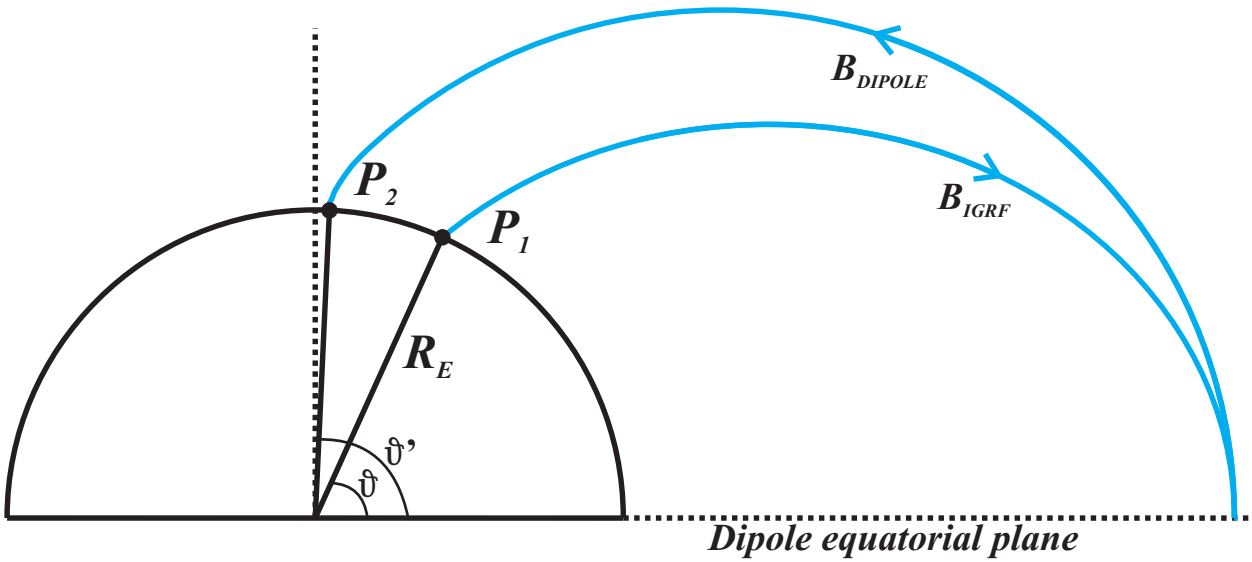

Figure A.3: A cartoon illustrating mapping of a point P_1 in the geocentric coordinate system with coordinates (λ, ϕ) to the CGM coordinates (λ', ϕ') at point P_2. The conversion is performed through a mapping of P_1 along the IGRF magnetic field line to the equatorial plane and back along the corresponding dipole magnetic field line. Although it is not indicated in this diagram, there may also be a deviation in the longitudinal coordinate ϕ to ϕ'.

To the first order the Earth's magnetic field may be represented by a magnetic dipole (*Hargreaves*, 1992). Although not strictly accurate, this approximation is useful for representing the inner magnetosphere within a few Earth radii (R_E). For a more accurate representation, it is common to express the geomagnetic field due to both internal and external sources by a spherical harmonic expansion over the surface of the Earth (*Blakely*, 1995). The IGRF fits all available observations of the Earth's magnetic field using spherical harmonic analysis up to a degree and order of at least 10 to generate a model of the Earth's magnetic field due to internal sources (*Blakely*, 1995). Since the Earth's magnetic field is constantly changing, coefficients for the spherical harmonic expansion are recalculated every five years. Coefficients in-between years are linearly interpolated from adjacent models, and coefficients following the last calculated model are predicted.

To map a point in the geocentric coordinate system to the CGM coordinate system both the dipole and the IGRF models are considered. Consider some point P_1 on the surface of a spherical Earth of radius R_E=6371.2 km (Figure A.3). The geocentric coordinates (λ, ϕ) are mapped to the CGM coordinate system by following the IGRF magnetic field line passing through P_1 to the dipole equator, and then following the dipole field line back to the surface

of the Earth at point P_2. The new coordinates (λ', ϕ') represent the CGM coordinate system. Transformation tables have been developed for speedy conversion from geographic to CGM coordinates (*Gustafsson et al.*, 1992).

The CGM coordinate system is limited. Points located above the Earth in the geographic coordinate system must first be mapped to the surface of the Earth before they can be transformed. Since the IGRF field line is mapped to the dipole equator, conjugate points in the northern and southern hemispheres are not mapped to conjugate locations in the CGM coordinate system, meaning points on the same IGRF field line are assigned different CGM coordinates. In addition, the CGM coordinate system is non-orthogonal; the reverse transformation from CGM to geocentric coordinates is not simple to perform. A new coordinate system was created to solve these problems.

The altitude adjusted corrected geomagnetic coordinate system (AACGM) (originally the Polar Anglo-American Conjugate Experiment (PACE) Geomagnetic (PGM) coordinate system) was adapted from the CGM coordinate system, and is described in *Baker and Wing* (1989) and *Bhavnani and Hein* (1994). Mapping point P_1 to P_2 is very similar, but P_1 and P_2 may be located on a shell of radius r=[R_E,R_E+2000 km], and the IGRF field line required for mapping is followed all the way down to the ground in the opposing hemisphere so that all points on the same IGRF field line have the same AACGM coordinates.

Field line mapping is a time consuming process; it is desirable to calculate AACGM coordinates directly from geographic coordinates (λ, ϕ). *Baker and Wing* (1989) accomplish this by first mapping an evenly spaced grid of coordinates (>2000 locations) at points (λ, ϕ) in the northern hemisphere along IGRF field lines to the ground in the southern hemisphere at points (λ_m, ϕ_m). The mapped coordinates in the southern hemisphere do not represent a similar evenly spaced grid and a relationship must be established between the geographic coordinates in the northern hemisphere, and their corresponding locations in the southern hemisphere. Before describing this relationship the northern and southern hemisphere coordinates undergo coordinate transformations. In the northern hemisphere, the geographic coordinates (λ, ϕ) are converted to a new coordinate system (λ_r, ϕ_r) having its z-axis aligned along the dipole axis of the CGM coordinate system. This is done by first rotating the geographic coordinate system about its z-axis by $-70.6°$, and then by $11.20°$ about the newly

rotated y-axis. In the southern hemisphere, coordinates (λ_m, ϕ_m) are transformed into rectangular coordinates x_m, y_m, z_m. The AACGM coordinates are then represented using a fourth order spherical harmonic expansion (*Baker and Wing*, 1989):

$$x_A = \sum_{l=0}^{L} \sum_{m=0}^{l} \left(A_{lm_x} cosm\phi_r + B_{lm_x} sinm\phi_r\right) P_l^m(cos\theta_r), \tag{A.13}$$

$$y_A = \sum_{l=0}^{L} \sum_{m=0}^{l} \left(A_{lm_y} cosm\phi_r + B_{lm_y} sinm\phi_r\right) P_l^m(cos\theta_r), \tag{A.14}$$

$$z_A = \sum_{l=0}^{L} \sum_{m=0}^{l} \left(A_{lm_z} cosm\phi - R + B_{lm_z} sinm\phi_r\right) P_l^m(cos\theta_r), \tag{A.15}$$

where $\theta_r = 90^\circ - \lambda_r$, $A_{lm_{x,y,z}}$ and $B_{lm_{x,y,z}}$ represent coefficients to be determined, $P_l^m(cos\theta_r)$ are the Associated Legendre Functions, and *Baker and Wing* (1989) truncate the series at L=4. The northern and southern hemisphere coordinate transformations described above improve convergence of the series and avoid singularities at the magnetic pole. Coefficients $A_{lm_{x,y,z}}$ and $B_{lm_{x,y,z}}$ are determined by minimizing the difference between x_m, y_m, z_m and x_A, y_A, z_A. Once the coefficients are determined, x_A, y_A, and z_A may be defined for any (λ, ϕ) location on the sphere and transformed to spherical coordinates (λ_A,ϕ_A). Coefficients are determined for altitudes of 0, 150, 300, and 450 km and can be interpolated for heights of 0-600 km (*Baker and Wing*, 1989). *Bhavnani and Hein* (1994) suggest solving the coefficients for altitudes of [0, 300, 1200] km and interpolating for altitudes of 0-2000 km. Since the magnetic field changes with time, the AACGM coefficients must be calculated for each set of IGRF coefficients, and care should be taken in using the correct coefficients for the year of observation. *Bhavnani and Hein* (1994) note that the AACGM coordinate system is not accurately defined at low latitudes or in the region of the South Atlantic Anomaly as closed magnetic field lines near the Earth are limited in altitude. They have developed an adapted AACGM technique to deal with these problems.

Figure A.4 shows the geocentric coordinate system on a rectangular grid with corresponding AACGM latitudes and longitudes overlaid (blue). It is important to realize that the conversion from geocentric to AACGM coordinates is not accomplished through a sim-

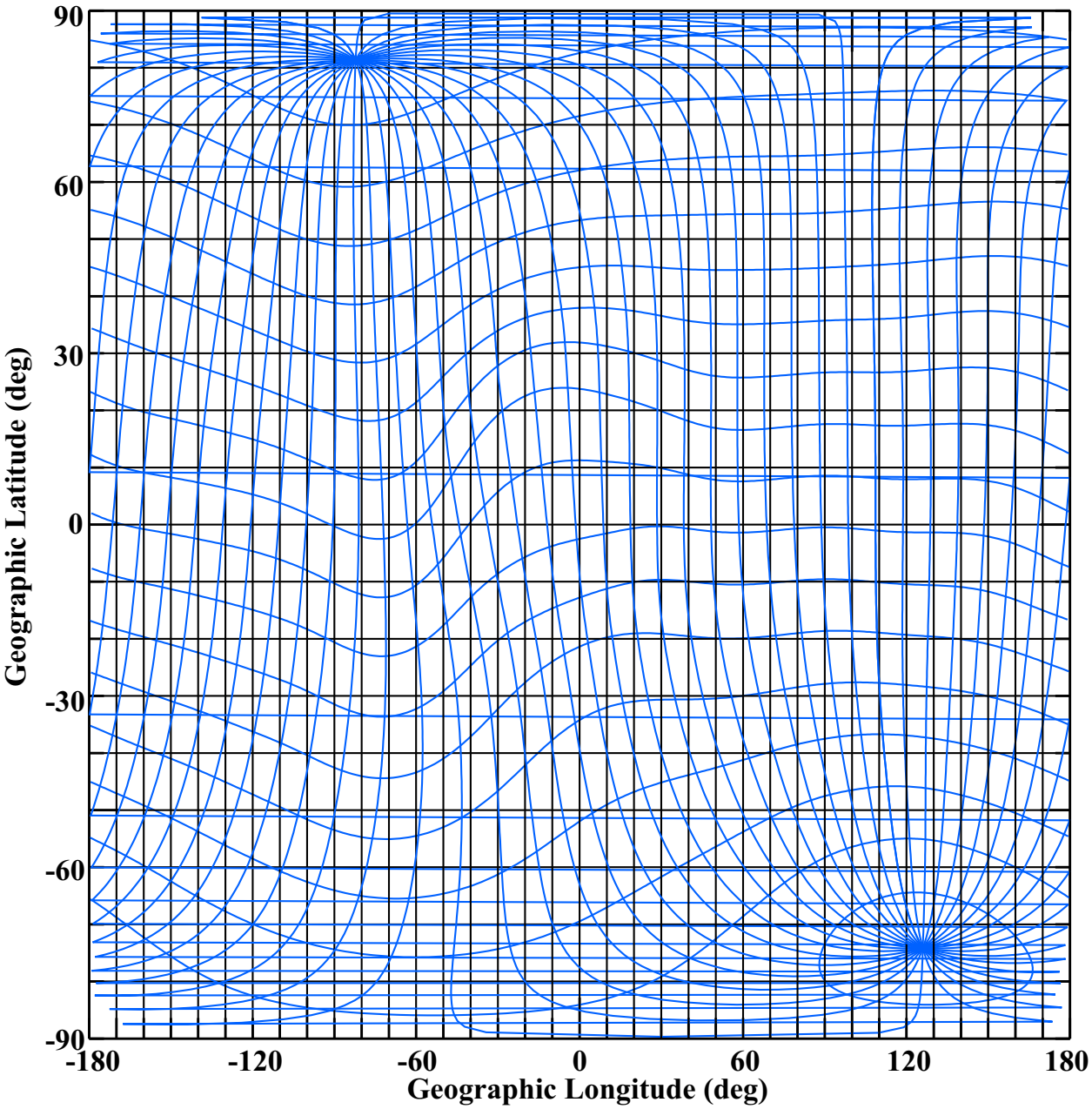

Figure A.4: Contours of constant AACGM latitudes and longitudes (blue) plotted in 10° increments in the geographic coordinate system (black).

ple series of rotations, and it is therefore difficult to transform vector directions between coordinate systems. A simple approximation may be performed by transforming both the head and tail of a given vector from one coordinate system to another and using spherical geometry to define the new azimuth.

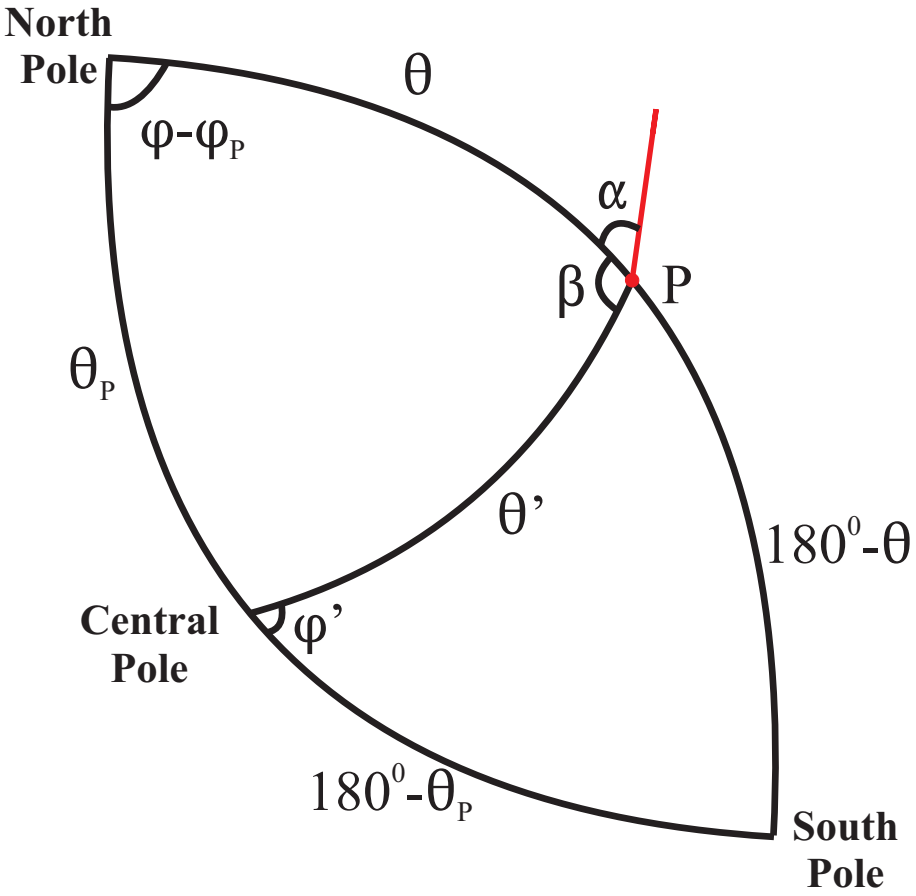

Figure A.5: A cartoon illustrating the transformation of a north-pole centered coordinate system to a system with an arbitrary pole.

A.4 Redefining the coordinate system about a central latitude

When measurements are made at coordinates roughly centered about some arbitrary location, it may be computationally helpful to re-define a spherical coordinate system about the central region of measurement or the 'central pole' opposed to the north pole. Consider a vector observation at point P having coordinates (θ, ϕ) with azimuth α in the original coordinate system, see Figure A.5. The central pole is located at (θ_P, ϕ_P). The coordinates (θ', ϕ') and pointing direction α' of the observed quantity are re-defined with respect to the central pole using spherical trigonometry from the following equations

$$cos\theta' = cos\theta cos\theta_p + sin\theta sin\theta_p cos(\phi - \phi_p), \tag{A.16}$$

$$cos(180^\circ - \theta) = cos\theta' cos(180 - \theta_p) + sin\theta' sin(180 - \theta_p) cos\phi', \quad \text{and} \tag{A.17}$$

$$\alpha' = \alpha + \beta, \quad \text{where} \tag{A.18}$$

$$cos\theta_P = cos\theta cos\theta' + sin\theta sin\theta' cos\beta, \tag{A.19}$$

where β is the angle formed between θ and θ', as shown in Figure A.5.